THE UNIVERSITY OF CHICAGO

NANOSCALE COORDINATION POLYMERS FOR CHEMOTHERAPEUTIC AND BIOLOGICAL CANCER THERAPY

A DISSERTATION SUBMITTED TO

THE FACULTY OF THE DIVISION OF THE PHYSICAL SCIENCES

IN CANDIDACY FOR THE DEGREE OF

DOCTOR OF PHILOSOPHY

DEPARTMENT OF CHEMISTRY

BY

CHRISTINA CHAN

CHICAGO, ILLINOIS

AUGUST 2019

© 2019

CHRISTINA CHAN

ALL RIGHTS RESERVED

To my family, old and new

TABLE OF CONTENTS

LIST OF SCHEMES

LIST OF TABLES

LIST OF FIGURES

LIST OF SYMBOLS AND ABBREVIATIONS

α-PD-L1	anti-PD-L1
%ID	Percent injected dose
%ID/g	Percent injected dose per gram
ACK	Ammonium-Chloride-Potassium
AEC	Amino-9-ethylcarbazole
ALT	Alanine aminotransferase
ANC	Absolute neutrophil count
APC	Antigen presenting cells
AST	Aspartate aminotransferase
ATCC	American Type Culture Collection
ATP	Adenosine triphosphate
AUC	Area under the curve
AUMC	Area under median curve
BRCA	Gene encoding breast cancer type 1 susceptibility protein
BSA	Bovine serum albumin
CAnP	Cisplatin and nab-paclitaxel
CAP	Cisplatin and paclitaxel
Cas9	CRISPR-associated protein 9
CCDC	Cambridge Crystallographic Data Center
Chol-DHA	Cholesterol-conjugated DHA
Chol-PTX	Cholesterol-conjugated PTX
Chol-pyro	Cholesterol-conjugated pyropheophytin a
CisPt	Cisplatin
CisPtbc	$Pt(NH_3)_2Cl_2$(biscarbamate)
CisPtbp	$Pt(NH_3)_2Cl_2$(bisphosphoramic acid)

CLSM	Confocal laser scanning microscopy
CRC	Colorectal cancer
CRISPR	Clustered Regularly Interspaced Short Palindromic Repeats
CRT	Calreticulin
CTLA-4	Cytotoxic T-lymphocyte associated protein 4
CYP	Cytochrome P450
D_2O	Deuterium oxide
dach	R, R-diaminocyclohexane
DAMP	Damage associated molecular pattern
DAPI	4′,6-diamidino-2-phenylindole
DCF	2',7'-dichlorofluorescein
DCM	Dichloromethane
DCs	Dendritic cells
DEPC	Diethylpyrocarbonate
DHA	Dihydroartemesinin
DLS	Dynamic light scattering
DMAP	4-N,N-dimethylaminopyridine
DMEM	Dulbecco's modified eagles medium
DMF	N,N-dimethylformamide
DMSO	Dimethyl sulfoxide
DNA	Deoxynucleic acid
DOPA	1,2-dioleoyl-sn-glycero-3-phosphate sodium salt
DOPC	1,2-dioleyl-sn-gylcero-3-phosphocholine
DOPE	1,2-Dioleoyl-sn-glycero-3-phosphoethanolamine
DOTAP	N-[1-(2,3-Dioleoyloxy)propyl]-N,N,N-trimethylammonium
DSPE	1,2-distearoyl-sn-glycero-3-phosphoethanolamine

DSPE-PEG2k	1,2-diastearoyl-sn-gylcero-3-phosphoethanolamine-N-[amino(polyethylene glycol)2000]
EDTA	Ethylenediaminetetraacetic acid
EGFR	Epidermal growth factor receptor
ELISA	Enzyme-linked immunosorbent assay
ELISpot	Enzyme-linked immunospot
EMT	Epithelial-to-mesenchymal transition
en	Ethylenediamine
EPR	Enhanced permeability and retention
ER	Endoplasmic reticulum
ESI	Electrospray ionization
Et_2O	Diethyl ether
EtBr	Ethidium bromide
EtOH	Ethanol
FBS	Fetal bovine serum
FDA	Food and Drug Administration
FITC	Fluorescein isothiocyanate
FOLFOX	Folinic acid, 5-fluorouracil, and oxaliplatin
FSC	Forward scatter
GM-CSF	Granulocyte-macrophage colony-stimulating factor
GMP	Gemcitabine monophosphate
GSH	Glutathione
H&E	Haemotoxylin and eoisin
H_2DCFA	2',7'-dichlorodihydrofluorescein diacetate
HMGB-1	High mobility group box 1
HNSCC	Head and neck squamous cell carcinoma
HR-LCMS	High resolution-LCMS

i.p.	Intraperitoneal
i.v.	Intravenous
IACUC	Institutional Animal Care and Use Committee
IC_{50}	Inhibitory concentration 50%
ICD	Immunogenic cell death
ICP-MS	Inductively Coupled Plasma Mass Spectrometry
IFN-γ	Interferon-gamma
IL-6	Interleukin 6
L2T	Leuciferin and tdTomato double labeled
LC/MS-MS	Liquid chromatography with tandem mass spectrometry
LC-MS	Liquid chromatography-mass spectrometry
m/z	Mass to charge ratio
MDSC	Myeloid derived suppressor cell
MFI	Median fluorescence intensity
MHC	Major histocompatibility complex
miRNA	micro RNAs
MPS	Mononuclear phagocyte system
MRT	Mean residence time
MSI	Microsatellite instability
MTD	Maximum tolerated dose
MTS	3-(4,5-dimethylthiazol-2-yl)-5-(3-carboxymethoxyphenyl)-2-(4-sulfophenyl)-2H-tetrazolium
nab	Nanoparticle albumin bound
NADPH	Reduced form of nicotinamide adenine dinucleotide phosphate
NCP	Nanoscale coordination polymer
NCP-1	NCPs carrying CisPtbp
NCP-1/PTX	NCPs carrying CisPtbp and chol-PTX

NCP-2	NCPs carrying Pt(dach)Cl_2bp
NCP-2/PTX	NCPs carrying Pt(dach)Cl_2bp and chol-PTX
NCP-Pt/Gem	NCPs carrying a Pt drug and GMP
NCP/siRNA	NCPs carrying naked siRNA
NCP/DSPE-siRNA	NCPs carrying DSPE-conjugated siRNA
NMR	Nuclear magnetic resonance
NSCLC	Non-small cell lung cancer
NT	Non-targeted
OCT	Optimal cutting temperature
OVA	Ovalbumin
OxPt	Oxaliplatin
OxPt/DHA	NCPs carrying OxPt and DHA
OxPt-bc	Pt(dach)(oxalate)(biscarbamate)
OxPt-bp	Pt(dach)(oxalate)(bisphosphoramidic acid)
PBS	Phosphate buffered saline
PD-1	Programmed cell death protein 1
PDI	Polydispersity index
PD-L1	Programmed death-ligand 1
PDT	Photodynamic therapy
PEG	Polyethylene glycol
PI	Propidium iodide
Pt(dach)Cl_2bp	Pt(dach)Cl_2(bisphosphoramic acid)
PtEN	NCPs containing $Pt^{IV}(en)_2$bp
Pt$(en)_2$bp	Pt$(en)_2$(bisphosphoramic acid)
PTTG1	Gene encoding securin protein
PTX	Paclitaxel
Pyrolipid	Lipid-conjugated pyrophoeophytin a

qPCR	quantitative polymerase chain reaction
r.t.	Room temperature
RNA	Ribonucleic acid
RNAi	RNA interference
RNase	Ribonuclease
ROS	Reactive oxygen species
RPMI	Roswell Park Memorial Institute 1640
RTV	Relative tumor volume
SENP6	Sentrin-specific protease 6
siRNA	small interfering RNA
SSC	Side scatter
$t_{1/2}$	Half-life
TAA	Tumor-associated antigen
TCR	T cell receptor
TEM	Transmission electron microscopy
TGF-β	Transforming Growth Factor beta
TGFBR2	Transforming Growth Factor Receptor Beta II
TGI	Tumor growth inhibition
THF	Tetrahydrofuran
TIL	Tumor infiltrating leukocyte
TMSBr	Bromotrimethylsilane
TNF-α	Tumor necrosis factor-alpha
TTR	Transtheyretin
VEGF	Vascular endothelial growth factor
WBC	White blood cell
Zn/DHA	Zn control NCPs carrying chol-DHA
Zn/PTX	Zn control NCPs carrying chol-PTX

ABSTRACT

Christina Chan: Nanoscale coordination polymers for chemotherapeutic and biological cancer therapy

Under the direction of Professor Wenbin Lin

Nanoscale coordination polymers (NCPs) were first developed as Pt(IV) – PO_4 – Zn coordination polymers to enhance the pharmacokinetics, biodistribution, and anticancer efficacy of platinum drugs. However, focusing on a single Pt chemotherapy underestimates the complexity of cancer treatment and the heterogeneity of patient needs. Chapter 1 broadly discusses the current cancer treatment options, as well as some of the current pitfalls and obstacles facing current treatment regimens, and a brief overview of previous nanoparticle and NCP work that serve as a foundation for Chapters 2-5. The work in this dissertation leverages chemistry to improve both proven and unproven drugs for anticancer therapy.

Chapter 2 describes the proof-of-concept of a nontoxic Pt(IV)-containing carrier delivering microRNA (miRNA) to limit the epithelial-to-mesenchymal transition (EMT) of human colorectal cancer (CRC) cells to limit metastasis formation and growth. An NCP was designed to contain a Pt(IV) prodrug of $[Pt(en)_2]^{2+}$, which released CO_2 upon degradation and aided the endosomal escape of a lipid-conjugated miR-655-3p mimic. This allowed for evaluation of the effects of miR-655-3p both in cells and in mice, reducing markers associated with EMT and cancer cell invasion/metastasis. NCP delivery of miRNAs opens the potential for limiting metastases without overdosing patients.

Chapter 3 details the design and development of an NCP combining a hydrophilic prodrug of cisplatin (CisPt) and a hydrophobic prodrug of paclitaxel (PTX). The release mechanisms and kinetics were investigated for each drug in solution and also in the blood, liver, or tumor of rodents.

NCP doublet therapy was compared head-to-head against the clinical combination of CisPt and albumin-bound PTX (CAnP) across a panel of human and murine ovarian, lung, and breast cancer models. In subcutaneous, experimentally metastatic, and spontaneously metastatic tumor models, NCPs at 1/8 the Pt dose consistently outperformed CAnP and lowered toxicity. NCPs incorporate prodrugs to reduce the toxicity of drug payloads and increase the efficacy, particularly on advanced and metastatic cancers.

Chapter 4 illustrates the potential for PTX in CRCs in combination with a dichloride oxaliplatin analogue [Pt(dach)Cl_2] and an immune checkpoint inhibitor. NCPs can sidestep metabolism of PTX by hepatic and intestinal P450s, and reduce the dose-limiting and dose-disrupting toxicities of these chemotherapies. The two drugs also synergize with an immune checkpoint inhibitor to alter the tumor microenvironments of murine CRC tumors by increasing the proportion of immunostimulatory tumor-infiltrating leukocytes and reducing the presence of suppressive immune cells. NCPs allow for low-dose, long-term management of CRCs in combination with current immunotherapy.

Chapter 5 reports the combination of an oxaliplatin (OxPt) prodrug with a highly reactive, endoperoxide containing antimalarial drug, dihydroartemesinin (DHA), and an immune checkpoint inhibitor. NCPs can isolate DHA in a hydrophobic environment and protect the reactive moiety from degradation in plasma. The endoperoxide in DHA can generate reactive oxygen species (ROS) and other radical species to synergize with OxPt to initiate an immune stimulatory effect and potentiate immunotherapy. NCPs stabilize reactive drugs and facilitate their use as anticancer drug agents, leading to the complete eradication of murine CRCs in combination with an immune checkpoint inhibitor.

NCPs represent a promising class of nanotechnology that can positively impact cancer therapy by improving currently existing drugs and facilitating delivery of other potential drugs. A diverse set of chemical and biological molecules can be stably loaded onto NCPs, improving both the pharmacokinetics and anticancer efficacy. However, experiments in solutions and small animals face certain limitations which should not be ignored. The research models are limited to relatively short timeframes with superficial readouts. Further investigation into the release mechanisms and long-term toxicity of NCPs are warranted for future clinical application.

ACKNOWLEDGMENTS

It is difficult to enumerate all the friends, colleagues, and mentors who have contributed to my work and my life over the course of this journey. I would like to start by thanking Prof. Wenbin Lin for his guidance over the last five years, and for giving me the opportunity to work on exciting and meaningful research. He has an unending enthusiasm for his work and a commitment to candid and critical discussion. These have served as an inspiration to me to keep challenging and pushing the boundaries of my own knowledge and experience in developing and pursuing projects. Under his mentorship, I have learned, grown, and accomplished more during my graduate tenure than I ever thought possible. For these, I am and will be forever grateful.

I would like to thank my committee members Prof. John Anderson and Prof. Steve Kron for their time and attention. I highly value the opportunity to present and discuss my work with them and appreciate their feedback and advice in reviewing my dissertation.

As a young and impressionable high school and undergraduate student, I was fortunate to to experience a lab setting courtesy of Prof. Vivian Yam from The University of Hong Kong and Prof. Kenneth Lo from City University of Hong Kong. I am so appreciative of the opportunities they gave me, as I cannot even begin to imagine how much precious time and material I must have wasted. I am also grateful for the continued contact, guidance, and support in my academic and scientific career since those times.

When I joined the Lin lab, I was extremely fortunate to meet and work with two extraordinary scientists in Dr. Chunbai He and Dr. Xiaopin Duan who extensively trained and developed my technical skills. They served as mentors, collaborators, sounding boards, and friends whom it has been my great pleasure to know and work with. I want to especially thank Dr. Nathan Thacker and

Dr. Zekai Lin for their advice, friendship, experimental help, and dogged effort over the years. I would also like to thank those others with whom I have worked most directly in Dr. Nining Guo, Wenbo Han, Xiaomin Jiang, Megan Rodriguez, and Selina Hes for the opportunity to both teach and learn from them, and proactively express my appreciation for their continuing effort in pursuit of our shared ideas. I would also like to acknowledge Dr. Christopher Poon, Dr. Kuangda Lu, Dr. Carter Abney, and Dr. Demin Liu for helpful advice and guidance as I was getting my feet wet and just starting to find my way. I want to thank all of those before and also Guangxu Lan, Kaiyuan Ni, Dr. Pengfei Ji, Yang Song, Dr. Dan Micheroni, and other friends for the shared conversations and experiences that have formed the basis of great memories. I would like to thank all other past and current group members for their contributions to our shared knowledge and those still to come who will improve and evolve this technology I have been privileged to work on.

I would also like to thank the NIH Chemistry-Biology Interface Predoctoral Training Program for funding support.

I especially want to thank my family, who have been endlessly kind, patient, supportive, and encouraging. This is for my parents, Paul and Connie Chan, who have dreamed of this milestone and my siblings, Matt and Johanna, who showed their love by laughing at my suffering from afar. This is for my uncle, Prof. Chi H. Chan, for his kind introductions and generous words of wisdom. And finally, this is for Andrew – my best friend and fiancé – without whom I would never have survived grad school. Thank you all for your love and support, for listening to me whine and vent and cry, and for keeping me afloat when I was drowning. This work is dedicated to all of you.

CHAPTER 1. Introduction and Background

1.1 Cancer and cancer therapies

Cancer refers to a group of diseases characterized by the aberrant and uncontrolled growth of cells, which can form growths referred to as tumors.[1] The classical hallmarks of cancer include: evading apoptosis, self-sufficiency in growth signals, insensitivity to anti-growth signals, tissue invasion and metastasis, limitless replicative potential, and sustained angiogenesis.[2] Typically, cancers are defined depending on the origin cell and where the tumor(s) are located, ranging from stage 0 precancerous cells to stage IV widespread disease.[3] In 2019, an estimated 1.8 million new cases of cancer will be diagnosed with an estimated 0.6 million cancer-related deaths, representing the second leading cause of death in the United States. Cancers in the digestive system (colon, pancreas, and rectum), respiratory system (lung and bronchus), and breast are particularly common, making up nearly half of all new cases.[4, 5] As of 2019, there are approximately 16.9 million cancer survivors, with 10.3 million patients surviving 5+ years after initial diagnosis due to current cancer treatments.[5] Patients' regimens can vary depending on the patient's age and health, cancer cell origin, disease stage, and biomarker expression on tumor cells.[6]

1.1.1 Surgery

The majority of patients with stage I disease will receive surgery, as removing all of the cancerous cells and some surrounding healthy tissue can be curative for patients with solid and localized tumors.[7] The margins of the excised tissue are examined for cancer cells and determined to be clear (cancer cell free within 5.0 mm) or positive (cancer cells present), with a traditional

cutoff of 5.0 mm.[8] However, full tumor resection is not always possible given the location of a tumor, when it is near a blood vessel.[9] In these cases, debulking surgery will often still occur to remove as much tumor as possible, allowing other cancer therapies to be more effective.[10]

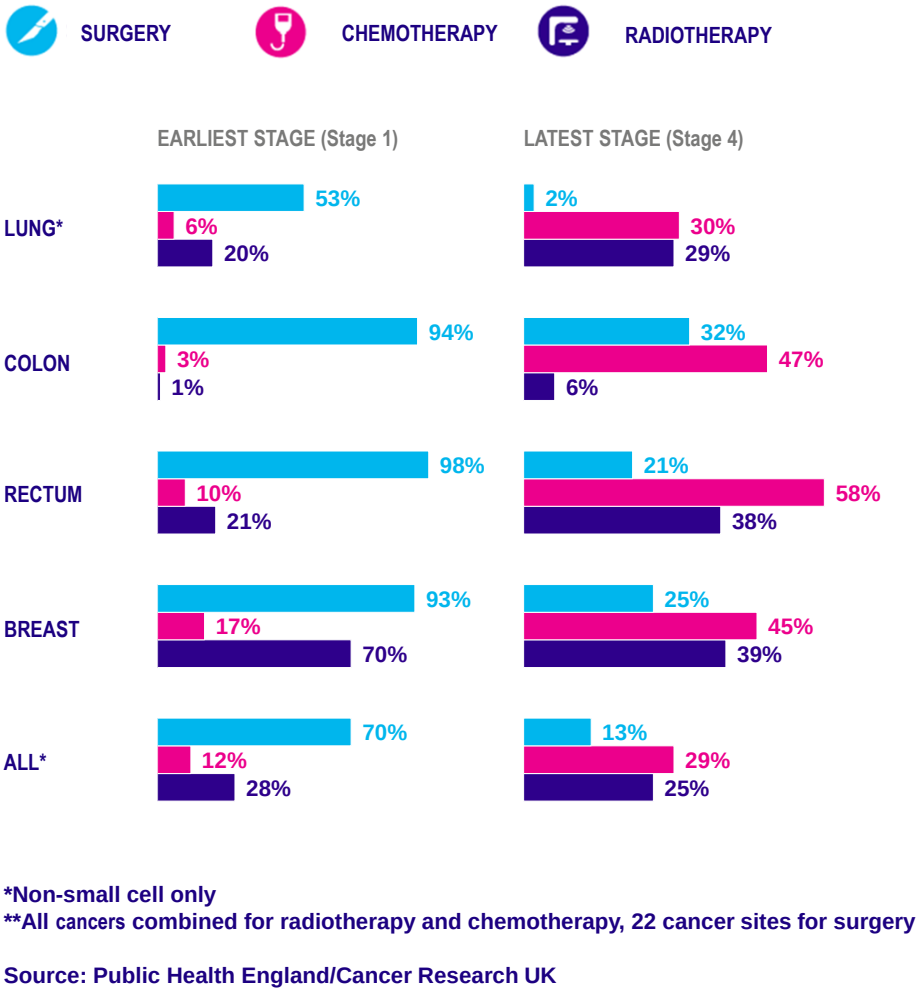

Figure 1-1 The most common cancers in England are treated in different ways, depending on the stage of disease at diagnosis. Adapted from Public Health England/Cancer Research UK[11, 12]

In England, 70% of all patients with stage I cancer will undergo surgery and those with colon, rectum, and breast cancer will receive surgery at rates of 93-98%. In comparison, stage IV cancer patients are treated with surgery 13% of the time. However, lung cancer patients are treated with surgery at much lower rates, with 53% of stage I patients and only 2% of stage IV patients, possibly

due to organ and tumor proximity to the heart (**Figure 1-1**).[11] In ovarian cancers, debulking surgery is common when the cancer has spread throughout the abdomen, removing visible tumors larger than 1 cm.[10, 13]

In addition to removing the primary tumors, surgeons will often remove nearby lymph nodes to evaluate whether the cancer has metastasized. In cases where the disease is not discovered until late-stage, surgery alone is typically not curative but can serve as palliation to reduce pain and/or increase quality of life.[7, 14] A survey of over 400 surgeons indicated that 20%+ of all cancer surgeries are for palliation, but literature rarely reports on these qualitative outcomes.[14 15]

1.1.2 Gene therapy

There are three primary areas of interest for gene therapy for the treatment of cancer: genetically engineered viruses, immunotherapy, and gene transfer.[16] Viruses can be engineered to carry genes to 1) infect cancer cells and produce proteins leading to cell death or 2) infect T cells to express a chimeric antigen receptor to specifically target and destroy cancer cells.[17] While the latter has recently been approved by the Food and Drug Administration (FDA),[15] I will instead focus on the two predominant forms of gene transfer: RNA interference (RNAi) and Clustered Regularly Interspaced Short Palindromic Repeats (CRISPR).[18]

Both small interfering RNA (siRNA) and micro RNA (miRNA) are classes of noncoding RNA known as RNAi. They each lead to transient gene suppression by inhibiting messenger RNA (mRNA) to limit gene translation and expression.[19, 20] Typically, siRNA are highly specific and fully complimentary to a single mRNA sequence, which is targeted for endonucleolytic cleavage.[19-21] A number of siRNAs targeting oncogenes, tumorigenic genes (cell cycle progression,

cell growth, and angiogenesis) or chemoresistance genes overexpressed in cancers have been investigated as cancer therapies in clinical trials.[21, 22] Down-regulating such genes can lead to pro-apoptotic and anti-metastatic effects in cancer cells, with theoretically negligible effects on healthy tissues.[23] In contrast to siRNAs, a single miRNA can regulate over a hundred genes and multiple miRNAs can have the same target gene, requiring only a partially complimentary sequence.[19, 24] Therapeutic miRNAs targeting tumorigenicity, drug resistance, epithelial-to-mesenchymal transition (EMT), and metastasis have been evaluated preclinically and clinically.[25] However, due to the broad range of targets, a single miRNA can have both pro- and anti-tumor effects in addition to effects on the tumor microenvironment and cancer-immune system interactions.[26] The dysregulation of miRNAs in cancerous tumors compared to healthy tissues has led to identification of therapeutic targets and also potential biomarkers.[24]

CRISPR is an integral part of antiviral immunity for bacteria, encoding DNA sequences derived from previous viral infections to help protect against future infections. CRISPR-associated protein 9 (Cas9) enzymes cleave DNA complimentary to CRISPR sequences in bacteria, or the guide RNA in engineered CRISPR-Cas9 systems.[27, 28] By editing the host DNA, CRISPR-Cas9 systems permanently modify the gene sequence to introduce point mutations or alter the genome according to template RNA strands. With regards to cancer, CRISPR-Cas9 allows for development of more representative cancer models by engineering genetic knockouts or introducing point mutations into oncogenes.[28, 29] High-throughput screening using CRISPR systems also facilitate the discovery of therapeutic targets, such as Werner syndrome ATP-dependent helicase in cancers with microsatellite instability (MSI).[30, 31] Therapeutically, CRISPR gene editing can also be used to edit genes related to drug efflux and drug inactivation in order to restore chemosensitivity.[32, 33]

Table 1-1 Chemotherapy and small molecule inhibitors commonly used in cancer therapy.

Group	Target	Function	Approved drugs
Alkylating agents	N7 of guanine	Alkylate DNA to interfere with DNA replication	Cyclophosphamide, Chlormethine, Uramustine
Platinum drugs	Purine base	Crosslink with DNA for DNA damage and to interfere with DNA replication	Cisplatin, Oxaliplatin, Carboplatin, Nedaplatin, Lobaplatin
Antimetabolite	DNA or deoxynucleotide	Incorporation of chemically altered nucleotide or deplete deoxynucleotide supply	5-Fluorouracil, Capecitabine, Gemcitabine, Methotrexed, Pemetrexed, Daunorubicin, Doxorubicin
Topoisomerase inhibitors	Enzyme maintaining phosphodiester backbone of DNA	Block ligation of DNA strands, leading to unrepaired single and double strand breaks	Irinotecan, Camptothecin, Etoposide, Doxorubicin, Mitoxantrone
Microtubule stabilizer	Microtubule	Stabilize or destabilize microtubules to interfere with mitosis	Paclitaxel, Docetaxel, Vincristine, Colchicine, Eribulin
Tyrosine kinase inhibitors	BCR-ABL	Inhibit activity of pathway leading to uncontrolled cell division	Imatinib, Dasatinib, Nilotinib
	MAP/ERK	Inhibit activity of pathway leading to uncontrolled growth	Trametinib, Cobimetinib, Binimiteb
	EGFR	Inhibit activity of pathway leading to uncontrolled cell division and angiogenesis	Gefitinib, Erlotinib, Afatinib (Cetuximab)[a]
	VEGF	Inhibit activity of pathway stimulating blood vessel formation	Sorafenib, Sunitinib, Axitinib (Bevicuzumab)[a]

[a] These are clinically approved antibodies against the same targets.

1.1.3 Chemotherapy

Serendipitously discovered in the 1940s, chemotherapy is an umbrella term for small molecules, but commonly refers to cytotoxic drugs which kill rapidly dividing cells.[34, 35] Based on myelosuppression in soldiers exposed to mustard gas, nitrogen mustard was first administered into the bloodstream of a patient with lymphoma. The masses briefly regressed due to DNA alkylation

at the N7 of guanine, inhibiting strand separation and subsequent replication.[34] Since then, many other drugs have also been established to inhibit cell division (**Table 1-1**). Platinum anticancer drugs, first discovered in 1979, can similarly crosslink to DNA;[36] antimetabolites can be directly incorporated (as chemically altered nucleotides) or deplete the nucleotides required for DNA replication;[37] natural products can inhibit topoisomerases which uncoil DNA or stabilize microtubules to disrupt mitotic spindle formation and depolymerization.[38-40]

1.1.4 Small molecule inhibitors

Small molecule inhibitors have specific molecular targets, typically tyrosine, serine, or threonine kinases related to cell proliferation, metastasis, and angiogenesis.[41] Some cancers have specific mutations which can be targeted, such as chronic myeloid leukemia which leads to the abnormal gene and protein BCR-ABL. Long-term disease management with a potent Abl tyrosine kinase inhibitor, imatinib (Gleevec), was associated with 83.3% overall survival rate at 10 years and acceptable toxicities.[42, 43] The specificity of the inhibitor, however, also leads to low inhibitory effect on a highly related tyrosine kinase with similar sequence identity (47%) and structural scaffolds.[44] Other tyrosine kinase inhibitors target the MAP/ERK pathway, a kinase cascade which leads to proliferation,[45] or growth factors. Epidermal growth factor receptor (EGFR) and vascular endothelial growth factor (VEGF), which also have intrinsic tyrosine kinase activity, are often constitutively active in human tumors.[46, 47] EGFR and VEGF expression both result in signals for angiogenesis, the formation of new blood vessels, which can lead to tumor growth and metastasis (**Table 1-1**).[46, 47] Such small molecule inhibitors are cytostatic rather than cytotoxic, inhibiting tumor growth rather than direct cell killing.

1.1.5 Immunotherapy

Antibodies naturally circulate in the blood as part of the immune response to protect against foreign substances, but exogenous antibodies can also be introduced as immunotherapy. These can be targeted therapies like the small molecule inhibitors (**Table 1-1**), for vascular and stromal cell ablation, to mediate an immune response against tumor cells, or for direct cell killing.[48] Though a cancer-specific group has not been found, antibodies have among the highest tumor specificity of targeted therapies. Target molecules can be involved in hematopoietic differentiation, growth and differentiation signaling, angiogenesis, tumor support, among other categories. The most successful antibodies for cancer therapy have been those targeting the ERBB family (including EGFR) and VEGF.[48] Patients treated with EGFR-specific antibodies have shown improved treatment response, disease control, and overall survival.[49, 50]

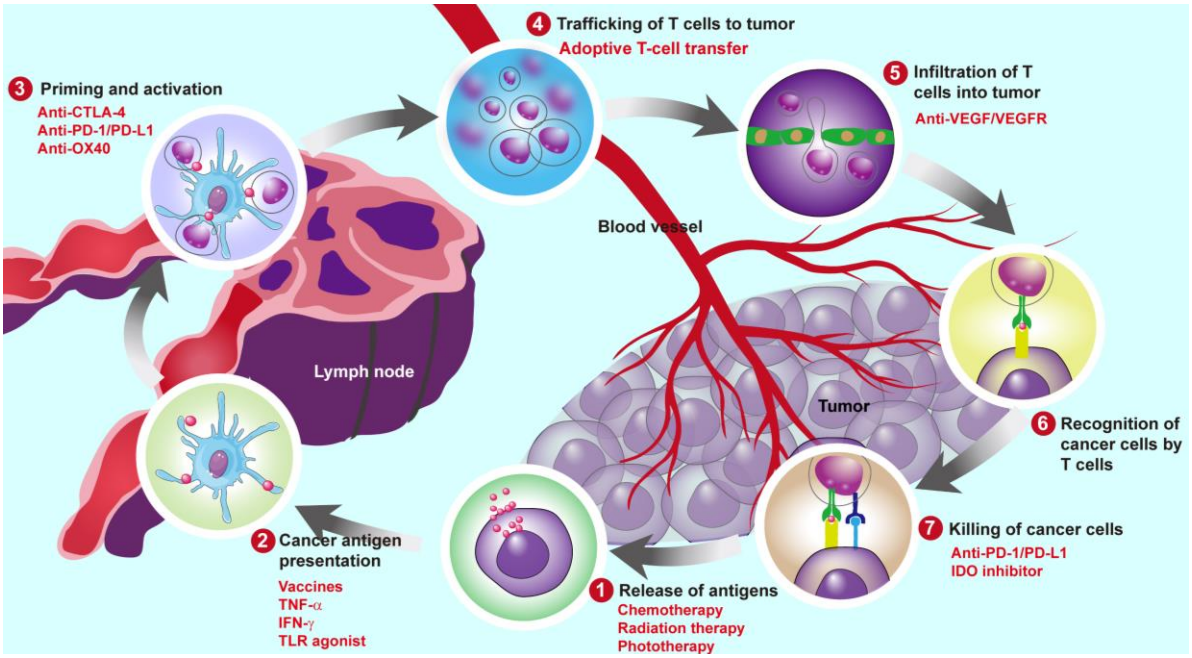

Figure 1-2 The cancer immunity cycle and effects of various cancer therapies. Dying cancer cells release antigens, which are taken up by dendritic cells and presented to T cells in the lymph node. The T cells infiltrate the tumor and selective recognize and kill cancer cells. Reprinted from *Angew Chem Int Ed Engl* **58**, 670-80 (2019).[51]

Stimulation of the immune system is another form of immunotherapy, which can target any of the key steps of the anti-cancer immune cycle (**Figure 1-2**):[52] first, antigens released from cancer cells are captured by antigen-presenting cells (APCs). Then, danger associated molecular patterns (DAMPs), such as pro-inflammatory cytokines and factors, released by the dying tumor cells signal APC maturation. Activated APCs travel to the lymph nodes to present the tumor antigens on major histocompatibility complex (MHC) I and MHC II molecules to T cells, resulting in the priming and activation of effector T cell responses against cancer-specific antigens. Finally, activated effector T cells traffic to and infiltrate the tumor bed where they specifically recognize cancer cells through interactions between T cell receptor (TCR) and MHC I-bound cognate antigen and kill cancer cells. Killing the cancer cell releases additional tumor-associated antigens (TAAs) to increase the breadth and depth of the immune response in subsequent revolutions of the cycle.[51]

It is now established that ablative cancer treatments (e.g. radiotherapy, photodynamic therapy, hyperthermia and photothermal therapy) and certain chemotherapeutics can cause tumor cell death in an immunogenic way.[53, 54] This immunogenic cell death (ICD) is characterized by release of TAAs, DAMPs, and pro-inflammatory cytokines, which facilitates the presentation of TAAs to adaptive immune cells, eliciting an antigen-specific immune response against a broad spectrum of solid tumors.[55] Ultimately, ICD can enhance immune stimulatory or subvert immune suppressive effects for the activation, proliferation, and tumor infiltration of T cells to synergize with current immunotherapies. Such in situ “tumor vaccines” provide a new way to broaden and enhance immunotherapy by combining with ICD-inducing modalities, such as radio-, photo-, and chemotherapy.

Cancer vaccines have been developed to prevent cancers associated with exposure to certain viruses or to treat cancers. Only Sipuleucel-T has been FDA approved for the treatment of

advanced prostate cancer.[56] Peripheral-blood mononuclear cells are taken from the blood, activated with the prostate antigen prostatic acid phosphatase and granulocyte-macrophage colony-stimulating factor (GM-CSF), and reintroduced into the patient.[57] Similarly, adoptive cell therapy takes a patient's T cells, expands them ex vivo, and then transfers them back into the patient. In some cases, the T cells are altered by introducing chimeric antigens receptors to the surface before re-introduction into the patient to make them more cytotoxic and specific to cancer cells.[58, 59] Certain activated T cells can be cytotoxic to cancer cells, but inhibitory signals known as immune checkpoints can inhibit T cell activity and proliferation.[59-62] Small molecules have been designed to block these signals,[63] in addition to targeted antibodies recently approved by the FDA for the treatments of multiple cancers, including melanoma, colorectal cancer, and non-small cell lung cancer (NSCLC).[64]

1.1.6 Photo- and radiotherapy

External X-rays, light waves, or magnetic waves can be applied to tumors for antitumor efficacy with spatiotemporal control. Photodynamic therapy (PDT) is a clinically used, minimally invasive therapeutic procedure with a two-step modus operandi involving the administration of a photosensitizer followed by irradiation with a specific wavelength light. Upon irradiation, photosensitizers in the presence of oxygen can generate highly cytotoxic ROS (e.g. $^1O_2$) to cause oxidative stress-based cell death and disrupts tumor vasculature.[65, 66] The shallow penetration depth of light through tissue, however, limits the use of PDT to superficial tumors such as skin and head and neck cancers.[67]

Light or magnetic fields can be applied to heat tissue to 39-45 °C, causing thermal ablation of cancer cells.[68, 69] Theoretically, photothermal agents are non-toxic in the dark and the light is locally applied on the tumor area, leading to high treatment efficacy with few side effects.[70, 71] An important consideration is that normal tissues may also be severely damaged under conventional hyperthermia treatment. Thus, specifically heating the tumor region to the desired temperature without damaging surrounding normal tissues is a major technical barrier.[72]

Radiotherapy is a powerful therapeutic modality for cancer, commonly used for its ability to kill cancer cells by causing DNA double strand breaks, which is not limited by tissue penetration. Nearly half of all patients will benefit from radiotherapy, with approximately half receiving treatment with curative intents and half for palliation. However, the radiation dose has to be tightly controlled to balance therapy and toxicity.[73]

1.1.7 Combination therapy

Concurrent use of two or more drugs or treatment modalities is considered combination therapy, such as the use of multiple chemotherapies or the combination of chemotherapy with radiotherapy.[74] Combination therapy has become a point of emphasis as it can theoretically increase chances of addressing tumor heterogeneity and drug resistance. Cancers involve multiple pathways and often develop different successive mutations and intrinsic or acquired resistance as they progress. In conventional mono-chemotherapy, it was long established that patients became less sensitive over the treatment courses as their cancers acquired resistance to the drug. Administration of multiple chemotherapeutics as a combination therapy has become a standard practice in conventional chemotherapy in order to take advantage of distinct mechanisms of action

to overcome cross-resistance and achieve synergistically enhanced therapeutic outcome without proportionally increasing toxicities.[75] Multiple treatment modalities are often combined clinically: surgery plus chemotherapy, chemotherapy plus radiotherapy, surgery plus radiotherapy, and immunotherapy plus chemotherapy are all common treatment paradigms. Furthermore, many different chemotherapies, radiotherapy, photodynamic therapy, and photothermal therapy affect the immune response to cancer, leading to natural synergies with immunotherapy.[51, 54]

1.2 Obstacles facing current cancer therapies

Despite advancements in cancer therapy, there are still many obstacles to overcome related to drug stability, toxicity, and disease progression (**Figure 1-3**).[76] In most instances, a small molecule or biological entity is introduced systemically into patients where it can interact with proteins in the blood or organs other than the tumor.[77] Particularly, small molecule chemotherapies and targeted therapies can be chemically altered in circulation, while gene therapies can be cleaved by nucleases leading to poor pharmacokinetics.[78, 79] Many drugs will be trafficked to the liver and degraded by enzymes before they can reach the tumor, leading to low tumor drug bioavailability.[80] In turn, this leads to high clinical doses of drug and significant toxicities (**Table 1-2**).[81] In addition to systemic distress (i.e. nausea, fatigue, and pain), cancer treatment can lead to damage to health organs (such as cardiomyocyte damage, cardiovascular toxicity, or myelosuppression), and even secondary cancers.[81] Though some toxicities can be managed with the introduction of other drugs or subside after cessation of treatment, some lead to irreversible damage and can lead to a lower quality-of-life for years.[82] During the treatment cycle, these side effects can be dose-limiting, dose-reducing, or dose-delaying leading to suboptimal treatment schedules.[83]

Table 1-2 Most common adverse effects of cancer therapy. Reprinted from *Nat Rev Clin Oncol* **9**, 471-478 (2012).[81]

Therapy	Associated effects	Examples
Surgery	Inflammation; anatomical complications or infection	Lymphoedema and pain induced by abdominal surgery Loss of voice after neck surgery
Radiotherapy	Damage to noncancerous tissue; other effects are site-dependent	Pneumonitis induced by thoracic radiation Fatigue, cognitive dysfunction, mood disorder induced by brain radiation Gastroenteritis (nausea, vomiting, diarrhoea, weight loss) induced by abdominal radiation
Cytotoxic chemotherapy	Cell death in noncancerous cells; systemic effects include, but are not limited to, central and peripheral neurotoxicity, cardiotoxicity, gastrointestinal toxicity and immune suppression	Peripheral neuropathy following taxane and platinum therapy Fatigue, cognitive dysfunction, depression induced by chemotherapy Cardiomyocyte damage (irreversible; can lead to left ventricular dysfunction and heart failure) induced by anthracyclines Vascular complications (ischaemia, thrombosis) induced by antimetabolites Gastroenteritis induced by chemotherapy Neutropenia (leading to high risk of infection) induced by chemotherapy
Hormone therapy	Disrupts endocrine system	Osteoporosis induced by androgen-deprivation therapy and aromatase inhibitors Sexual dysfunction induced by oestrogen therapy
Targeted therapy	Disrupts signaling pathways required for normal cell growth and function; other effects are pathway-dependent	Metabolic toxicities (hyperglycaemia, hypertriglyceridaemia, hypercholersterolaemia) induced by mTOR inhibitors Dermatologic toxicity induced by EGFR inhibitors Cardiovascular toxicity (hypertension, thrombosis, angioedema) induced by tyrosine kinase inhibitors and angiogenesis inhibitors Immunosuppression induced by B-cell therapy

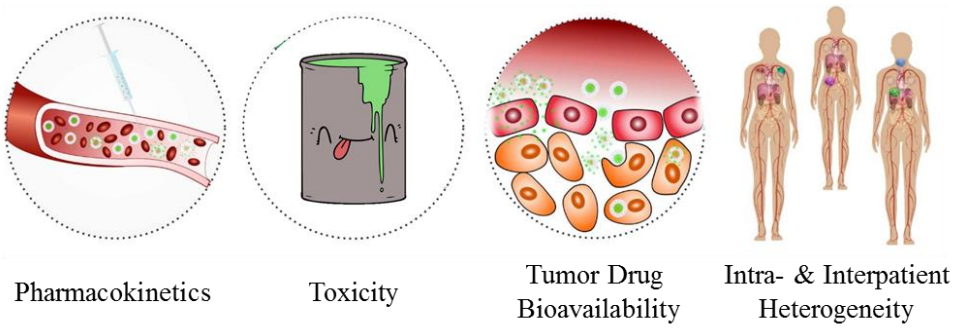

Figure 1-3 Barriers facing current cancer therapies include pharmacokinetics, toxicity, tumor drug bioavailability, and cancer cell heterogeneity. Adapted from *Adv Drug Deliv Rev* **91**, 7-22 (2015).[80]

The heterogeneity of cancer cells in tumors also leads to new obstacles developing over the course of treatment. Tumors can have intrinsic or acquired resistance mechanisms, including upregulation of pathways inhibiting apoptosis, alterations to drug metabolism and efflux, enhancing DNA repair, or amplification of certain genes. Over the repeated doses of a treatment regimen, the resistant cells will be more likely to survive and proliferate. Similarly, metastases also require a degree of selection and adaptation – most tumor cells are poorly suited to colonize and proliferate in tissues outside of the primary tumor.[84, 85] Those tumor cells which can form metastases are typically more resistant to treatment.[86, 87] Unfortunately, many cancers including NSCLC and ovarian cancer are often not diagnosed until they are late stage and/or metastatic.

1.3 Nanoparticles with biomedical applications

Nanoparticles refer to materials with sizes, typically from 1-100 nanometer (nm), which can be developed with many different biocompatible materials, molded into different sizes and shapes, and allow different surface chemistry.[88] Broadly, there are inorganic nanoparticles (e.g. quantum dots, metal oxides, and colloidal gold), organic nanoparticles (e.g. liposomes and polymer

micelles), and protein-bound drugs (**Figure 1-4**). In cancer therapy, nanoparticles can be used for imaging, diagnostics, or drug delivery, with intrinsic activity or drugs loaded into the core or surface. Inorganic nanoparticles often have surface functionalization with organic molecules or polymers to adjust the physical and chemical properties. The surface ligands can be chosen to limit aggregation, promote binding, or bind to biomolecules. Quantum dots (2-6 nm) are semiconducting nanoparticles made of silicon, germanium, or cadmium with tunable optical properties, making them ideal for bioimaging and sensing applications.[89-91] Cornell's version of quantum dots (< 10nm) are near-infrared-labeled silica nanoparticles designed to map lymph nodes in cancer patients.[92] Metal oxides including titanium,[93] zinc,[94] iron, magnesium, zirconium, and hafnium oxides (10-400 nm) have been explored for biomedical applications from MRI imaging, drug delivery, radioenhancement, to cell adhesion promotion and anti-inflammatory effects.[95] Among these, iron oxide nanoparticles have been the most studied both in laboratories and clinically as iron supplements, MRI contrast agents, and agents for local tissue hyperthermia of glioblastomas.[96] Similarly, colloidal gold (2-150 nm) can have different optical properties depending on the size and shape of the nanoparticle. Its physical, electronic, and chemical properties theoretically allow for a wide variety of applications including drug delivery, sensing, and radiosensitization.[97, 98] Liposomes (20-250 nm) are composed of phospholipids that assemble into unilamellar or multilamellar vesicles, with an aqueous core that can load hydrophilic drugs and a lipid bilayer for hydrophobic drugs.[99] Polymer micelles (20-250 nm) generally load poorly water-soluble drugs into the core of amphiphilic block copolymers consisting of a hydrophobic domain (e.g. lipids or polyesters like poly(Lactic acid) or poly(L-lysine)) and a hydrophilic domain (e.g. polyethylene glycol (PEG) or poly(N-vinyl pyrrolidone)).[100] Protein-bound drugs linking a ligand to a protein carrier are also considered by some to be nanoparticles. Typical carriers include

gelatin, collagen, casein, whey protein, and albumin (i.e. ovalbumin, bovine serum albumin, and human serum albumin). Albumin nanoparticles can also be surface modified with functional groups for covalent bonding to drugs rather than noncovalent binding in the protein binding pockets.[101]

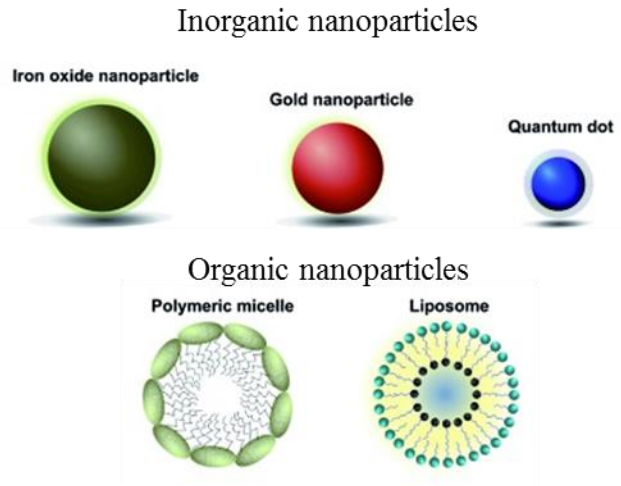

Figure 1-4 Types of nanoparticles commonly used for biomedical applications. Adapted from *Chem Sci* **8**, 63-77 (2017).[89]

1.3.1 Rationale for cancer therapy by nanoparticles

Nanomedicines that carry therapeutic agents may hold the potential to improve tumor control and reduce treatment side effects by improving the pharmacokinetics and tumor deposition of the drug payloads.[102] Pharmacokinetics can be improved by controlling the nanoparticle size to be greater than 10 nm and less than 200 nm to avoid clearance by the reticuloendothelial and mononuclear phagocyte systems.[103] In animal models, monotherapy nanomedicines successfully take advantage of prolonged blood circulation times to efficiently deliver therapeutic agents to improve biodistribution. In 1986, a passive targeting effect of nanoparticles to tumors was described by Matsumura and Maeda, now known as the enhanced permeability and retention (EPR)

effect.[92] Nanomedicines have since been modified with active targeting ligand and/or endowed with controlled release properties to further enhance tumor selectivity and drug deposition in cancer cells which in turn enhances efficacy and reduces toxicity.[102]

1.3.2 Preclinical data

Over 40,000 pieces of literature have been published on nanoparticle delivery due to the favorable properties discussed. A meta-analysis of publications reporting nanoparticle delivery in animals reported that only a median of 0.7% injected dose (% ID) of injected nanoparticles reached the tumor.[104] Study and nanoparticle design both impacted the observed tumor uptake: inorganic nanoparticles and near neutral zeta-potential nanoparticles showed greater uptake than organic nanoparticles or charged nanoparticles, respectively. Organic nanoparticles are degraded and eliminated by cells; charged nanoparticles have greater uptake by macrophages. Rod-shaped nanoparticles were found to have the highest tumor uptake, over spherical, plate, or flake-shaped nanoparticles, in contrast to other studies showing spherical nanoparticles internalized at higher rates than other shaped nanoparticles in cell culture. [104-107] Furthermore, orthotopic tumors showed higher median tumor uptake compared to heterotopic tumors.[104]

A number of inorganic nanoparticles and organic nanoparticles have shown strong efficacy in preclinical results, which have led to investigations in clinical trials.[105, 106] The original report of Aurolase, silica gold nanoshells coated with PEG, in 2003 showed thermal ablation when a near-infrared light was applied, leading to cell shrinkage and thermal damage.[105, 108] The hafnium oxide (HfO_2) nanoparticle, NXBTR3, sensitizes mice to radiation, leading to decreased colony-forming potential and controlling or eradicating tumor growth in mice receiving concurrent irradiation.[109]

A liposomal version of cisplatin showed increased cytotoxicity in cell lines and decreased nephrotoxicity, while maintaining strong anticancer efficacy in a tumor xenograft.[110, 111] Similarly, polymeric micelles and nanoparticles of docetaxel, cisplatin, and camptothecin (known as BIND-014, NC-6004, and CRLX101, respectively) have shown near equivalent anticancer efficacy in tumor xenografts, but reduced toxicity in rodents in preclinical studies.[112-114] These promising results, however, have not always been replicated in the clinic.

Table 1-3 List of FDA-approved nanomedicines stratified by material category before 2016. Adapted from *Pharm Res* **33**, 2373-2387 (2016).[96]

Name	Material Description	Nanoparticle Advantage	Indication(s)	Year(s) approved
Polymer Nanoparticles – synthetic polymer particles combined with drugs or biologics				
Eligard® (Tolmar)	Leuoprolide acetate and polymer (PLGH (poly (DL-Lactide-co-glycolide))	Controlled delivery of payload with longer circulation time	Prostate Cancer	2002
Neulasta®/pegfilgratism (Amgen)	PEGylated GCSF protein	Improved stability of protein through PEGylation	Neutropenia, Chemotherapy induced	2002
Oncaspar®/pegaspargase (Enzon Pharmaceuticals)	Polymer-protein conjugate (PEGylated L-asparaginase)	Improved stability of protein through PEGylation	Acute lymphoblastic leukemia	1994
Liposome formulations combined with drugs or biologics				
DaunoXome® (Galen)	Liposomal Daunorubicin	Increased delivery to tumour site; lower systemic toxicity arising from side-effects	Karposi's Sarcoma	1996
Marqibo® (Onco TCS)	Liposomal Vincristine	Increased delivery to tumour site; lower systemic toxicity arising from side-effects	Acute Lymphoblastic Leukemia	2012
Onivyde® Merrimack	Liposomal Irinotecan	Increased delivery to tumour site; lower systemic toxicity arising from side-effects	Pancreatic Cancer	2004

Table 1-3 continued List of FDA-approved nanomedicines stratified by material category before 2016. Adapted from *Pharm Res* **33**, 2373-2387 (2016).[96]

Liposome formulations combined with drugs or biologics				
Doxil® /Caelyx™ (Janssen)	Liposomal doxorubicin	Improved delivery to site of disease; decrease in systemic toxicity of free drug	Karposi's Sarcoma; Ovarian cancer; multiple myeloma	1995 2005 2008
Protein nanoparticles combined with drugs or biologics				
Abraxane®/ABI-007 (Celgene)	Albumin-bound paclitaxel nanoparticles	Improved solubility; improved delivery to tumor	Breast cancer; NSCLC; Pancreatic cancer	2005 2012 2013
Ontak® (Eisai Inc)	Engineered Protein combining IL-2 and diphtheria toxin	Targeted T-cell specificity; lysosomal escape	Cutaneous T-Cell Lymphoma	1999
Inorganic and metallic nanoparticles				
Nanotherm® (MagForce)	Iron Oxide	Allows cell uptake and introduces superparamagnetism	Glioblastoma	2010

1.3.3 Clinically approved nanoparticles

Clinically, only a few nanoparticles have been approved by the FDA but these nanomedicine formulations have largely failed to meaningfully improve the efficacy of chemotherapeutic interventions (**Table 1-3**).[96] The two FDA-approved liposomal doxorubicin formulations Doxil® (PEGylated liposomal doxorubicin) and Myocet® (non-PEGylated liposomal doxorubicin) reduce most side effects (i.e. cardiomyopathy, bone marrow depression, alopecia and nausea) while increasing a few (palmar-plantar erythrodysesthesia and dermatologic toxicity). However, the formulations do not enhance anti-tumor effects in metastatic breast cancer, multiple myeloma, or Kaposi's sarcoma. Myocet® reduced the incidence of cardiac events and congestive heart failure, but showed no improvements in response rate or progression-free survival when compared to free

doxorubicin in a Phase III trial in metastatic breast cancer patients.[75] Abraxane®, a 130-nanometer albumin-bound paclitaxel nanoparticle (nab-PTX), was approved to eliminate the need for Cremophor, a toxic castor oil excipient. The advantages of Abraxane® vs solvent-based PTX have been widely disputed,[115] with large-scale clinical trials suggesting that nab-PTX is more efficacious than solvent-based paclitaxel in early breast cancer,[115] but inferior in locally advanced or metastatic breast cancer.[116] Generally, nab-PTX is accepted to increase overall response rates due to uptake by endogenous 60-kDa glycoprotein receptors and glycoproteins over-expressed in cancers.[101, 117]

1.3.4 Combination nanoparticles

Several clinical trials have evaluated the feasibility of combining chemotherapeutic nanomedicines with radiotherapy or small molecule drugs (such as gemcitabine). PEGylated liposomal doxorubicin has shown improved therapeutic efficacy when combined with radiotherapy in several animal studies and clinical trials. A Phase I trial of poly(L-glutamic acid)-bound paclitaxel (Xyotax) and fractionated radiotherapy reported four complete and seven partial responses (with reductions in tumor volume of > 50%) in 12 patients with advanced esophageal and gastric cancers.[118] A Phase 1b/2 investigator-initiated trial of CRLX101 combined CRLX101, capecitabine, and radiotherapy for treating patients with non-metastatic rectal cancer showed few adverse effects with promising pathologic complete response (NCT02010567).[119] NC-6004, a polymeric nanoformulation carrying cisplatin, showed reduced ototoxicity and neurotoxicity while appearing to maintain therapeutic efficacy in combination with gemcitabine in Phase II clinical trials of pancreatic cancer in the UK and Japan. In the clinical trial in Japan, 55% of the 22 patients had tumor shrinkage and 85% of patients had disease control.[120] This combination demonstrated

activity and tolerability of the combination in heavily pretreated patients.[120] This combination chemotherapy has entered Phase III clinical trials for the treatment of locally advanced and/or metastatic pancreatic cancer (NCT02043288) and Phases I & II clinical trials for the treatment of advanced solid tumors or NSCLC (NCT02240238).[121] In 2017, a liposomal formulation encapsulating both cytarabine and daunorubicin (Vyxeos®), was approved for the treatment of acute myeloid leukemia.[122] Incorporation into the same particle can overcome the different pharmacokinetic properties and fix the molar ratio between the two drugs at 5:1, which is synergistic, for at least 24 h in circulation. Vyxeos limits drug metabolism, drug elimination, and potentially bypasses P-glycoprotein efflux pumps which can mediate drug resistance.[122, 123] In the Phase III clinical trial (NCT01696084), the nanoparticle was compared against standard "7+3" daunorubicin and cyarabine combination therapy, and improved median overall survival from 5.9 months to 9.6 months with a similar toxicity profile.[122]

1.4 Nanoscale coordination polymers

First reported in 2014, the current generation of nanoscale coordination polymers (NCPs) are a class of hybrid nanoparticles composed of a Pt-PO_4-Zn coordination polymer in the core and a lipid bilayer shell. NCPs are synthesized via a modular, two-step process which allows for wide compositional and structural diversity for a variety of biomedical applications, including drug delivery (**Scheme 1-1**).[124, 125] Pt(IV) bisphosphonate prodrugs of cisplatin and an oxaliplatin analogue, Pt(dach)Cl_2, were synthesized and self-assembled with Zn^{2+} ions and DOPA via a reverse microemulsion with a 7.4 water to surfactant ratio. The Zn-CisPt or Zn-Pt(dach)Cl_2 cores were then coated with the phospholipid DOPC to form a lipid bilayer, cholesterol to structure the lipid bilayer, and DSPE-PEG2k which contains a lipid component of the bilayer and PEG for

"stealth" properties in circulation and a near-neutral surface charge in PBS. The PEG layer can stabilize the nanoparticles to avoid aggregation, opsonization, and subsequent interaction with plasma proteins and cell-surface proteins.[126, 127] The high drug-loading NCPs extended the Pt blood circulation half-lives from 0.03-0.25 h to 12.0-16.4 h, leading to significantly increased blood exposure. The resulting NCPs showed promising biodistribution with low mononuclear phagocyte uptake and strong anticancer efficacy in a number of tumor xenograft models.[124] These nanomedicines can be used to deliver multiple drugs or accommodate multiple therapeutic modalities which offer the unique features of vehicle uniformity, ratiometric drug loading and spatiotemporal drug release. Concurrent with my work, NCPs have been advanced for combination therapy with multiple drugs or treatment modalities.

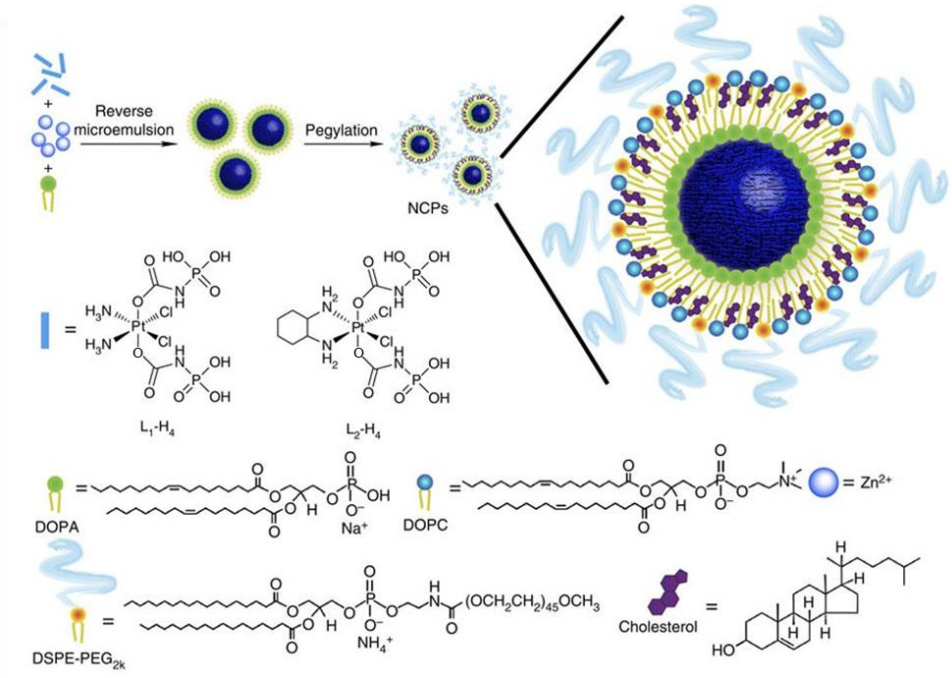

Scheme 1-1 General procedure for the synthesis of nanoscale coordination polymers. Reprinted from *Nat Commun* **5**, 4182 (2014).[124]

NCPs combining two chemotherapeutics were developed by combining a Pt(IV) prodrug with gemcitabine monophosphate (GMP), a hydrophilic precursor to the pharmacologically active diphosphate and triphosphate forms of gemcitabine.[128-130] The synthesis allowed for a modification to load both the Pt(IV) prodrugs and GMP into the core at various controlled ratios, as necessary. These combination NCPs (NCP-Pt/Gem) were similarly coated with DOPC, cholesterol, and DSPE-PEG2k, with consistently smaller particle sizes and greater monodispersity compared to the monotherapy NCP counterparts. Blood analysis of mice dosed with NCP-Pt/Gem showed that both the Pt and GMP components track well in circulation, with blood circulation half-lives within error of one another. NCP-Pt/Gem retained the similarly favorable biodistribution profile and enhanced anticancer efficacy against pancreatic and ovarian cancers.[128-130]

siRNAs were loaded onto the lipid bilayer shell of Pt-containing NCPs to overcome multi-drug resistance mechanisms. These NCPs were formulated with the cationic DOTAP rather than DOPC to load the siRNA via electrostatic interactions, leading to protection of siRNAs from degradation by serum RNase. NCP/siRNAs showed endosomal escape and *in vitro* transfection, significantly lowering the Pt IC_{50} values of Pt-resistant ovarian cancer cells.[131] A lipid-conjugated siRNA was developed to remove the requirement for a cationic lipid, while retaining the endosomal escape and transfection properties. The resulting NCP/DSPE-siRNAs were long-circulating nanoparticles with both Pt and siRNA content tracking well in circulation. NCP/DSPE-siRNAs were effective in treating subcutaneous tumor xenografts and widely disseminated, intraperitoneal models of Pt-resistant ovarian cancer.[128]

A phospholipid-conjugated porphyrin (pyrolipid) was loaded onto the NCP shell and delivered to tumors as a photosensitizer for effective PDT. In cells and tumors, pyrolipid predominantly accumulated in the lipid membranes, allowing for spatiotemporal control and generation of lipid

ROS upon irradiation.[132] The combination of PDT and chemotherapy from one NCP was effective for the treatment of HNSCC and CRCs, but could also be harnessed to synergize with immunotherapy.[128, 132, 133] NCP-mediated PDT combined with a checkpoint blockade inhibitor could not only control the tumor being irradiated with light, but could initiate an immune response to both prevent lung metastasis from mammary fat pad breast cancer tumors and treat established metastatic breast and colon cancer tumors.[133, 134]

1.5 Scope of work

This thesis outlines recent developments in NCP technology and discusses the implications of these findings on future nanoparticle drug development and development as anticancer therapies. Specifically, this work expands on previously reported NCP literature, featuring chemotherapy, gene therapy, and a PDT-inspired project. The breadth of this work also highlights the modular structure of the platform technology: four different Pt(IV) species are described as components of the NCP core and three different species are used on the nanoparticle shell. Broadly, this work revolves around leveraging triggered release properties of chemical prodrugs delivered by nanoparticles. The central themes of these works include dose reduction in the treatment of difficult-to-treat cancers, and expanding the available therapy options by protecting drugs from degradation. Chapters 2 and 3 discuss the prevention and treatment of metastases, while Chapters 4 and 5 focus on NCPs stimulating tumors with suppressive tumor microenvironments. The miRNA described in Chapter 2 was shielded from RNase in blood circulation, the PTX prodrug in Chapters 3 and 4 sidestepped P450 metabolism, and DHA was isolated in a hydrophobic environment to limit radical formation in circulation. In parallel, Coordination Pharmaceuticals Inc., a startup company founded by Dr. Wenbin Lin, has licensed the NCP technology and

advanced two nanomedicine candidates, CPI-100 and CPI-200, into Phase I clinical trials (NCT03781362 and NCT03953742). Together, these developments illustrate the potential of NCPs for drug delivery to improve cancer treatment.

1.6 References

1. Cooper, G.M. in The Cell: A Molecular Approach. 2nd edition (Sinauer Associates, Sunderland, MA; 2000).
2. Hanahan, D. & Weinberg, R.A. The hallmarks of cancer. *Cell* **100**, 57-70 (2000).
3. Gospodarowicz, M. et al. History and international developments in cancer staging. *Cancer Prev Control* **2**, 262-268 (1998).
4. Siegel, R.L., Miller, K.D. & Jemal, A. Cancer statistics, 2019. *CA Cancer J Clin* **69**, 7-34 (2019).
5. Miller, K.D. et al. Cancer treatment and survivorship statistics, 2019. *CA Cancer J Clin* (2019).
6. Arruebo, M. et al. Assessment of the evolution of cancer treatment therapies. *Cancers (Basel)* **3**, 3279-3330 (2011).
7. Dare, A.J. et al. in Cancer: Disease Control Priorities, Third Edition (Volume 3). (eds. H. Gelband, P. Jha, R. Sankaranarayanan & S. Horton) (Washington (DC); 2015).
8. Zanoni, D.K. et al. A Proposal to Redefine Close Surgical Margins in Squamous Cell Carcinoma of the Oral Tongue. *JAMA Otolaryngol Head Neck Surg* **143**, 555-560 (2017).
9. Li, Z. et al. Surgical treatment for locally advanced pancreatic cancer localized in the pancreatic body and tail (report of 11 cases). *Int J Clin Exp Med* **8**, 4676-4681 (2015).
10. Silberman, A.W. Surgical debulking of tumors. *Surg Gynecol Obstet* **155**, 577-585 (1982).
11. Service, N.C.R.a.A. (ed. P.H. England) (London, UK; 2017).
12. Testori, S. (Cancer Research UK; 2017).
13. Schorge, J.O., McCann, C. & Del Carmen, M.G. Surgical debulking of ovarian cancer: what difference does it make? *Rev Obstet Gynecol* **3**, 111-117 (2010).
14. McCahill, L. & Ferrell, B. Palliative surgery for cancer pain. *West J Med* **176**, 107-110 (2002).
15. Seimetz, D., Heller, K. & Richter, J. Approval of First CAR-Ts: Have we Solved all Hurdles for ATMPs? *Cell Med* **11**, 2155179018822781 (2019).
16. Cross, D. & Burmester, J.K. Gene therapy for cancer treatment: past, present and future. *Clin Med Res* **4**, 218-227 (2006).

17. Waehler, R., Russell, S.J. & Curiel, D.T. Engineering targeted viral vectors for gene therapy. *Nat Rev Genet* **8**, 573-587 (2007).

18. Unniyampurath, U., Pilankatta, R. & Krishnan, M.N. RNA Interference in the Age of CRISPR: Will CRISPR Interfere with RNAi? *Int J Mol Sci* **17**, 291 (2016).

19. Lam, J.K., Chow, M.Y., Zhang, Y. & Leung, S.W. siRNA Versus miRNA as Therapeutics for Gene Silencing. *Mol Ther Nucleic Acids* **4**, e252 (2015).

20. Mansoori, B., Sandoghchian Shotorbani, S. & Baradaran, B. RNA interference and its role in cancer therapy. *Adv Pharm Bull* **4**, 313-321 (2014).

21. Chakraborty, C., Sharma, A.R., Sharma, G., Doss, C.G.P. & Lee, S.S. Therapeutic miRNA and siRNA: Moving from Bench to Clinic as Next Generation Medicine. *Mol Ther Nucleic Acids* **8**, 132-143 (2017).

22. Mahmoodi Chalbatani, G. et al. Small interfering RNAs (siRNAs) in cancer therapy: a nano-based approach. *Int J Nanomedicine* **14**, 3111-3128 (2019).

23. Babu, A. et al. Nanoparticles for siRNA-Based Gene Silencing in Tumor Therapy. *IEEE Trans Nanobioscience* **15**, 849-863 (2016).

24. Uppal, A. et al. 14q32-encoded microRNAs mediate an oligometastatic phenotype. *Oncotarget* **6**, 3540-3552 (2015).

25. Takahashi, R.U., Prieto-Vila, M., Kohama, I. & Ochiya, T. Development of miRNA-based therapeutic approaches for cancer patients. *Cancer Sci* **110**, 1140-1147 (2019).

26. Svoronos, A.A., Engelman, D.M. & Slack, F.J. OncomiR or Tumor Suppressor? The Duplicity of MicroRNAs in Cancer. *Cancer Res* **76**, 3666-3670 (2016).

27. Doudna, J.A. & Charpentier, E. Genome editing. The new frontier of genome engineering with CRISPR-Cas9. *Science* **346**, 1258096 (2014).

28. Yin, H., Xue, W. & Anderson, D.G. CRISPR-Cas: a tool for cancer research and therapeutics. *Nat Rev Clin Oncol* **16**, 281-295 (2019).

29. Oppel, F., Schurmann, M., Goon, P., Albers, A.E. & Sudhoff, H. Specific Targeting of Oncogenes Using CRISPR Technology. *Cancer Res* **78**, 5506-5512 (2018).

30. Martinez-Lage, M., Puig-Serra, P., Menendez, P., Torres-Ruiz, R. & Rodriguez-Perales, S. CRISPR/Cas9 for Cancer Therapy: Hopes and Challenges. *Biomedicines* **6** (2018).

31. Behan, F.M. et al. Prioritization of cancer therapeutic targets using CRISPR-Cas9 screens. *Nature* **568**, 511-516 (2019).

32. Bialk, P., Wang, Y., Banas, K. & Kmiec, E.B. Functional Gene Knockout of NRF2 Increases Chemosensitivity of Human Lung Cancer A549 Cells In Vitro and in a Xenograft Mouse Model. *Mol Ther Oncolytics* **11**, 75-89 (2018).

33. Kim, W. et al. Targeting mutant KRAS with CRISPR-Cas9 controls tumor growth. *Genome Res* (2018).

34. Chabner, B.A. & Roberts, T.G., Jr. Timeline: Chemotherapy and the war on cancer. *Nat Rev Cancer* **5**, 65-72 (2005).

35. DeVita, V.T., Jr. & Chu, E. A history of cancer chemotherapy. *Cancer Res* **68**, 8643-8653 (2008).

36. Wang, D. & Lippard, S.J. Cellular processing of platinum anticancer drugs. *Nat Rev Drug Discov* **4**, 307-320 (2005).

37. Kaye, S.B. New antimetabolites in cancer chemotherapy and their clinical impact. *Br J Cancer* **78 Suppl 3**, 1-7 (1998).

38. Huang, C.Y., Ju, D.T., Chang, C.F., Muralidhar Reddy, P. & Velmurugan, B.K. A review on the effects of current chemotherapy drugs and natural agents in treating non-small cell lung cancer. *Biomedicine (Taipei)* **7**, 23 (2017).

39. Nitiss, J.L. Targeting DNA topoisomerase II in cancer chemotherapy. *Nat Rev Cancer* **9**, 338-350 (2009).

40. Perez, E.A. Microtubule inhibitors: Differentiating tubulin-inhibiting agents based on mechanisms of action, clinical activity, and resistance. *Mol Cancer Ther* **8**, 2086-2095 (2009).

41. Hoelder, S., Clarke, P.A. & Workman, P. Discovery of small molecule cancer drugs: successes, challenges and opportunities. *Mol Oncol* **6**, 155-176 (2012).

42. Hochhaus, A. et al. Long-Term Outcomes of Imatinib Treatment for Chronic Myeloid Leukemia. *N Engl J Med* **376**, 917-927 (2017).

43. Longo, D.L. Imatinib Changed Everything. *N Engl J Med* **376**, 982-983 (2017).

44. Lin, Y.L., Meng, Y., Jiang, W. & Roux, B. Explaining why Gleevec is a specific and potent inhibitor of Abl kinase. *Proc Natl Acad Sci U S A* **110**, 1664-1669 (2013).

45. McCubrey, J.A. et al. Roles of the Raf/MEK/ERK pathway in cell growth, malignant transformation and drug resistance. *Biochim Biophys Acta* **1773**, 1263-1284 (2007).

46. Yang, Z. et al. Comparison of gefitinib, erlotinib and afatinib in non-small cell lung cancer: A meta-analysis. *Int J Cancer* **140**, 2805-2819 (2017).

47. Ahmed, S.I., Thomas, A.L. & Steward, W.P. Vascular endothelial growth factor (VEGF) inhibition by small molecules. *J Chemother* **16 Suppl 4**, 59-63 (2004).

48. Scott, A.M., Wolchok, J.D. & Old, L.J. Antibody therapy of cancer. *Nat Rev Cancer* **12**, 278-287 (2012).

49. Amado, R.G. et al. Wild-type KRAS is required for panitumumab efficacy in patients with metastatic colorectal cancer. *J Clin Oncol* **26**, 1626-1634 (2008).

50. Karapetis, C.S. et al. K-ras mutations and benefit from cetuximab in advanced colorectal cancer. *N Engl J Med* **359**, 1757-1765 (2008).

51. Duan, X., Chan, C. & Lin, W. Nanoparticle-Mediated Immunogenic Cell Death Enables and Potentiates Cancer Immunotherapy. *Angew Chem Int Ed Engl* **58**, 670-680 (2019).

52. Chen, D.S. & Mellman, I. Oncology meets immunology: the cancer-immunity cycle. *Immunity* **39**, 1-10 (2013).

53. Zitvogel, L. et al. Immunogenic tumor cell death for optimal anticancer therapy: the calreticulin exposure pathway. *Clin Cancer Res* **16**, 3100-3104 (2010).

54. Gotwals, P. et al. Prospects for combining targeted and conventional cancer therapy with immunotherapy. *Nat Rev Cancer* **17**, 286-301 (2017).

55. Krysko, D.V. et al. Immunogenic cell death and DAMPs in cancer therapy. *Nat Rev Cancer* **12**, 860-875 (2012).

56. Terbuch, A. & Lopez, J. Next Generation Cancer Vaccines-Make It Personal! *Vaccines (Basel)* **6** (2018).

57. Kantoff, P.W. et al. Sipuleucel-T immunotherapy for castration-resistant prostate cancer. *N Engl J Med* **363**, 411-422 (2010).

58. June, C.H. & Sadelain, M. Chimeric Antigen Receptor Therapy. *N Engl J Med* **379**, 64-73 (2018).

59. Whiteside, T.L., Demaria, S., Rodriguez-Ruiz, M.E., Zarour, H.M. & Melero, I. Emerging Opportunities and Challenges in Cancer Immunotherapy. *Clin Cancer Res* **22**, 1845-1855 (2016).

60. Houot, R., Schultz, L.M., Marabelle, A. & Kohrt, H. T-cell-based Immunotherapy: Adoptive Cell Transfer and Checkpoint Inhibition. *Cancer Immunol Res* **3**, 1115-1122 (2015).

61. Darvin, P., Toor, S.M., Sasidharan Nair, V. & Elkord, E. Immune checkpoint inhibitors: recent progress and potential biomarkers. *Exp Mol Med* **50**, 165 (2018).

62. Ribas, A. & Wolchok, J.D. Cancer immunotherapy using checkpoint blockade. *Science* **359**, 1350-1355 (2018).

63. Skalniak, L. et al. Small-molecule inhibitors of PD-1/PD-L1 immune checkpoint alleviate the PD-L1-induced exhaustion of T-cells. *Oncotarget* **8**, 72167-72181 (2017).

64. Wei, S.C., Duffy, C.R. & Allison, J.P. Fundamental Mechanisms of Immune Checkpoint Blockade Therapy. *Cancer Discov* **8**, 1069-1086 (2018).

65. Castano, A.P., Mroz, P. & Hamblin, M.R. Photodynamic therapy and anti-tumour immunity. *Nat Rev Cancer* **6**, 535-545 (2006).

66. Agostinis, P. et al. Photodynamic therapy of cancer: an update. *CA Cancer J Clin* **61**, 250-281 (2011).

67. Lan, G. et al. Nanoscale Metal-Organic Layers for Deeply Penetrating X-ray-Induced Photodynamic Therapy. *Angew Chem Int Ed Engl* **56**, 12102-12106 (2017).

68. Toraya-Brown, S. et al. Local hyperthermia treatment of tumors induces CD8(+) T cell-mediated resistance against distal and secondary tumors. *Nanomedicine* **10**, 1273-1285 (2014).

69. Kobayashi, T. Cancer hyperthermia using magnetic nanoparticles. *Biotechnol J* **6**, 1342-1347 (2011).

70. Zou, L. et al. Current Approaches of Photothermal Therapy in Treating Cancer Metastasis with Nanotherapeutics. *Theranostics* **6**, 762-772 (2016).

71. Ito, A., Matsuoka, F., Honda, H. & Kobayashi, T. Heat shock protein 70 gene therapy combined with hyperthermia using magnetic nanoparticles. *Cancer Gene Ther* **10**, 918-925 (2003).

72. Moy, A.J. & Tunnell, J.W. Combinatorial immunotherapy and nanoparticle mediated hyperthermia. *Adv Drug Deliv Rev* **114**, 175-183 (2017).

73. Jaffray, D.A. & Gospodarowicz, M.K. in Cancer: Disease Control Priorities, Third Edition (Volume 3). (eds. H. Gelband, P. Jha, R. Sankaranarayanan & S. Horton) (Washington (DC); 2015).

74. Rationalizing combination therapies. *Nat Med* **23**, 1113 (2017).

75. He, C. et al. Nanomedicine for Combination Therapy of Cancer. *EBioMedicine* **2**, 366-367 (2015).

76. Zugazagoitia, J. et al. Current Challenges in Cancer Treatment. *Clin Ther* **38**, 1551-1566 (2016).

77. McFedries, A., Schwaid, A. & Saghatelian, A. Methods for the elucidation of protein-small molecule interactions. *Chem Biol* **20**, 667-673 (2013).

78. Liang, X.J., Chen, C., Zhao, Y. & Wang, P.C. Circumventing tumor resistance to chemotherapy by nanotechnology. *Methods Mol Biol* **596**, 467-488 (2010).

79. Chen, Y., Gao, D.Y. & Huang, L. In vivo delivery of miRNAs for cancer therapy: challenges and strategies. *Adv Drug Deliv Rev* **81**, 128-141 (2015).

80. Eetezadi, S., Ekdawi, S.N. & Allen, C. The challenges facing block copolymer micelles for cancer therapy: In vivo barriers and clinical translation. *Adv Drug Deliv Rev* **91**, 7-22 (2015).

81. Cleeland, C.S. et al. Reducing the toxicity of cancer therapy: recognizing needs, taking action. *Nat Rev Clin Oncol* **9**, 471-478 (2012).

82. Anderson, H. & Palmer, M.K. Measuring quality of life: impact of chemotherapy for advanced colorectal cancer. Experience from two recent large phase III trials. *Br J Cancer* **77 Suppl 2**, 9-14 (1998).

83. Grisold, W., Cavaletti, G. & Windebank, A.J. Peripheral neuropathies from chemotherapeutics and targeted agents: diagnosis, treatment, and prevention. *Neuro Oncol* **14 Suppl 4**, iv45-54 (2012).

84. Scheel, C., Onder, T., Karnoub, A. & Weinberg, R.A. Adaptation versus selection: the origins of metastatic behavior. *Cancer Res* **67**, 11476-11479; discussion 11479-11480 (2007).

85. Klein, C.A. Selection and adaptation during metastatic cancer progression. *Nature* **501**, 365-372 (2013).

86. Holohan, C., Van Schaeybroeck, S., Longley, D.B. & Johnston, P.G. Cancer drug resistance: an evolving paradigm. *Nat Rev Cancer* **13**, 714-726 (2013).

87. Kelderman, S., Schumacher, T.N. & Haanen, J.B. Acquired and intrinsic resistance in cancer immunotherapy. *Mol Oncol* **8**, 1132-1139 (2014).

88. Tran, S., DeGiovanni, P.J., Piel, B. & Rai, P. Cancer nanomedicine: a review of recent success in drug delivery. *Clin Transl Med* **6**, 44 (2017).

89. Richards, D.A., Maruani, A. & Chudasama, V. Antibody fragments as nanoparticle targeting ligands: a step in the right direction. *Chem Sci* **8**, 63-77 (2017).

90. Bera, D., Qian, L., Tseng, T.-K. & Holloway, P.H. Quantum Dots and Their Multimodal Applications: A Review. *Materials (Basel)* **3**, 2260-2345 (2010).

91. Matea, C.T. et al. Quantum dots in imaging, drug delivery and sensor applications. *Int J Nanomedicine* **12**, 5421-5431 (2017).

92. Rosenblum, D., Joshi, N., Tao, W., Karp, J.M. & Peer, D. Progress and challenges towards targeted delivery of cancer therapeutics. *Nat Commun* **9**, 1410 (2018).

93. Rajh, T., Dimitrijevic, N.M., Bissonnette, M., Koritarov, T. & Konda, V. Titanium dioxide in the service of the biomedical revolution. *Chem Rev* **114**, 10177-10216 (2014).

94. Singh, A., Singh, N.B., Afzal, S., Singh, T. & Hussain, I. Zinc oxide nanoparticles: a review of their biological synthesis, antimicrobial activity, uptake, translocation and biotransformation in plants. *J Mater Sci* **53**, 185-201 (2018).

95. Andreescu, S., Ornatska, M., Erlichman, J.S., Estevez, A. & Leiter, J.C. in Fine Particles in Medicine and Pharmacy. (ed. E. Matijević) 57-100 (Springer US, Boston, MA; 2012).

96. Bobo, D., Robinson, K.J., Islam, J., Thurecht, K.J. & Corrie, S.R. Nanoparticle-Based Medicines: A Review of FDA-Approved Materials and Clinical Trials to Date. *Pharm Res* **33**, 2373-2387 (2016).

97. Saha, K., Agasti, S.S., Kim, C., Li, X. & Rotello, V.M. Gold nanoparticles in chemical and biological sensing. *Chem Rev* **112**, 2739-2779 (2012).

98. Dreaden, E.C., Austin, L.A., Mackey, M.A. & El-Sayed, M.A. Size matters: gold nanoparticles in targeted cancer drug delivery. *Ther Deliv* **3**, 457-478 (2012).

99. Torchilin, V.P. Recent advances with liposomes as pharmaceutical carriers. *Nat Rev Drug Discov* **4**, 145-160 (2005).

100. Cabral, H., Miyata, K., Osada, K. & Kataoka, K. Block Copolymer Micelles in Nanomedicine Applications. *Chem Rev* **118**, 6844-6892 (2018).

101. Elzoghby, A.O., Samy, W.M. & Elgindy, N.A. Albumin-based nanoparticles as potential controlled release drug delivery systems. *J Control Release* **157**, 168-182 (2012).

102. Davis, M.E., Chen, Z.G. & Shin, D.M. Nanoparticle therapeutics: an emerging treatment modality for cancer. *Nat Rev Drug Discov* **7**, 771-782 (2008).

103. Albanese, A., Tang, P.S. & Chan, W.C. The effect of nanoparticle size, shape, and surface chemistry on biological systems. *Annu Rev Biomed Eng* **14**, 1-16 (2012).

104. Wilhelm, S. et al. Analysis of nanoparticle delivery to tumours. *Nature Reviews Materials* **1**, 16014 (2016).

105. Anselmo, A.C. & Mitragotri, S. A Review of Clinical Translation of Inorganic Nanoparticles. *AAPS J* **17**, 1041-1054 (2015).

106. Anselmo, A.C. & Mitragotri, S. Nanoparticles in the clinic. *Bioeng Transl Med* **1**, 10-29 (2016).

107. Foroozandeh, P. & Aziz, A.A. Insight into Cellular Uptake and Intracellular Trafficking of Nanoparticles. *Nanoscale Res Lett* **13**, 339 (2018).

108. Hirsch, L.R. et al. Nanoshell-mediated near-infrared thermal therapy of tumors under magnetic resonance guidance. *Proc Natl Acad Sci U S A* **100**, 13549-13554 (2003).

109. Maggiorella, L. et al. Nanoscale radiotherapy with hafnium oxide nanoparticles. *Future Oncol* **8**, 1167-1181 (2012).

110. Stathopoulos, G.P. & Boulikas, T. Lipoplatin formulation review article. *J Drug Deliv* **2012**, 581363 (2012).

111. Casagrande, N. et al. Preclinical activity of the liposomal cisplatin lipoplatin in ovarian cancer. *Clin Cancer Res* **20**, 5496-5506 (2014).

112. Hrkach, J. et al. Preclinical development and clinical translation of a PSMA-targeted docetaxel nanoparticle with a differentiated pharmacological profile. *Sci Transl Med* **4**, 128ra139 (2012).

113. Uchino, H. et al. Cisplatin-incorporating polymeric micelles (NC-6004) can reduce nephrotoxicity and neurotoxicity of cisplatin in rats. *Br J Cancer* **93**, 678-687 (2005).

114. Lin, C.J., Lin, Y.L., Luh, F., Yen, Y. & Chen, R.M. Preclinical effects of CRLX101, an investigational camptothecin-containing nanoparticle drug conjugate, on treating glioblastoma multiforme via apoptosis and antiangiogenesis. *Oncotarget* **7**, 42408-42421 (2016).

115. Untch, M. et al. Nab-paclitaxel versus solvent-based paclitaxel in neoadjuvant chemotherapy for early breast cancer (GeparSepto-GBG 69): a randomised, phase 3 trial. *Lancet Oncol* **17**, 345-356 (2016).

116. Rugo, H.S. et al. Randomized Phase III Trial of Paclitaxel Once Per Week Compared With Nanoparticle Albumin-Bound Nab-Paclitaxel Once Per Week or Ixabepilone With Bevacizumab As First-Line Chemotherapy for Locally Recurrent or Metastatic Breast Cancer: CALGB 40502/NCCTG N063H (Alliance). *J Clin Oncol* **33**, 2361-2369 (2015).

117. Vishnu, P. & Roy, V. Safety and Efficacy of nab-Paclitaxel in the Treatment of Patients with Breast Cancer. *Breast Cancer (Auckl)* **5**, 53-65 (2011).

118. Dipetrillo, T. et al. Paclitaxel poliglumex (PPX-Xyotax) and concurrent radiation for esophageal and gastric cancer: a phase I study. *Am J Clin Oncol* **29**, 376-379 (2006).

119. Wang, A. et al. Phase IB/II study of neoadjuvant chemoradiotherapy with CRLX101 and capecitabine for locally advanced rectal cancer. *Journal of Clinical Oncology* **33**, TPS3629-TPS3629 (2015).

120. Subbiah, V. et al. Phase Ib/II Trial of NC-6004 (Nanoparticle Cisplatin) Plus Gemcitabine in Patients with Advanced Solid Tumors. *Clin Cancer Res* **24**, 43-51 (2018).

121. Cabral, H. & Kataoka, K. Progress of drug-loaded polymeric micelles into clinical studies. *J Control Release* **190**, 465-476 (2014).

122. Krauss, A.C. et al. FDA Approval Summary: (Daunorubicin and Cytarabine) Liposome for Injection for the Treatment of Adults with High-Risk Acute Myeloid Leukemia. *Clin Cancer Res* **25**, 2685-2690 (2019).

123. Mayer, L.D., Tardi, P. & Louie, A.C. CPX-351: a nanoscale liposomal co-formulation of daunorubicin and cytarabine with unique biodistribution and tumor cell uptake properties. *Int J Nanomedicine* **14**, 3819-3830 (2019).

124. Liu, D., Poon, C., Lu, K., He, C. & Lin, W. Self-assembled nanoscale coordination polymers with trigger release properties for effective anticancer therapy. *Nat Commun* **5**, 4182 (2014).

125. Lammers, T. Nanomedicine on the move: from monotherapeutic regimens to combination therapies. *Expert Rev Clin Pharmacol* **5**, 105-108 (2012).

126. Owens, D.E., 3rd & Peppas, N.A. Opsonization, biodistribution, and pharmacokinetics of polymeric nanoparticles. *Int J Pharm* **307**, 93-102 (2006).

127. Immordino, M.L., Dosio, F. & Cattel, L. Stealth liposomes: review of the basic science, rationale, and clinical applications, existing and potential. *Int J Nanomedicine* **1**, 297-315 (2006).

128. He, C., Poon, C., Chan, C., Yamada, S.D. & Lin, W. Nanoscale Coordination Polymers Codeliver Chemotherapeutics and siRNAs to Eradicate Tumors of Cisplatin-Resistant Ovarian Cancer. *J Am Chem Soc* **138**, 6010-6019 (2016).

129. Poon, C., Duan, X., Chan, C., Han, W. & Lin, W. Nanoscale Coordination Polymers Codeliver Carboplatin and Gemcitabine for Highly Effective Treatment of Platinum-Resistant Ovarian Cancer. *Mol Pharm* **13**, 3665-3675 (2016).

130. Poon, C., He, C., Liu, D., Lu, K. & Lin, W. Self-assembled nanoscale coordination polymers carrying oxaliplatin and gemcitabine for synergistic combination therapy of pancreatic cancer. *J Control Release* **201**, 90-99 (2015).

131. He, C., Liu, D. & Lin, W. Self-assembled nanoscale coordination polymers carrying siRNAs and cisplatin for effective treatment of resistant ovarian cancer. *Biomaterials* **36**, 124-133 (2015).

132. He, C., Liu, D. & Lin, W. Self-assembled core-shell nanoparticles for combined chemotherapy and photodynamic therapy of resistant head and neck cancers. *ACS Nano* **9**, 991-1003 (2015).

133. Duan, X. et al. Photodynamic Therapy Mediated by Nontoxic Core-Shell Nanoparticles Synergizes with Immune Checkpoint Blockade To Elicit Antitumor Immunity and Antimetastatic Effect on Breast Cancer. *J Am Chem Soc* **138**, 16686-16695 (2016).

134. He, C. et al. Core-shell nanoscale coordination polymers combine chemotherapy and photodynamic therapy to potentiate checkpoint blockade cancer immunotherapy. *Nat Commun* **7**, 12499 (2016).

CHAPTER 2. Systemic miRNA delivery by nontoxic nanoscale coordination polymers limits epithelial-to-mesenchymal transition and suppresses liver metastases of colorectal cancer

2.1 Introduction

Metastases are responsible for ~90% of cancer deaths, accounting for nearly 1,500 deaths each day in the United States.[1-3] The metastatic process is proposed as the last step of cancer progression, but it has recently been found that cancer cells will disseminate much earlier in both animal models and human patients.[4-6] Due to the potential risks of metastasis, patients are often treated with radiotherapy, systemic adjuvant chemotherapy, or targeted therapies after surgery to eliminate residual tumors and prevent or treat metastatic disease.[7-10] However, these treatment modalities are accompanied by significant toxicities and can lead to overtreatment of patients, particularly in young breast, colon cancer, and prostate cancer patients.[11-15] As cancer cells can form undetectable micrometastases, systemic therapies that can specifically treat tumors or suppress growth without damaging healthy tissues are a high priority in advancing cancer therapy to treat metastatic disease. Nanoparticles are an ideal platform for these purposes due to improvements in circulation half-lives and preferential accumulation in cancerous tissues via the enhanced permeability and retention (EPR) effect.

One promising strategy has been miRNAs, short non-coding regions of RNA commonly found in cancer-associated genomic regions.[16-20] The miRNA profile in cancerous tumors is often found to be deregulated compared to normal tissues, opening a window for both diagnosis and therapy.[20-

[24] Specifically, the chromosomal locus 14q32, which is frequently translocated in myeloma patients, encodes miR-655-3p, a miRNA regulating key metastatic pathways including the epithelial-to-mesenchymal transition EMT.[25, 26] It was found to be significantly down-regulated in human hepatocellular carcinomas, among other cancers, compared to healthy livers.[27] Low expression of miR-655-3p was clinically associated with poor prognosis and a metastatic phenotype.[25, 27] However, patients with only limited metastases, or oligometastasis, and associated with more favorable outcomes were found to overexpress miR-655-3p, suggesting there may be a therapeutic benefit to its ectopic expression. [25, 28]

Though the tumor suppressing capabilities of miR-655-3p have been demonstrated in a number of cell lines, miRNAs are unstable in systemic circulation and require often toxic vehicles for delivery and transfection.[26, 29-31] Delivery of small RNA therapeutics has also been plagued by poor pharmacokinetics and unexpected immunotoxicity,[21, 31-35] but the recent successes of two oligonucleotides in clinical trials for transtheyretin (TTR)-mediated amyloidosis demonstrate the potential of gene therapy if these limitations can be overcome.[33, 36-41] One is a lipid nanoparticle delivering RNAi to hepatocytes, which has inspired a number of platforms for the delivery of small molecule therapeutics to tumors in vivo.[42-50] The pharmacokinetics of drugs encapsulated in nanoparticles can be altered by reducing binding to serum proteins or cells.

We have recently used cytotoxic nanoscale coordination polymers (NCPs) for the delivery of double-stranded RNAs for cancer treatment.[51, 52] Specifically, NCP-encapsulated small interfering RNAs (siRNAs) could be effectively shielded from degradation in sera, while maintaining gene silencing in vivo. Drug resistance gene-targeting siRNAs potentiated cisplatin-carrying NCPs resulting in substantially improved anticancer efficacy in animal models. [51]

In this work, we take advantage of platinum coordination chemistry to design a nontoxic vehicle for effective miRNA delivery in vitro and in vivo. NCPs with prolonged blood circulation and triggered release allow for the direct investigation of the molecular mechanisms of miR-655-3p on human colorectal cancer HCT116 cells. Only NCPs containing the Pt(IV) coordination polymer showed effective miRNA delivery. The miRNA-carrying NCPs limited cell proliferation, nuclear localization of β-catenin, and tumor cell invasion in vitro. NCP/miRNAs showed favorable biodistribution and minimal toxicity, allowing for in vivo transfection to effectively limit epithelial-to-mesenchymal transition (EMT) and suppress the formation and growth of tumor colonies in a xenogenic hepatic metastasis model of colorectal cancer.

2.2 Results

2.2.1 Synthesis and characterization of NCP-PtEN

Dichlorobis(ethylenediamine)platinum(II), $[Pt^{II}(en)_2]Cl_2$, was synthesized according to literature and characterized by NMR and mass spectrometry (**Scheme 2-1**).[53] K_2PtCl_4 (0.5g) was stirred in the dark with excess ethylenediamine (en; 0.4 mL) in 10 mL H_2O at room temperature for 2 h. The yellow solid was collected by vacuum filtration and then refluxed in the dark with excess en (0.8mL) in 10 mL H_2O for 2 h. The resultant white solid was collected by vacuum filtration and washed with cold H_2O and EtOH. Yield for $[Pt^{II}(en)_2]Cl_2$: 77%. ^1H NMR in D_2O: δ 2.60 (triplet, 8H, **Figure 2-1**). The m/z of $[M+H]^+$ for $[Pt^{II}(en)_2]^{2+}$ was determined to be 314.1 (expected 314.1, **Figure 2-2**).

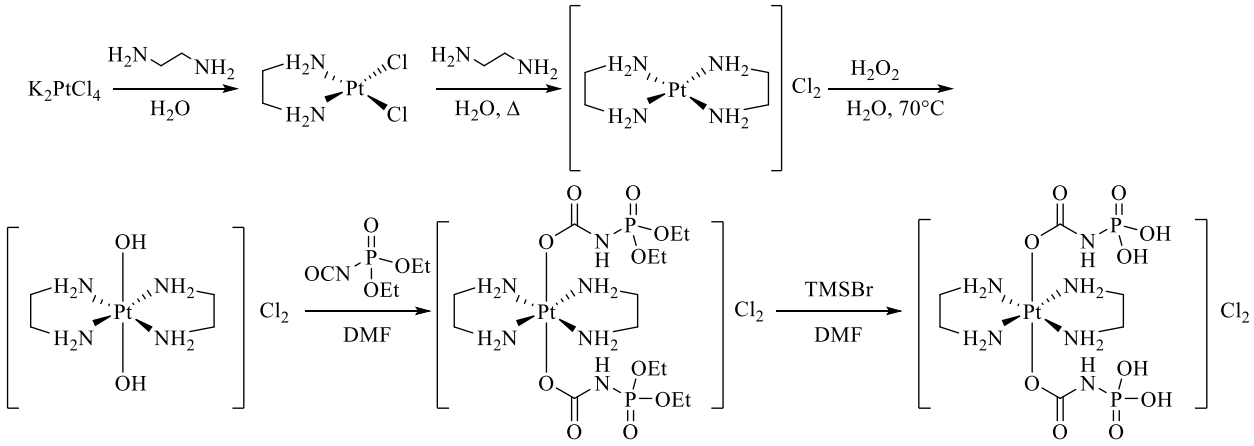

Scheme 2-1 Synthetic scheme for $[Pt^{IV}(en)_2bp]Cl_2$. Reprinted from *Biomaterials* **210**, 94-104 (2019).

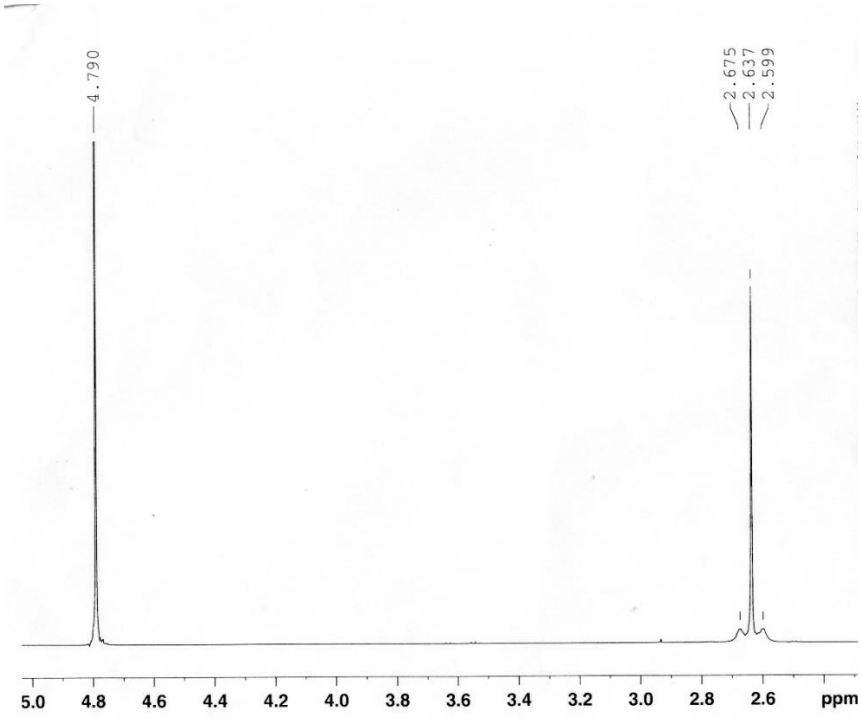

Figure 2-1 ^1H NMR spectrum of $[Pt^{II}(en)_2]Cl_2$. Reprinted from *Biomaterials* **210**, 94-104 (2019).

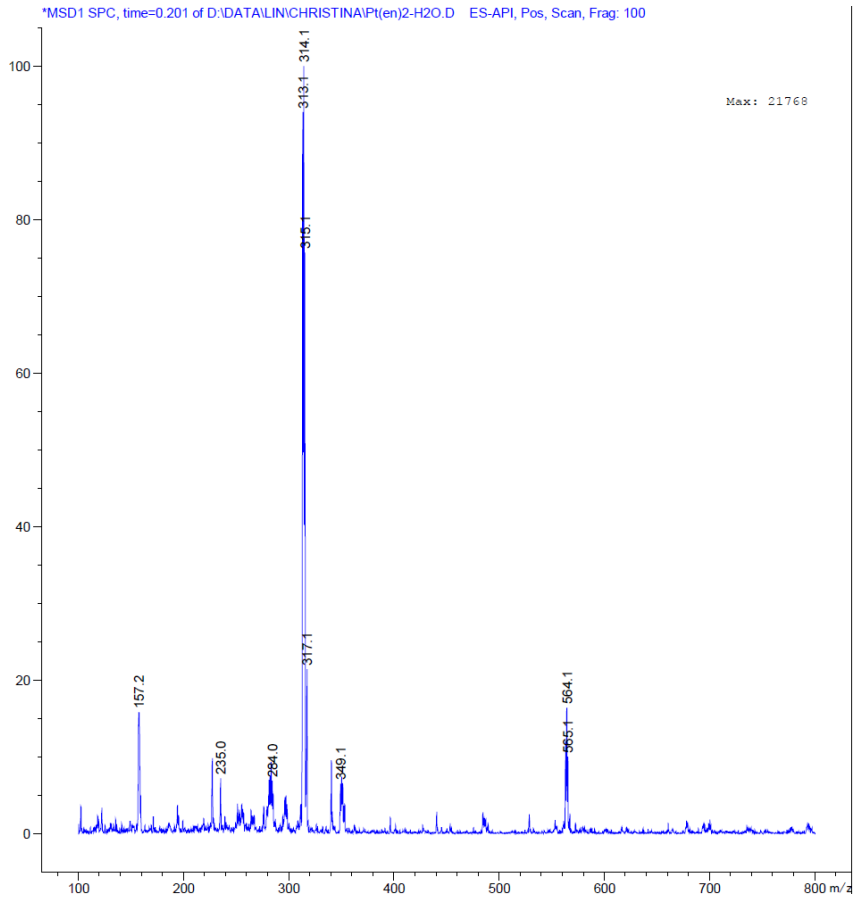

Figure 2-2 ESI-MS of $[Pt^{II}(en)_2]Cl_2$. Reprinted from *Biomaterials* **210**, 94-104 (2019).

$[Pt^{II}(en)_2]Cl_2$ was converted into $[Pt^{IV}(en)_2bp]Cl_2$ in accordance with analogous Pt^{IV} complexes.[54, 55] $[Pt^{II}(en)_2]Cl_2$ (0.35 g) was reacted with 2.5 mL 30% H_2O_2 in 5 mL H_2O at 70°C for 5 h in the dark. EtOH was added to the solution and cooled to -20 °C overnight to yield a white solid, $[Pt^{IV}(en)_2(OH)_2]Cl_2$. The solid was collected and washed twice with cold EtOH. Yield: 71%. ^1H NMR in D_2O: δ 2.94 (triplet, 8H). The m/z of $[M+H]^+$ for $[Pt^{IV}(en)_2(OH)_2]^{2+}$ was determined to be 348.1 (expected 348.1).

$[Pt^{IV}(en)_2(OH)_2]Cl_2$ (0.28 g) was dissolved in minimal DMF, to which 4 equivalents of diethoxyphosphinyl isocyanate (0.45 mL) was added at 4 °C. The mixture was allowed to warm

to room temperature and then reacted overnight in the dark. The solution was filtered, and the resulting white product $[Pt^{IV}(en)_2bis(phosphoester)]Cl_2$ was precipitated by addition of Et_2O. The product was washed twice with cold Et_2O. Yield: 65%. ^1H NMR in D_2O: δ 4.18 (m, 8H); δ 2.98 (m, 8H); δ 1.33 (t, 12H). The m/z of $[MH]^+$ for $[Pt^{IV}(en)_2bis(phosphoester)]^{2+}$ was determined to be 706.3 (expected 706.2).

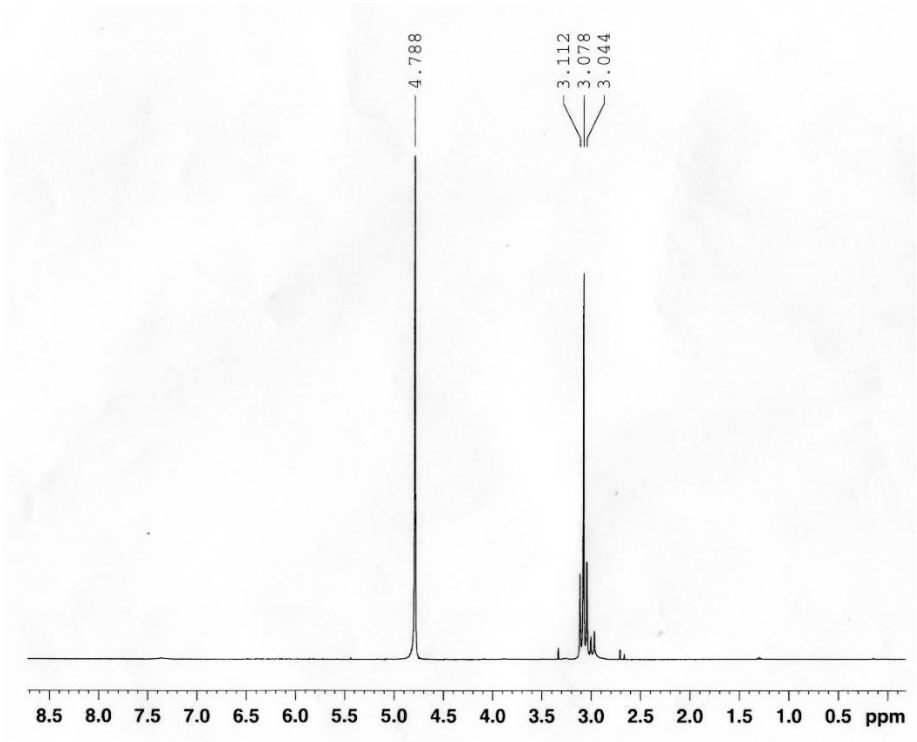

Figure 2-3 NMR spectrum of $[Pt^{IV}(en)_2bp]Cl_2$. Reprinted from *Biomaterials* **210**, 94-104 (2019).

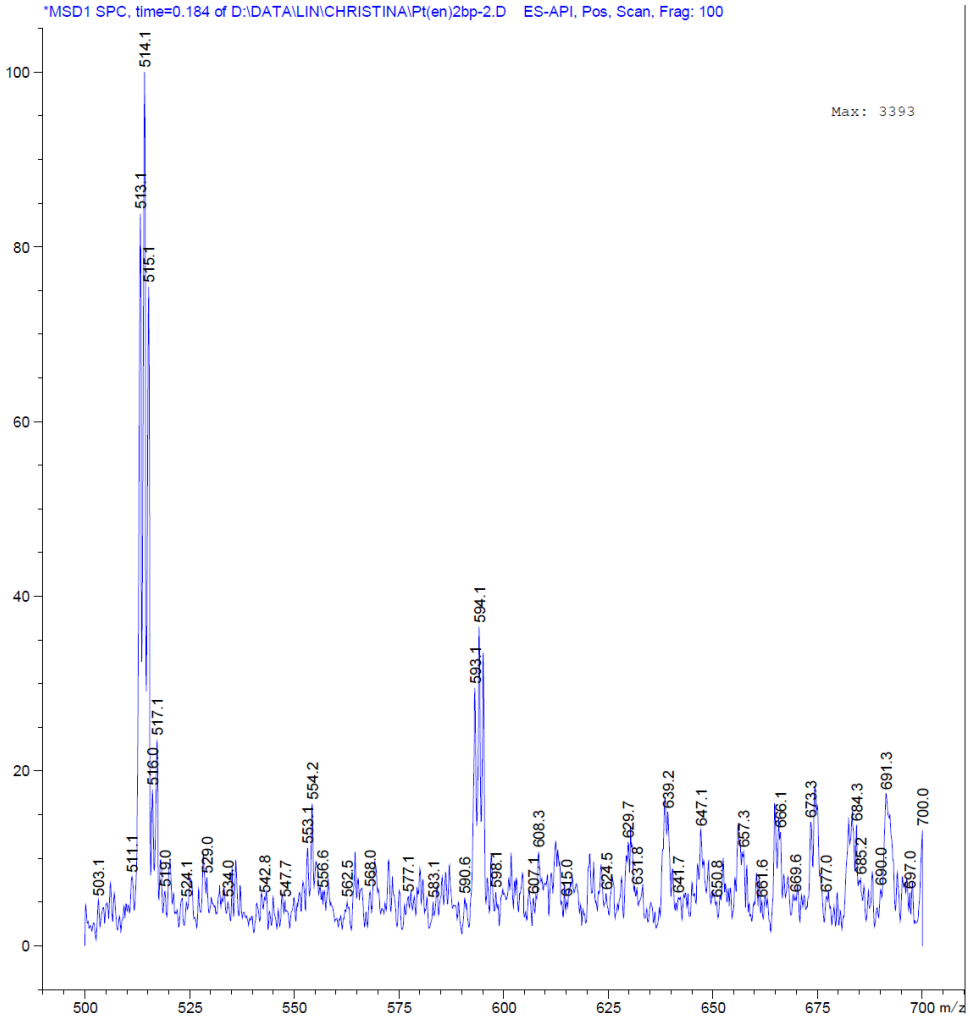

Figure 2-4 ESI-MS of $[Pt^{IV}(en)_2bp]Cl_2$. Reprinted from *Biomaterials* **210**, 94-104 (2019).

Trimethylsilyl bromide (TMSBr, 0.58 mL) was added slowly to a solution of $[Pt^{IV}(en)_2$bis(phosphoester)$]Cl_2$ (0.30 g) in DMF (3 mL) at 4 °C and stirred at r.t. in the dark under N_2 protection for 18 h. A yellow solid was collected after addition of dichloromethane and then washed twice with additional dichloromethane. The solid was dissolved in MeOH and stirred overnight to hydrolyze the TMS-ester intermediate. The final product, $[Pt^{IV}(en)_2bp]Cl_2$ (bp = bisphosphonic acid $[OCONHP(O)(OH)_2]_2$), was collected by precipitation with dichloromethane and then washed twice with dichloromethane. Yield: 80%. ^{1}H NMR in D_2O: δ 3.08 (t, 8H,

Figure 2-3). The m/z of $[M+H]^+$ for $[Pt^{IV}(en)_2bp]^{2+}$ was determined to be 594.1 (expected 594.3, **Figure 2-4**).

To prepare $Pt^{IV}(en)_2$-containing NCPs (PtEN), $[Pt^{IV}(en)_2bp]Cl_2$ was deprotonated and polymerized with Zn^{II} ions in the presence of the phospholipid 1,2-dioleoyl-sn-glycero-3-phosphate sodium salt (DOPA) via reverse microemulsion. A self-assembled lipid bilayer in the presence of cholesterol and the phospholipids 1,2-dioleyl-sn-gylcero-3-phosphocholine (DOPC) and 1,2-diastearoyl-sn-gylcero-3-phosphoethanolamine-N-[amino(polyethylene glycol)2000] (DSPE-PEG2k) in a 2:2:1 molar ratio yielded nontoxic PtEN. Cholesterol ordered and stabilized the DOPC and DSPE-portion of DSPE-PEG2k, while the PEG portion endowed "stealth" properties to evade clearance by mononuclear phagocyte system (MPS). The Pt loading was determined to be 9.2 wt% by inductively coupled plasma-mass spectrometry (ICP-MS). The Z-average diameter, PDI, and ζ-potential of PtEN were determined by dynamic light scattering (DLS) to be 96.9 ± 0.7, 0.14 ± 0.01, and –15.2 ± 2.0 mV in water. In PBS, the ζ-potential of PtEN was determined to be slightly negative, -1.85 ± 0.261 mV.

The most prominent members of the Pt family of anticancer drugs form inter- and intra-strand Pt-DNA adducts to interfere with DNA replication. $[Pt^{IV}(en)_2bp]Cl_2$ was designed as a nontoxic, kinetically inert core for PtEN due to the low spin d^6 electronic configuration of octahedral Pt complexes. While other Pt^{IV} prodrugs release active Pt^{II} species to bind to DNA,[56, 57] the resultant $[Pt^{II}(en)_2]^{2+}$ does not have a substitution-labile coordination site and cannot bind to DNA. To test our hypothesis, we first investigated the kinetics of $[Pt^{IV}(en)_2bp]^{2+}$ reduction and Pt-en dissociation.

In the presence of 5 mM ascorbate at 37°C, $[Pt^{IV}(en)_2bp]Cl_2$ can be reduced to $[Pt^{II}(en)_2]^{2+}$ in 5 h by electron transfer from ascorbate to the Pt^{IV} center via the axial ligands (**Figure 2-5**, **Scheme 2-2**). This allows for generation of CO_2 as a product, akin to the previously reported Pt^{IV}

prodrug of cisplatin, $Pt(NH_3)_2Cl_2(bp)$ (**Figure 2-6**). $[Pt^{II}(en)_2]^{2+}$ is highly stable as Pt-en coordination will not dissociate in an aqueous solution at 37 °C for up to two weeks, as determined by stable integration of the $[Pt^{II}(en)_2]^{2+}$ signal by LC-MS (**Figure 2-7**). The chemically inert $[Pt^{II}(en)_2]Cl_2$ is thus unable to bind to DNA.

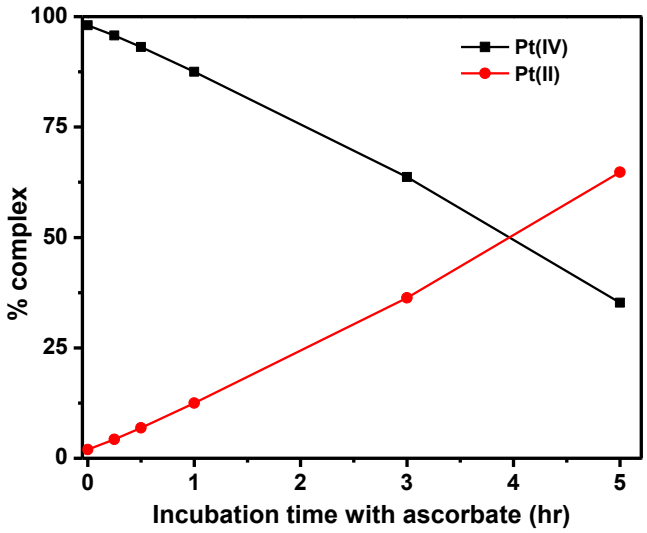

Figure 2-5 Reduction of $[Pt^{IV}(en)_2bp]Cl_2$ in the presence of 5mM ascorbate to $[Pt^{II}(en)_2]^{2+}$ over time. Reprinted from *Biomaterials* **210**, 94-104 (2019).

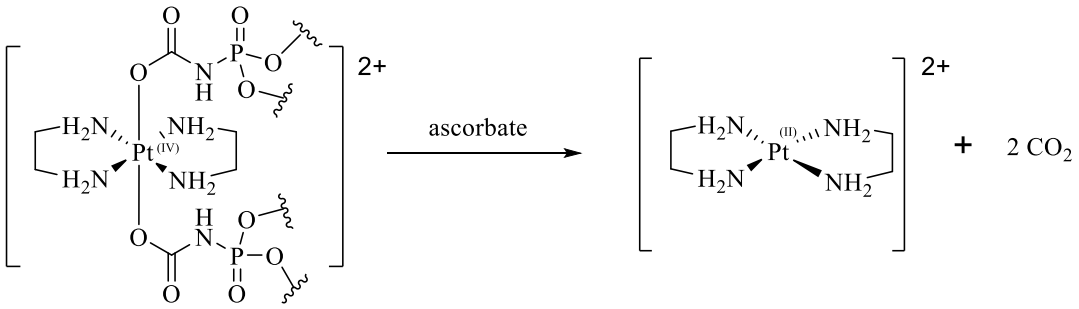

Scheme 2-2 Reduction of $[Pt^{IV}(en)_2bp]Cl_2$ to $[Pt^{II}(en)_2]^{2+}$ in the presence of ascorbate. Reprinted from *Biomaterials* **210**, 94-104 (2019).

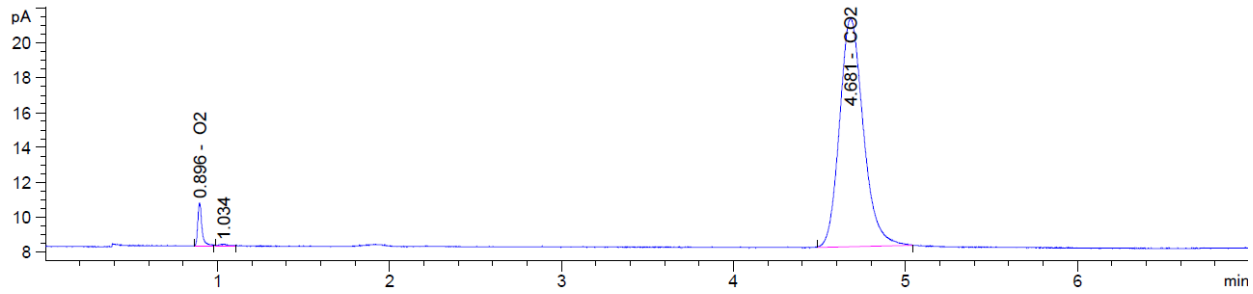

Figure 2-6 CO_2 generation during reduction of $[Pt^{IV}(en)_2bp]Cl_2$. Reprinted from *Biomaterials* **210**, 94-104 (2019).

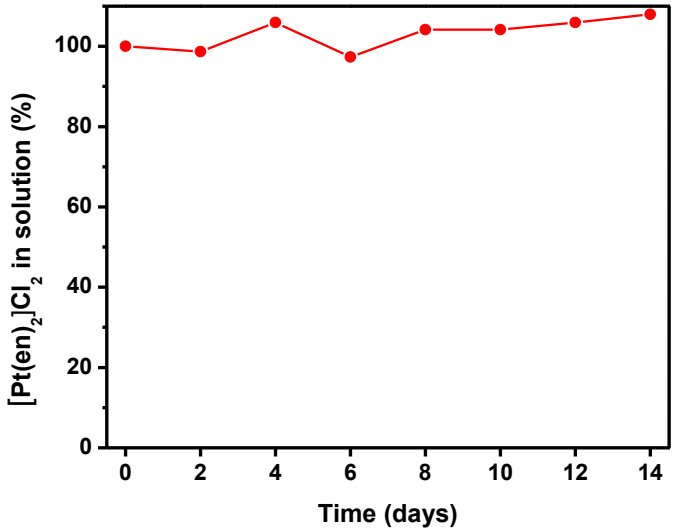

Figure 2-7 Relative concentration of $[Pt^{II}(en)_2]^{2+}$ in PBS at 37 °C over time. Reprinted from *Biomaterials* **210**, 94-104 (2019).

Charged Pt^{II} complexes with two N-N' bidentate ligands have also been investigated as metallointercalators.[58, 59] The planar, aromatic rings must be on the size of a base pair, ~3.4 Å, to insert into the DNA bases.[59] The planar $[Pt^{II}(en)_2]^{2+}$ could not displace ethidium bromide (EtBr) intercalated with DNA, with consistent fluorescence from EtBr-bound DNA at Pt:DNA ratios ranging from 0.01:1 to 10:1 (**Figure 2-8**).

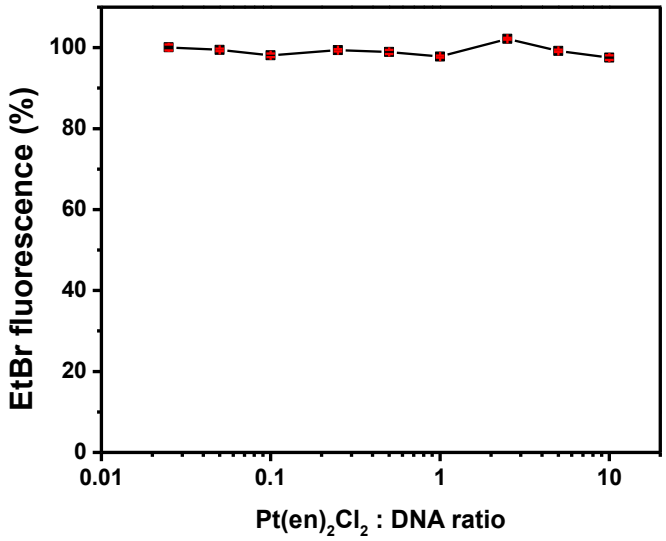

Figure 2-8 DNA intercalation by $[Pt^{II}(en)_2]Cl_2$. Reprinted from *Biomaterials* **210**, 94-104 (2019).

As a result, no cytotoxicity was observed on HCT116 cells by MTS assay. Negligible changes in cell viability were observed after treatment with $[Pt^{II}(en)_2]Cl_2$, $[Pt^{IV}(en)_2bp]Cl_2$, or PtEN at up to 100 μM after up to 72 h incubation (**Figure 2-9**). $[Pt^{II}(en)_2]Cl_2$ and $[Pt^{IV}(en)_2bp]Cl_2$ were further directly compared against cisplatin (CisPt) in platinum-sensitive H460 cells by MTS assay. The IC_{50} of CisPt was determined to be 5.58 ± 0.26 μM compared to > 100 μM by $[Pt^{II}(en)_2]Cl_2$, as determined by ~100% cell viability at this dose (**Figure 2-10**). These data indicate that any observed anticancer effects from PtEN delivered payloads are intrinsic to the payload itself.

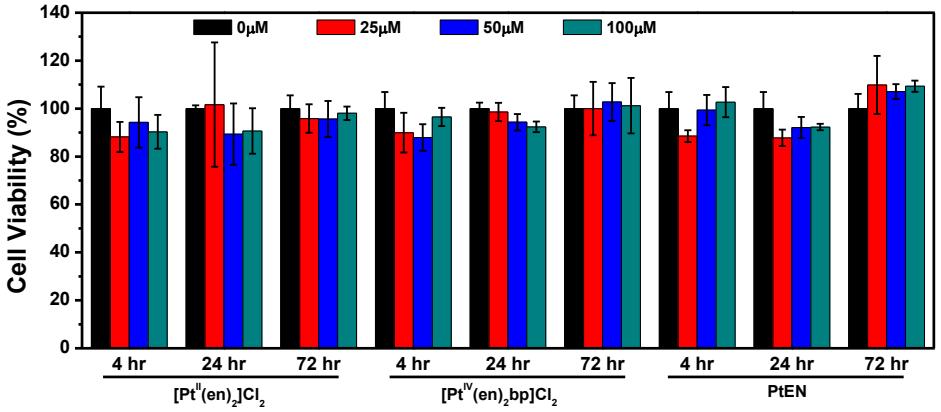

Figure 2-9 Negligible cytotoxicity in HCT116 cells treated with $[Pt^{II}(en)_2]Cl_2$, $[Pt^{IV}(en)_2bp]^{2+}$, or PtEN at up to 100μM equivalents of Pt for up to 72 h. Reprinted from *Biomaterials* **210**, 94-104 (2019).

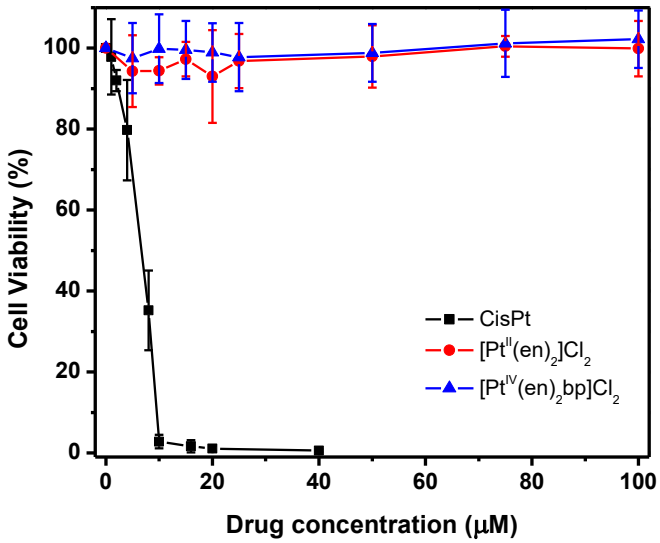

Figure 2-10 MTS assay of H460 Pt-sensitive cells treated with CDDP, $[Pt^{II}(en)_2]Cl_2$, or $[Pt^{IV}(en)_2bp]^{2+}$ at up to 100μM equivalents of Pt for 72 h. Reprinted from *Biomaterials* **210**, 94-104 (2019).

The pharmacokinetic properties of intravenously injected PtEN were investigated on subcutaneous murine colorectal cancer CT26 tumor-bearing BALB/c mice. As shown in

Figure 2-11a, PtEN did not significantly accumulate in the lung, liver, or kidney (< 10% ID/g). In contrast, there was high tumor uptake of PtEN (13.8 ± 1.4 %ID/g) 24 h post injection and a long blood circulation half-life of 14.3 ± 2.8 h (**Figure 2-11**).

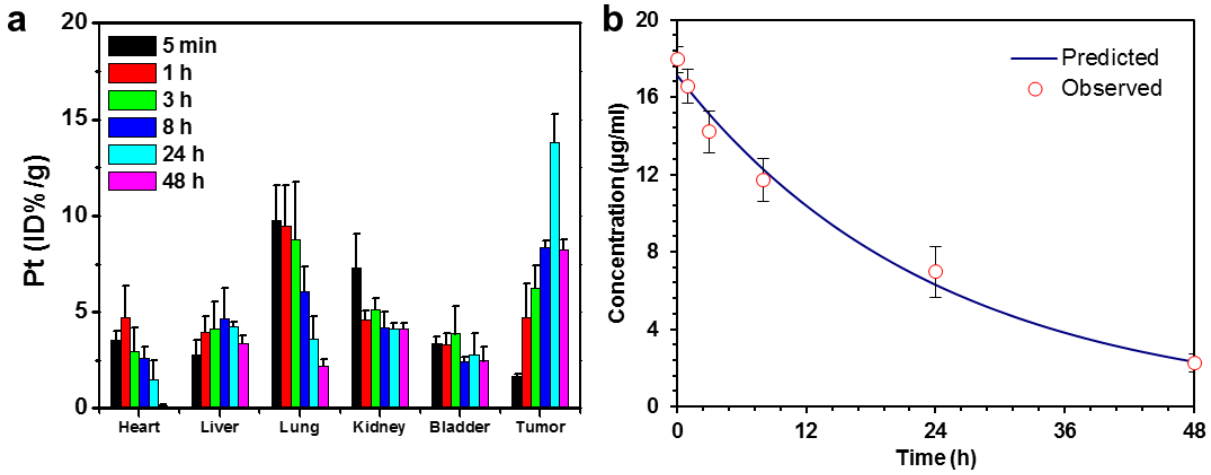

Figure 2-11 (a) Biodistribution, tumor uptake, and (b) blood concentration of Pt over time after i.v. injection of PtEN in CT26 tumor-bearing BALB/c mice at a dose of 3.0 mg/kg Pt. Reprinted from *Biomaterials* **210**, 94-104 (2019).

Even after ten daily doses of PtEN (10 × 3 mg/kg Pt), no significant toxicity was observed by monitoring mouse body weights and activities (**Figure 2-12**). Thirty days after the last dose, the mice were sacrificed to investigate the PtEN clearance and toxicity in organs with significant accumulation. There was significantly less PtEN in major mononuclear phagocyte system organs, with < 1% ID/g in the liver and kidneys (**Figure 2-13**). The histology of five major organs with relatively high PtEN accumulation showed no obvious signs of damage or significant differences compared to those of 5% dextrose-treated mice (**Figure 2-14**). These data indicate that PtEN is a nontoxic nanovehicle platform, which is ideal for delivering biological materials such as miRNAs.

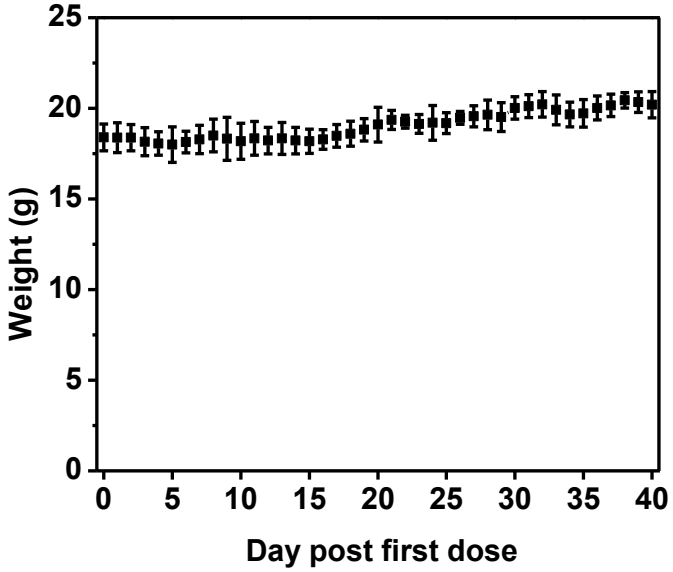

Figure 2-12 Body weight evolution of mice treated daily from day 0-10 with PtEN. Reprinted from *Biomaterials* **210**, 94-104 (2019).

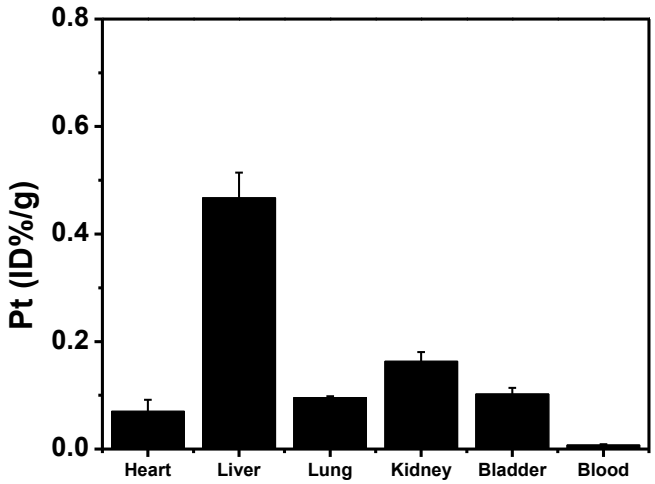

Figure 2-13 Biodistribution of Pt 30 days post final injection of PtEN. Reprinted from *Biomaterials* **210**, 94-104 (2019).

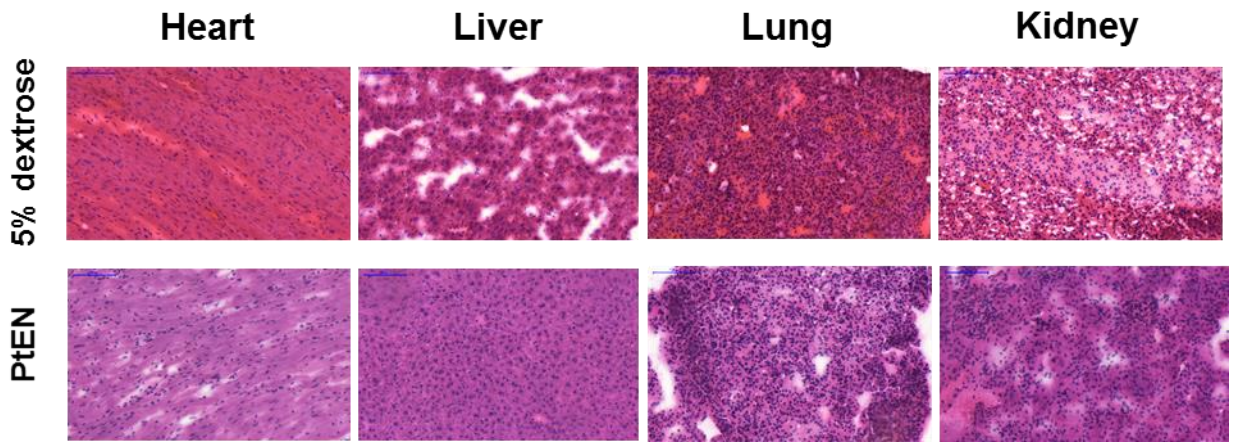

Figure 2-14 Histology of organs with significant Pt uptake 30 days post MTD. Reprinted from *Biomaterials* **210**, 94-104 (2019).

2.2.2 Synthesis and characterization of NCP-PtEN/miR-655-3p

Cationic lipids are typically required to encapsulate negatively charged mi- and siRNAs, leading to rapid clearance and short circulation half-lives. However, NCP/miRNA retains a slightly negative surface charge by incorporating an Alexa647-labeled miRNA mimic (Alexa), nontargeted miRNA (NT), miR-655-3p thiolated on the 5' end of the sense strand and conjugated to DSPE as previously described. [51, 52] PtEN/miRNAs were prepared in the presence of cholesterol, DOPC, DSPE-PEG2k, and DSPE-conjugated miRNAs (DSPE-miRNA, **Scheme 2-3**). The miRNA was loaded at 8.6 wt % into the lipid bilayer shell with 89% efficiency, as determined by Quant-iT RiboGreen RNA kit. DSPE-PEG2k was used to protect the DSPE-miRNAs from degradation by nucleases in physiological environments, but allowed for intracellular cleavage of DSPE-miRNA by reducing agents (**Scheme 2-4**). The Z-average diameter, PDI, and ζ-potential of PtEN/miR-655-3p were determined to be 99.2 ± 0.4, 0.15 ± 0.01, and –18.8 ± 1.9 mV in water, with similar size and shape to PtEN (**Figure 2-15, Figure 2-16**). A control lipid nanoparticle formulation containing DSPE-NT (N/NT) or DSPE-miR-655-3p (N/655) was synthesized by the same procedure in the absence of PtEN.

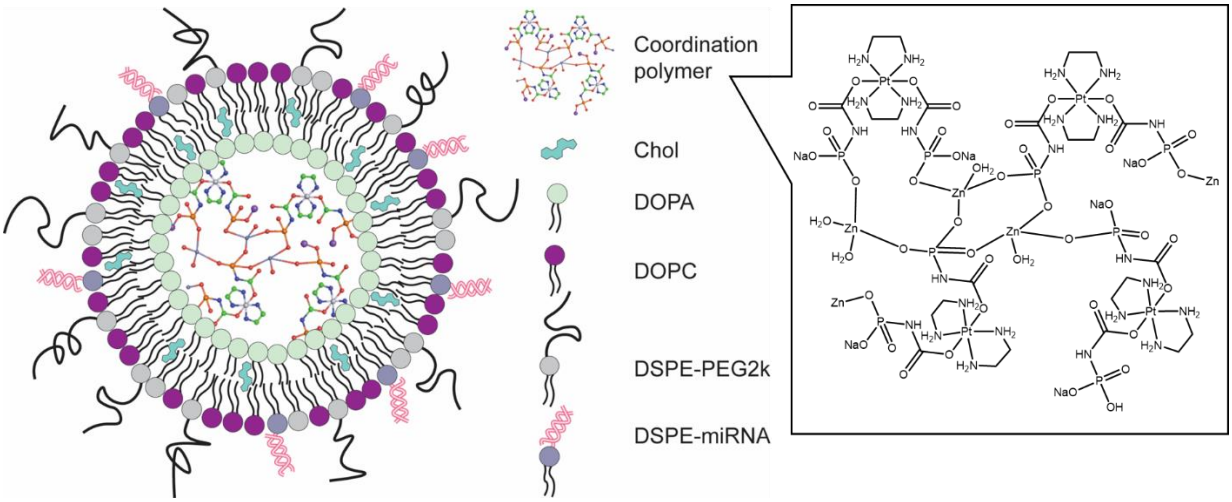

Scheme 2-3 Schematic representation of PtEN/miRNA carrying a nontoxic coordination polymer in the core and miRNA in the lipid shell, protected by DSPE-PEG2k. Reprinted from *Biomaterials* **210**, 94-104 (2019).

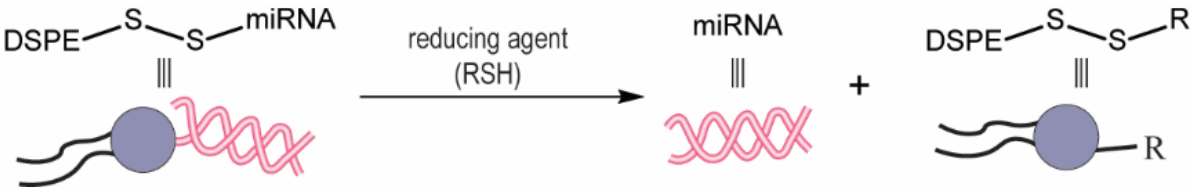

Scheme 2-4 Schematic illustration of miRNA release from DSPE-miRNA. Reprinted from *Biomaterials* **210**, 94-104 (2019).

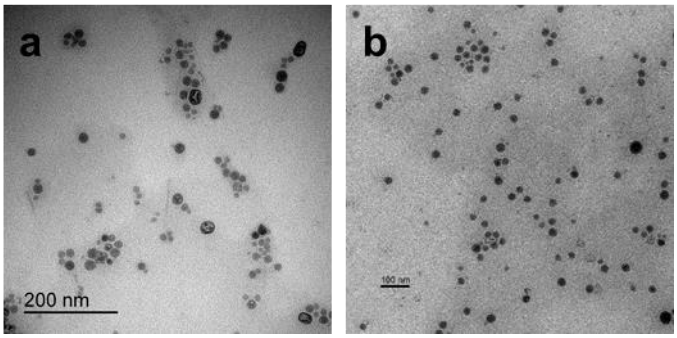

Figure 2-15 TEM image of (a) PtEN and (b) PtEN/miRNA showing the approximate size and monodispersity of the spherical nanostructure. Bar = 100 nm. Reprinted from *Biomaterials* **210**, 94-104 (2019).

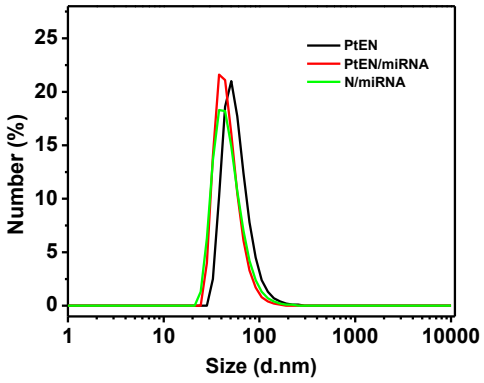

Figure 2-16 Number-average size distribution of PtEN, PtEN/miRNA, and N/miRNA in H_2O. Reprinted from *Biomaterials* **210**, 94-104 (2019).

2.2.3 In vitro endosomal escape and cytotoxicity

The cell uptake of PtEN was not affected by loading miRNA onto the particle surface (**Figure 2-17**). This was visualized by confocal laser scanning microscopy (CLSM) of PtEN/Alexa rapidly internalized by HCT116 cells (**Figure 2-18a**). Cells were incubated with PtEN/Alexa for up to 2 h, fixed, stained with Lysotracker Green and DAPI to visualize the endosome/lysosome and nuclei. PtEN/Alexa taken up by the HCT116 cells could release their payload into the cytoplasm, which was observed as a decrease in the colocalization between PtEN/Alexa and the endosome/lysosome by confocal laser scanning microscopy (**Figure 2-18b**). Over 24 h, this led to significant uptake of Alexa when delivered as PtEN/Alexa or N/Alexa with no observed uptake of the Alexa647-miRNA mimic alone (**Figure 2-19**).

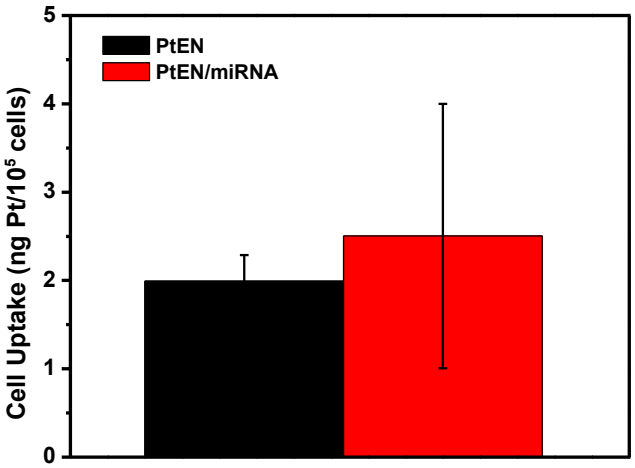

Figure 2-17 Cellular uptake of PtEN with or without loading miRNA. Reprinted from *Biomaterials* **210**, 94-104 (2019).

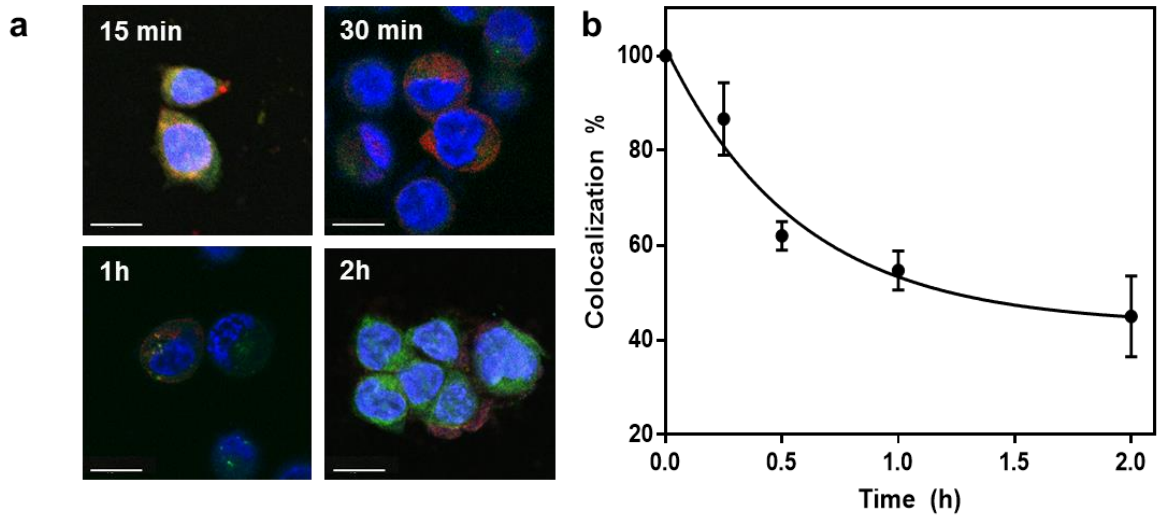

Figure 2-18 (a) Time-dependent endosomal escape of PtEN/Alexa (red fluorescence) in HCT116 cells by CLSM. Alexa overlap with endo/lysosomes stained by Lysotracker Green (green fluorescence) can be observed as yellow fluorescence. Bar = 10 µm. (b) Percentage co-localization of Alexa with endo/lysosomes over time in (a) as quantified by Image J. Reprinted from *Biomaterials* **210**, 94-104 (2019).

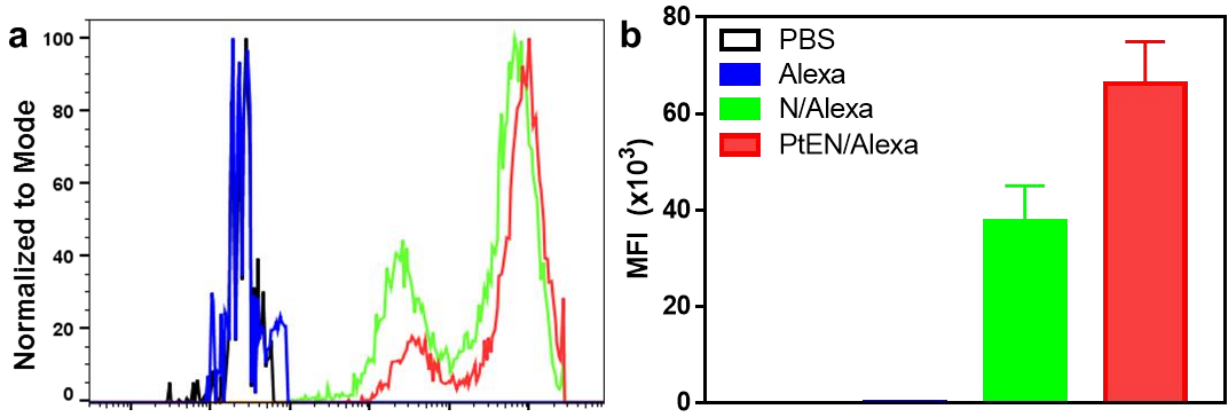

Figure 2-19 (a) Cellular uptake and (b) median fluorescence intensity of Alexa by HCT116 cells dosed with the Alexa647-miRNA mimic or PtEN/Alexa by flow cytometry. Reprinted from *Biomaterials* **210**, 94-104 (2019).

PtEN/miR-655-3p at a dose of 50 nM miRNA only showed slight cytotoxicity (89.0 ± 3.5% cell viability) in HCT116 cells after incubation for 24 h, but significantly decreased cell viability after 72 h (32.4 ± 7.3% cell viability). In contrast, cells treated with PtEN/NT or $[Pt^{II}(en)_2]Cl_2$ plus miR-655-3p showed no impact or increase in cell viability, respectively (**Figure 2-20**). This confirms that neither $Pt(en)_2Cl_2$ nor PtEN are inherently toxic and that miR-655-3p requires a transfection agent for activity.

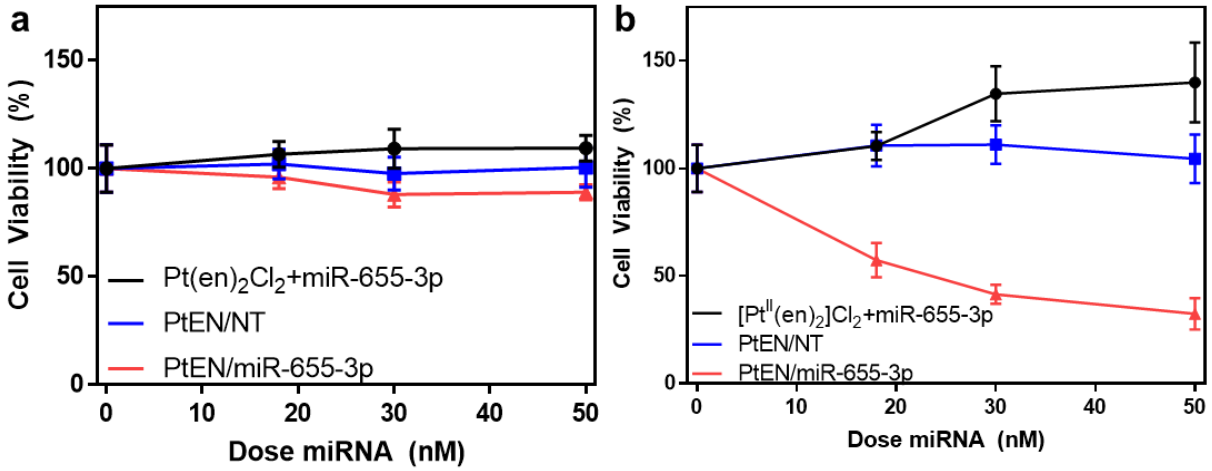

Figure 2-20 In vitro cytotoxicity of PtEN/miR-655-3p on HCT116 cells after (a) 24 h or (b) 72 h by MTS assay. Reprinted from *Biomaterials* **210**, 94-104 (2019).

To elucidate the mechanisms behind the observed cytotoxicity, we probed treated HCT116 cells for Annexin V and propidium iodide (PI) to assess apoptosis and necrosis, respectively. Though there have been reports of cytotoxicity by necrosis by liposomes producing large amounts of CO_2,[60-62] the CO_2 released as a byproduct of the reduction of $[Pt^{IV}(en)_2bp]Cl_2$ was not cytotoxic. We did not observe any apoptosis/necrosis in HCT116 cells dosed with PtEN, PtEN/NT or PtEN/miR-655-3p for up to 72 h (**Figure 2-21**, **Table 2-1**).

Table 2-1 Percentages of healthy, apoptotic, and necrotic HCT116 cells incubated 50 nM miRNA or equivalent 3.5 μM Pt for up to 72 h. Reprinted from *Biomaterials* **210**, 94-104 (2019).

		Healthy	Early apoptotic	Necrotic	Late apoptotic/necrotic
4 h	PBS	96.7	0.97	0.29	2.05
	PtEN	97.9	0.59	0.25	1.25
	PtEN/NT	97.3	1.07	0.19	1.45
	PtEN/miR-655-3p	97.0	0.83	0.43	1.70
24 h	PBS	96.7	0.76	0.61	1.96
	PtEN	94.9	1.17	0.23	3.69
	PtEN/NT	97.9	0.96	0.24	0.89
	PtEN/miR-655-3p	97.3	0.87	0.22	1.62
72 h	PBS	97.6	0.50	1.28	0.59
	PtEN	98.0	0.16	1.54	0.29
	PtEN/NT	98.3	0.32	0.94	0.46
	PtEN/miR-655-3p	97.0	1.74	0.27	1.01

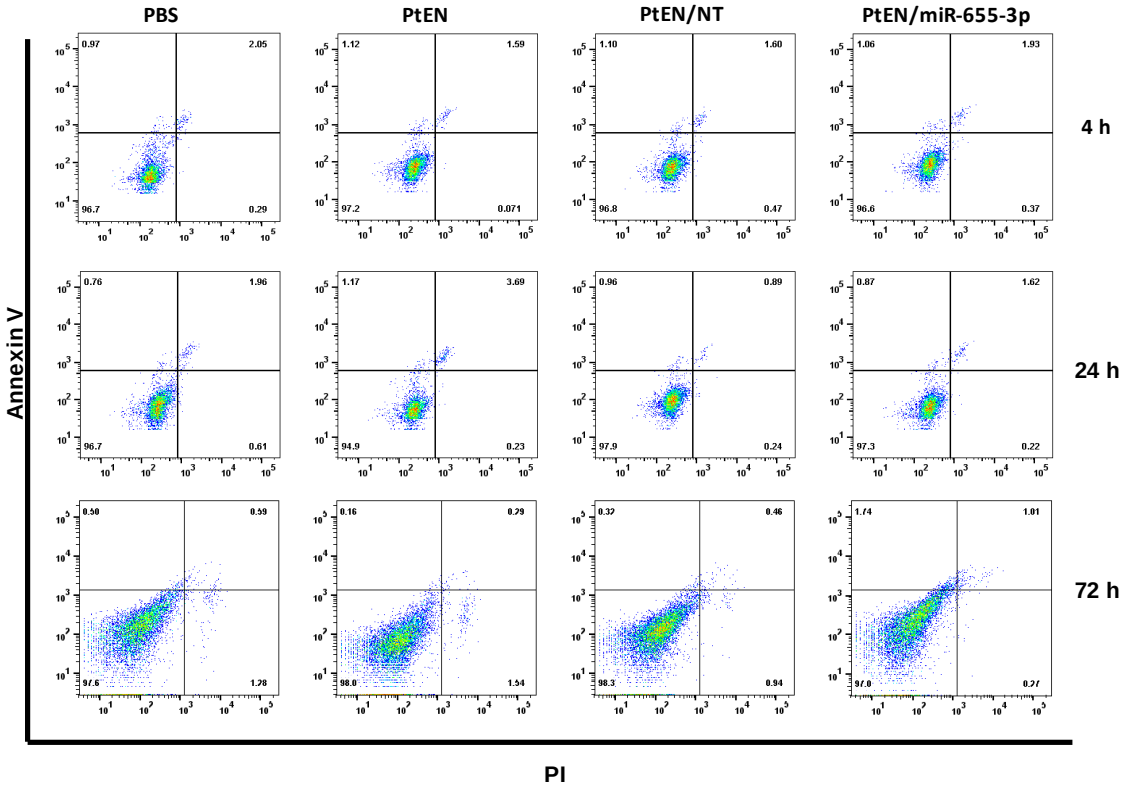

Figure 2-21 Annexin V/PI analysis of HCT116 cells incubated with 50 nM miRNA or equivalent 3.5μM Pt. Quadrants clockwise from lower left to upper left represent healthy, early apoptotic, late apoptotic, and necrotic cells, respectively. Reprinted from *Biomaterials* **210**, 94-104 (2019).

2.2.4 In vitro mechanism analysis

Given that PtEN/miR-655-3p does not directly induce cytotoxicity by apoptosis or necrosis, we hypothesized that miR-655-3p may suppress cell proliferation by impacting cell cycle regulation and DNA synthesis. HCT116 cells treated with PBS, $[Pt^{II}(en)_2]Cl_2$ plus miR-655-3p, or PtEN/NT for 24 h had proliferated to 1.7-1.9 times of the seed amount, compared to 0.96 ± 0.17 times of adherent cells in the group treated with PtEN/miR-655-3p (**Figure 2-22**). Interestingly, miRNA-carrying nanoparticles without the NCP core had no effect on cell proliferation despite

strong uptake due to an inability to escape from the endosome. After 72 h, PtEN/miR-655-3p treated cells proliferated 5.5 ± 1.2 times compared to 11.4-12.0 times for controls (**Figure 2-22**).

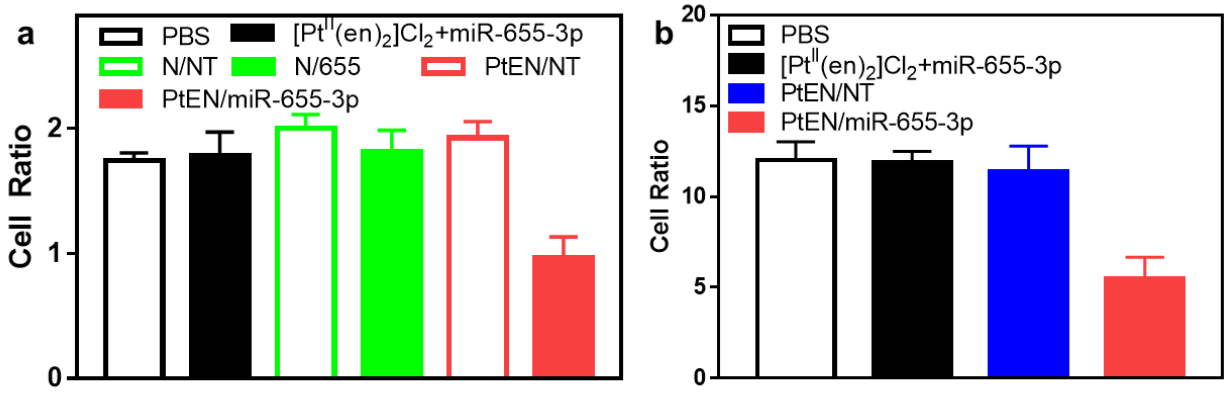

Figure 2-22 Reduced cell proliferation after treatment of HCT116 with PtEN/miR-655-3p for (a) 24 h or (b) 72 h by cell counting. Reprinted from *Biomaterials* **210**, 94-104 (2019).

To probe the mechanisms behind reduced proliferation, mRNA levels of several target genes were investigated by real-time qPCR with primers found in **Table 2-2**. HCT116 cells transfected with PtEN/miR-655-3p for 48 h showed significant downregulation of TGFBR2 (53% of PtEN/NT, p=0.0001, **Figure 2-23a**), whereas transfection with N/655 did not show any effect on TGFBR2 expression (**Figure 2-23b**). TGF-β signaling by TGF-β ligand binding to TGFBR2 is a known regulator of the G_1/S checkpoint, which arrests normal cell cycle progression but promotes metastatic progression in cancer cells.[63] The G_1 checkpoint regulates whether a cell will enter the S phase committing to cell division or enter G_0 to become quiescent/senescent. One observed molecular effect associated with cell cycle exit is the downregulation of PTTG1,[64] which is decreased in HCT116 cells treated with PtEN/miR-655-3p (53% of PtEN/NT, p=0.0009, **Figure 2-23c**). Interestingly, SENP6 was also downregulated (42% of PtEN/NT, p=0.0028), which leads to reduced DNA synthesis and increased DNA breaks (**Figure 2-23d**).[65]

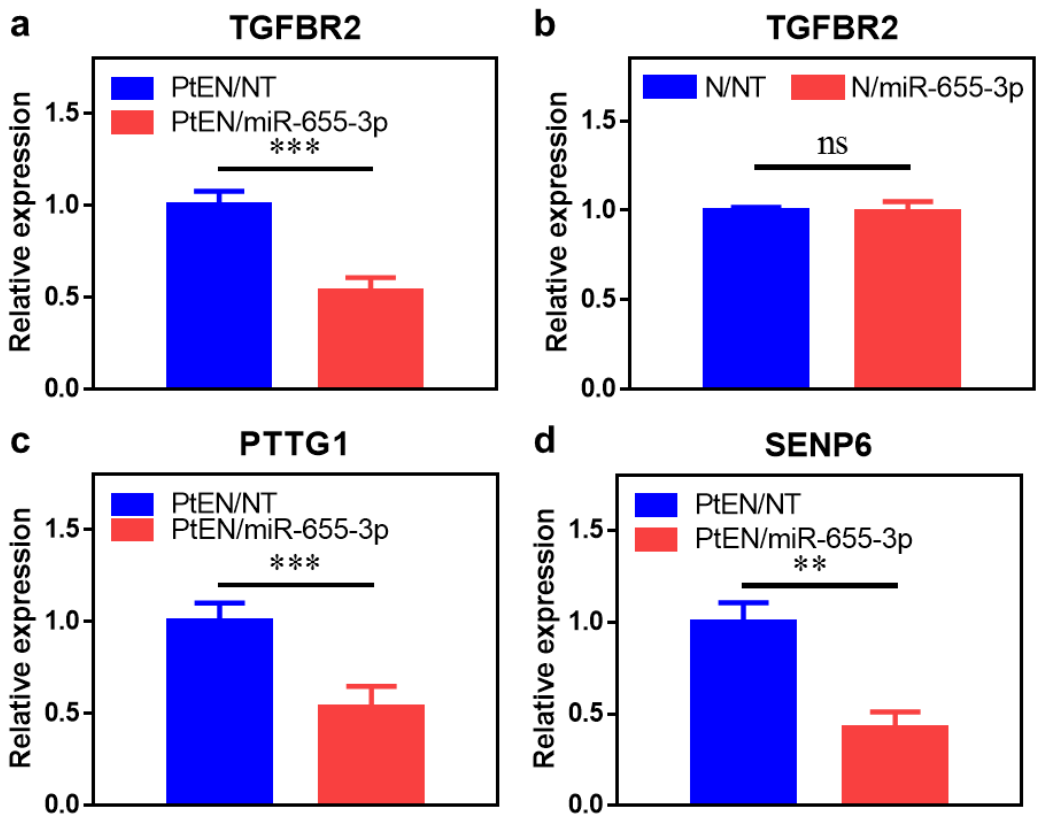

Figure 2-23 mRNA expression levels of miR-655-3p target genes (a,b) TGFBR2, (c) PTTG1, and (d) SENP6 after 48 h. Reprinted from *Biomaterials* **210**, 94-104 (2019).

Table 2-2 Primer sequences of TGFBR2, PTTG1, SENP6, and for real-time qPCR. (PTTG1 and SENP primers are from PrimerBank, 11038651c1 and 156105702c1).[66]

	Primer F	Primer R
TGFBR2	GTAGCTCTGATGAGTGCAATGAC	CAGATATGGCAACTCCCAGTG
PTTG1	ACCCGTGTGGTTGCTAAGG	ACGTGGTGTTGAAACTTGAGAT
SENP6	TCCTGTAAGGTTAAGTCGGCT	AGATAGAGGAGGAGTAGGCTGAT

Wnt/β-catenin signaling has been correlated with EMT, cancer cell proliferation, and metastasis. In a study of spontaneous breast cancer in mice, normal and precancerous mammary tissue showed β-catenin localization in the cell membrane and cytoplasm, respectively, compared

to cancerous tissue displaying β-catenin in the cytoplasm and nuclei of cells.[67] After treatment with PtEN/miR-655-3p for 48 h, HCT116 cells showed significantly decreased nuclear β-catenin (**Figure 2-24a**). The fluorescence signal is primarily sequestered to the cell membrane after treatment with PtEN/miR-655-3p, whereas β-catenin is non-specifically found across the cell in PBS or PtEN/NT treated cells (**Figure 2-24b**). Nuclear β-catenin is typically associated with cancer progression and metastasis due to its effects on transcription, whereas β-catenin sequestration at the cell membrane suggests decreased EMT activity.[68] PtEN/miR-655-3p represses invasion of HCT116 cells in a transwell assay, reducing the number of invading cells by 81.4%, from 134.67 ± 56.0 to 25.0 ± 5.0 for PBS and PtEN/miR-655-3p treated groups, respectively (**Figure 2-25**, **Figure 2-26**). Expectedly, PtEN/NT did not significantly affect the number of invading cells (134.67 ± 56.0 vs. 109.42 ± 42.0 for PBS and PtEN/NT, respectively).

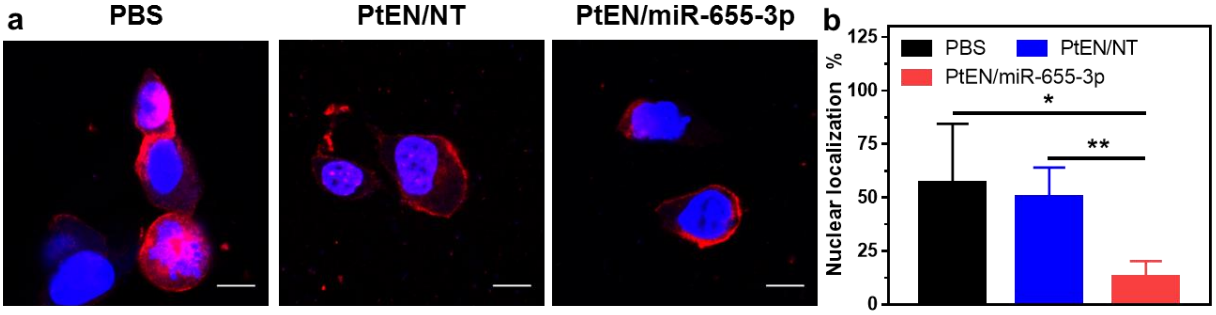

Figure 2-24 (a) Representative immunofluorescence images and (b) quantification of β-catenin nuclear localization in HCT116 cells. Scale bar = 10 μm. Reprinted from *Biomaterials* **210**, 94-104 (2019).

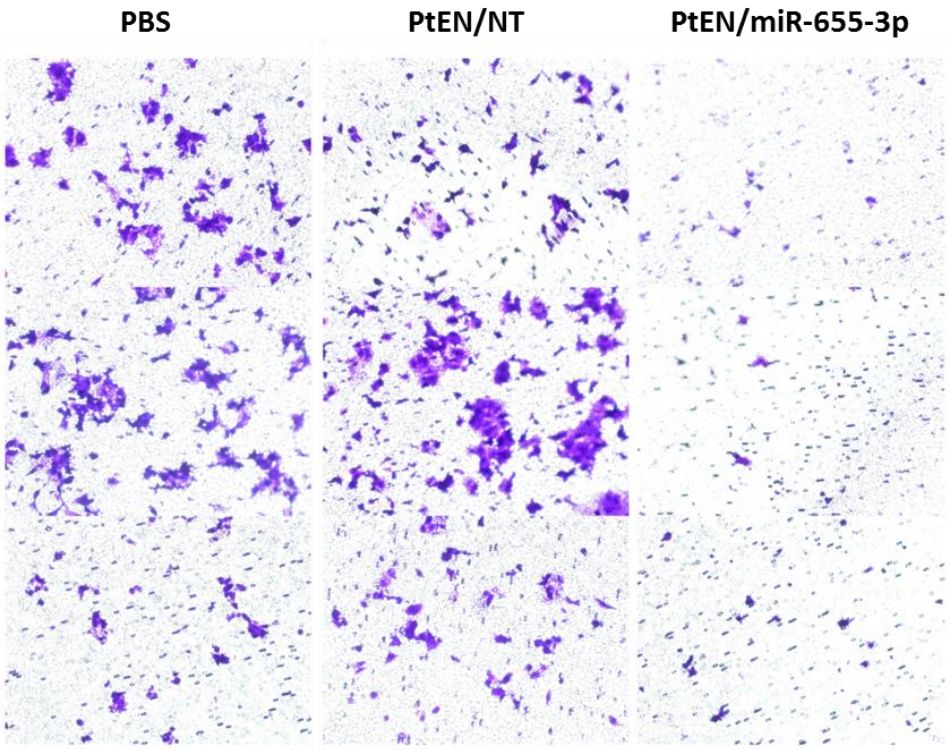

Figure 2-25 Crystal violet-stained invading HCT116 cells after treatment with PBS, PtEN/NT or PtEN/miR-655-3p by transwell invasion assay. Reprinted from *Biomaterials* **210**, 94-104 (2019).

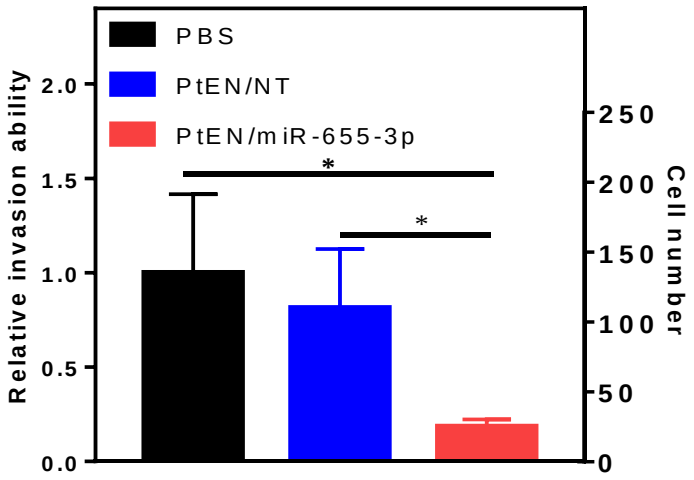

Figure 2-26 Quantification of crystal violet-stained invading HCT116 cells represented as a ratio of PBS control and as discrete cell counts. Reprinted from *Biomaterials* **210**, 94-104 (2019).

2.2.5 In vivo toxicity of NCP-PtEN/miR-655-3p

Inspired by our in vitro results, we next evaluated the possibility of PtEN/miR-655-3p for in vivo anti-metastatic activity. The serum levels of pro-inflammatory cytokines in immunocompetent BALB/c mice did not significantly increase after dosing with PtEN or PtEN/miR-655-3p, suggesting the miRNA therapy does not cause immunotoxicity by cytokine release (**Figure 2-27**). After three doses of PtEN or PtEN/miR-655-3p with 1.875 mg/kg miRNA and 4.5 mg/kg Pt given once every three days, no liver damage was observed by histology in mice (**Figure 2-28**). Liver damage will also lead to increased levels of AST and ALT in the blood, but mice treated with PBS, PtEN, or PtEN/miR-655-3p all showed similar levels of these enzymes (**Figure 2-29**). The tumor accumulation of miRNA payloads was further investigated in a liver metastasis model of HCT116 doubly labeled with luciferase and tdTomato (HCT116-L2T) with multiple nodules developing inside the liver. Athymic nude mice were given splenic injections of HCT116-L2T, after which the spleens were removed and the HCT116-L2T cells primarily metastasized to the liver. Intraperitoneally injected PtEN/Alexa was found to primarily co-localize with the liver tumors, with minimal Alexa signal observed in the lung, heart, or kidney (**Figure 2-30, Figure 2-31**). Even when there were few or small liver tumors, PtEN/Alexa showed low accumulation in normal liver parenchyma (**Figure 2-30**). ICP-MS analysis of the lung, heart, or kidney confirmed minimal deposition in these organs after 3 or 24 h, with < 3 %ID Pt/g (**Figure 2-32**), consistent with our subcutaneous biodistribution where PtEN showed higher accumulation in the tumor than other healthy tissues.

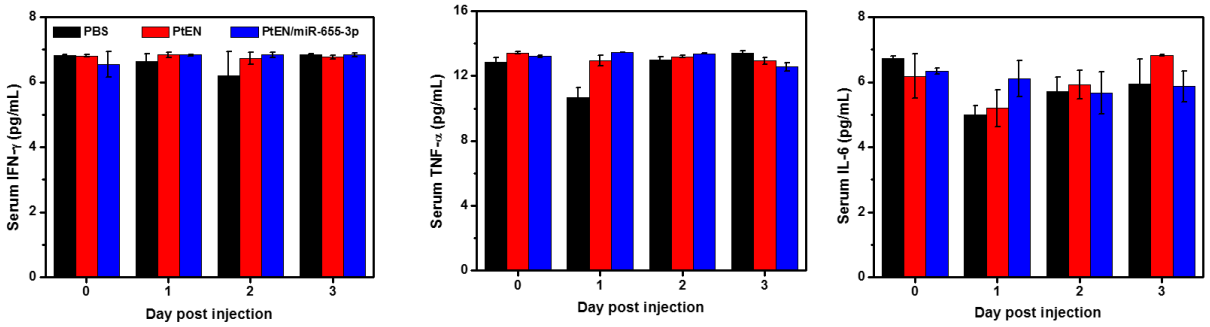

Figure 2-27 Serum levels of pro-inflammatory cytokines in mice treated with PtEN or PtEN/miR-655-3p. Reprinted from *Biomaterials* **210**, 94-104 (2019).

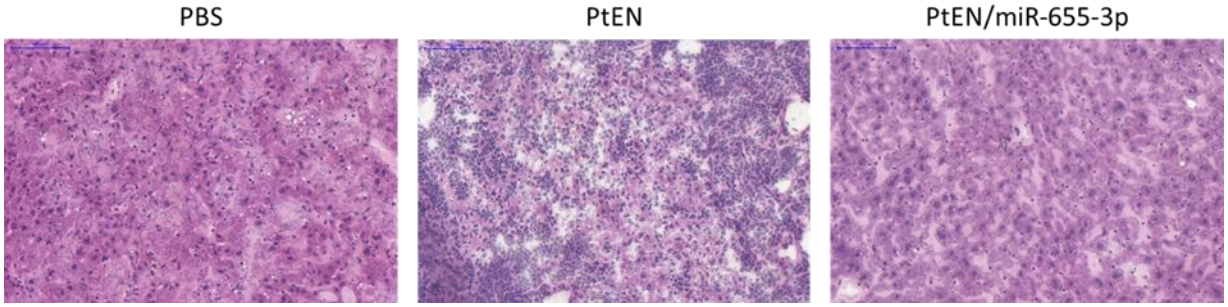

Figure 2-28 Liver histology of mice treated with repeated doses of PtEN or PtEN/miR-655-3p. Reprinted from *Biomaterials* **210**, 94-104 (2019).

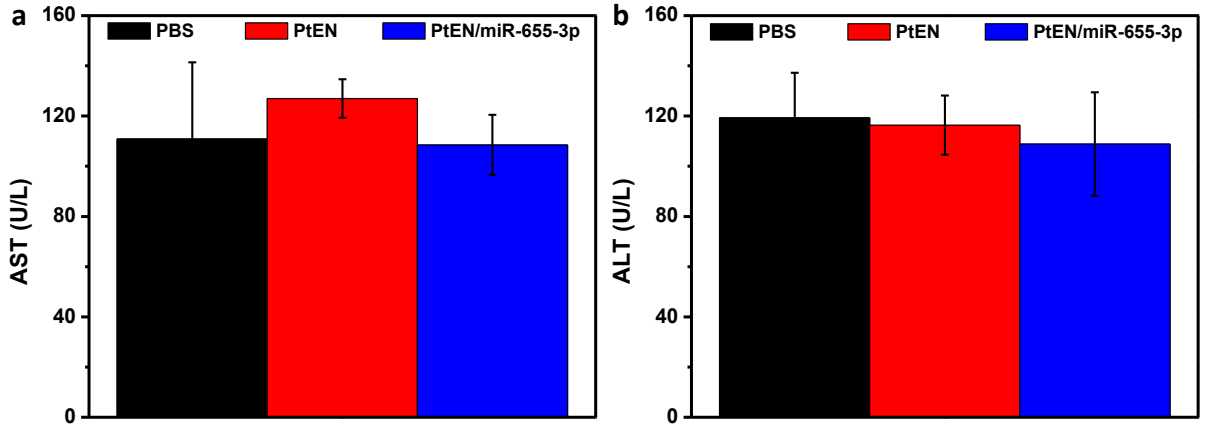

Figure 2-29 Serum levels of AST and ALT activity in mice treated with repeated doses of PtEN or PtEN/miR-655-3p. Reprinted from *Biomaterials* **210**, 94-104 (2019).

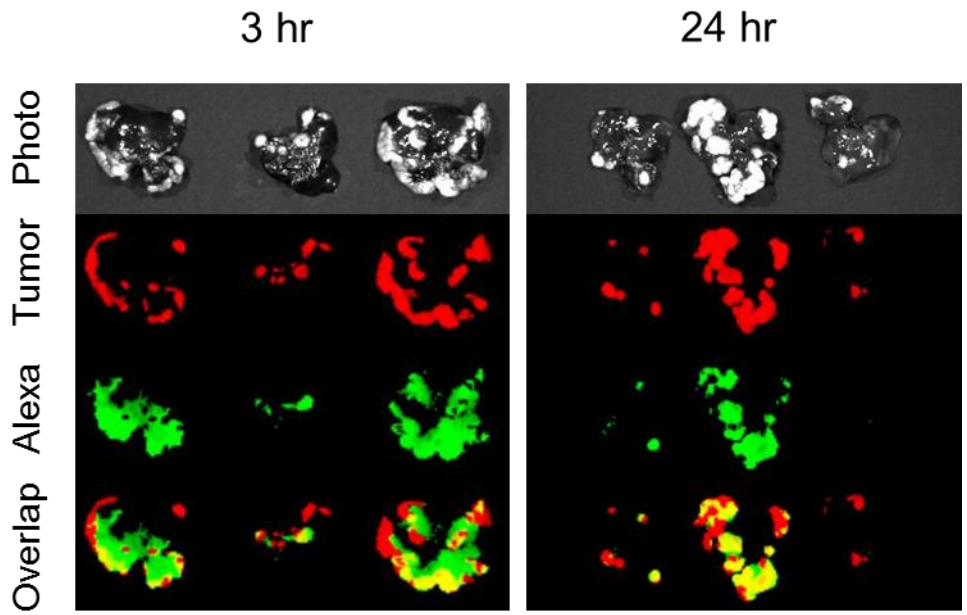

Figure 2-30 Ex vivo imaging of the liver after treatment with PtEN/Alexa. Reprinted from *Biomaterials* **210**, 94-104 (2019).

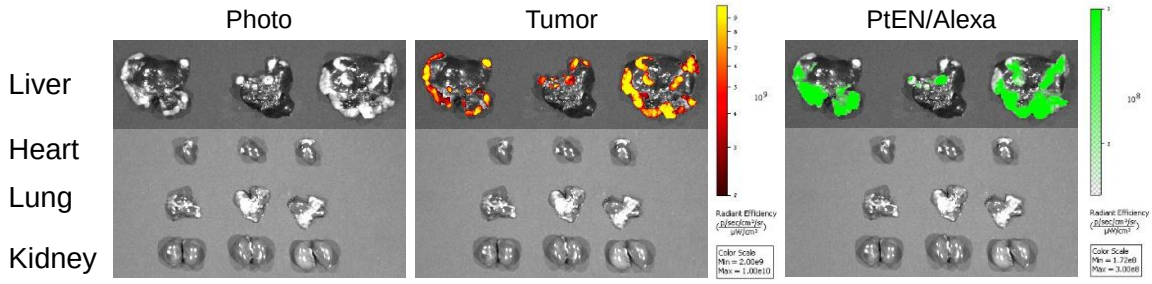

Figure 2-31 Ex vivo imaging of the heart, lung, and kidneys 3 h after treatment with PtEN/Alexa. Reprinted from *Biomaterials* **210**, 94-104 (2019).

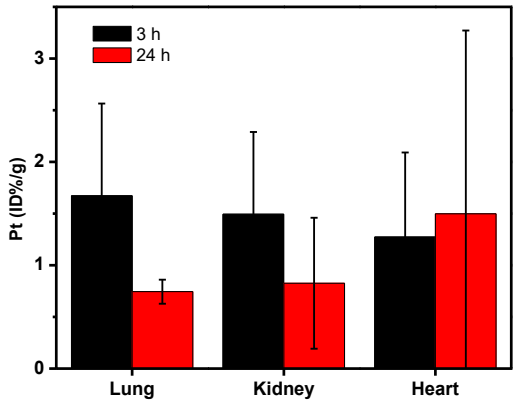

Figure 2-32 Lung, kidney, and heart concentration of Pt over time after .i.p injection of PtEN/miR-655-3p in a hepatic xenograft model. Reprinted from *Biomaterials* **210**, 94-104 (2019).

2.2.6 In vivo inhibition of liver metastases

After establishing that the miRNA-loaded particles were safe, the anti-metastatic activity of PtEN/miR-655-3p was evaluated on the metastatic model of HCT116-L2T. Beginning one day after intrasplenic injection, the mice were treated with PtEN/NT or PtEN/miR-655-3p in a 5% dextrose (w/v) solution at equivalent doses of 625 μg/kg miRNA and 1.5 mg/kg Pt once every three days. Mice treated with 5% dextrose (w/v) alone served as control. The low toxicity of both the Pt core and the miRNA allowed for repeated doses throughout the entirety of the study for a total of nine doses. Beginning 7 days after tumor inoculation by intrasplenic injection, mice were injected weekly with luciferin, anesthetized with 2% isoflurane (v/v) to visualize tumors by bioluminescence imaging (**Figure 2-33, Figure 2-34, Figure 2-35, Figure 2-36**). The tumor burden of PtEN/miR-655-3p-treated mice was significantly lower than either control group at the end of the study, as quantified by bioluminescence (**Figure 2-36, Figure 2-37**). 28 days post intrasplenic injection, the mice were euthanized for ex vivo quantification of tumor burden. These

results further confirmed our in vivo imaging results, with a significant decrease in both liver weight and ex vivo fluorescence compared to both PtEN/NT and 5% dextrose treated mice (**Figure 2-38, Figure 2-39, Figure 2-40**).

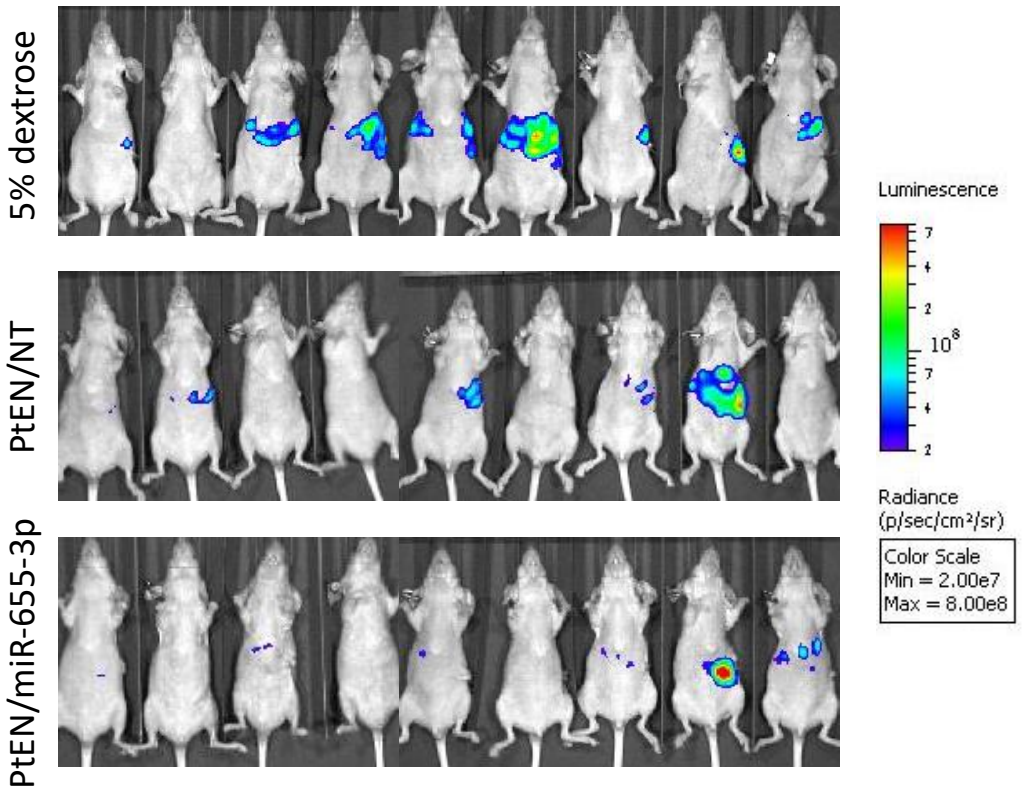

Figure 2-33 Bioluminescent images of mice bearing a hepatic metastasis model of HCT116 intraperitoneally injected with (top) 5% dextrose (w/v) control, (middle) PtEN/NT, or (bottom) PtEN/miR-655-3p 7 days post tumor inoculation. Reprinted from *Biomaterials* **210**, 94-104 (2019).

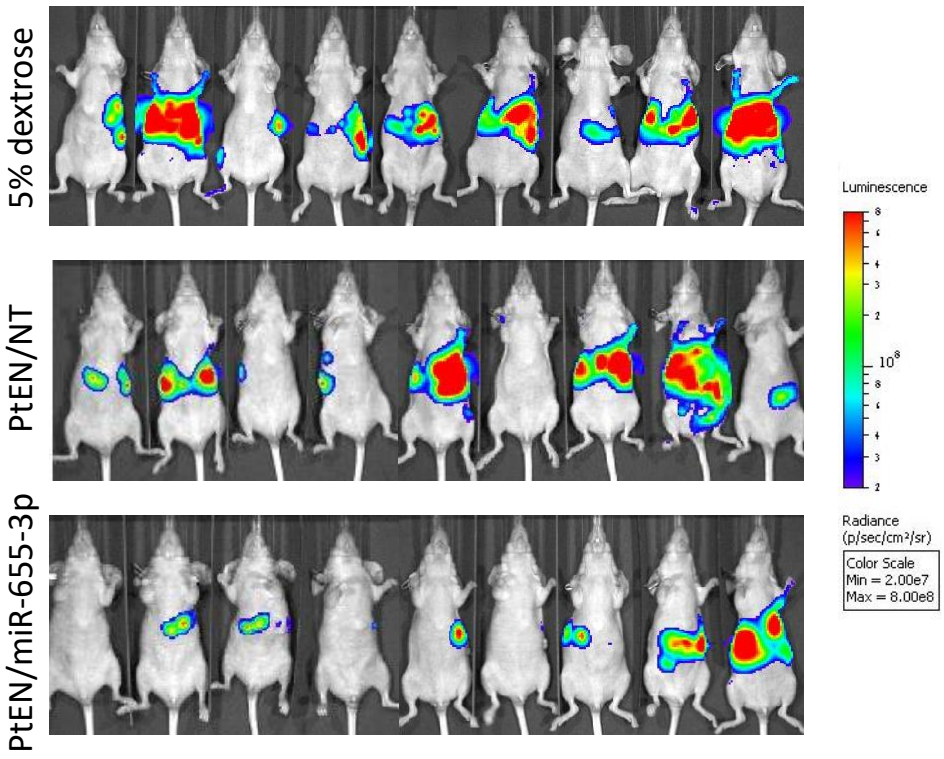

Figure 2-34 Bioluminescent images of mice bearing a hepatic metastasis model of HCT116 intraperitoneally injected with (top) 5% dextrose (w/v) control, (middle) PtEN/NT, or (bottom) PtEN/miR-655-3p 14 days post tumor inoculation. Reprinted from *Biomaterials* **210**, 94-104 (2019).

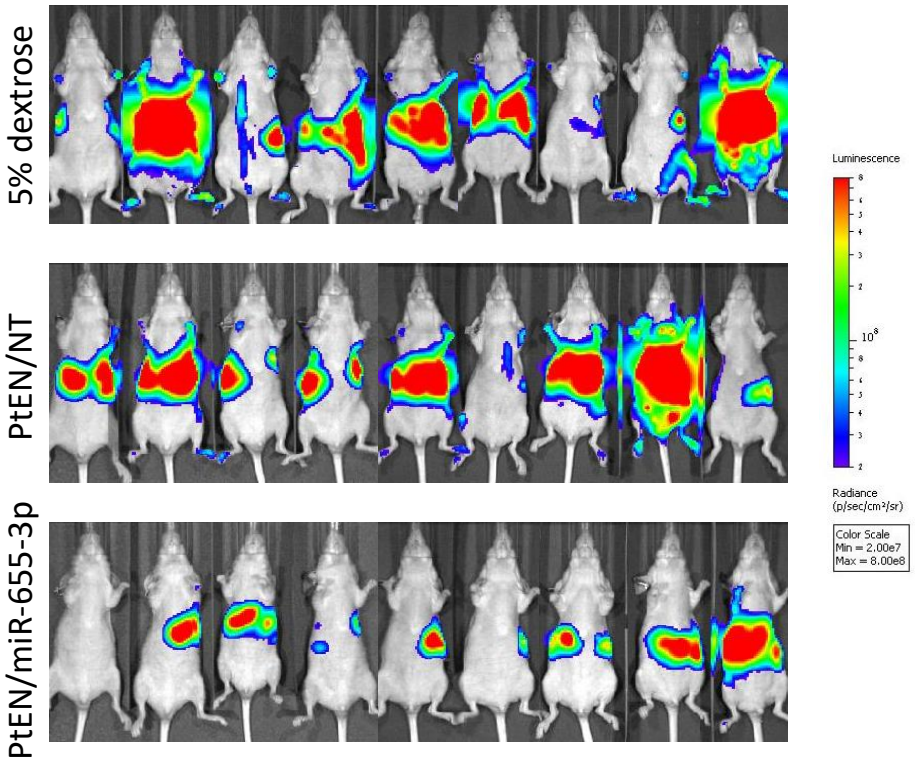

Figure 2-35 Bioluminescent images of mice bearing a hepatic metastasis model of HCT116 intraperitoneally injected with (top) 5% dextrose (w/v) control, (middle) PtEN/NT, or (bottom) PtEN/miR-655-3p 21 days post tumor inoculation. Reprinted from *Biomaterials* **210**, 94-104 (2019).

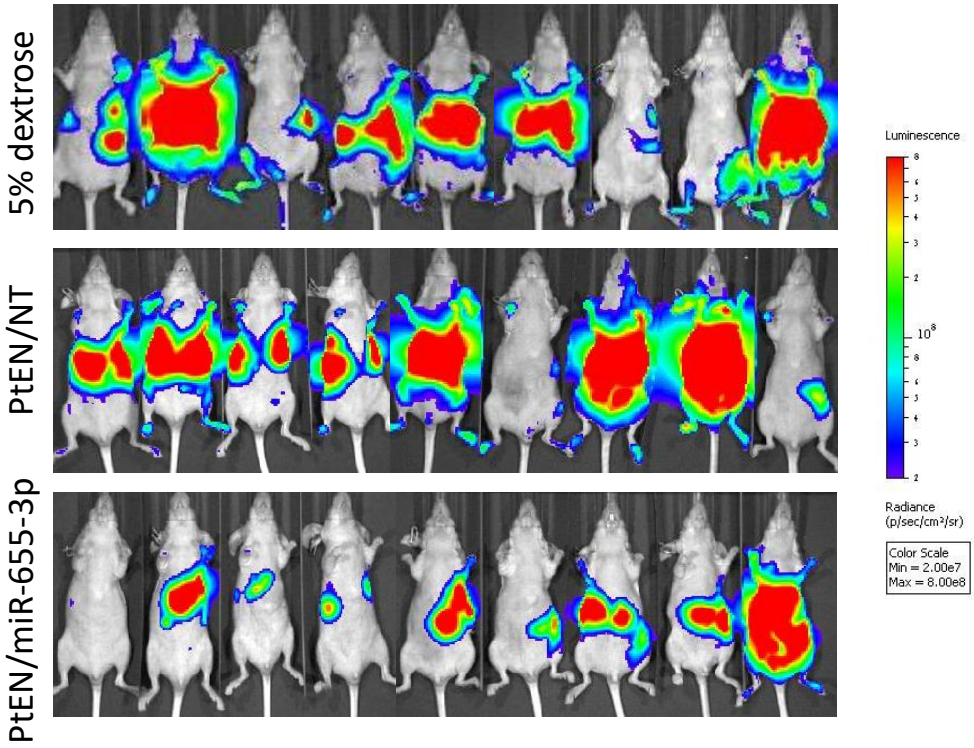

Figure 2-36 Bioluminescent images of mice bearing a hepatic metastasis model of HCT116 intraperitoneally injected with (top) 5% dextrose (w/v) control, (middle) PtEN/NT, or (bottom) PtEN/miR-655-3p 28 days post tumor inoculation. Reprinted from *Biomaterials* **210**, 94-104 (2019).

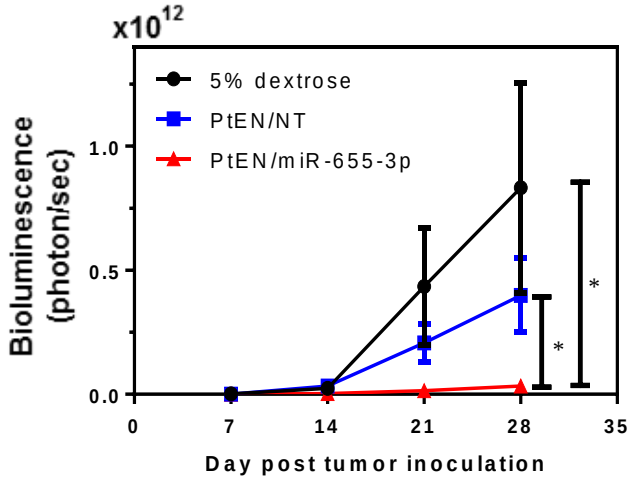

Figure 2-37 Quantification of tumor burden by bioluminescence signal for mice imaged weekly beginning 7 days post tumor inoculation. Reprinted from *Biomaterials* **210**, 94-104 (2019).

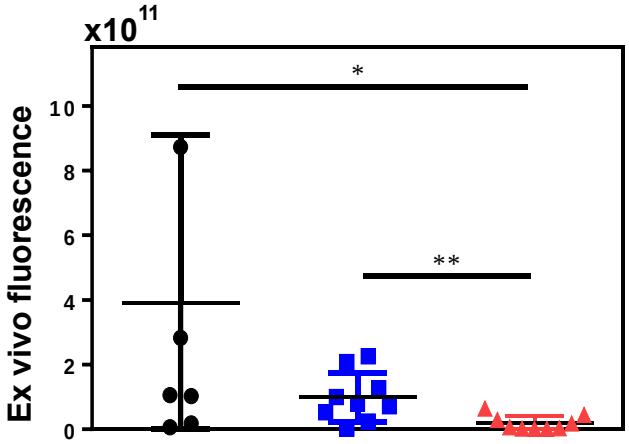

Figure 2-38 Quantification of the ex vivo fluorescence of the livers harvested 28 days post tumor inoculation. Reprinted from *Biomaterials* **210**, 94-104 (2019).

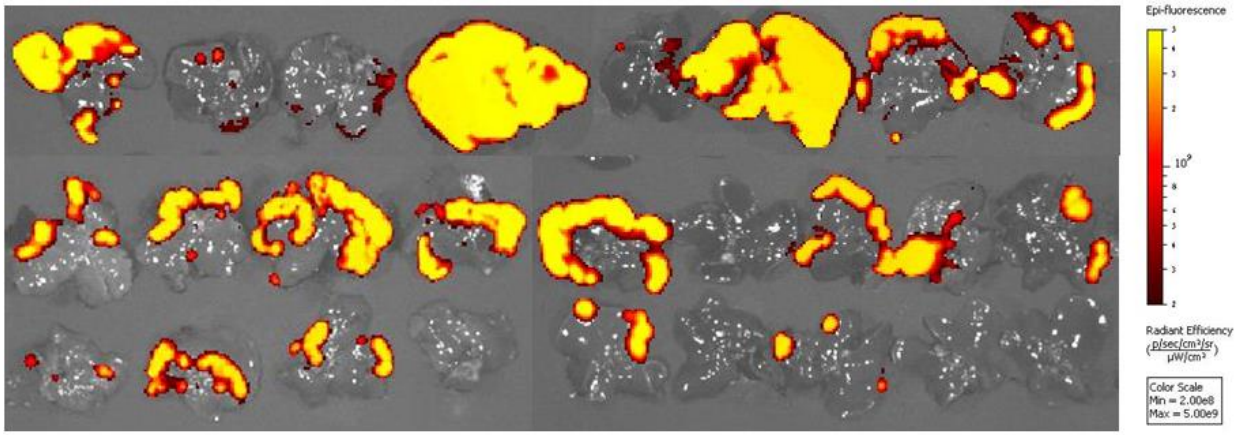

Figure 2-39 Ex vivo fluorescence of livers excised from mice bearing a hepatic metastasis model of HCT116 intraperitoneally injected with (top) 5% dextrose (w/v) control, (middle) PtEN/NT, or (bottom) PtEN/miR-655-3p 28 days post tumor inoculation. Reprinted from *Biomaterials* **210**, 94-104 (2019).

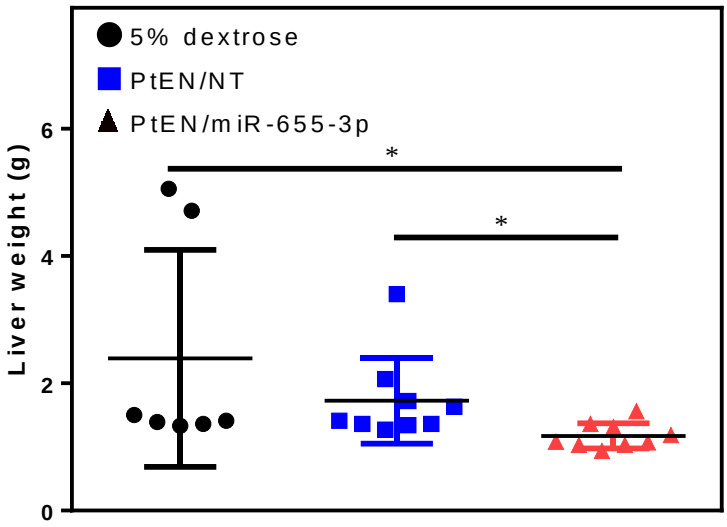

Figure 2-40 Weights of livers excised from mice bearing a hepatic metastasis model of HCT116 treated for anti-metastatic efficacy 28 days post tumor inoculation. Reprinted from *Biomaterials* **210**, 94-104 (2019).

The in vivo transfection of PtEN/miR-655-3p were further validated in the HCT116-L2T system. 28 days after establishing the liver metastasis model, mice received a single dose of PtEN/NT or PtEN/miR-655-3p at a miRNA dose of 625 μg/kg, equivalent to the efficacy dose. 2 days after treatment, the liver was excised and the tumor was isolated from half the liver metastases for RNA extraction with Trizol. The mRNA levels of miR-655-3p regulated genes were found to be down-regulated, similar to in vitro transfected cells (**Figure 2-41**). The other half of the liver and associated tumor was sectioned and stained for histology and immunofluorescence of β-catenin (**Figure 2-42**). The localization of β-catenin in mice treated with PtEN/miR-655-3p primarily showed localized in the cell membrane in both the tumor and liver tissue. There was similar sequestration of β-catenin to the membrane in the liver parenchyma of PtEN/NT-treated mice, whereas there was nonspecific distribution of β-catenin in the labeled tumor cells.

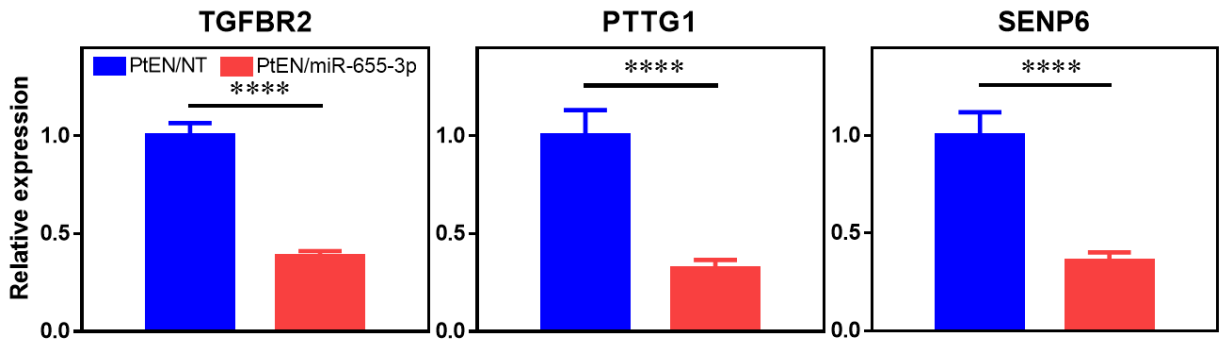

Figure 2-41 mRNA expression levels of miR-655-3p target genes TGFBR2, PTTG1, and SENP6 in tumor nodules excised from the hepatic metastasis model of mice treated with PtEN/NT or PtEN/miR-655-3p. Reprinted from *Biomaterials* **210**, 94-104 (2019).

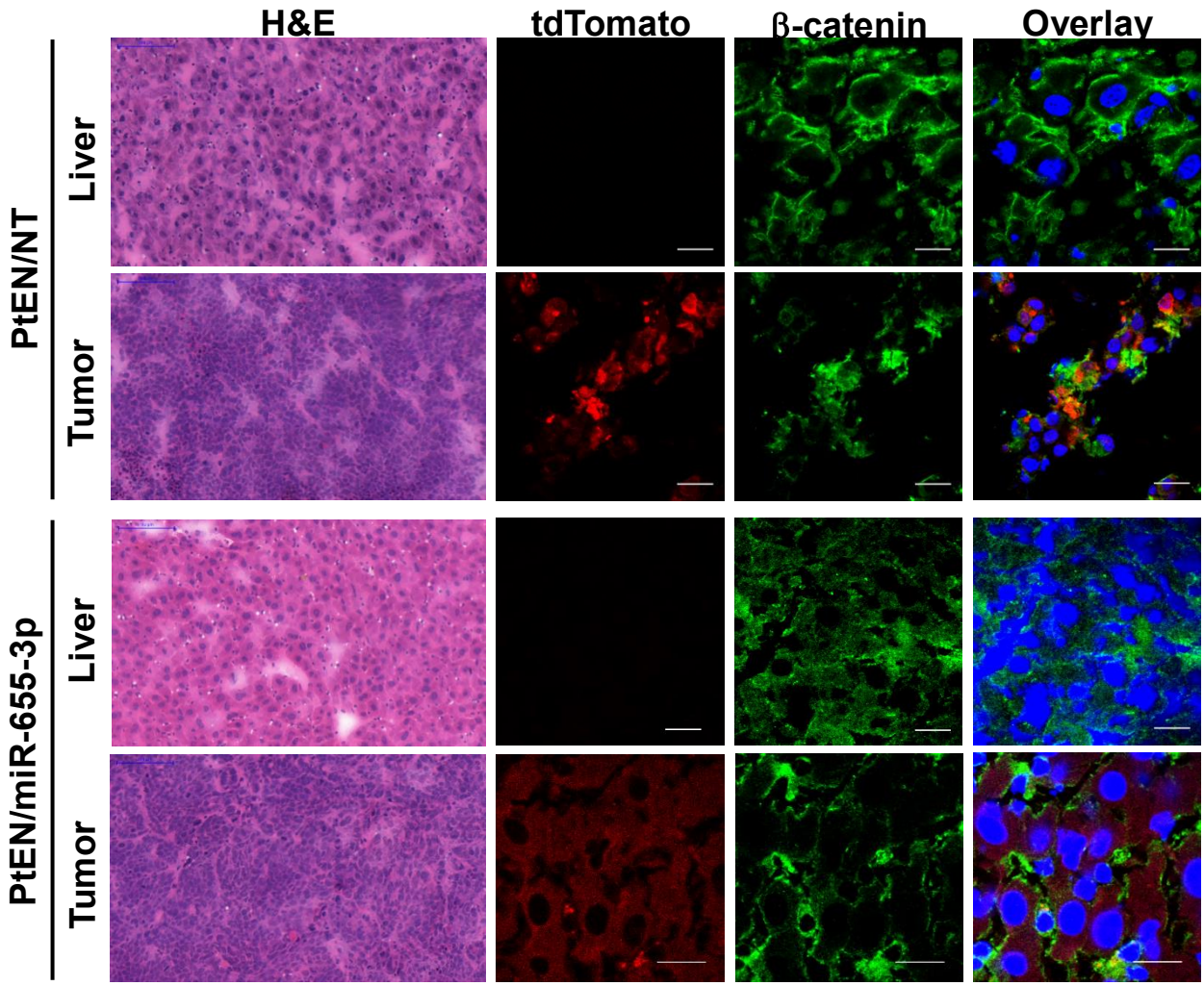

Figure 2-42 Representative histology and immunofluorescence images of β-catenin (green fluorescence) in the liver parenchyma and the tumor nodules (tdTomato red fluorescence) in livers treated once with PtEN/NT or PtEN/miR-655-3p. Scale bar = 200 μm for H&E staining; scale bar = 20 μm for immunofluorescence. Reprinted from *Biomaterials* **210**, 94-104 (2019).

2.3 Discussion

Though there has been significant progress in early detection and personalized medicines for cancer treatment, cancer metastases have remained a preeminent challenge. Metastases can occur long before detectable both in animal models and human patients, emphasizing the need for effective treatment strategies.[69, 70] Currently, patients are treated systemically with radiotherapy,

chemotherapies, or targeted therapies to stop or slow the growth of tumors, but the associated toxicities limit the frequency and total dose which can be given.[7-10] In some cases, the aggressive regimen represents overtreatment with minimal gains.[11-15] As endogenous molecules often downregulated by cancers, miRNAs represent a promising class of gene therapy to prevent and control metastasis without introducing significant toxicities. A nanoplatform for miRNA delivery with a long circulation half-life can both lower the total and frequency of drug dose by increasing effective drug exposure, allowing for thorough preparation against and facile management of metastatic disease.

The transient nature of miRNA delivery endows unique advantages and disadvantages to this therapy. By not directly integrating into the genome, there are arguably less off-target gene mutations or chromosomal aberrations. However, long-term management of a disease such as cancer requires repeated treatments to prevent and/or control tumor metastasis. Although conventional transfection agents are accompanied by cytotoxicity and initiation of the innate immune response,[31] we have demonstrated that mice can tolerate multiple successive treatments of both the PtEN carrier and PtEN/miRNA treatment without inducing any obvious signs of toxicity.

Though miRNAs can act as either tumor suppressors or promoters, miR-655-3p is known to regulate genes involved in suppressing cellular adhesion, invasion, and motility.[26, 29] The multitude of targets is less likely to lead to compensatory mechanisms of resistance which impede current chemo- and targeted therapies.[31] As miR-655-3p is specifically down-regulated by cancer cells compared to healthy tissues, some accumulation in normal cells should not drastically change the cellular levels of miRNA to alter activity whereas cancer cell proliferation will be significantly inhibited.[20]

Ectopic expression of miR-655-3p has inhibited tumor migration and invasion of multiple cancer cell lines, but miRNAs have thus far had limited application in living systems due to low stability in serum. An effective vehicle for miRNA delivery can protect it from degradation, but release the cargo into the cytoplasm of tumor cells of which it preferentially accumulates. Typically, cationic lipids are required for efficient escape from the endosome, but negatively affect blood circulation of nanoparticles leading to two opposing requirements. Ionis's antisense oligonucleotide products, such as Inotersen, are given subcutaneously to circumvent the issues with stability in blood circulation, but has broad applicability as its target, TTR, accumulates in all major organs. Even Alnylam's Patisiran, a lipid nanoparticle formulation, is primarily uptaken by hepatocytes, limiting its use to liver disease.

To this end, we have developed a nontoxic nanocarrier that maintains its structural integrity over its long circulation time, but the lipid bilayer will dissociate upon endocytosis, exposing the miRNA and the PtEN core. The exposed Pt(IV) compound was designed to enable endosomal escape upon degradation, releasing carbon dioxide when reduced to the inert, nontoxic, charged Pt(II) compound without a coordination site for Pt binding or intercalation. A neutral charge lipid nanoparticle formulation of miRNA led to significant uptake, but lack of efficacy even in vitro, underscoring the advantages of the PtEN core. Both Pt and the Alexa-miRNA mimic showed higher accumulation in tumor cells than in the liver, leading to suppression of liver metastases of colorectal cancer in mice treated with PtEN/miR-655-3p. We anticipate PtEN can thus be applied to a variety of therapeutic miRNAs outside the liver in addition to other therapeutics currently limited by poor pharmacokinetics or stability in circulation.

2.4 Conclusion

We have demonstrated that a nontoxic platinum-containing self-assembled core-shell nanoparticle can deliver miRNA to effectively suppress cancer metastasis in a xenogenic hepatic metastasis model of colorectal cancer. PtEN is distinctly superior to existing nanocarriers as it is inherently nontoxic and non-immunogenic, but can carry high loadings of miRNA with a long 14 h circulation half-life and favorable biodistribution and tumor accumulation after systemic injection. PtEN/miRNA can be transfected into cultured cells or tumors without cationic lipids by loading miRNA onto the lipid shell to protect from degradation in sera, while releasing the cargo into the cytoplasm of the tumor cells. PtEN/miR-655-3p suppressed cancer cell proliferation and EMT by limiting β-catenin nuclear translocation and resultant cell invasion in vitro. Systemic administration of PtEN/miR-655-3p transfected circulating and/or invading tumor cells in vivo, limiting liver colonization by HCT116 cells. The successful application of PtEN/miR-655-3p to suppress tumor metastasis provides proof of concept for an effective nontoxic delivery vehicle. The versatility of this platform provides a significant step towards overcoming the complex barriers inhibiting successful application of promising biologic therapies, such as nucleic acids and peptides.

2.5 Materials and methods

Materials, cell lines, and animals. All starting materials were purchased from Sigma-Aldrich and Fisher (USA) unless otherwise noted and used without further purification. 1,2-dioleoyl-sn-glycero-3-phosphate (DOPA), 1,2-distearoyl-sn-glycero-3-phosphoethanolamine (DSPE), cholesterol, and 1,2-distearoyl-sn-glycero-3-phosphoethanolamine-N-[amino(polyethylene

glycol)2000] (DSPE-PEG2k) were purchased from Avanti Polar Lipids (USA). The miRNAs were supplied by Integrated DNA Technologies (USA) or GE Dharmacon (USA) and dissolved in diethylpyrocarbonate (DEPC)-treated water before use. miR-655-3p, nontargeted control miRNA, and AlexaFluor647-miRNA mimic contained anti-sense sequences of 5'-AUAAUACAUGGUUAACCUCUUU-3', 5'-UCACAACCUCCUAGAAAGAGUAGA-3', and 5'-AGUACAUCCAUUAUAAGCUUU-3', respectively. A thiol modification was put on the 5' end of the sense strand of each miRNA in order to avoid potential inhibition on the antisense strand.

The murine colorectal cancer cell line CT26, human colorectal cancer cell line HCT116, and human lung cancer cell line H460 were purchased from the American Type Culture Collection (Rockville, MD, USA). CT26 and H460 were cultured in RPMI 1640 containing 10% fetal bovine serum (VWR), and HCT116 was cultured in Dulbecco's Modified Eagle Medium (GE Healthcare) containing 10% fetal bovine serum (VWR). HCT116 cells were stably transfected with luciferase and tdTomato via lentiviral transfection with a Luc2-tdTomato plasmid graciously provided by Dr. Geoffrey Greene. BALB/c and athymic female nude mice (6-8 weeks old, 20-25 g) were provided by Harlan-Envigo, Inc. (USA) or via inbreeding. The study protocol was reviewed and approved by the Institutional Animal Care and Use Committee (IACUC) at the University of Chicago.

Instrumentation. Pt concentrations were determined by ICP-MS (Agilent 7700X, Agilent Technologies, USA). The encapsulation of miRNA was quantified by Quant-iT RiboGreen RNA kit (Invitrogen, USA). The particle size and ζ-potential of PtEN/miRNA was determined by Zetasizer (Nano ZS, Malvern, UK). Transmission electron microscopy (TEM, Tecnai Spirit, FEI, USA) was used to observe morphology. NMR spectra were collected by Bruker AVANCE II+ 500, 11.7 Tesla Spectrometer at 500 MHz. MS spectra were collected with an Agilent 6130 ESI.

Preparation and characterization of PtEN/miRNAs. A microemulsion of 0.27 mL aqueous $Zn(NO_3)_2 \cdot 6H_2O$ (100 mg/mL) was added to 10mL surfactant (0.3 M TritonX-100, 1.5 M hexanol in cyclohexane). This was added dropwise to a vigorously stirring microemulsion of 0.27 mL aqueous $[Pt^{IV}(en)_2bp]Cl_2$ (25 mg/mL, pH=4) and 40 μL of DOPA (200mg/mL in $CHCl_3$) in 10 mL surfactant. The solution was stirred in the dark for thirty minutes at room temperature, followed by precipitation with 20 mL EtOH. DOPA-coated PtEN was collected by centrifugation at 12,000 rpm (16,743 ×g) for 20 min at 4 °C. The supernatant was discarded and the pellet was washed once with 50% cyclohexane/EtOH, once with 50% THF/EtOH, and then finally dispersed into THF and filtered through a 0.2 μm PTFE filter.

PtEN was prepared by adding a THF solution (80 μL) of cholesterol, DSPC (cholesterol/DOPC=1:2 in molar ratio), 20 mol% DSPE-PEG2k, and DOPA-coated NCP to 500 μL of 30% (v/v) EtOH/H_2O at 50 °C. The mixture was stirred at 1,700 rpm for 1 min. THF and EtOH were completely evaporated, and the PtEN solution was allowed to cool down to room temperature. PtEN/miRNA was similarly prepared with 10 μL DSPE-miRNA (2 mg/mL) added to EtOH/DEPC-H_2O at a 10:1 weight ratio of DOPA-PtEN:DSPE-miRNA. The suspensions were prepared in water or 5% dextrose for in vitro and in vivo studies, respectively.

$[Pt^{IV}(en)_2bp]Cl_2$ reduction and stability. A solution of 1 mM $[Pt^{IV}(en)_2bp]Cl_2$ and 5 mM ascorbate was heated in PBS (pH 7.2) at 37 °C for up to 5 h. $[Pt^{IV}(en)_2bp]^{2+}$ and $[Pt^{II}(en)_2]^{2+}$ in the samples were quantified by liquid chromatography-mass spectrometry (LC-MS, Agilent 6540, Agilent Technologies, USA). $[Pt^{II}(en)_2]Cl_2$ was stored in PBS (pH 7.2) at 37 °C for 2 weeks followed by analysis of $[Pt^{II}(en)_2]^{2+}$ to evaluate the stability of the Pt-en bond.

CO_2 generation. A solution of 0.25 mM $[Pt^{IV}(en)_2bp]Cl_2$ and 5mM ascorbate in H_2O was sealed under N_2 and heated for 5 h at 37 °C. The gases in the headspace were analyzed by gas chromatography.

Pt-DNA binding. $[Pt^{II}(en)_2]Cl_2$ was titrated against a solution of DNA and EtBr with saturated DNA binding (3:1) from 0.01:1 to 10:1 ratios of Pt : DNA at 37 °C in 0.4 M NaCl. The fluorescence of EtBr-bound DNA was measured by excitation at 546 nm and emission at 590 nm on a Shimadzu RF-5301 spectrofluorophotometer (Shimadzu). The extent of DNA intercalation was determined as observed fluorescence relative to the fluorescence of EtBr-DNA in the absence of any Pt complex.

Cytotoxicity assays. HCT116 cells were seeded at 2×10^3 cells/well and cultured overnight. The culture media was replaced by 100 μL of fresh culture media containing 10% FBS containing various concentrations of free drugs or nanoparticles and incubated for 4, 24, or 72 h. Cell viability was determined by (3-(4,5-dimethylthiazol-2-yl)-5-(3-carboxymethoxyphenyl)-2-(4-sulfophenyl)-2H-tetrazolium) (MTS) assay (Promega, USA) according to the manufacturer's instructions.

Pharmacokinetics and biodistribution. BALB/c mice were subcutaneously implanted with 5×10^6 CT26 cells. After the tumors were allowed to grow to ~100 mm^3, the mice were intravenously injected with PtEN at a Pt dose of 3 mg/kg. Mice were sacrificed at predetermined time points, and their blood, livers, lungs, kidneys, bladders, and tumors were harvested and digested with concentrated nitric acid to determine Pt concentration by ICP-MS.

Toxicity analysis and Pt retention. BALB/c mice were intraperitoneally injected with PtEN at a Pt dose of 3 mg/kg daily for a total of 10 doses. 30 days after the final dose, the mice were sacrificed and their blood, livers, spleens, lungs, kidneys, and bladders were harvested. A portion of the organs were embedded into optimal cutting temperature (OCT) medium, sectioned into 5 μm slices with a cryostat (NX50, Thermo, USA), and stained with haemotoxylin and eoisin (H&E) for histological examination by light microscopy. The rest of the organs were digested with concentrated nitric acid to determine Pt concentration by ICP-MS.

Cell uptake and cellular distribution of PtEN/miRNA. 5×10^5 HCT116 cells/well were seeded onto 6-well plates and cultured overnight. The Pt uptake was detected in cells treated with PtEN or PtEN/NT at equivalent Pt concentrations of 25 μM for 24 h. After incubation, the cells were collected, washed three times with PBS, counted with a hemocytometer and digested with concentrated nitric acid to determine Pt concentration by ICP-MS. The miRNA uptake was detected in cells treated with PBS, Alexa, or PtEN/Alexa at equivalent Alexa concentrations of 18 nM for 24 h. After incubation, the cells were collected, washed three times with PBS, and then analyzed for AlexaFluor647 fluorescence with the APC filter by flow cytometry (LSR II 3-8, BD, USA).

The intracellular distribution of PtEN/Alexa after internalization was evaluated by seeding 1×10^5 HCT116 cells/well onto 6-well plates with cover slips and cultured overnight. The culture medium was replaced with PtEN/Alexa at a concentration of 18 nM miRNA in serum-free culture medium and incubated for 15 min, 30 min, 1 h, or 2 h. The cells were washed three times with PBS, stained with 100 nM Lysotracker DND-26 for 2 h at 37 °C, fixed with 4% paraformaldehyde,

and stained with 1 μg/mL DAPI for 15 min at room temperature. The DAPI (blue), Lysotracker (green), and Alexa (red) fluorescence were observed by confocal microscopy (CLSM; FV1000, Olympus, Japan) and analyzed for colocalization by ImageJ.

Cell apoptosis. 5×10^5 HCT116 cells/well were seeded onto 6-well plates and cultured overnight. Cells were treated with PBS, PtEN, PtEN/NT, or PtEN/miR-655-3p for 4, 24, or 72 h at equivalent Pt and miRNA concentrations of 25 μM and 50 nM, respectively. After incubation, both the floating and adherent cells were collected and stained with AlexaFluor488-annexin V and propidium iodide in the Annexin V/dead cell apoptosis kit (Invitrogen, USA) according to the manufacturer's instructions. The cells were analyzed for fluorescence by flow cytometry (LSR II 3-8, BD, USA).

Cell proliferation. 1×10^6 HCT116 cells/well were seeded onto 6-well plates together with PBS, $Pt(en)_2Cl_2$ + miR-655-3p, PtEN/NT, or PtEN/miR-655-3p at equivalent doses of Pt and miRNA concentrations of 25 μM and 50 nM, respectively. 24 or 72 h after seeding, the adherent cells were collected, washed three times with PBS, and counted with a hemocytometer. The ratio was determined as number of adherent cells after dosing divided by number of cells seeded.

Transfection efficiency. For in vitro transfection, 2×10^5 HCT116 cells/well were seeded onto 24-well plates and cultured overnight. Cells were treated with PtEN/NT, or PtEN/miR-655-3p at equivalent Pt and miRNA concentrations of 25 μM and 50 nM, respectively. The transfection medium was replaced with fresh medium after 4 h and further incubated for 44 h. The RNA was isolated using TRIzol reagent (Invitrogen, USA) per manufacturer's instructions, and reverse

transcribed with the High Capacity cDNA Synthesis Kit (Applied Biosystems, USA). Real-time PCR was performed with primers (Table S2) using an iCycler thermal cycler with an iQ5 real-time qPCR detection system attached (Bio-Rad, USA) according to manufacturer's instructions.

In vitro β-catenin immunostaining and nuclear localization. For in vitro analysis, 1×10^5 HCT116 cells/well were seeded onto 6-well plates with cover slips and cultured overnight. The cells were treated with PBS, PtEN/NT or PtEN/miR-655-3p for 48 h at equivalent Pt and miRNA concentrations of 25 μM and 50 nM, respectively. After incubation, the medium was removed and the cover slips were washed three times with PBS. The cells were fixed with 4% paraformaldehyde and then permeabilized with 0.25% Triton X-100 in PBS. The cells were stained with a primary antibody against β-catenin (CAT-5H10, Invitrogen, USA) overnight at 4 ^{o}C, followed by incubation with an AlexaFluor647-conjugated secondary antibody (Invitrogen, USA) for 1 h at room temperature. The cells were stained with DAPI for 15 minutes, washed with PBS, and then observed under CLSM. The nuclear localization was calculated by ImageJ as a ratio of the β-catenin fluorescence intensity in the DAPI-stained nucleus over the β-catenin fluorescence intensity in the entire field.

Transwell invasion. HCT116 cells were transfected with PBS, PtEN/NT or PtEN/miR-655-3p for 48 h at equivalent Pt and miRNA concentrations of 25 μM and 50 nM, respectively. The cells were collected, washed three times with PBS, and then adjusted to a concentration of 2×10^5 cells/mL in serum-free medium. 200μL of the cell suspension was seeded onto the upper chamber of a Millicell Cell Culture Insert with 8.0 μm pores (Millipore, USA). The lower chamber contained 0.6 mL medium with 10% FBS. After 24 h, the non-invading cells on the upper surface of the

removed with a cotton swab and the invading cells on the lower surface were fixed with 4% paraformaldehyde and stained with 0.1% crystal violet. The invading cells were counted in five random visual fields with an inverted microscope at 100× magnification. The relative invasion ability was determined as the invading cell number over that of the PBS-control group.

Cytokine release. Healthy BALB/c mice were intraperitoneally injected with PBS, PtEN, or PtEN/miR-655-3p on day 0. Blood was collected on days 0, 1, 2, and 3, and the serum IFN-γ, TNF-α, and IL-6 levels were determined by enzyme-linked immunosorbent assay (ELISA, eBioscience, USA) to evaluate immunotoxicity.

Liver function assay. Healthy BALB/c mice were intraperitoneally injected with PBS, PtEN, or PtEN/miR-655-3p once every 3 days for a total of 3 doses starting on day 0. Blood was collected on day 12 and the serum AST and ALT levels were determined using an AST Activity Assay Kit and ALT Activity Assay Kit, respectively (Sigma-Aldrich).

Biodistribution in a hepatic metastasis tumor model. Two weeks after intrasplenic injection of CT26-L2T, BALB/c mice were intraperitoneally injected with PtEN/Alexa at a dose of 625 μg/kg Alexa. The mice were euthanized after 3 or 24 h, and the livers were harvested. The heart, lung, and kidneys were also collected after 3 h. The PtEN/Alexa accumulation and localization were visualized in the organs by ex vivo fluorescence imaging using an IVIS Spectrum 200 (Xenogen, USA) in the Integrated Small animal Imaging Research Resource at the University of Chicago. Data were analyzed using Living Image 4.0 Software (Caliper Life Sciences, USA). The livers

from 8 h post injection were also embedded in OCT medium, sectioned into 5 μM slices, and then stained with Hoechst for CLSM.

In vivo validation of PtEN/miR-655-3p. 28 days after intrasplenic injection of HCT116-L2T cells, athymic nude mice were intraperitoneally injected with a single dose of PtEN/NT or PtEN/miR-655-3p at a dose of 625 μg/kg miRNA. After 48 h, the mice were euthanized and the livers were harvested for RNA extraction and immunofluorescence. For in vivo transfection, individual tumor colonies were isolated from the livers 48 h days after treatment and mechanically homogenized with an Omni TH Tissue Homogenizer (Omni International, USA). A lobe of the liver was embedded into OCT medium and sectioned into 5 μm slices. The sections were fixed in acetone for 20 min at -20 °C, washed three times with PBS, and incubated with a primary antibody against β-catenin overnight at 4 °C. The slides were washed three times with PBS, incubated with an AlexaFluor647-conjugated secondary antibody for 1 h at room temperature, and then stained with Hoechst for 15 minutes in darkness for CLSM.

Establishment of a xenogenic hepatic metastasis tumor model. Liver metastases of colorectal cancer were established as previously described.[71] Briefly, 2×10^6 HCT116-L2T cells stably transfected with luciferin and tdTomato were slowly injected into the spleens of athymic nude mice, respectively, anesthetized with 2% isoflurane in oxygen (v/v). The spleens were removed 5 min later to reduce tumor growth in the spleen and the abdominal cavity.

In vivo anti-metastatic efficacy. Beginning 24 h after intrasplenic injection of HCT116-L2T, athymic nude mice were dosed with 5% dextrose (w/v), PtEN/NT, or PtEN/miR-655-3p at

equivalent doses of 625 μg/kg miRNA once every three days until day 28. Once weekly, the mice were anesthetized with 2% isoflurane in oxygen (v/v) and subjected to bioluminescence imaging by an IVIS Spectrum 200 (Xenogen, USA). On day 28, the mice were euthanized and the livers were harvested for ex vivo fluorescence and liver weight.

2.6 References

1. Seyfried, T.N. & Huysentruyt, L.C. On the origin of cancer metastasis. *Crit Rev Oncog* **18**, 43-73 (2013).
2. Mehlen, P. & Puisieux, A. Metastasis: a question of life or death. *Nat Rev Cancer* **6**, 449-458 (2006).
3. Steeg, P.S. & Theodorescu, D. Metastasis: a therapeutic target for cancer. *Nat Clin Pract Oncol* **5**, 206-219 (2008).
4. Sanger, N. et al. Disseminated tumor cells in the bone marrow of patients with ductal carcinoma in situ. *Int J Cancer* **129**, 2522-2526 (2011).
5. Rocken, M. Early tumor dissemination, but late metastasis: insights into tumor dormancy. *J Clin Invest* **120**, 1800-1803 (2010).
6. Narod, S.A., Iqbal, J., Giannakeas, V., Sopik, V. & Sun, P. Breast Cancer Mortality After a Diagnosis of Ductal Carcinoma In Situ. *JAMA Oncol* **1**, 888-896 (2015).
7. Nelson, V.M. & Benson, A.B., 3rd Status of targeted therapies in the adjuvant treatment of colon cancer. *J Gastrointest Oncol* **4**, 245-252 (2013).
8. Midgley, R. & Kerr, D.J. Adjuvant chemotherapy for stage II colorectal cancer: the time is right! *Nat Clin Pract Oncol* **2**, 364-369 (2005).
9. Steeg, P.S. Targeting metastasis. *Nat Rev Cancer* **16**, 201-218 (2016).
10. Brandi, G. et al. Adjuvant chemotherapy for resected colorectal cancer metastases: Literature review and meta-analysis. *World J Gastroenterol* **22**, 519-533 (2016).
11. Chibaudel, B., Bonnetain, F., Tournigand, C. & de Gramont, A. Maintenance treatment in metastatic colorectal cancer. *Lancet Oncol* **16**, e583-584 (2015).
12. Cleeland, C.S. et al. Reducing the toxicity of cancer therapy: recognizing needs, taking action. *Nat Rev Clin Oncol* **9**, 471-478 (2012).
13. Esserman, L.J. et al. Addressing overdiagnosis and overtreatment in cancer: a prescription for change. *Lancet Oncol* **15**, e234-242 (2014).
14. Jorgensen, K.J., Gotzsche, P.C., Kalager, M. & Zahl, P.H. Breast Cancer Screening in Denmark: A Cohort Study of Tumor Size and Overdiagnosis. *Ann Intern Med* **166**, 313-323 (2017).

15. Kneuertz, P.J. et al. Overtreatment of young adults with colon cancer: more intense treatments with unmatched survival gains. *JAMA Surg* **150**, 402-409 (2015).

16. Price, C. & Chen, J. MicroRNAs in Cancer Biology and Therapy: Current Status and Perspectives. *Genes Dis* **1**, 53-63 (2014).

17. Reddy, K.B. MicroRNA (miRNA) in cancer. *Cancer Cell Int* **15**, 38 (2015).

18. Schetter, A.J., Okayama, H. & Harris, C.C. The role of microRNAs in colorectal cancer. *Cancer J* **18**, 244-252 (2012).

19. Bartel, D.P. MicroRNAs: genomics, biogenesis, mechanism, and function. *Cell* **116**, 281-297 (2004).

20. Bader, A.G., Brown, D. & Winkler, M. The promise of microRNA replacement therapy. *Cancer Res* **70**, 7027-7030 (2010).

21. Wang, H. et al. Recent progress in microRNA delivery for cancer therapy by non-viral synthetic vectors. *Adv Drug Deliv Rev* **81**, 142-160 (2015).

22. Esau, C.C. & Monia, B.P. Therapeutic potential for microRNAs. *Adv Drug Deliv Rev* **59**, 101-114 (2007).

23. Bader, A.G., Brown, D., Stoudemire, J. & Lammers, P. Developing therapeutic microRNAs for cancer. *Gene Ther* **18**, 1121-1126 (2011).

24. Cheng, C.J. et al. MicroRNA silencing for cancer therapy targeted to the tumour microenvironment. *Nature* **518**, 107-110 (2015).

25. Uppal, A. et al. 14q32-encoded microRNAs mediate an oligometastatic phenotype. *Oncotarget* **6**, 3540-3552 (2015).

26. Harazono, Y. et al. miR-655 Is an EMT-suppressive microRNA targeting ZEB1 and TGFBR2. *PLoS One* **8**, e62757 (2013).

27. Zhao, X.Q., Liang, B., Jiang, K. & Zhang, H.Y. Down-regulation of miR-655-3p predicts worse clinical outcome in patients suffering from hepatocellular carcinoma. *Eur Rev Med Pharmacol Sci* **21**, 748-752 (2017).

28. Niibe, Y. & Hayakawa, K. Oligometastases and oligo-recurrence: the new era of cancer therapy. *Jpn J Clin Oncol* **40**, 107-111 (2010).

29. Wu, G. et al. MicroRNA-655-3p functions as a tumor suppressor by regulating ADAM10 and beta-catenin pathway in Hepatocellular Carcinoma. *J Exp Clin Cancer Res* **35**, 89 (2016).

30. Raemdonck, K., Vandenbroucke, R.E., Demeester, J., Sanders, N.N. & De Smedt, S.C. Maintaining the silence: reflections on long-term RNAi. *Drug Discov Today* **13**, 917-931 (2008).

31. Chen, Y., Gao, D.Y. & Huang, L. In vivo delivery of miRNAs for cancer therapy: challenges and strategies. *Adv Drug Deliv Rev* **81**, 128-141 (2015).

32. Garzon, R., Marcucci, G. & Croce, C.M. Targeting microRNAs in cancer: rationale, strategies and challenges. *Nat Rev Drug Discov* **9**, 775-789 (2010).

33. Zatsepin, T.S., Kotelevtsev, Y.V. & Koteliansky, V. Lipid nanoparticles for targeted siRNA delivery - going from bench to bedside. *Int J Nanomedicine* **11**, 3077-3086 (2016).

34. Kaczmarek, J.C., Kowalski, P.S. & Anderson, D.G. Advances in the delivery of RNA therapeutics: from concept to clinical reality. *Genome Med* **9**, 60 (2017).

35. Burnett, J.C. & Rossi, J.J. RNA-based therapeutics: current progress and future prospects. *Chem Biol* **19**, 60-71 (2012).

36. Jayaraman, M. et al. Maximizing the potency of siRNA lipid nanoparticles for hepatic gene silencing in vivo. *Angew Chem Int Ed Engl* **51**, 8529-8533 (2012).

37. Coelho, T. et al. Safety and efficacy of RNAi therapy for transthyretin amyloidosis. *N Engl J Med* **369**, 819-829 (2013).

38. Suhr, O.B. et al. Efficacy and safety of patisiran for familial amyloidotic polyneuropathy: a phase II multi-dose study. *Orphanet J Rare Dis* **10**, 109 (2015).

39. Adams, D. et al. Trial design and rationale for APOLLO, a Phase 3, placebo-controlled study of patisiran in patients with hereditary ATTR amyloidosis with polyneuropathy. *BMC Neurol* **17**, 181 (2017).

40. Rizk, M. & Tuzmen, S. Update on the clinical utility of an RNA interference-based treatment: focus on Patisiran. *Pharmgenomics Pers Med* **10**, 267-278 (2017).

41. Benson, M.D., Ackermann, E.J. & Monia, B.P. Treatment of transthyretin cardiomyopathy with a TTR-specific antisense oligonucleotide (IONIS-TTRRx). *Amyloid* **24**, 134-135 (2017).

42. Chen, W. & Yang, L. Targeted Delivery with Imaging Assessment of siRNA Expressing Nanocassettes into Cancer. *Methods Mol Biol* **1372**, 49-59 (2016).

43. Cho, Y.S. et al. Targeted delivery of siRNA-generating DNA nanocassettes using multifunctional nanoparticles. *Small* **9**, 1964-1973 (2013).

44. Barnaby, S.N. et al. Design Considerations for RNA Spherical Nucleic Acids (SNAs). *Bioconjug Chem* **27**, 2124-2131 (2016).

45. Rosi, N.L. et al. Oligonucleotide-modified gold nanoparticles for intracellular gene regulation. *Science* **312**, 1027-1030 (2006).

46. Garbuzenko, O.B. et al. Combinatorial treatment of idiopathic pulmonary fibrosis using nanoparticles with prostaglandin E and siRNA(s). *Nanomedicine* **13**, 1983-1992 (2017).

47. Jensen, S.A. et al. Spherical nucleic acid nanoparticle conjugates as an RNAi-based therapy for glioblastoma. *Sci Transl Med* **5**, 209ra152 (2013).

48. Anchordoquy, T.J. et al. Mechanisms and Barriers in Cancer Nanomedicine: Addressing Challenges, Looking for Solutions. *ACS Nano* **11**, 12-18 (2017).

49. Wang, W., Yang, Z., Patanavanich, S., Xu, B. & Chau, Y. Controlling self-assembly within nanospace for peptide nanoparticle fabrication. *Soft Matter* **4**, 1617-1620 (2008).

50. Goodwin, T.J. & Huang, L. Investigation of phosphorylated adjuvants co-encapsulated with a model cancer peptide antigen for the treatment of colorectal cancer and liver metastasis. *Vaccine* **35**, 2550-2557 (2017).

51. He, C., Poon, C., Chan, C., Yamada, S.D. & Lin, W. Nanoscale Coordination Polymers Codeliver Chemotherapeutics and siRNAs to Eradicate Tumors of Cisplatin-Resistant Ovarian Cancer. *J Am Chem Soc* **138**, 6010-6019 (2016).

52. Oshima, G. et al. In Vivo Delivery and Therapeutic Effects of a MicroRNA on Colorectal Liver Metastases. *Mol Ther* **25**, 1588-1595 (2017).

53. Drew, H.D.K. 332. The behaviour of chelate groupings attached to platinum and to palladium. *Journal of the Chemical Society (Resumed)*, 2328-2331 (1932).

54. Liu, D., Poon, C., Lu, K., He, C. & Lin, W. Self-assembled nanoscale coordination polymers with trigger release properties for effective anticancer therapy. *Nat Commun* **5**, 4182 (2014).

55. Poon, C., Duan, X., Chan, C., Han, W. & Lin, W. Nanoscale Coordination Polymers Codeliver Carboplatin and Gemcitabine for Highly Effective Treatment of Platinum-Resistant Ovarian Cancer. *Mol Pharm* **13**, 3665-3675 (2016).

56. Chin, C.F., Wong, D.Y., Jothibasu, R. & Ang, W.H. Anticancer platinum (IV) prodrugs with novel modes of activity. *Curr Top Med Chem* **11**, 2602-2612 (2011).

57. Johnstone, T.C., Suntharalingam, K. & Lippard, S.J. The Next Generation of Platinum Drugs: Targeted Pt(II) Agents, Nanoparticle Delivery, and Pt(IV) Prodrugs. *Chem Rev* **116**, 3436-3486 (2016).

58. Liu, H.K. & Sadler, P.J. Metal complexes as DNA intercalators. *Acc Chem Res* **44**, 349-359 (2011).

59. Zeglis, B.M., Pierre, V.C. & Barton, J.K. Metallo-intercalators and metallo-insertors. *Chem Commun (Camb)*, 4565-4579 (2007).

60. Chung, M.F. et al. A liposomal system capable of generating CO2 bubbles to induce transient cavitation, lysosomal rupturing, and cell necrosis. *Angew Chem Int Ed Engl* **51**, 10089-10093 (2012).

61. Han, H.D. et al. Therapeutic efficacy of doxorubicin delivery by a CO2 generating liposomal platform in breast carcinoma. *Acta Biomater* **24**, 279-285 (2015).

62. Chen, K.J. et al. A thermoresponsive bubble-generating liposomal system for triggering localized extracellular drug delivery. *ACS Nano* **7**, 438-446 (2013).

63. Blobe, G.C., Schiemann, W.P. & Lodish, H.F. Role of transforming growth factor beta in human disease. *N Engl J Med* **342**, 1350-1358 (2000).

64. Ishitsuka, Y. et al. Pituitary tumor-transforming gene 1 enhances proliferation and suppresses early differentiation of keratinocytes. *J Invest Dermatol* **132**, 1775-1784 (2012).

65. Dou, H., Huang, C., Singh, M., Carpenter, P.B. & Yeh, E.T. Regulation of DNA repair through deSUMOylation and SUMOylation of replication protein A complex. *Mol Cell* **39**, 333-345 (2010).

66. Spandidos, A., Wang, X., Wang, H. & Seed, B. PrimerBank: a resource of human and mouse PCR primer pairs for gene expression detection and quantification. *Nucleic Acids Res* **38**, D792-799 (2010).

67. Zhang, D. et al. The role of beta-catenin in the initiation and metastasis of TA2 mice spontaneous breast cancer. *J Cancer* **8**, 2114-2123 (2017).

68. Jamieson, C., Sharma, M. & Henderson, B.R. Targeting the beta-catenin nuclear transport pathway in cancer. *Semin Cancer Biol* **27**, 20-29 (2014).

69. Husemann, Y. et al. Systemic spread is an early step in breast cancer. *Cancer Cell* **13**, 58-68 (2008).

70. Kang, Y. & Pantel, K. Tumor cell dissemination: emerging biological insights from animal models and cancer patients. *Cancer Cell* **23**, 573-581 (2013).

71. Oshima, G. et al. Imaging of tumor clones with differential liver colonization. *Sci Rep* **5**, 10946 (2015).

CHAPTER 3. Nanoscale coordination polymer co-deliver cisplatin and paclitaxel for enhanced combination chemotherapy of advanced and metastatic cancers

3.1 Introduction

While a nontoxic Pt entity allowed NCPs to be used as a carrier in Chapter 2, Pt compounds are extremely useful drugs for cancer therapy. The three main platinum drugs–cisplatin, oxaliplatin, and carboplatin—are alkylating agents which inhibit DNA replication, with nearly 50% of all tumor chemotherapy regimens including cisplatin (CisPt).[1] Platinum-based doublet therapy is frequently used in the clinic for the treatments of ovarian, cervical, lung, and triple-negative breast cancer and has been further investigated in many cancers as first-line, second-line, or salvage therapies. These are often given in combination with topoisomerase inhibitors or mitotic inhibitors, such as paclitaxel (PTX).[2-4] Combination therapy is often valuable due to the heterogeneity of cells in the tumor: some cells may be mitotically active while others are senescent, some cells may be resistant to one drug but not the other.[5-8] CisPt and PTX were approved in 1978 and 1992, respectively, by the Food and Drug Administration as anticancer drugs.[9, 10] As early as 1996, CisPt and PTX combination therapy (CAP) was investigated for activity and subsequently used clinically in breast and ovarian cancer patients and early 2000s in lung cancer patients.[11-14]

CAP is an ideal combination in that each drug elicits a different mechanism of action: PTX is a cell-cycle specific agent which stabilizes microtubules during mitosis while CisPt is an alkylating agent which is not cell-cycle specific.[15, 16] Furthermore, the dose-limiting nephrotoxicity of CisPt

and neutropenia of PTX are non-overlapping, allowing for dosing at or near the maximum dose allowed for single agent chemotherapy.[17, 18] In early stage cancers, platinum and/or paclitaxel chemotherapy is often given after surgery depending on the risk of recurrence or metastasis.[19, 20] Even with early detection options including mammograms and known genetic risk factors such as BRCA, over 100,000 women are living with metastatic breast cancer.[21] The majority of ovarian and lung cancer patients have advanced or metastatic disease at the time of diagnosis,[22, 23] for which chemotherapy is essential; combination chemotherapy regimens were the first indications that non-localized disease could be cured.[24-26] Combination chemotherapy regimens have proven to be more clinically effective than single agent therapies in controlling and curing tumors, with the majority of cancer types requiring two or more drugs to cure.[26]

Nanoparticles provide the ideal platform for chemotherapy delivery by controlling physical properties such as surface charge to improve the pharmacokinetic behavior and change the toxicity profile.[27] PTX is a hydrophobic molecule originally formulated with Cremophor EL/ethanol to solubilize the drug in water solutions.[28] However, the Cremophor EL formulation led to "severe anaphylactoid hypersensitivity reactions, hyperlipidaemia, abnormal lipoprotein patterns, aggregation of erythrocytes and peripheral neuropathy."[29] In 2005, a solvent-free albumin-bound paclitaxel (nab-paclitaxel) nanoparticle was approved in the US and shifted the primary toxicity to neutropenia, the severity of which is correlated to the peak and sustained levels of free drug circulating in the bloodstream.[28] While CisPt also leads to peripheral neuropathy and myelosuppression, nephrotoxicity is its major toxicity and requires cumbersome hydration protocols to ameliorate.[18, 30] Nanoparticle delivery of CAP can reduce the additive toxicities and lessen the major nephrotoxicity and neutropenia associated with free drugs in the plasma.

Here we report the development and evaluation of a core-shell nanoscale coordination polymer (NCP) for the co-delivery of the hydrophilic and hydrophobic drug combination CAP on a single nanoparticle (NCP-1/PTX). Using prodrugs for CisPt and PTX self-assembled into NCP-1/PTX allowed for controlled and triggered release of each drug. NCP-1/PTX improved the pharmacodynamics profiles of both drugs, significantly increasing the drug exposures of CisPt-bp and chol-PTX while preventing premature degradation. This limited free drug exposure and metabolism in the blood, spleen, and liver while simultaneously increasing and sustaining active drug accumulation in the tumor. Due to the increased drug exposure and tumor accumulation, significantly lower drug doses were required for strong anticancer efficacy in subcutaneous, metastatic, and orthotopic models of human and murine cancer. In an experimental metastasis model of advanced lung cancer, NCP-1/PTX significantly extended the median survival time of mice. In an orthotopic model of triple-negative breast cancer with spontaneous metastases, NCP-1/PTX controlled both the primary tumor and limited the number of metastatic nodules in the lung.

3.2 Results

3.2.1 Synthesis and characterization of NCP-1/PTX

A Pt(IV) prodrug of cisplatin cis,cis,trans-[$Pt(NH_3)_2Cl_2$(bisphosphoramic acid)] (CisPt-bp) was synthesized as previously reported.[31] PTX was conjugated to cholesterol (cholest-5-en-3-ol (3ß)-,3-((2-((paclitaxelcarbonyl)oxy)ethyl)disulfanyl)ethyl carbonate, chol-PTX) via a disulfide bond. To a mixture of cholesterol (500 mg, 1.3 mmol) and 4-N,N-dimethylaminopyridine (DMAP, 0.32 g, 2.8 mmol) in anhydrous DCM, a solution of triphosgene (128 mg, 0.43 mmol) in anhydrous DCM (2 mL) was added dropwise over an ice bath with stirring. The resultant solution was warmed

to room temperature and further stirred for 20 min and then added dropwise to a solution of bis(2-hydroxyethyl) disulfide (440 mg, 2.8 mmol) in anhydrous DCM (5 mL) over an ice bath. The reaction mixture was then warmed to room temperature and stirred for 12 h. After removal of solvent, the residue was purified to afford cholest-5-en-3-ol (3β)-, 3-(3-((2-hydroxyethyl)disulfanyl)ethyl) carbonate (Chol-S-S-OH) by column chromatography on silica gel with ethyl acetate/hexane (1:2, v/v). Yield: 0.44 g (60%).

To a mixture of Chol-S-S-OH (83.5 mg, 0.15 mmol) and DMAP (54 mg, 0.44 mmol) in anhydrous DCM (2 mL), a solution of triphosgene (15 mg, 0.05 mmol) in anhydrous DCM (1 mL) was added dropwise over an ice bath with stirring. The resultant solution was warmed to room temperature and further stirred for 1 h and then added dropwise to a solution of PTX (130 mg, 0.15 mmol) in anhydrous DCM (5 mL) over an ice bath. The reaction mixture was then warmed to room temperature and stirred for 12 h. After removal of solvent, the residue was purified by column chromatography on silica gel with hexane/ethyl acetate (7:1, v/v) to yield 66 mg of Chol-PTX.

DOPA-capped NCPs carrying CisPt-bp were synthesized according to previous report.[31] DOPA-NCP-1 was then coated with a mixture of DOPC, cholesterol, DSPE-PEG, and chol-PTX at an 8:8:4:1 molar ratio to afford the core-shell nanoparticles NCP-1/PTX. The particles were observed to be spherical in nature by transmission electron microscopy (TEM) in aqueous solutions (**Figure 3-1**). Dynamic light scattering (DLS) measurements of NCP-1/PTX gave Z-average, number average, and PDI as 92.70 ± 0.70 nm, 58.3 ± 1.6 nm, and 0.146 ± 0.001 (**Figure 3-2**), respectively. The cholesterol-conjugated prodrug allowed for stable incorporation into the NCP core-shell structure, as opposed to free PTX which precipitated out of the NCP bilayer within 5 hrs. NCP-1/PTX containing the chol-PTX were stable for at least two weeks at room temperature and at least 37 ^{o}C for 24 h in the presence of bovine serum albumin (BSA,

Figure 3-3). Importantly, only 2-5% of Pt and 1.0-1.2% of PTX existed outside of the NCP when determined by ultrafiltrate or by dialysis (**Figure 3-4**). Negligible platinum and PTX were observed outside of NCP-1/PTX stored at room temperature over the course of one week (**Figure 3-5**).

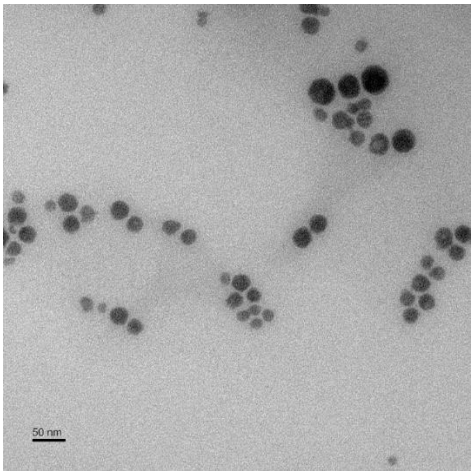

Figure 3-1 TEM image of NCP-1/PTX showing the approximate size and shape of the spherical nanoparticles. Scale bar = 50 nm.

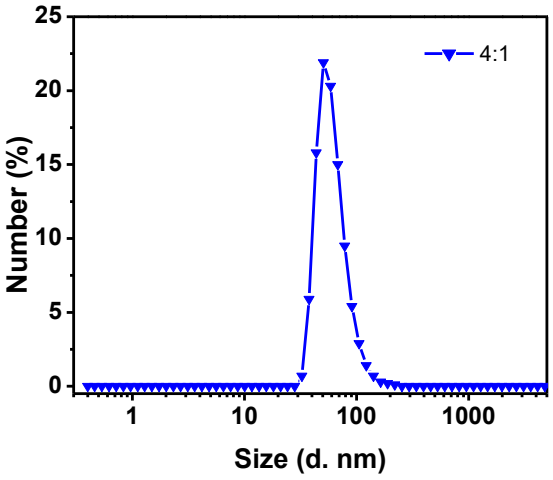

Figure 3-2 Number-average size distribution of NCP-1/PTX in H_2O by DLS.

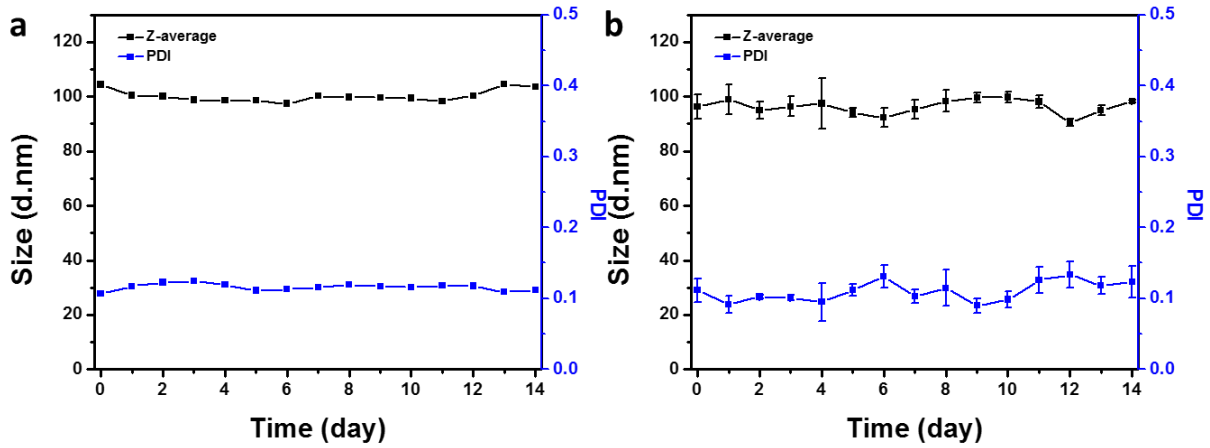

Figure 3-3 Stability of NCP-1/PTX in (a) 5% dextrose at room temperature or (b) in BSA at 37 °C for 14 days by DLS.

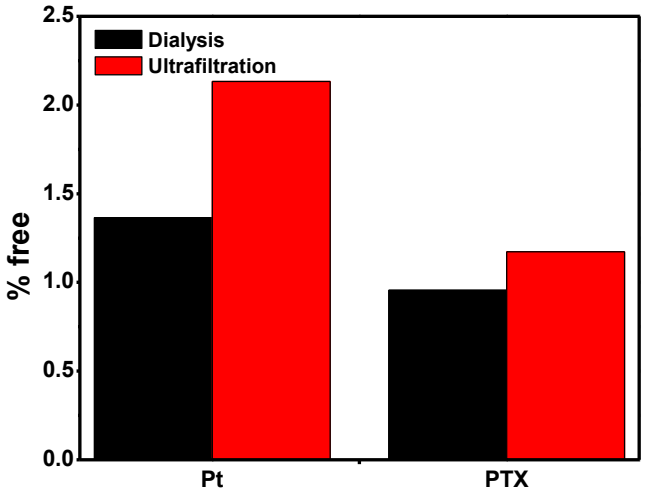

Figure 3-4 The percentages of dialyzable and ultrafilterable Pt or PTX detected outside of NCP-1/PTX by ICP-MS and LC/MS-MS, respectively.

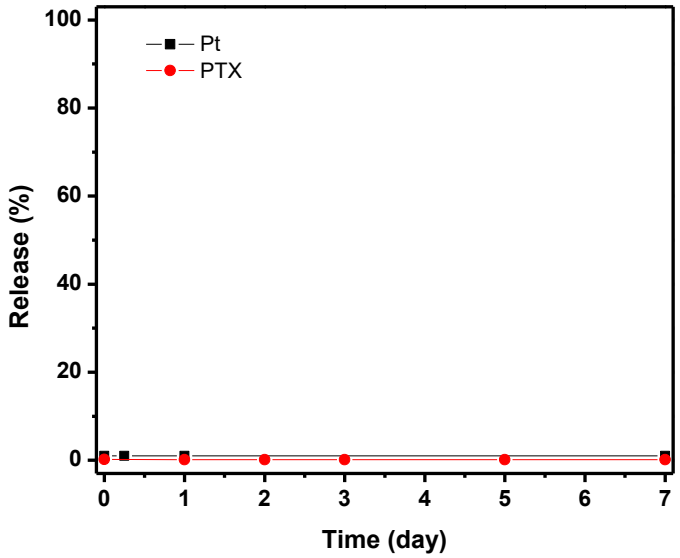

Figure 3-5 Free Pt and PTX observed outside of NCP-1/PTX over time by ultrafiltration.

3.2.2 Triggered release of prodrugs and drugs from NCP-1/PTX

NCP-1/PTX can release the CisPt-bp and chol-PTX prodrugs for reduction to the active parent species. CisPt-bp can be hydrolyzed to a Pt(IV) intermediate and, ultimately, to active Pt(II) species (**Scheme 3-1**). The disulfide bond in chol-PTX can be also be cleaved to release PTX in the presence of specific biological triggers (**Scheme 3-2**). However, the core-shell structure of NCPs can protect the prodrugs from degradation by limiting exposure to reducing agents. Less than 5% of Pt and PTX were observed outside of the NCP and susceptible to reducing agents (**Figure 3-4**) when NCP-1/PTX was incubated with 1 mM ascorbate or 5 mM GSH, respectively. However, when the lipid bilayer is compromised by a detergent such as Triton X-100 or during endocytosis, CisPt-bp and chol-PTX can be released and reduced.

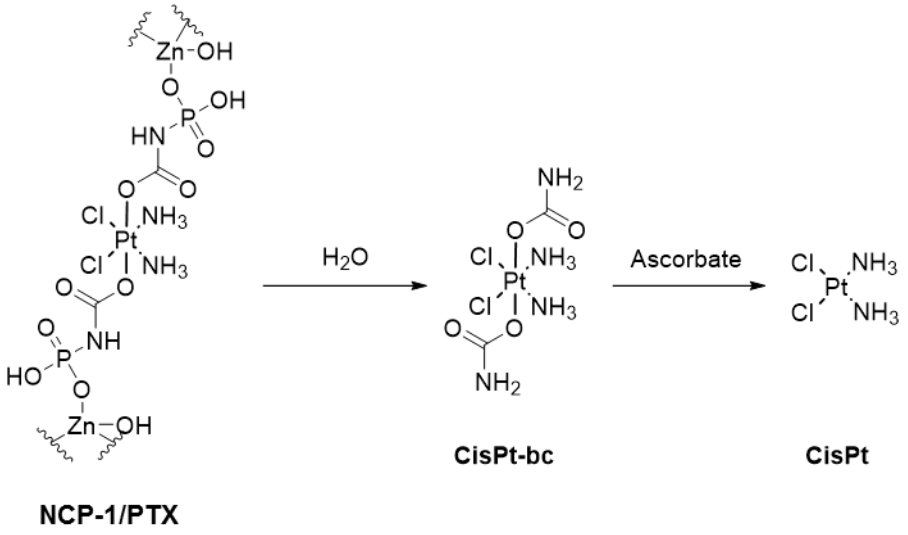

Scheme 3-1 Release of CisPt from NCP-1/PTX.

When NCP-1/PTX was titrated against different amounts of Triton X-100 in PBS for 30 min, 0.25% Triton X-100 (v/v) was sufficient for the release of over 80% of Pt (**Figure 3-6**). When incubated in 0.5% Triton X-100 for up to 24 h, HR-LCMS showed that a novel chemical species with m/z of 420.9782 $[M+H]^+$ could be released (**Figure 3-7a**). This species could be isolated, crystallized, and identified as cis,cis,trans-$[Pt(NH_3)_2Cl_2$(biscarbamate)] (CisPt-bc, **Figure 3-8**). LC/MS-MS analysis showed that CisPt-bc was the only Pt species present. An aqueous solution of CisPt-bp showed a similar m/z peak of 420.9787 $[M+H]^+$ (**Figure 3-7b**). When NCP-1/PTX was incubated without Triton X-100, negligible Pt was released. The samples were then vortexed for 30 sec in the presence of 0.5% Triton X-100, and the Pt species was determined to be nearly 100% CisPt-bc. Similar results were found when NCP-1/PTX was incubated without Triton X-100 in the presence of a reducing agent such as ascorbate (1 mM). When NCP-1/PTX was incubated with ascorbate in the presence of 0.5% Triton X-100 in PBS (v/v), nearly 100% of total Pt was released in 5 h; 27.9% existed as the Pt(IV) species CisPt-bc, while 72.1% existed as Pt(II) species with m/z of 317.9874 $[M+NH_4]^+$ by LC/MS-MS (**Figure 3-7c, Figure 3-9**).

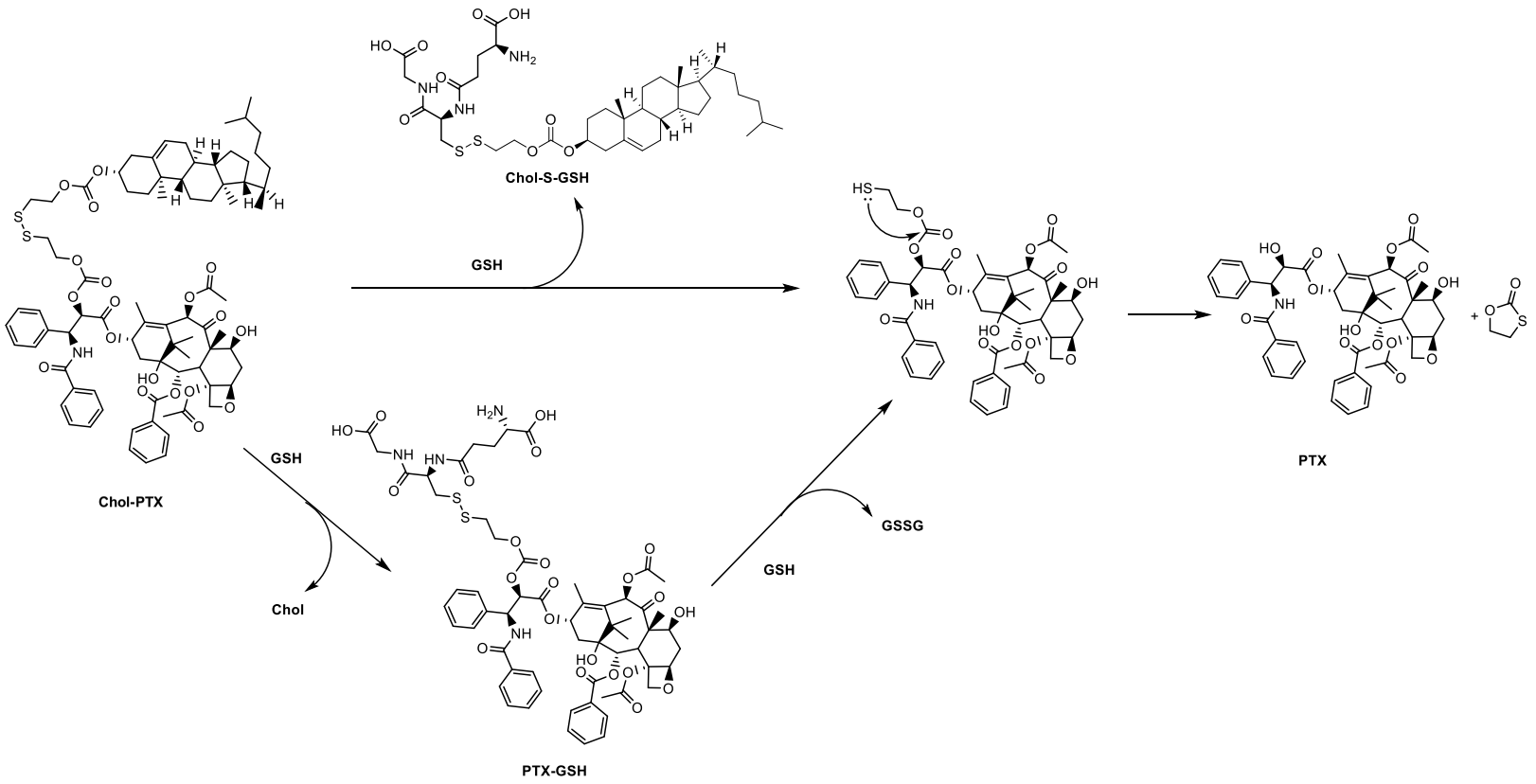

Scheme 3-2 Release of PTX from chol-PTX.

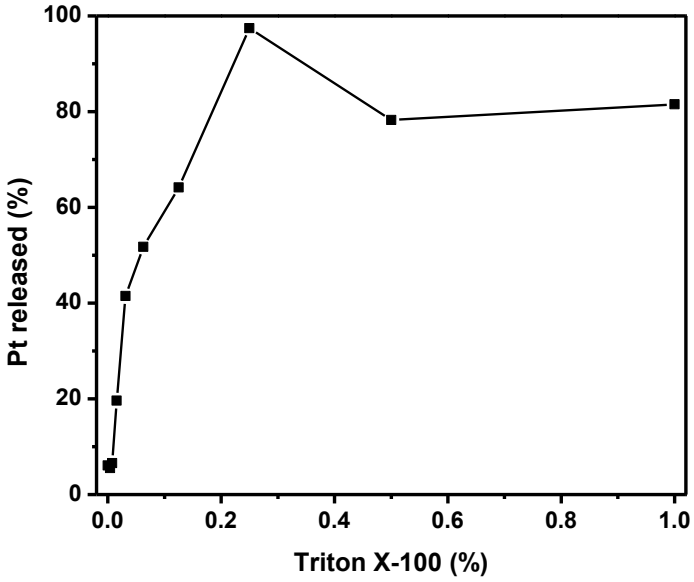

Figure 3-6 Total Pt release from NCP-1/PTX in varying concentrations of TritonX-100 in PBS.

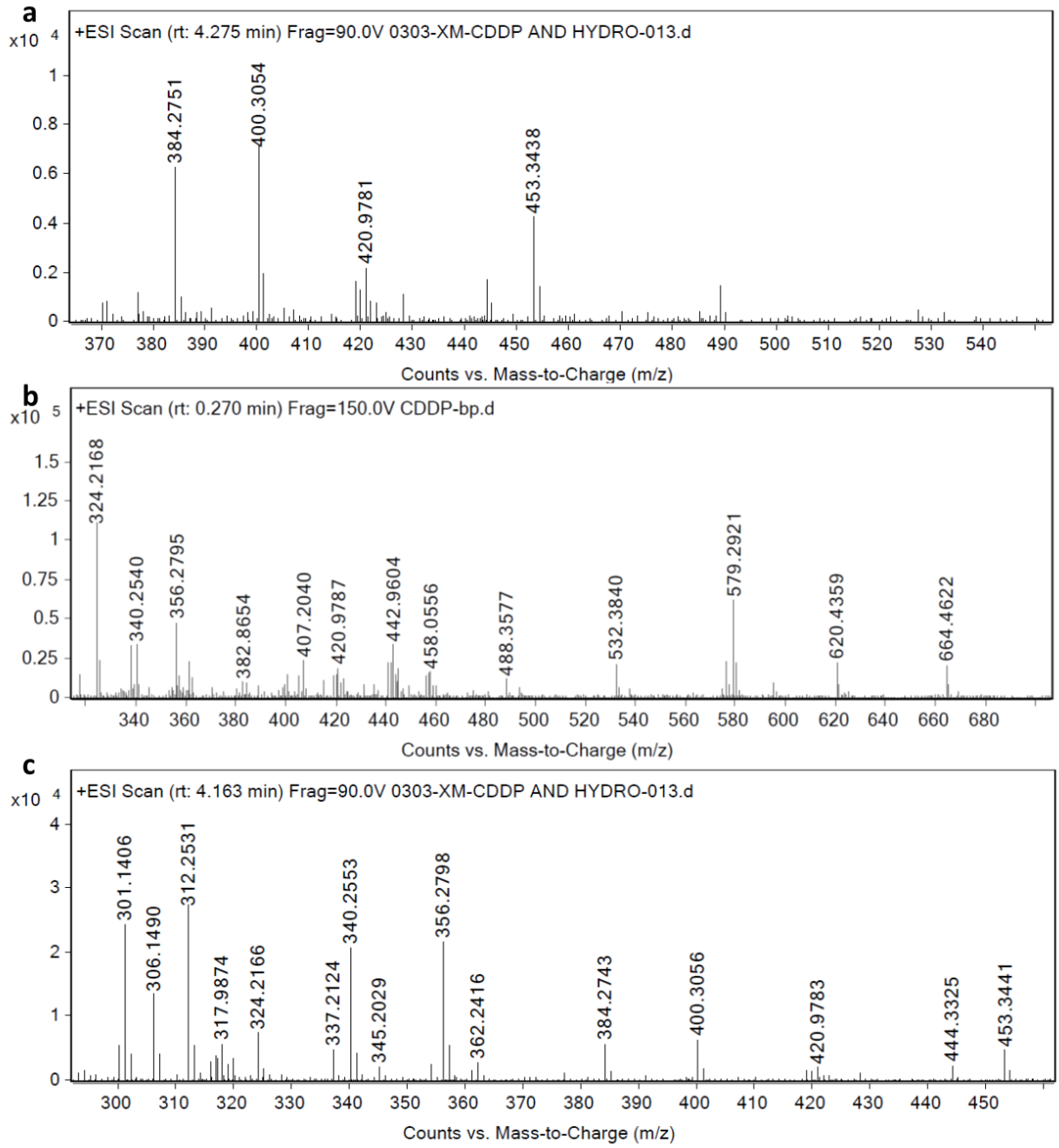

Figure 3-7 Mass-spectrometry investigating release of CisPt and CisPt-bc from CisPt-bp or NCP-1/PTX. (a) HR-LCMS of NCP-1/PTX incubated in PBS with Triton X-100 showing the formation of CisPt-bc (m/z = 420.9781 for $[M+H]^+$). (b) HR-MS of CisPt-bc (m/z = 420.9787 for $[M+H]^+$) from an aqueous solution of CisPt-bp. (c) HR-LCMS of NCP-1/PTX incubated in PBS with Triton X-100 and 1mM ascorbate showing the formation of CisPt-bc (m/z = 420.9783) and CisPt (m/z = 317.9874).

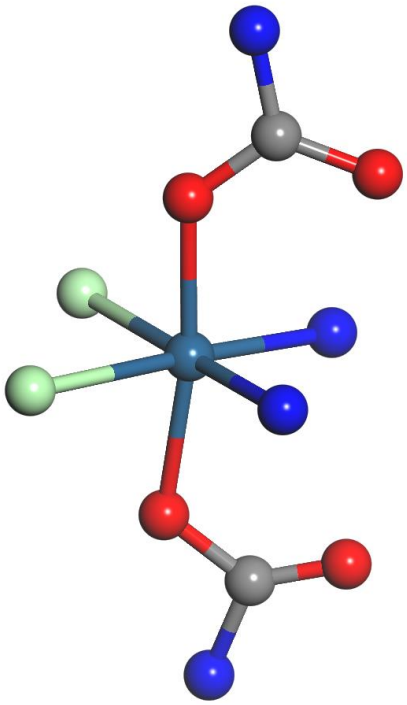

Figure 3-8 Crystal structure of CisPt-bc (Pt: blue, O: red, N: blue, C: grey, H: white, Cl: green).

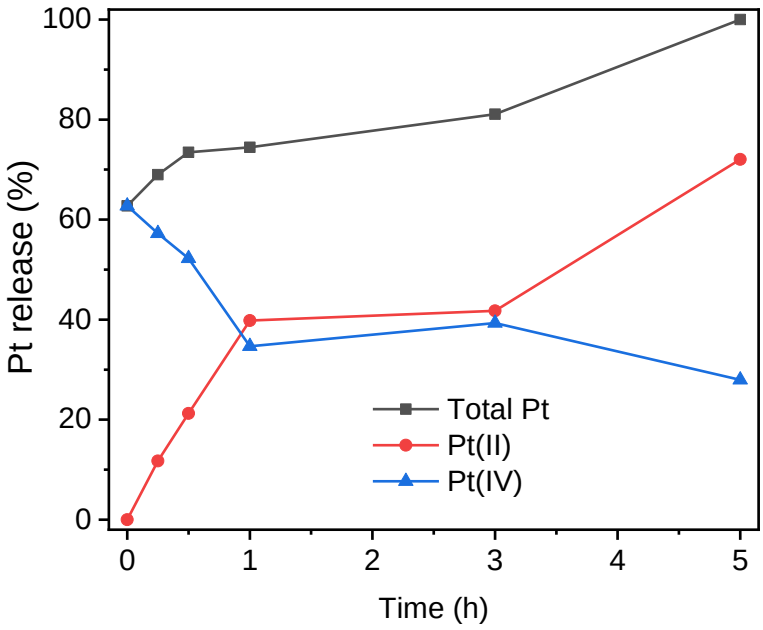

Figure 3-9 Pt release from NCP-1/PTX incubated in PBS at 37 °C with 0.5% Triton X-100 and 5 mM ascorbate.

The release of chol-PTX and PTX from NCP-1/PTX was similarly investigated in the presence of a thiol-containing reducing agent, glutathione (GSH). When chol-PTX was incubated in a solution of 5 mM GSH in 50% THF/PBS (v/v), two distinct disulfide exchange products could be determined from the solution by HRMS: chol-S-GSH (m/z = 796.4221, **Figure 3-10a**) and PTX-GSH (m/z = 1263.4121, **Figure 3-10b**). NCP-1/PTX incubated in PBS, 0.5% Triton X-100 in PBS (v/v), or 5 mM GSH in PBS for up to 5 h showed that nearly all PTX species were observed as chol-PTX. When NCP-1/PTX was incubated in the presence of 5 mM GSH in 0.5% Triton X-100 in PBS, chol-PTX was rapidly cleaved by GSH (**Figure 3-11**). After 3 h, 96.0% of the chol-PTX was cleaved to free PTX (**Figure 3-11**). The core-shell structure of NCP-1/PTX thus protects the CisPt-bp and the chol-PTX prodrugs from exposure to reductants during circulation and ensures selective drug activity in cells with abundant reducing agents, such as cancer cells.

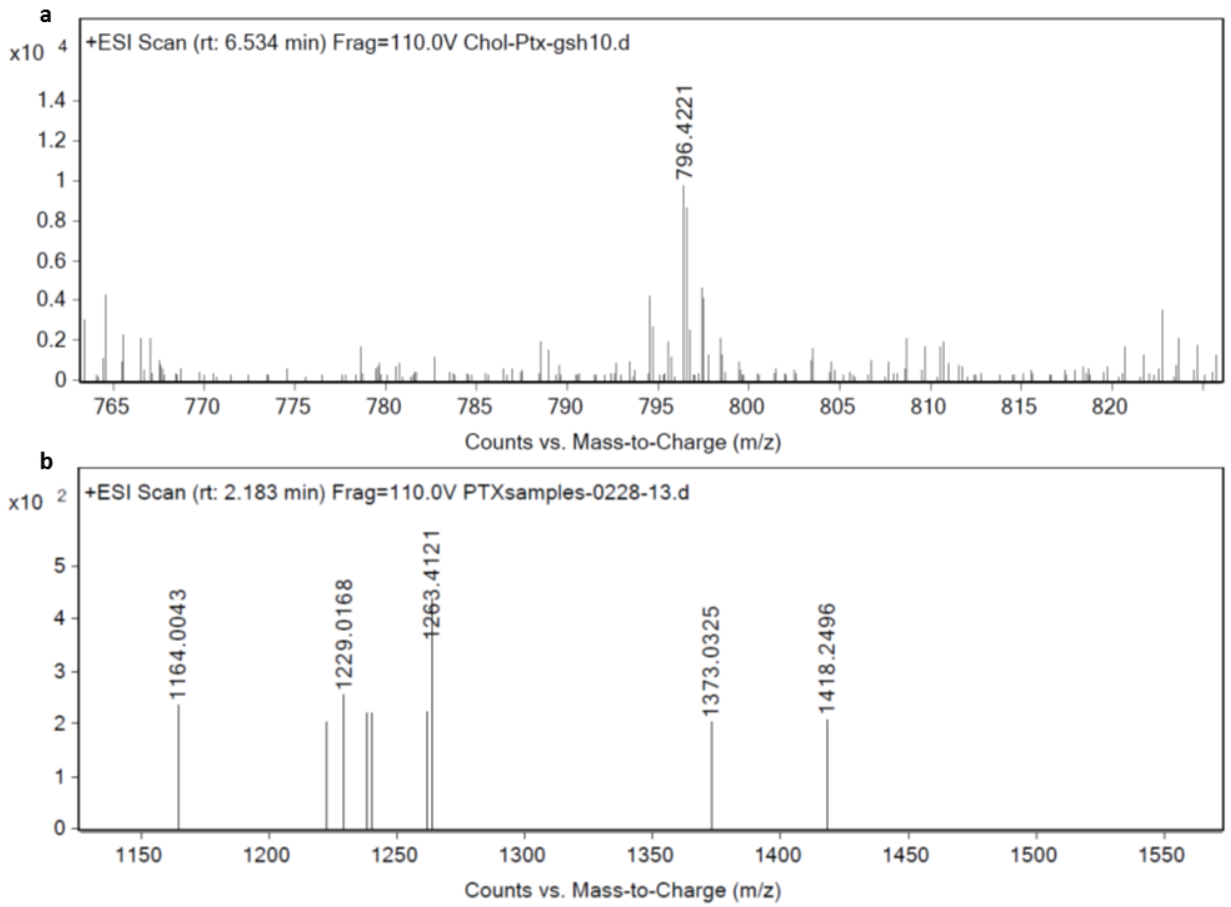

Figure 3-10 Mass-spectrometry investigating release of PTX from chol-PTX. Chol-PTX incubated with 5 mM GSH in PBS was reduced by disulfide exchange, leading to (a) Chol-S-GSH (m/z = 796.4221) and (b) PTX-GSH (m/z = 1263.4121).

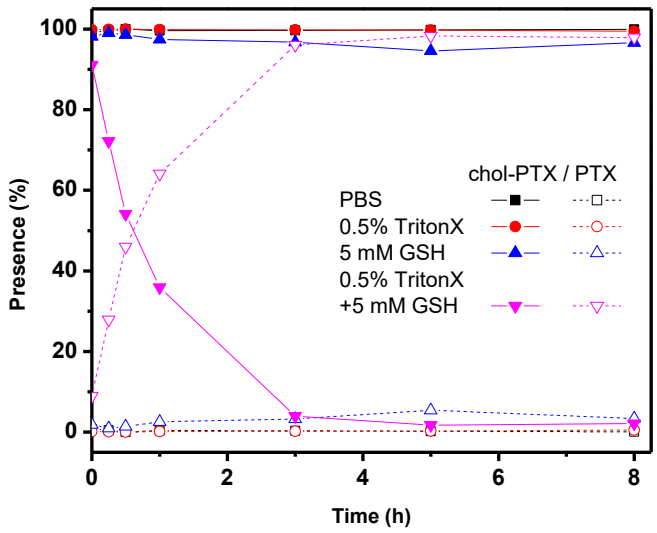

Figure 3-11 PTX released from NCP-1/PTX incubated in PBS at 37°C with or without 0.5% Triton X-100 and 5 mM GSH.

3.2.3 In vitro cell death

CisPt is a strong cytotoxic agent, inducing apoptosis in 76.4% of H460 cells when dosed with 5 μM Pt. Interestingly, 1.25 μM free PTX did not induce significant apoptosis (10.2%) but primarily necrosis (78.7%). The combination of cisplatin and paclitaxel increased the percentage of apoptotic cells to 95.31%. However, NCP-1, Zn/PTX, and NCP-1/PTX all led to significant apoptosis at the same concentrations, primarily AnnexinV^+PI^+ cells indicating late apoptosis. NCP-1 led to a similar amount of apoptosis as CisPt (74.1%), whereas Zn/PTX and NCP-1/PTX both led to apoptosis and cell death in >90% of cells (**Figure 3-12, Table 3-1**).

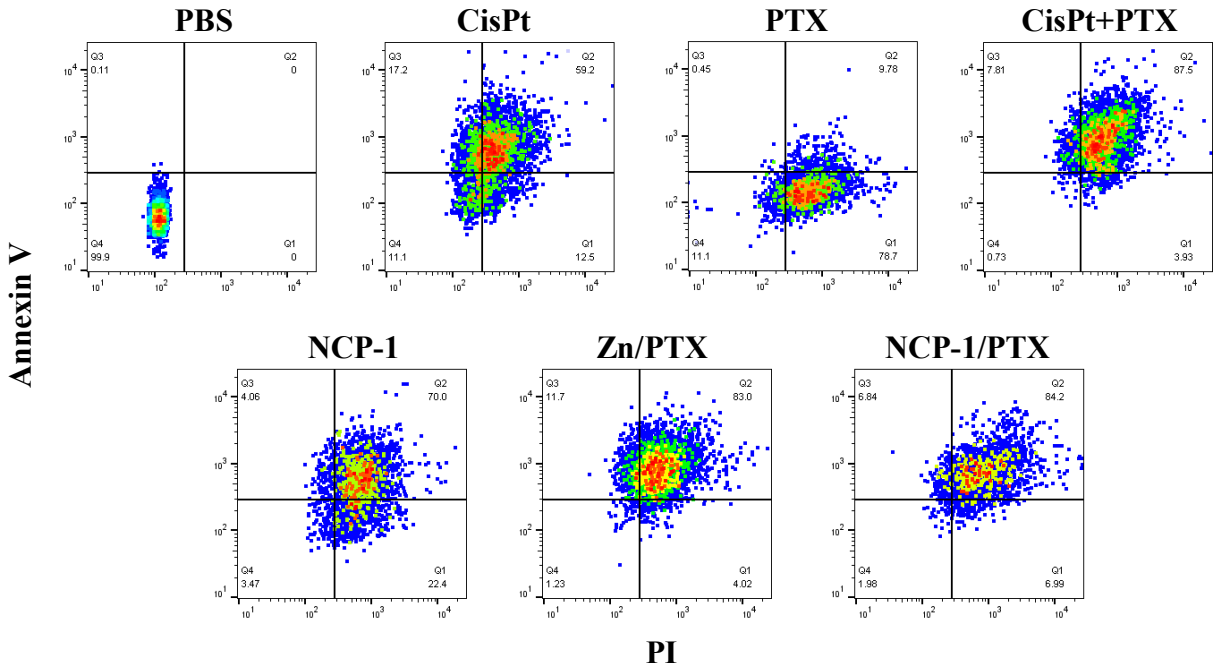

Figure 3-12 Annexin V/PI analysis of H460 cells dosed with CisPt, PTX, CisPt+PTX, NCP-1, Zn/PTX, or NCP-1/PTX in H460 cells at 5 μM CisPt and/or 1.25 μM PTX equivalents. Quadrants clockwise from the lower left to lower right represent healthy, early apoptotic, late apoptotic/necrotic, and necrotic cells, respectively.

Table 3-1 Percentages of healthy, apoptotic, and necrotic H460 cells incubated with equivalent doses of 5 μM CisPt and/or 1.25 μM PTX.

	Healthy	Early apoptotic	Necrotic	Late apoptotic/necrotic
PBS	99.9	0.11	0	0
CisPt	11.1	17.2	12.5	59.2
PTX	11.1	0.45	78.7	9.78
CisPt+PTX	0.73	7.81	3.93	87.5
NCP-1	3.47	4.06	22.4	70
Zn/PTX	1.23	11.7	4.02	83.0
NCP-1/PTX	1.98	6.84	6.99	84.2

The cytotoxicity of NCPs carrying CisPt-bp alone (NCP-1), chol-PTX alone (Zn/PTX), or the combination of CisPt-bp and chol-PTX (NCP-1/PTX) were compared against a panel of human

and murine cancer cells. As shown in **Table 3-2**, NCP-1/PTX significantly lowered the Pt and PTX IC_{50} values compared to the NCP-1 and Zn/PTX monotherapeutics in all tested cell lines. In the platinum-sensitive human ovarian cancer cell line A2780, both CisPt and PTX were potent anticancer drugs, with IC_{50} values in the single micromolar and hundreds of nanomolar range, respectively. The Pt and PTX IC_{50s} decreased 10 and 2 times, respectively, after treatment with NCP-1/PTX. Similar results were observed in H460 and LL/2 cells. In the platinum-resistant human ovarian cell line A2780/CDDP, there was nearly 100% cell viability at the highest tested concentration of 20 μM Pt for NCP-1. However, the PTX IC_{50} value was decreased by the combination in NCP-1/PTX compared to Zn/PTX, suggesting that the drugs may have some synergistic effects. Similar results were observed in the platinum-resistant SKOV-3 cells.

Table 3-2 Pt and PTX IC_{50} values (μM) in a panel of human and murine cancer cells.

	Origin	Cell line	NCP-1	Zn/PTX	NCP-1/PTX
Ovarian	Human	A2780	4.78 ± 0.04	(0.22 ± 0.15)[a]	0.50 ± 0.21 (0.13 ± 0.05)[a]
	Human	A2780/CDDP	>20	(0.62 ± 0.19)[a]	0.84 ± 0.18 (0.21 ± 0.15)[a]
	Human	SKOV-3	>20	(0.11 ±0.02)[a]	0.09 ± 0.04 (0.02 ± 0.01)[a]
Lung	Human	H460	2.34 ± 0.39	(0.42 ± 0.04)[a]	0.28±0.04 (0.070 ± 0.01)[a]
	Murine	LL/2	5.51 ± 1.32	(0.69 ± 0.13)[a]	1.40 ± 0.36 (0.35 ± 0.09)[a]

[a] The numbers in parentheses refer to PTX equivalents.

3.2.4 Pharmacokinetics and biodistribution

Encapsulation into NCPs significantly increased the drug exposure of both Pt and PTX. Pharmacokinetic studies were carried out in SD/CD rats receiving a bolus injection of free CisPt,

free PTX, or NCP-1/PTX at equivalent doses of 1.95 mg Pt/kg and 2.1 mg PTX/kg. As shown in **Figure 3-13** and **Table 3-3**, the plasma Pt and PTX concentrations are ~12 and ~35 times higher, respectively, beginning 5 min after injection. By 24 h after injection, free Pt and PTX were below the limit of detection by ICP-MS and LC-MS, respectively, while both Pt and chol-PTX were detectable in rats dosed with NCP-1/PTX. In total, this led to increases of ~357 and 377 times in the drug exposure to the blood, determined by the areas under the curve ($AUC_{0-\infty}$ values) of Pt and PTX equivalent by chol-PTX, by NCP-1/PTX over free CisPt and PTX, respectively. Importantly, the circulating drug appeared to have existed in nanoparticle form. Plasma ultrafiltrate was prepared by passing plasma through 3kDa Amicon Ultra Centrifugal Filter at 10,000 rpm (6708 xg) for 30 min. Ultrafilterable Pt was consistently observed at 4-6% of the total Pt content, similar to the background Pt release following this procedure (**Figure 3-14, Figure 3-4**). Importantly, free PTX was below the detection limit at all time points and all PTX was observed as chol-PTX (**Figure 3-14**). Similar improvements in the pharmacokinetics were observed in BALB/c mice: 45.6% of Pt remained in the plasma 3 h after injection by NCP-1/PTX compared to 2.5% and 1.3% remaining by CisPt-bc and CisPt, respectively (**Figure 3-15**). This further supports that the circulating Pt existed primarily in the form of NCPs. At this dose, NCP-1/PTX was found to be relatively nontoxic to mice for at least two weeks, as observed by consistent body weight and activity (**Figure 3-16**).

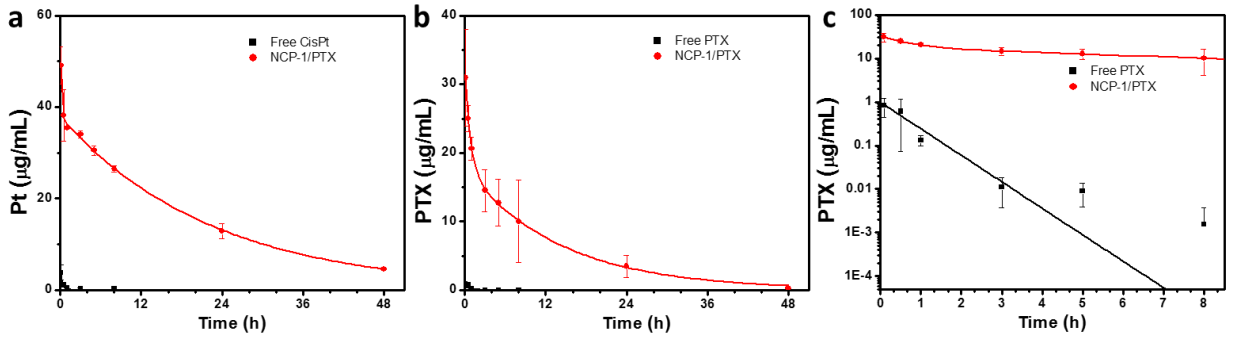

Figure 3-13 Plasma concentrations of (a) Pt and (b, c) PTX in rats dosed with free CisPt, PTX, or NCP-1/PTX The NCP-1/PTX levels in (b) were detected as chol-PTX and expressed as equivalent PTX concentrations.

Table 3-3 Pt and PTX pharmacokinetic parameters of NCP-1/PTX i.v. injected into rats.

Parameter (Unit)	$AUC_{0\rightarrow\infty}$ (μg/mL•h)	AUMC (μg/mL•h^2)	$t_{½\alpha}$ (h)	$t_{½\beta}$ (h)	MRT (h)
Free CisPt[a]	1.71 ± 0.35	0.65 ± 0.23	0.27 ± 0.09	____	0.39 ± 0.13
Free PTX	(0.70 ± 0.46)[b]	(0.50 ± 0.38)[b]	(0.49 ± 0.08)[b]	____	(0.71 ± 0.11)[b]
NCP-1/PTX[a]	610.5 ± 174.2 (264.6 ± 113.8)[c]	11883.5 ± 5081.7 (3624.0 ± 2424.0)[c]	0.57 ± 1.37 (0.54 ± 0.91)[c]	13.65 ± 2.53 (12.62 ± 1.86)[b]	19.47 ± 3.42 (13.69± 2.60)[c]

[a] Pt content was used for pharmacokinetic analysis.
[b] The numbers in parentheses refer to PTX.
[c] These numbers were detected as chol-PTX but expressed as PTX equivalent.

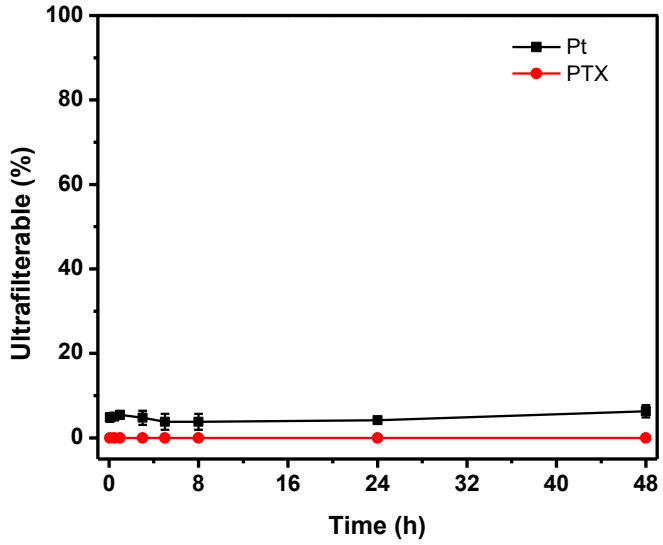

Figure 3-14 Ultrafilterable Pt and PTX from the plasma of rats dosed with NCP-1/PTX.

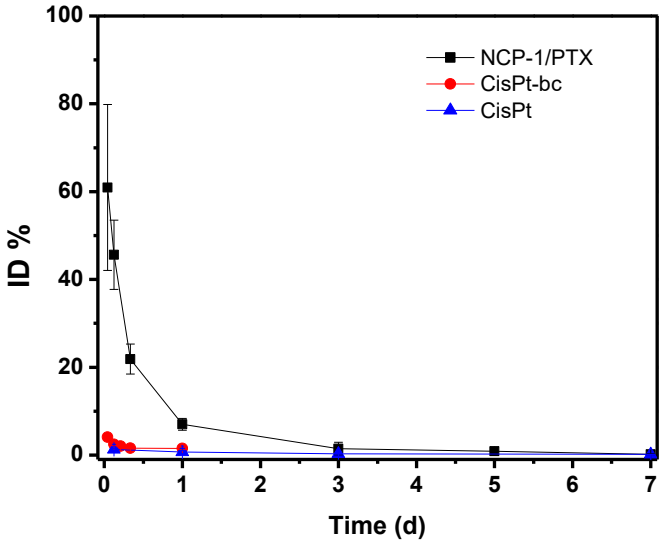

Figure 3-15 Plasma Pt concentrations of BALB/c mice dosed with CisPt, CisPt-bc, or NCP-1/PTX.

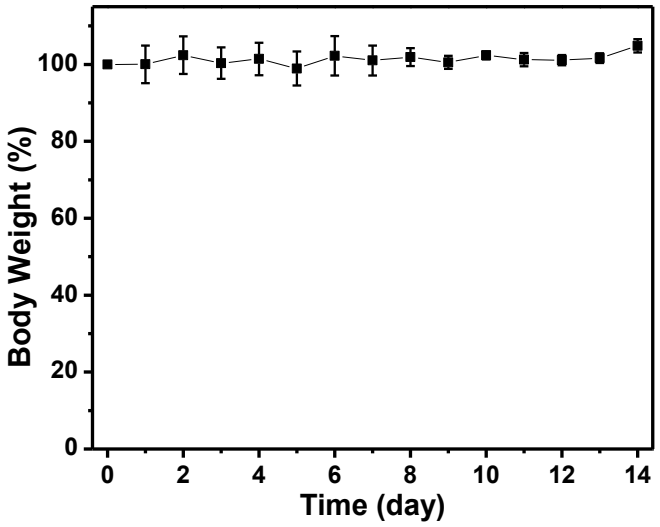

Figure 3-16 Body weight of BALB/c mice receiving an i.v. injection of NCP-1/PTX at a dose of 1.95 mg Pt/kg and 2.13 mg PTX/kg.

We synthesized a bovine serum albumin (BSA)-bound PTX (nab-PTX) according to literature for comparison with NCP-1/PTX-delivered PTX in vivo. The nab-PTX had a z-average and number-average size of 348.5 ± 4.0 nm and 59.73 ± 18.29 nm, respectively, by DLS and was well tolerated when injected into BALB/c mice at 10 mg PTX/kg. There was no aggregation leading to limb paralysis, death, or changes in the serum inflammatory cytokine interferon-gamma (IFN-γ) for at least 48 h after injection (**Figure 3-17**). Female mice bearing 4T1 tumors approximately ~80-120mm^3 in size were randomly divided into two groups and intravenously injected with CisPt and nab-PTX (CAnP) or NCP-1/PTX at equivalent doses of 0.65 mg Pt/kg and 0.71 mg PTX/kg. At predetermined time points, the mice were euthanized and the blood, tumor, spleen, kidney, liver, heart, lung, and bladder were harvested to determine the Pt concentrations by ICP-MS and the chol-PTX and PTX concentrations by LC/MS, where applicable. The Pt distribution was normalized against the injected dose and organ weight. NCP-1/PTX significantly alters Pt

circulation and distribution, with enhanced tumor uptake and relatively low accumulation (<10 percent injected dose per gram tissue [% ID/g]) in the kidney, lung, and bladder. The tumor concentration reached a maximum of 10.5 ± 2.8% ID/g 24 h after intravenous injection with NCP-1/PTX, compared to a maximum of 3.4 ± 0.7% ID/g 3 h after intravenous injection with CisPt (**Figure 3-18**).

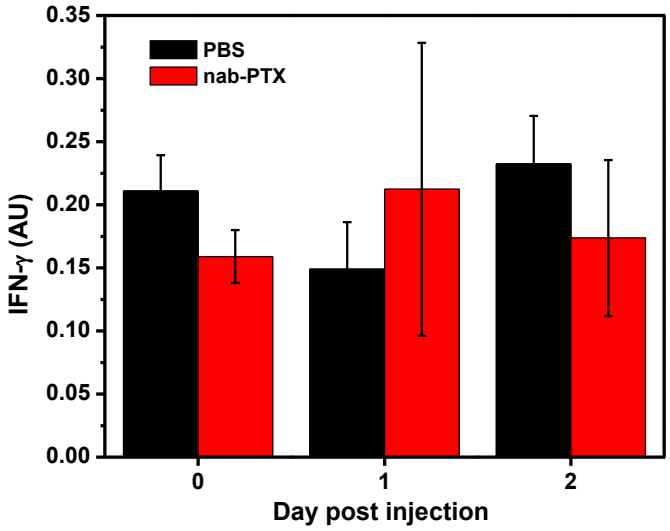

Figure 3-17 Serum IFN-γ levels in mice i.v. injected with nab-PTX at a dose of 10 mg PTX/kg.

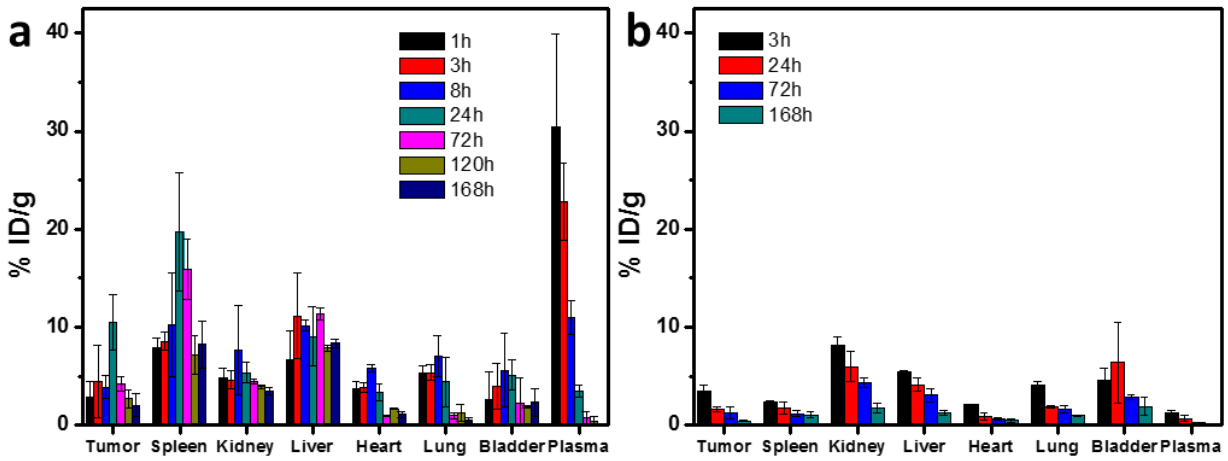

Figure 3-18 Biodistribution and tumor uptake of total Pt in 4T1 tumor-bearing mice after i.v. injection of (a) NCP-1/PTX or (b) CisPt and nab-PTX (CAnP).

As a proxy for renal clearance, the Pt accumulation in the kidney was not significantly different in mice dosed with NCP-1/PTX compared to CisPt. The kidney/tumor Pt ratio was fairly consistent in mice dosed with NCP-1/PTX, whereas the kidney/tumor Pt ratio in mice dosed with CisPt steadily decreased over time. Taken together with the biodistribution data, this indicates that the renal clearance of free CisPt is rapid compared to that of NCP-1/PTX. In comparison, the liver to tumor Pt ratio increases with prolonged exposure to CisPt, potentially due to faster clearance of Pt from the tumor than the liver. In NCP-1/PTX treated mice, the liver to tumor Pt ratio decreases with time due to faster clearance from the liver compared to the tumor (**Figure 3-19**). Significant liver accumulation of chol-PTX (up to 54.4 ± 9.2% ID/g) occurred in mice dosed with NCP-1/PTX (**Figure 3-20a**). Importantly, chol-PTX shows little to no cytotoxic activity compared to PTX and does not appear easily metabolized by liver enzymes, leading to sustained chol-PTX and subsequent PTX concentrations in both the tumor and the liver (**Figure 3-20, Figure 3-21**). The free PTX levels remain only ~1-2% ID/g for at least 72 h after injection (**Figure 3-20b**). Chol-PTX in the tumor hovers around 2.5-7.0% ID/g for up to one week, with corresponding free PTX

levels continuously around 0.6% ID/g. This represents an intratumoral drug concentration of ~100 nM, which is higher than most reported IC_{50} levels for PTX. Taken together, the tumor environment reduces chol-PTX to PTX much more efficiently than the liver environment. In comparison, the highest tumor accumulation mice dosed with nab-PTX occurs 3 hrs after administration. This level of 0.56 ± 0.31% ID/g is similar to the peak concentration in NCP-1/PTX treated mice, but the PTX concentration cannot be maintained (**Figure 3-20c**).

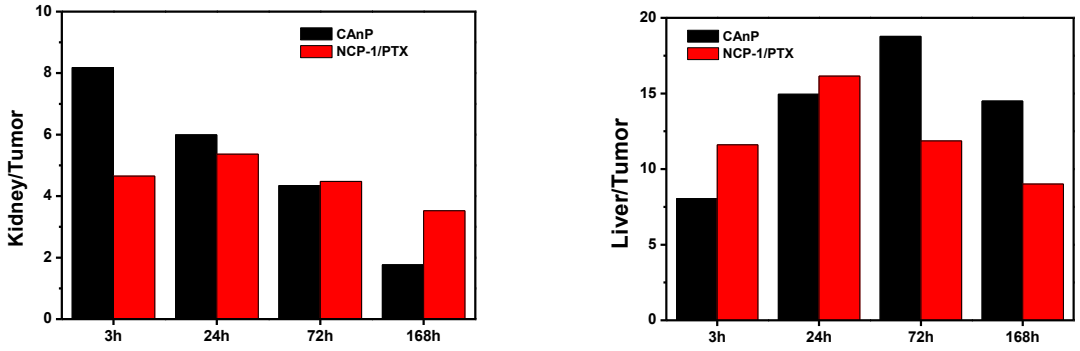

Figure 3-19 (a) Kidney to tumor and (b) liver to tumor ratios of Pt in 4T1 tumor-bearing mice treated with NCP-1/PTX or CAnP.

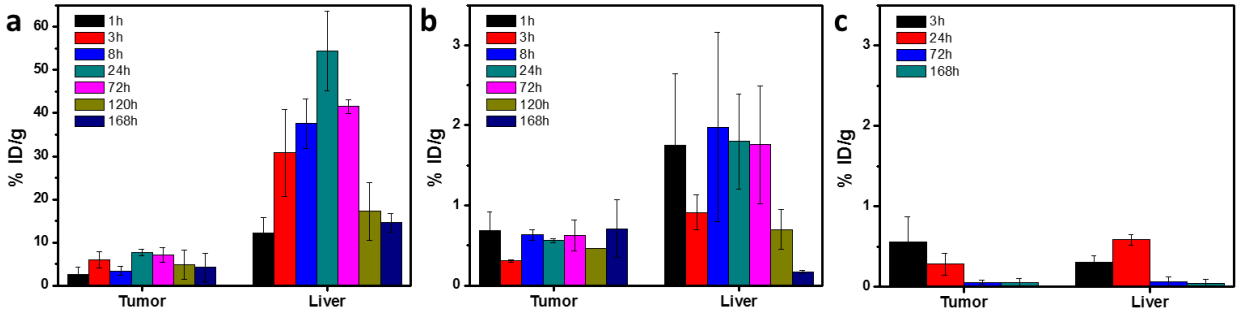

Figure 3-20 Biodistribution and tumor uptake of (a) total chol-PTX and (b, c) PTX in 4T1 tumor-bearing mice after i.v. injection of (a, b) NCP-1/PTX or (c) CAnP.

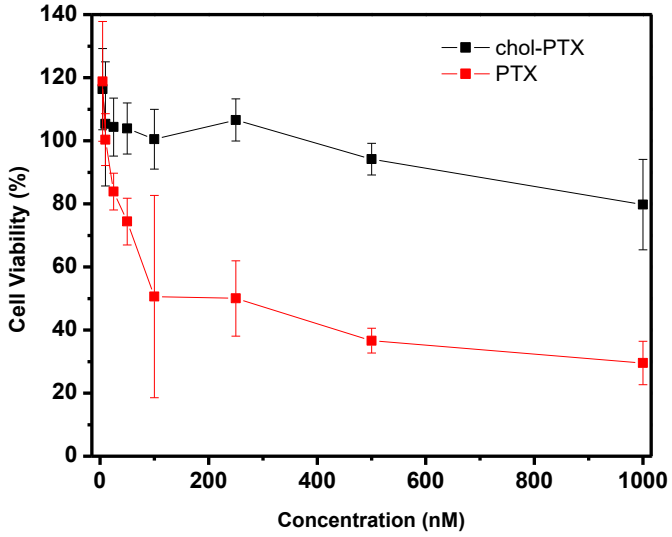

Figure 3-21 Cytotoxicity in A2780 cells treated with chol-PTX or PTX.

3.2.5 Anticancer efficacy in subcutaneous models

The in vivo anticancer efficacy of NCP-1/PTX was evaluated in subcutaneous human and murine ovarian (human A2780, A2780/CDDP, and SKOV-3), lung (human H460 and murine LL/2), and breast (murine 4T1) xenografts. When the tumors reached 70-120 mm^3 in volume, mice were injected intravenously once a week with NCP-1/PTX at a dose of 0.49 mg Pt/kg and 0.53 mg PTX/kg or with the combination of free CAnP at a dose of 3.9 mg Pt/kg and 8.0 mg PTX/kg (**Figure 3-22**). In all tested models, NCP-1/PTX led to significant tumor growth inhibition with minimal toxicity observed by both weight and histopathology of the major organs (**Figure 3-23**, **Figure 3-24**). In the human xenograft model of Pt-sensitive ovarian carcinoma A2780 on athymic nude mice, 25% of NCP-1/PTX treated mice had no discernible tumor by day 13 post first treatment and a total of 99.5% tumor growth inhibition (TGI, defined as 1-(RTV_t/RTV_c) where RTV = relative tumor volume, **Figure 3-22a**). NCP-1/PTX also showed significant anticancer efficacy controlling tumor growth in the platinum-resistant A2780/CDDP and SKOV-3 models

(**Figure 3-22b,c**). In the human H460 and murine LL/2 lung cancer models on athymic nude mice and C57BL/6 mice, respectively, NCP-1/PTX showed significantly greater anticancer efficacy than CAnP. Despite an 8 times increase in CisPt dose and 15 times increase in PTX dose, the anticancer efficacy of CAnP (65.2% and 69.6% TGI for H460 and LL/2, respectively) led to less tumor growth inhibition than NCP-1/PTX (88.1% and 83.8% TGI for H460 and LL/2, respectively, **Figure 3-22d,e**). The nanoparticle monotherapies NCP-1 and Zn/PTX showed less tumor growth control than NCP-1/PTX. Importantly, NCP-1/PTX was well tolerated by mice compared to CAnP, where several mice were moribund by the end of the study with splenic hemorrhage, seen as orange-brown spots indicative of hemosiderin, and necrosis in the liver (**Figure 3-24**). Similar results were observed in the murine 4T1 triple-negative breast cancer model on BALB/c mice (**Figure 3-22f**).

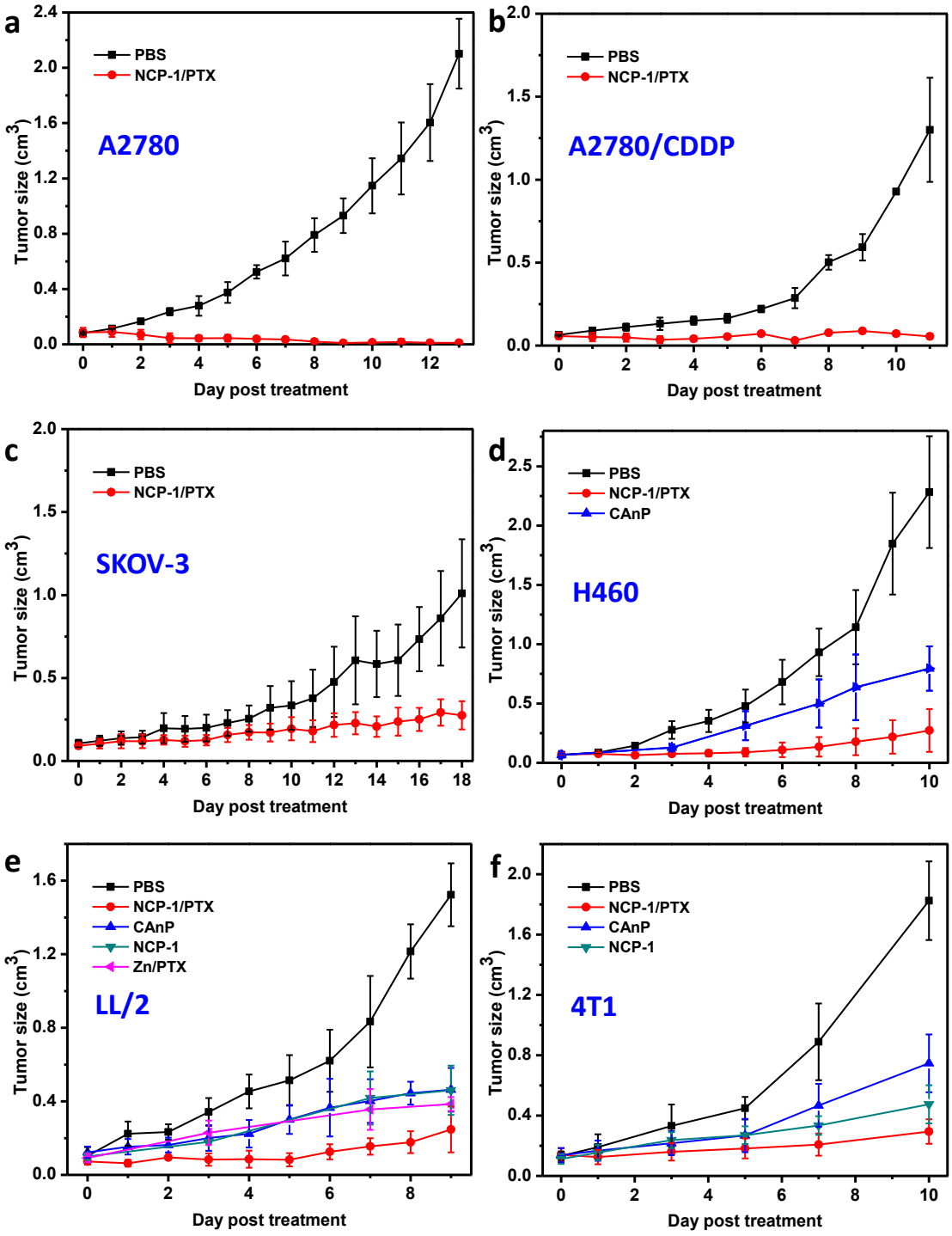

Figure 3-22 Tumor growth curves in a panel of subcutaneous human and murine xenografts in (a) A2780, (b) A2780/CDDP, (c) SKOV-3, (d) H460, (e) LL/2 and (f) 4T1 tumor-bearing mice treated with PBS, CAnP (3.9 mg Pt/kg and 8 mg PTX/kg), and NCP-1/PTX (0.49 mg Pt/kg and 0.53 mg PTX/kg) once a week for two doses.

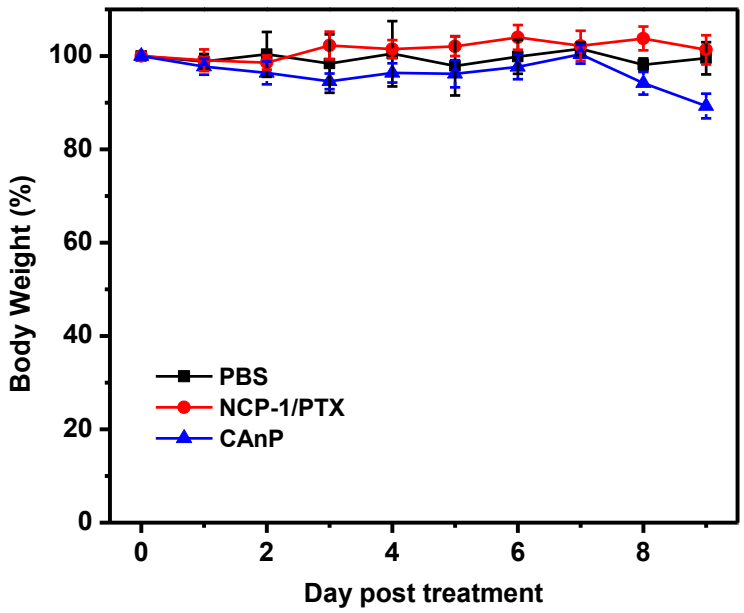

Figure 3-23 Body weight of LL/2 tumor-bearing mice treated with CAnP and NCP-1/PTX. Mice were treated once every 7 days for a total of 2 doses.

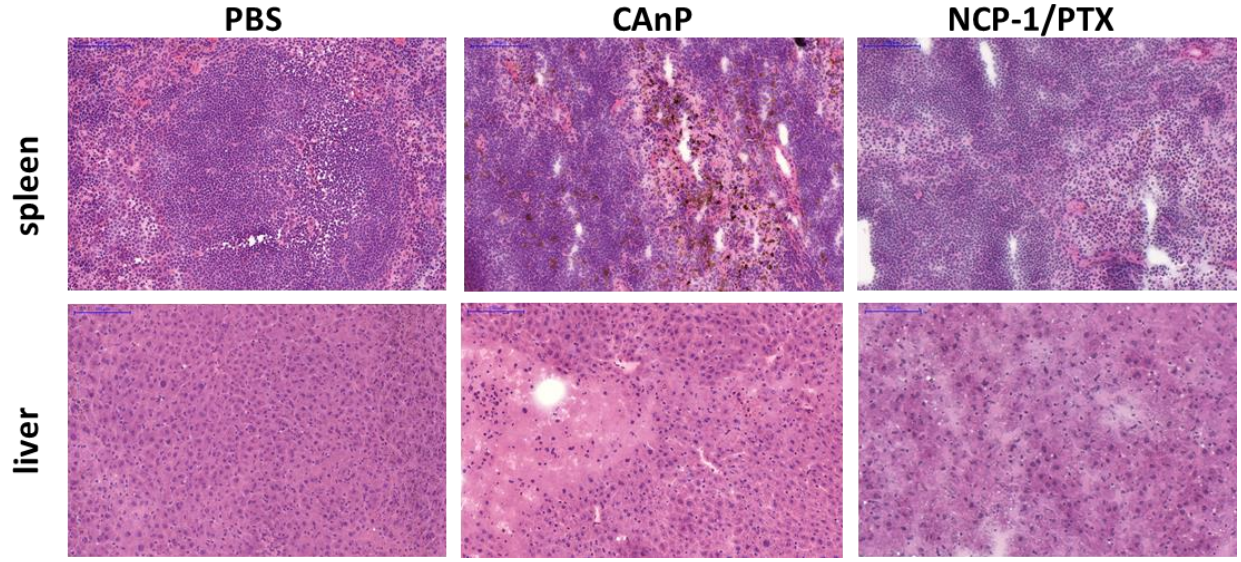

Figure 3-24 H&E staining of the spleen and liver, major clearance organs, in LL/2 tumor-bearing mice treated with PBS, CAnP, or NCP-1/PTX. Mice were treated once every 7 days for a total of 2 doses.

3.2.6 Anticancer efficacy in metastasis models

Though transplanted subcutaneous tumors are valuable models for preclinical drug development, these ectopic tumors are typically non-metastatic and are not histopathologically representative of advanced human tumors. To establish a model of disseminated disease, an experimental metastasis model of lung cancer was established by tail-vein injection of LL/2 cells. According to the seed-and-soil hypothesis, this should primarily lead to pulmonary metastases. By ten days after tail-vein injection, gross examination of the lungs showed preliminary indications of tumor nodules on the surface (**Figure 3-25**). The lungs of untreated mice twenty-five days after tail-vein injection showed significant tumor growth, such that the lung tissue was visually obscured (**Figure 3-25**). To determine the anticancer efficacy of NCP-1/PTX on advanced lung cancer, mice were inoculated with LL/2 by tail-vein injection and treated twice on days 10 and 17 after inoculation. Mice were dosed with PBS, CAnP (3.9 mg Pt/kg and 8.0 mg PTX/kg), NCP-1 (0.49 mg Pt/kg), or NCP-1/PTX (0.49 mg Pt/kg and 0.53 mg PTX/kg). The mice were sacrificed when severe health problems, such as labored breathing, or significant body weight loss were noticed. Mice treated with CAnP or NCP-1 showed no difference in median survival time compared to PBS (30.5 and 27 days, respectively, compared to 31.5 days). Treatment with NCP-1/PTX significantly prolonged the life expectancy of mice, extending the median survival time to 50.5 days (**Figure 3-26, Figure 3-27**).

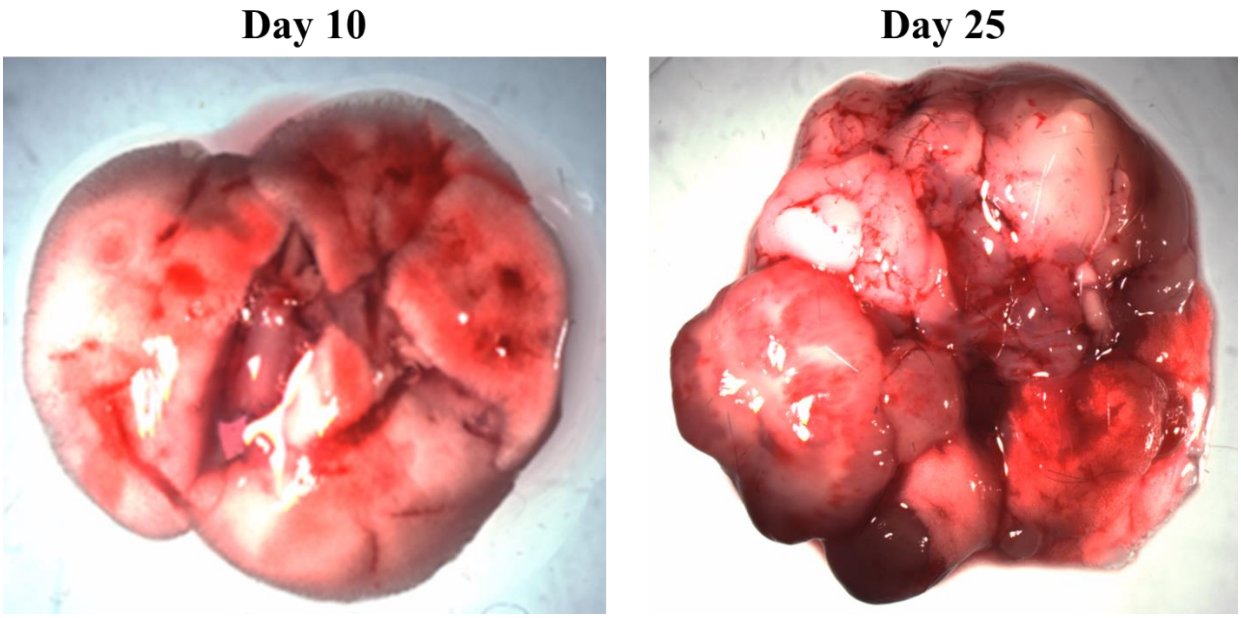

Figure 3-25 Gross examination of lungs excised from untreated mice 10 and 25 days after tail-vein injection with LL/2 cells.

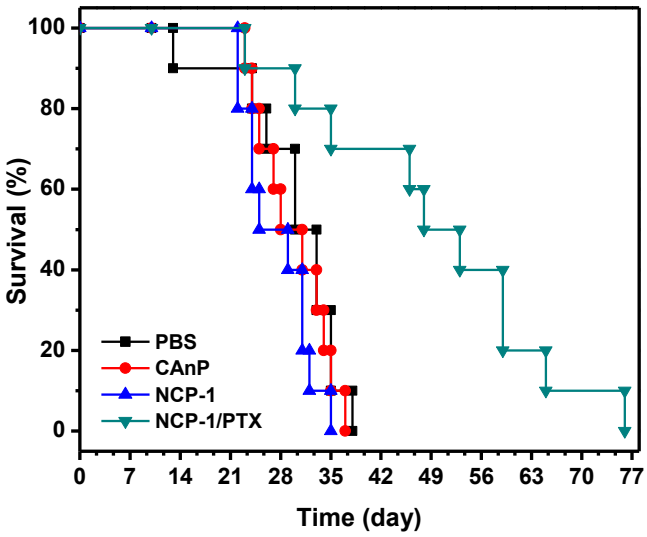

Figure 3-26 Kaplan-Meier survival curves of mice intravenously dosed with PBS, CAnP, NCP-1, or NCP-1/PTX on days 10 and 17 after tail-vein injection with LL/2 cells.

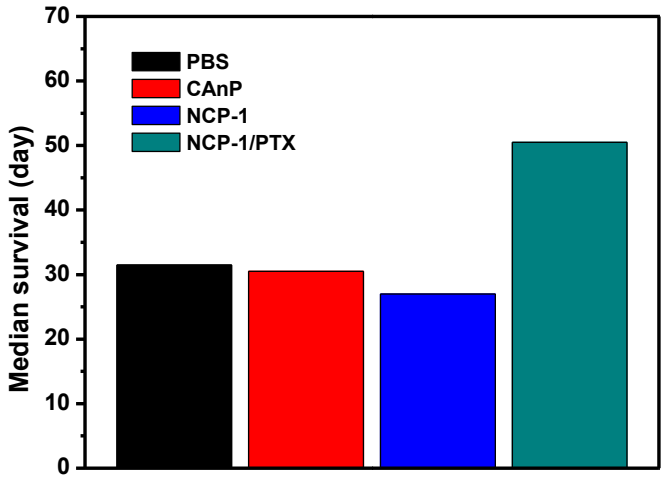

Figure 3-27 Median survival of mice receiving tail-vein injection with LL/2 cells after treatment.

The experimental metastasis model allows for investigation of drug candidates against existing disseminated disease, but eliminates important early steps in the metastatic cascade including selection and intravasation. A spontaneous metastasis model can more accurately recapitulate human histopathology with respect to tumor histology and vascularity than subcutaneous models. 4T1 cells can be implanted into the mammary fat pad of female mice to generate an orthotopic model that spontaneously metastasizes to the lungs. 4T1 tumor-bearing mice were i.v. injected with CAnP, Zn/PTX, NCP-1, or NCP-1/PTX once a week beginning 12 days after tumor inoculation for a total of two doses. 10 days after the first treatment, mice were sacrificed and assessed for pulmonary tumor nodules. NCP-1/PTX showed marginally better tumor growth inhibition than CAnP, NCP-1, or Zn/PTX at the mammary site, but led to significantly less tumor nodules in the lung (**Figure 3-28**).

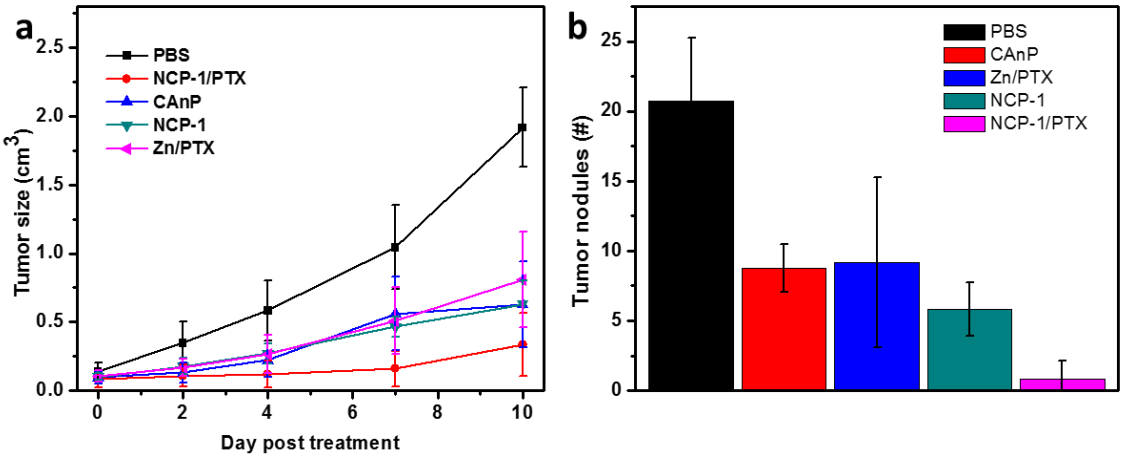

Figure 3-28 Anticancer efficacy and antimetastasis effect of NCP-1/PTX in an orthotopic metastasis model of 4T1. (a) Tumor growth curve of the primary 4T1 tumor in the mammary fat pad of female BALB/c mice. (b) The number of tumor nodules visible on the surface of the lung at endpoint.

3.3 Discussion

Paclitaxel is a potent anticancer drug, widely used in chemotherapy regimens across a range of cancers with solid tumors. Though preclinical in vitro data has consistently shown the cytotoxicity of PTX on cancer cells, the in vivo preclinical and clinical doses have been similar to or higher than doses of drugs with IC_{50} values one or two orders of magnitude higher than PTX. This may be related to the inefficient delivery of PTX to the tumor in both the Cremophor EL/ethanol and albumin-bound forms as well as rapid metabolism of PTX in the liver. Our prodrug approach of conjugating cholesterol and PTX via a disulfide bond minimizes active drug exposure in normal tissues, such as the liver, by requiring a biological trigger (i.e. a reducing environment) for drug release. Chol-PTX can escape intact from the liver and be transported to the tumor for continual chol-PTX accumulation and reduction, sustaining active drug levels in the tumor for up to one week.

Using a single nanoparticle to deliver a frequently used clinical combination chemotherapy regimen can simplify therapy. The dose-limiting toxicities of CisPt and PTX are associated with the free drug levels circulating in the bloodstream, requiring pre- and post-hydration for CisPt treatment and long infusion times of up to 24 h for PTX treatment. The NCP core-shell structure limits drug exposure in the bloodstream and drug activity in organs other than the target cancer cells. The long circulation half-life and sustained tumor drug concentrations allows for infrequent dosing. Furthermore, the tunable drug loading can accommodate variable drug regimens, dependent on the requirements of the patient.

Each different cancer model (ectopic subcutaneous, experimental metastasis, and orthotopic with spontaneous metastasis) contributes unique perspective onto the merits and deficits of the NCP-1/PTX as a treatment paradigm. Human xenograft models show more intratumoral hetereogeneity and genetic complexity than murine syngeneic models due to cell origins, but often require immunocompromised hosts and limit the interplay between the tumor cells and the tumor microenvironment. Tail-vein injected experimental metastasis can model some portions of advanced or disseminated disease, which remains the most significant problem in cancer, but also overlook selection processes involved in metastasis. Orthotopic models with spontaneous metastasis more closely resemble human tumors and cancers, with respect to histopathology and responsiveness to chemotherapy. In each of these models, NCP-1/PTX has equal or greater anticancer efficacy than the combination of CisPt and nab-PTX at 8 and 15 times lower drug doses, respectively.

3.4 Conclusion

NCP-1/PTX uses nanotechnology to improve the well-established combination CAP therapy. Prodrugs for CisPt and PTX allowed for stable incorporation into the NCP structure and triggered release of active drug components. This allowed for nontoxic prodrug depots in the liver to continuously feed PTX concentration in the tumors. The improved pharmacokinetic properties led to increased anticancer efficacy at lower doses in human xenograft models and a range of syngeneic models for localized disease with primary tumors, advanced disease with disseminated tumors, and disease progression with localized disease spontaneously metastasizing. NCP-1/PTX led to more than 80% tumor growth inhibition in primary tumors, extended median survival from 31.5 to 50.5 days, and inhibited metastasis in the various preclinical models. These data support the potential for NCP-1/PTX as a clinical candidate for the treatment of advanced lung and gynecological cancers.

3.5 Materials and methods

Materials, Cell Lines, and Animals. All starting materials were purchased from Sigma-Aldrich and Fisher (USA), unless otherwise noted, and used without further purification. 1,2-dioleoyl-snglycero-3-phosphate (DOPA) was purchased from Avanti Polar Lipids (USA). 1,2-dioleyl-sn-glycero-3-phosphocholine (DOPC), cholesterol, and 1,2-distearoyl-sn-glycero-3-phosphoethanolamine-N-[amino(polyethylene glycol)2000] (DSPE-PEG2k) were purchased from Lipoid (USA).

Human ovarian cancer cell line sensitive to cisplatin A2780 was from Developmental Therapeutics Core, Northwestern University. Human ovarian cancer cell lines resistant to cisplatin SKOV-3 and A2780/CDDP were from the American Type Culture Collection (Rockville, MD,

USA) and Developmental Therapeutics Core, Northwestern University, respectively. Murine mammary carcinoma cell 4T1 and murine Lewis lung carcinoma cell LL/2 were all obtained from the ATCC. SKOV-3 cells were cultured in McCoy's 5a medium containing 10% fetal bovine serum (FBS). A2780 and A2780/CDDP cells were cultured in RPMI-1640 medium (Gibco, Grand Island, NY, USA) containing 10% FBS. MC38, 4T1 and LL/2 were grown in Dulbecco's Modified Eagle's Medium (DMEM), supplemented with 10% FBS, 100 U/mL penicillin G sodium and 100 μg/mL streptomycin sulfate in a humidified atmosphere containing 5% CO_2 at 37 ºC.

BALB/c mice (6 weeks, 18-22 g), C57BL/6 mice (6 weeks, 18-22 g), $Rag^{2-/-}$ mice (6 weeks, 18-22 g), and SD/CD rats (6 weeks, 160-200 g) were provided by Harlan-Envigo Laboratories, Inc (USA). The study protocol was reviewed and approved by the Institutional Animal Care and Use Committee (IACUC) at the University of Chicago.

Apoptosis/necrosis. 5×10^4 H460 cells per well were seeded in 6-well plates and allowed to adhere for 24 h. Cells were then treated with CisPt, PTX, CAP, NCP-1, Zn/PTX, or NCP-1/PTX at equivalent concentrations of 5 μM Pt and 1.25 μM PTX. The cells were harvested after 24 h, washed twice with ice-cold PBS, and then stained with Alexa Fluor 488-Annexin V and propidium iodide (PI) for 15 min at room temperature in the dark for analysis by flow cytometry (LSR II, BD, USA).

Cytotoxicity. 2×10^3 cells per well were seeded in 96-well plates and allowed to adhere for 24 h. Cells were then treated with NCPs and incubated for an additional 72 h. Cell viability was detected

by 3-(4,5-dimethylthiazol-2-yl)-5-(3-carboxymethoxyphenyl)-2-(4-sulfophenyl)-2H-tetrazolium (MTS) assay (Promega, Madison, WI) according to the manufacturer's instructions.

Pharmacokinetics and biodistribution. Free CisPt, free PTX in diluted Cremophor EL/EtOH, or NCP-1/PTX at equivalent doses of 1.95 mg Pt/kg and 8.53 mg PTX/kg were administered by tail-vein injection. The blood was collected at 5 min, 30 min, 1 h, 3 h, 5 h, 8 h, 24 h, and 48 h post-injection into EDTA tubes and centrifuged at 604 x g for 10 min to collect the plasma. 25 μL plasma was digested with concentrated nitric acid for 24 h and analyzed for Pt concentration by ICP-MS. Another 25 μL plasma was added to 10 μL 5% Triton X-100 to disrupt the lipid bilayer and 100 μL ethyl acetate was added to extract chol-PTX. The samples were centrifuged at 6708g prior to analysis by LC-MS.

4T1 tumor-bearing female BALB/c mice were i.v. dosed with CAnP or NCP-1/PTX at equivalent doses of 0.65 mg Pt/kg and 2.84 mg PTX/kg. Mice were euthanized 1 h, 3 h, 8 h, 24 h, 48 h, 72 h, 120 h, or 168 h post-injection. The livers, lungs, hearts, spleens, kidneys, bladders, tumors, and blood were harvested. Each organ was split into two, massed, and then one portion was digested with concentrated nitric acid for 24 h for analysis of Pt content by ICP-MS. The other was homogenized with 500 μL 0.5% Triton X-100. 500 μL ethyl acetate was added to extract the chol-PTX and then centrifuged before analysis of PTX and chol-PTX content by LC/MS-MS.

Healthy BALB/c mice were i.v. dosed with 0.65 mg Pt/kg CisPt-bc. Blood was collected 1 h, 3 h, 5h, 8 h, and 24 h post-injection into EDTA tubes and centrifuged at 604 x g for 10 min to collect the plasma. 50 μL plasma was digested with concentrated nitric acid for 24 h and analyzed for Pt concentration by ICP-MS.

Synthesis of nab-PTX. PTX (20 mg) was dissolved in 1 mL of DCM and added to an aqueous suspension of BSA (5% w/v, 4 mL). This was mixed with a motorized pellet pestle (DWK, Millville, NJ) and then transferred to a sonic dismembrator with a 1/2" probe set at 30% power for 5 min with pulses of 1 sec on / 1 sec off. DCM was removed by rotary evaporator and then the suspension was lyophilized to afford a colorless foam.

Immunotoxicity of nab-PTX. Healthy BALB/c mice were intravenously injected with PBS or nab-PTX on day 0. Blood was collected on days 0, 1, 2, and 3, and the serum IFN-γ levels were determined by enzyme-linked immunosorbent assay according to the manufacturer's instructions (ELISA, eBioscience, USA).

Anticancer efficacy in subcutaneous tumor models. 5×10^6 A2780, A2780/CDDP, or SKOV-3 cells were subcutaneously injected onto the right flank of female athymic nude mice aged 6-8 weeks old. 2×10^6 H460, LL/2, or 4T1 cells were subcutaneously injected onto the right flank of athymic nude mice, C57BL/6, or BALB/c mice, respectively. After the tumors reached 70-120 mm^3, the mice were i.v. injected with PBS, CAnP, NCP-1, Zn/PTX, or NCP-1/PTX once a week for two doses. Free CisPt and nab-PTX were dosed at 3.9 mg Pt/kg and 8 mg PTX/kg, whereas NCPs were all dosed at 0.49 mg Pt/kg and 0.53 mg PTX/kg. Tumor growth was monitored by measurement with a digital caliper, where tumor volumes were calculated as follows: $(\text{width}^2 \times \text{length})/2$.

When the mice were euthanized on day 10, the spleens and livers were harvested, embedded in OCT medium, sectioned into 5 μm slices with a Cryostat (NX50, Thermo, USA), and then stained with H&E for histological examination by light microscopy.

Intravenous model of LL/2. C57Bl/6 mice aged 6-8 weeks were given 2×10^6 cells by tail-vein injection. On days 10 and 17 after LL/2 injection, mice were i.v. dosed with PBS, CAnP, NCP-1, or NCP-1/PTX. Free CisPt and nab-PTX were dosed at 3.9 mg Pt/kg and 8 mg PTX/kg, whereas NCPs were all dosed at 0.49 mg Pt/kg and 0.53 mg PTX/kg. The body weight was monitored twice a week and activity was monitored daily. Mice were euthanized if they showed rapidly decreasing body weight or significant signs of distress (i.e. laying on its side with labored breathing). Each mouse was dissected and confirmed to have tumor nodules in the lung cavity to be included into the survival data.

4T1 mammary fat pad model. 2×10^6 cells were inoculated into the right mammary fat pad of female BALB/c mice. When the tumors reached 80-120 mm^3, mice were i.v. dosed with PBS, CAnP, NCP-1, Zn/PTX, or NCP-1/PTX once a week for a total of two doses. Free CisPt and nab-PTX were dosed at 3.9 mg Pt/kg and 8 mg PTX/kg, whereas NCPs were all dosed at 0.49 mg Pt/kg and 0.53 mg PTX/kg. At the end of the experiment, the mice were dissected for visual examination of metastasis, particularly in the lungs.

3.6 References

1. Galanski, M., Jakupec, M.A. & Keppler, B.K. Update of the preclinical situation of anticancer platinum complexes: novel design strategies and innovative analytical approaches. *Curr Med Chem* **12**, 2075-2094 (2005).
2. Zeghari-Squalli, N., Raymond, E., Cvitkovic, E. & Goldwasser, F. Cellular pharmacology of the combination of the DNA topoisomerase I inhibitor SN-38 and the diaminocyclohexane platinum derivative oxaliplatin. *Clin Cancer Res* **5**, 1189-1196 (1999).
3. Rigas, J.R. Taxane-platinum combinations in advanced non-small cell lung cancer: a review. *Oncologist* **9 Suppl 2**, 16-23 (2004).
4. Raja, F.A. et al. Platinum versus platinum-combination chemotherapy in platinum-sensitive recurrent ovarian cancer: a meta-analysis using individual patient data. *Ann Oncol* **24**, 3028-3034 (2013).
5. Zhao, B., Hemann, M.T. & Lauffenburger, D.A. Intratumor heterogeneity alters most effective drugs in designed combinations. *Proc Natl Acad Sci U S A* **111**, 10773-10778 (2014).
6. Palmer, A.C. & Sorger, P.K. Combination Cancer Therapy Can Confer Benefit via Patient-to-Patient Variability without Drug Additivity or Synergy. *Cell* **171**, 1678-1691 e1613 (2017).
7. Bayat Mokhtari, R. et al. Combination therapy in combating cancer. *Oncotarget* **8**, 38022-38043 (2017).
8. Lopez, J.S. & Banerji, U. Combine and conquer: challenges for targeted therapy combinations in early phase trials. *Nat Rev Clin Oncol* **14**, 57-66 (2017).
9. Chabner, B.A. & Roberts, T.G., Jr. Timeline: Chemotherapy and the war on cancer. *Nat Rev Cancer* **5**, 65-72 (2005).
10. DeVita, V.T., Jr. & Chu, E. A history of cancer chemotherapy. *Cancer Res* **68**, 8643-8653 (2008).
11. McGuire, W.P., 3rd & Markman, M. Primary ovarian cancer chemotherapy: current standards of care. *Br J Cancer* **89 Suppl 3**, S3-8 (2003).
12. Thomas, A., Liu, S.V., Subramaniam, D.S. & Giaccone, G. Refining the treatment of NSCLC according to histological and molecular subtypes. *Nat Rev Clin Oncol* **12**, 511-526 (2015).
13. Gelmon, K.A. et al. Phase I/II trial of biweekly paclitaxel and cisplatin in the treatment of metastatic breast cancer. *J Clin Oncol* **14**, 1185-1191 (1996).
14. Goldberg, J.M., Piver, M.S., Hempling, R.E. & Recio, F.O. Paclitaxel and cisplatin combination chemotherapy in recurrent epithelial ovarian cancer. *Gynecol Oncol* **63**, 312-317 (1996).
15. Florea, A.M. & Busselberg, D. Cisplatin as an anti-tumor drug: cellular mechanisms of activity, drug resistance and induced side effects. *Cancers (Basel)* **3**, 1351-1371 (2011).

16. Horwitz, S.B. Taxol (paclitaxel): mechanisms of action. *Ann Oncol* **5 Suppl 6**, S3-6 (1994).

17. Rowinsky, E.K., Eisenhauer, E.A., Chaudhry, V., Arbuck, S.G. & Donehower, R.C. Clinical toxicities encountered with paclitaxel (Taxol). *Semin Oncol* **20**, 1-15 (1993).

18. Hanigan, M.H. & Devarajan, P. Cisplatin nephrotoxicity: molecular mechanisms. *Cancer Ther* **1**, 47-61 (2003).

19. Chao, C. et al. Adjuvant chemotherapy for breast cancer: how presentation of recurrence risk influences decision-making. *J Clin Oncol* **21**, 4299-4305 (2003).

20. Derks, M.G.M. & van de Velde, C.J.H. Neoadjuvant chemotherapy in breast cancer: more than just downsizing. *Lancet Oncol* **19**, 2-3 (2018).

21. Mariotto, A.B., Etzioni, R., Hurlbert, M., Penberthy, L. & Mayer, M. Estimation of the Number of Women Living with Metastatic Breast Cancer in the United States. *Cancer Epidemiol Biomarkers Prev* **26**, 809-815 (2017).

22. Molina, J.R., Yang, P., Cassivi, S.D., Schild, S.E. & Adjei, A.A. Non-small cell lung cancer: epidemiology, risk factors, treatment, and survivorship. *Mayo Clin Proc* **83**, 584-594 (2008).

23. Doubeni, C.A., Doubeni, A.R. & Myers, A.E. Diagnosis and Management of Ovarian Cancer. *Am Fam Physician* **93**, 937-944 (2016).

24. Einhorn, L.H. & Donohue, J. Cis-diamminedichloroplatinum, vinblastine, and bleomycin combination chemotherapy in disseminated testicular cancer. *Ann Intern Med* **87**, 293-298 (1977).

25. Arruebo, M. et al. Assessment of the evolution of cancer treatment therapies. *Cancers (Basel)* **3**, 3279-3330 (2011).

26. Crawford, S. Is it time for a new paradigm for systemic cancer treatment? Lessons from a century of cancer chemotherapy. *Front Pharmacol* **4**, 68 (2013).

27. Lee, M.S., Dees, E.C. & Wang, A.Z. Nanoparticle-Delivered Chemotherapy: Old Drugs in New Packages. *Oncology (Williston Park)* **31**, 198-208 (2017).

28. Green, M.R. et al. Abraxane, a novel Cremophor-free, albumin-bound particle form of paclitaxel for the treatment of advanced non-small-cell lung cancer. *Ann Oncol* **17**, 1263-1268 (2006).

29. Gelderblom, H., Verweij, J., Nooter, K. & Sparreboom, A. Cremophor EL: the drawbacks and advantages of vehicle selection for drug formulation. *Eur J Cancer* **37**, 1590-1598 (2001).

30. Astolfi, L. et al. Correlation of adverse effects of cisplatin administration in patients affected by solid tumours: a retrospective evaluation. *Oncol Rep* **29**, 1285-1292 (2013).

31. Liu, D., Poon, C., Lu, K., He, C. & Lin, W. Self-assembled nanoscale coordination polymers with trigger release properties for effective anticancer therapy. *Nat Commun* **5**, 4182 (2014).

CHAPTER 4 Nanoscale coordination polymer overcomes paclitaxel metabolism and combines with oxaliplatin for chemoimmunotherapy of colorectal cancer

4.1 Introduction

As demonstrated in Chapter 3, PTX is extremely potent in many cancer cells in vitro and in vivo in many types of tumors, but clinical trials of PTX have shown little or no activity in colon, rectal,[1] and liver cancer patients.[2] This may be related to the abundance of P450s, specifically CYP3A4 and CYP2A8, in the liver and intestinal epithelium; both enzymes oxidize PTX to hydroxypaclitaxel,[3-6] lowering the cytotoxicity by ~30 times and thus significantly detoxifying the drug.[7, 8] PTX metabolites are more abundant than parent PTX in excreted bile, requiring high clinical doses despite the high cytotoxicity observed in cell culture.[8, 9]

High clinical doses of PTX lead to long infusion times (up to 24 h), which disproportionately affect the C_{max} in the blood. Sustained levels of PTX above a certain threshold (0.05-0.2 μM), however, are related to the major toxicities of PTX: neuropathy and myelosuppression in the form of neutropenia.[10-15] Peripheral neuropathy, particularly, led to treatment disruptions (dose delay, dose reduction, or discontinuation) in 31.7% of patients in one study, after an average of eight weekly doses.[10] Other combination chemotherapy regimens including PTX also showed similar or higher rates of dose disruption (24-70%).[16-20] Up to 37% of breast, colon, lymphoma, lung, and ovarian cancer patients experience chemotherapy-induced neutropenia, which can lend to lengthy hospital stays and lower overall quality of life.[21-25]

Though often combined with the platinum chemotherapeutics cisplatin and carboplatin, PTX and the platinum chemotherapy oxaliplatin (OxPt) is not standard of care for any cancer.[26, 27] OxPt is primarily used for the treatments of colorectal, pancreatic, and gastric cancers;[26-29] however, the combination of OxPt and PTX has been investigated in NSCLC, ovarian, gastric, and cervical cancer patients with positive results.[30-34] Both drugs are considered immunogenic cell death (ICD) inducers capable of stimulating the immune system by inducing DC activation and subsequent T cell infiltration.[35, 36] A limiting factor, however, is the two drugs' overlapping toxicities, particularly of neuropathy.[37, 38]

We herein report the design of nanoscale coordination polymers (NCPs) carrying an OxPt analogue [Pt(dach)Cl_2] and PTX (NCP-2/PTX) for effective treatment of colorectal cancers in combination with anti-PD-L1. Using a cholesterol-conjugated PTX prodrug can overcome metabolism by hepatic and intestinal P450s and lower the concentration of free drug in circulation, leading to decreased chemotherapy-induced neutropenia and neuropathy. NCP-2/PTX combination therapy leads to transportation of CRT to the cell surface and release of HMGB-1, two hallmarks of ICD, and subsequent vaccination effects protecting against tumor challenges. Low doses of NCP-2/PTX were combined with anti-PD-L1 for the long-term management of established, immunosuppressive models of colorectal cancer.

4.2 Results and discussion

4.2.1 Synthesis and characterization of NCP-2/PTX

Pt(dach)Cl_2bis(phosphoramic acid), cholesterol-conjugated paclitaxel, and DOPA-capped NCP-2 particles were synthesized with minor modifications to previously reported protocols.[39]

Briefly, a mixture of $Zn(NO_3)_2$, $Pt(dach)Cl_2bp$ (dach = R, R-diaminocyclohexane), and 1,2-dioleoyl-sn-glycero-3-phosphate sodium salt (DOPA) in a reverse microemulsion containing Triton X-100/hexanol/cyclohexane was stirred vigorously at room temperature for 30 min to afford a spherical DOPA-NCP-2 particles. DOPA-NCP-2 were further coated with 1,2-dioleoyl-sn-glycero-3-phosphocholine, cholesterol, 1,2-diastearoyl-sn-gylcero-3-phosphoethanolamine-N-[methoxy(polyethylene glycol)-2000], and chol-PTX at a 7:3:3:2 ratio. NCP-2/PTX particles were synthesized to carry Pt in the core and chol-PTX in a lipid shell containing DOPC, cholesterol, and DSPE-PEG. The NCPs were relatively monodispersed in aqueous solutions by transmission electron microscopy (TEM) and gave z-average, number average, and PDI of 121.7 ± 0.97 nm, 67.3 ± 2.0 nm, and 0.139 $\pm$ 0.010, respectively, by DLS (**Figure 4-1**, **Figure 4-2**).

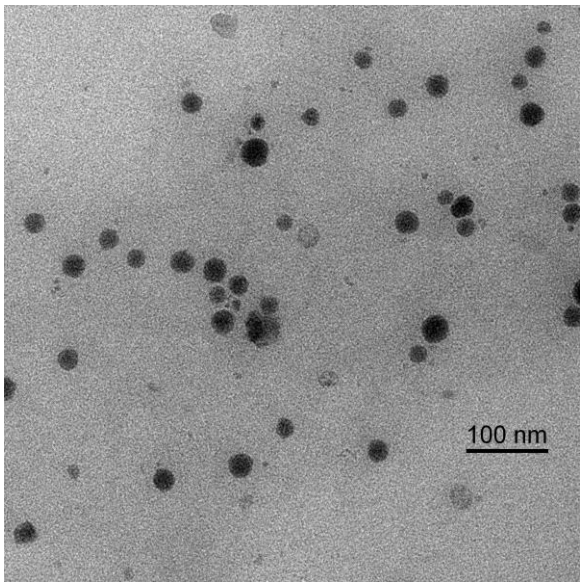

Figure 4-1 TEM image of NCP-2/PTX showing the approximate size and shape of the spherical nanoparticles. Bar = 100 nm.

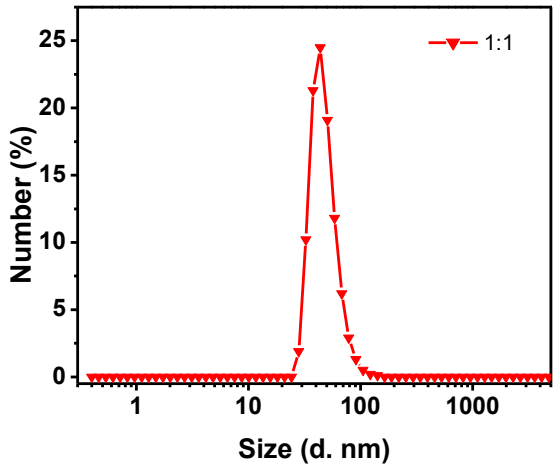

Figure 4-2 Number-average size distribution of NCP-2/PTX in H_2O.

4.2.1 Pharmacokinetics and biodistribution

NCP-2/PTX can improve the therapeutic window by increasing drug exposure and the biodistribution of Pt and PTX. CT26 tumor-bearing mice were i.p. injected with NCP-2/PTX and the liver, lung, spleen, kidney, tumor, and blood were collected at pre-determined time points. The organs and blood were digested with concentrated nitric acid and then analyzed for Pt content by inductively coupled plasma-mass spectrometry (ICP-MS). NCP-2/PTX reached a maximum tumor accumulation of 9.62 ± 6.95 %ID/g tissue at 48 h post injection (**Figure 4-3**) with a blood circulation half-life of Pt was determined to be 9.5 ± 2.5 h. Our previously reported data showed that OxPt given by i.p. injection showed the highest tumor accumulation at 8 h post injection, with 0.56 ± 0.23 %ID/g.[40]

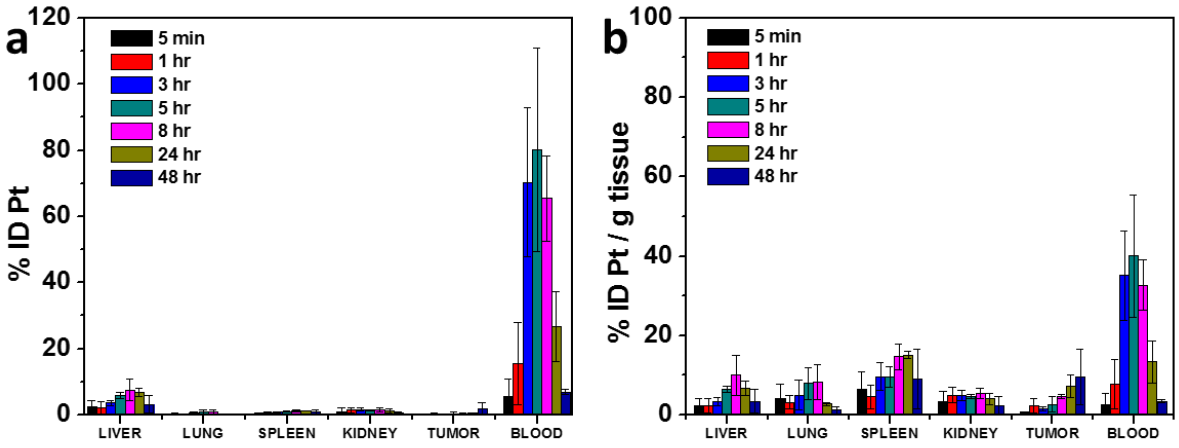

Figure 4-3 Biodistribution, tumor uptake, and blood concentration of Pt over time after i.p. injection of NCP-2/PTX in CT26 tumor-bearing BALB/c mice at a dose of 1.5 mg Pt/kg expressed as (a) %ID or (b) %ID Pt/g tissue.

When moving into larger animals, we found that NCP-2/PTX given by i.v. injection into beagle dogs significantly increases the circulation half-life and the area under the curve (AUC) blood exposure of both Pt and PTX (**Table 4-1**). NCP-2/PTX extends the Pt $t_{1/2\alpha}$ from 0.18 to 0.28 h, respectively, and increases the $AUC_{0\rightarrow\infty}$ by ~2 times (**Figure 4-4**). The PTX half-life is extended from 0.28 to 13.93 h by NCP-2/PTX, leading to an increase of ~100 times in the $AUC_{0\rightarrow\infty}$ (**Figure 4-5**). PTX dropped below the 0.05-0.2 μM threshold for neutropenia within 3 h, whereas the circulating chol-PTX levels after treatment with NCP-2/PTX remained above this threshold for over 2 days (**Figure 4-5**). Importantly, the ratio of Pt : PTX remained consistent within the first 24 h after injection, after which the drugs diverged due to their different clearance rates and differential limits of detection (**Figure 4-6**).

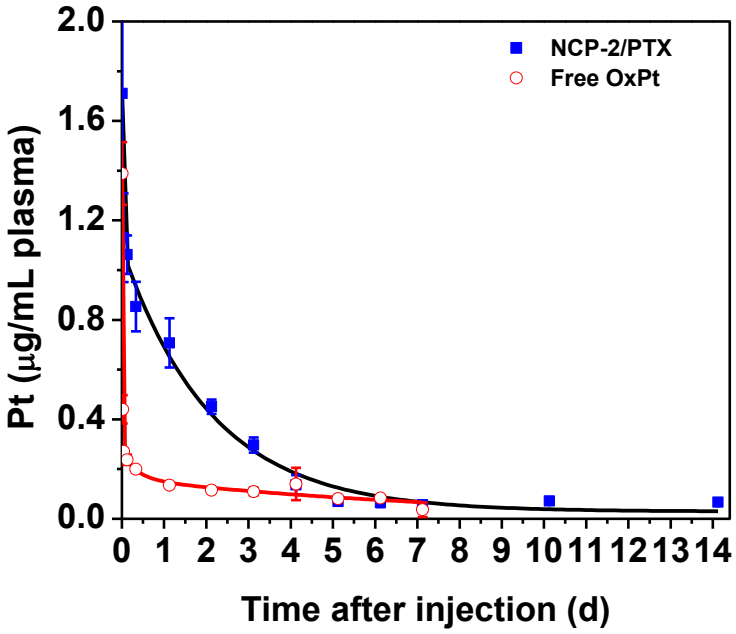

Figure 4-4 Plasma concentration of Pt over time after i.v. injection of NCP-2/PTX or free OxPt into Beagle dogs at equivalent Pt concentrations.

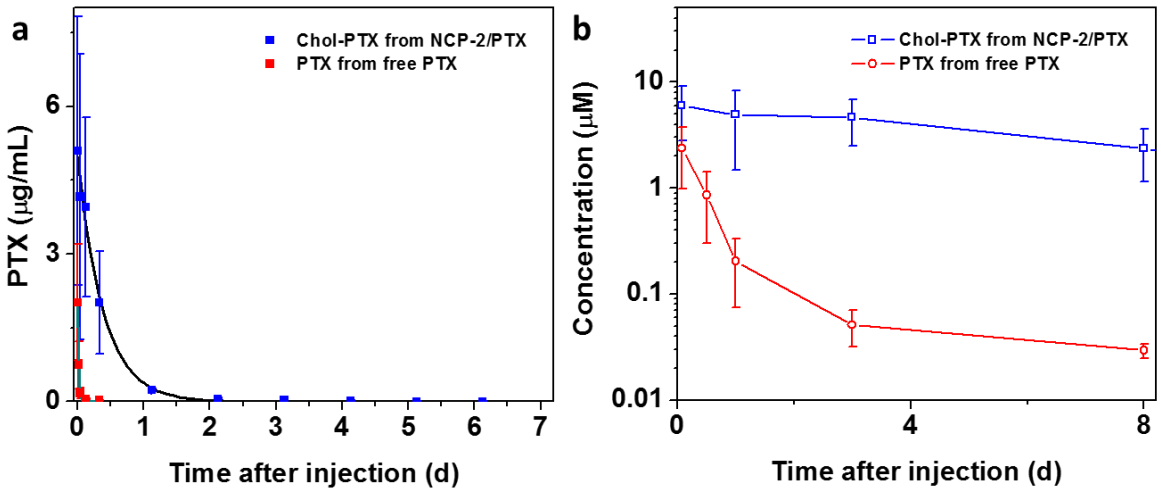

Figure 4-5 Plasma concentration of PTX equivalents over time after i.v. injection of NCP-2/PTX or free PTX into Beagle dogs at equivalent PTX concentrations. The NCP-2/PTX levels were detected as chol-PTX and expressed as equivalent PTX concentrations.

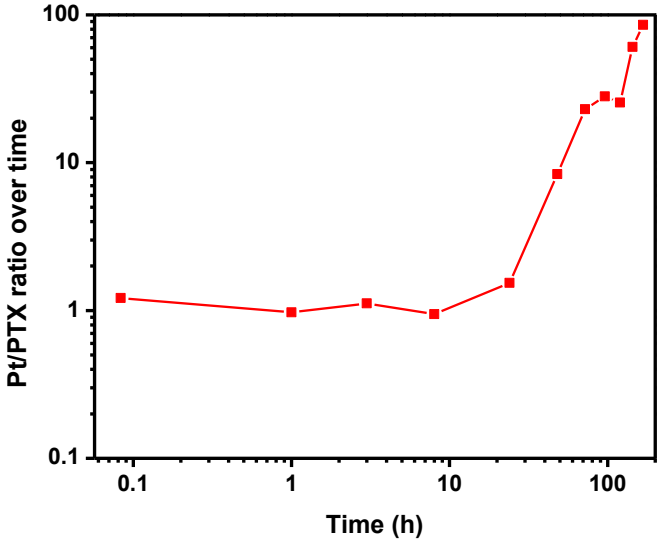

Figure 4-6 Molar ratio of Pt and PTX detected in the plasma after i.v. injection of NCP-2/PTX in Beagle dogs.

Table 4-1 Pharmacokinetic parameters of Pt and chol-PTX/PTX in Beagle dogs.

Parameter (unit)	$t_{1/2\alpha}$ (h)	$t_{1/2\beta}$ (h)	$AUC_{0\rightarrow\infty}$ (μg/mL*h)	AUMC (μg/mL*h^2)	MRT (h)
OxPt[a]	0.18 ± 0.02	94.03 ± 25.54	29.53 ± 8.04	3949.93 ± 2385.91	133.74 ± 37.10
PTX	(0.28 ± 0.07)[b]	–	(10.00 ± 6.10)[b]	(4.02 ± 2.70)[b]	(0.40 ± 0.10)[b]
NCP-2/PTX[a]	0.29 ± 0.18 (11.35 ± 9.57)[c]	37.98 ± 1.22 (16.96 ± 2.18)[c]	59.50 ± 3.85 (1238.18 ± 582.65)[c]	3424.54 ± 152.51 (29070.15 ± 9946.35)[c]	54.50 ± 1.87 (24.33 ± 3.11)[c]

[a] Pt content was used for pharmacokinetic analysis.
[b] The numbers in parentheses refer to PTX.
[c] These numbers were detected as chol-PTX but expressed as PTX equivalent.

4.2.3 PTX metabolism and toxicity

PTX is metabolized by P450 enzymes commonly found in the liver and intestines, yielding hydroxypaclitaxel and subsequently dihydroxypaclitaxel.[3-6] Due to the prevalence of these enzymes in the intestinal epithelium,[3] PTX is not typically used for the treatment of CRC. To this

end, we investigated whether the chol-PTX conjugate can protect PTX from metabolism by these enzymes. The liver of a healthy C57BL/6 mouse was harvested and microsomes were isolated using a Microsome Isolation Kit by BioVision. PTX and chol-PTX were incubated with microsomes in the presence of an NADPH-regenerating system at 37 °C. After 24 h, ethyl acetate was added to extract the chol-PTX and PTX products. PTX and chol-PTX levels were quantified in the organic phase by LC/MS-MS against a standard curve, and compared against samples prepared in the absence of microsomes. Nearly all of the chol-PTX was retained after incubation with the liver microsomes, compared to 54.5% of free PTX (**Figure 4-7**).

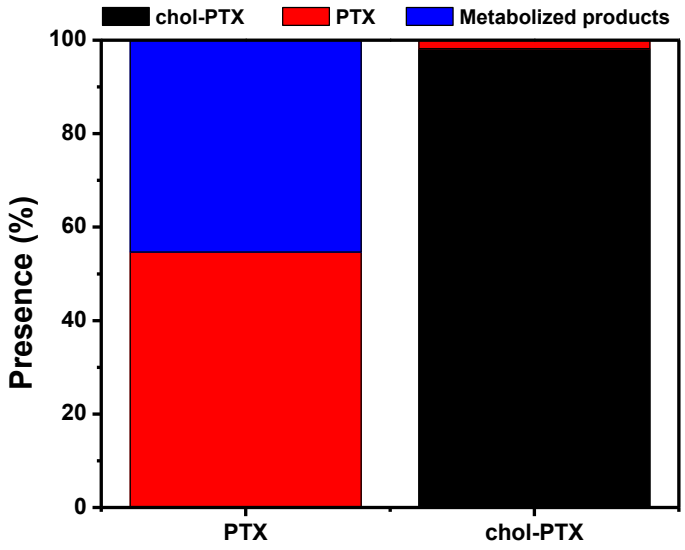

Figure 4-7 PTX and chol-PTX remaining after incubation with liver microsomes and an NADPH-regenerating system for 24 h at 37 °C.

Peripheral neuropathy and neutropenia are the primary toxicities associated with OxPt and PTX, respectively. Due to the decrease in blood exposure of free drugs, these toxicities were

significantly reduced. C57BL/6 mice were intraperitoneally dosed with PBS, OxPt+PTX, or NCP-2/PTX at equivalent doses of 3.0 mg Pt/kg and 13.5 mg PTX/kg. Four days later, the mice were tested for cold sensitivity. Mice were placed on a 3/8" glass plate and allowed to acclimate for several minutes. While the mice were active but at rest, a syringe filled with crushed dry ice was applied to the bottom side of the glass plate directly under a hind paw. The time to paw withdrawal was measured as the peripheral neuropathy of cold sensitivity. After only one dose, OxPt+PTX led to significantly decreased time to paw withdrawal from the cold stimulus compared to PBS (6.15 ± 0.46 vs. 9.02 ± 1.38, p=0.02). NCP-2/PTX showed no significant effect on cold sensitivity relative to PBS (**Figure 4-8**).[41] In MC38 tumor-bearing mice receiving three doses of OxPt+PTX or NCP-2/PTX, blood was collected to determine WBC and neutrophil count according to **Scheme 4-1**. The $CD45^+$ leukocyte count was significantly reduced after treatment with OxPt+PTX compared to both PBS and NCP-2/PTX (p=0.0007 and p=0.0442, respectively, **Figure 4-9**). No difference was observed in mice treated with NCP-2/PTX and with PBS. The neutrophils were gated as SSC^{hi} by FSC/SSC on the $CD45^+$ population and confirmed to be $CD11b^+$ and $Gr\text{-}1^+$. Similar trends were observed in the absolute neutrophil count (ANC) as in the total leukocyte population, with no significant difference observed between PBS and NCP-2/PTX, but a reduction in ANC after treatment with OxPt+PTX (p=0.0005 and p=0.0139, **Figure 4-10**). Together, these data suggest that leukopenia and neutropenia are ameliorated by treatment with NCPs as opposed to free drugs.

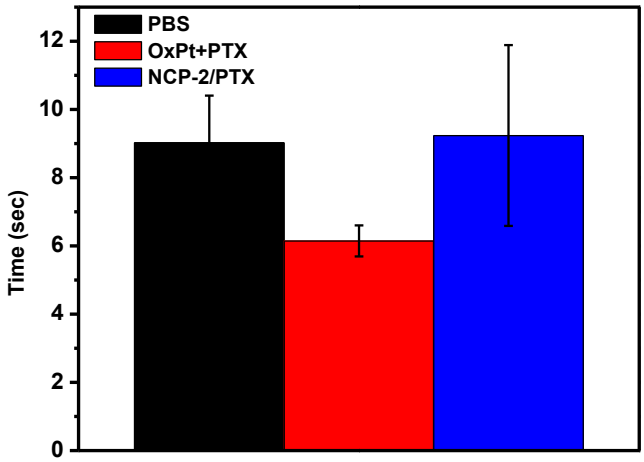

Figure 4-8 Time to paw withdrawal from a cold stimulus applied under the hind paw of C57BL/6 mice dosed once with PBS, OxPt+PTX, or NCP-2/PTX.

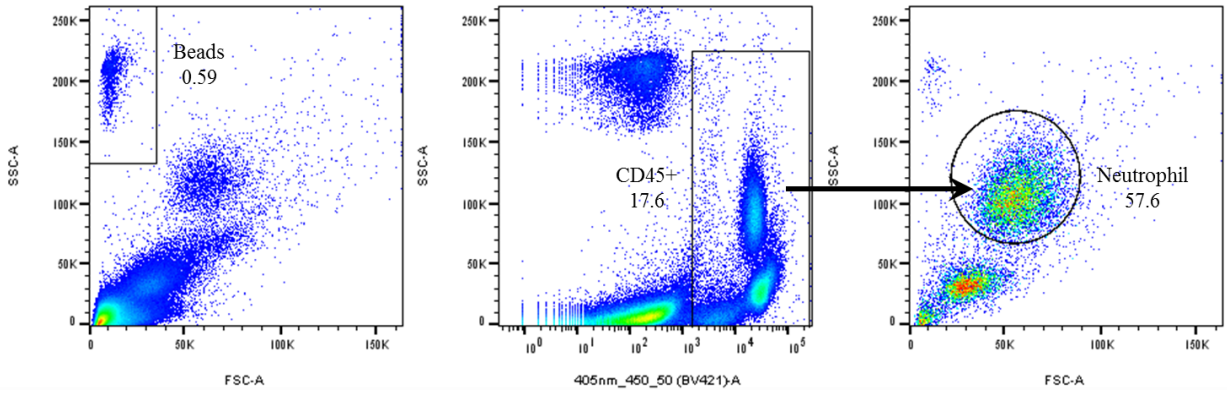

Scheme 4-1 Representative flow cytometry scheme depicting gating strategy to determine leukocyte and neutrophil counts.

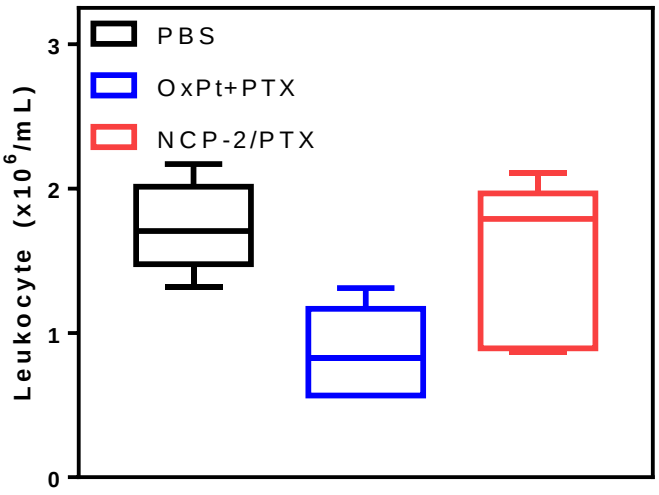

Figure 4-9 Total $CD45^+$ leukocyte counts as determined by flow cytometry after treatment with 3 total doses of PBS, OxPt+PTX, or NCP-2/PTX**.**

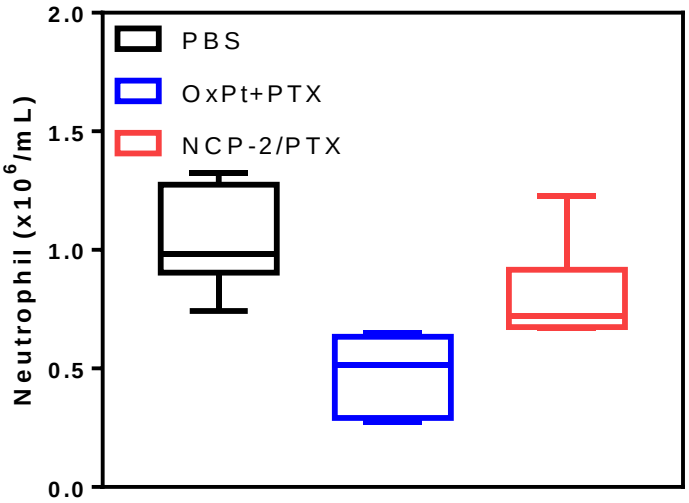

Figure 4-10 Absolute neutrophil counts as determined by flow cytometry after treatment with 3 total doses of PBS, OxPt+PTX, or NCP-2/PTX**.**

4.2.4 Mechanisms of cell death

The cytotoxicity of monotherapeutic NCPs and NCP-2/PTX were investigated in the murine cell lines, CT26 and MC38. PTX dosed with 1% DMSO showed < 10% cell viability at doses in the low-mid nanomolar range, which were not compatible with the cytotoxicity of OxPt in vitro. However, NCPs carrying the chol-PTX conjugate showed IC_{50} values on the same order as both OxPt, and NCP-2 (**Table 4-2**). Importantly, the combination of NCP-2/PTX led to both lower Pt and PTX IC_{50} values. These results were consistent with the early apoptosis and late apoptosis/necrosis induced by treatment. Zn/PTX led to an increase in healthy cells and decrease in apoptotic cells compared to PTX dosed in DMSO. The free drug combination of $Pt(dach)Cl_2$ + PTX induced similar amounts of apoptosis and necrosis to free PTX, whereas NCP-2/PTX led to increased apoptosis and necrosis compared to both NCP-2 and Zn/PTX and consistent with levels in the $Pt(dach)Cl_2$ + PTX treated group (**Table 4-3**, **Figure 4-11**).

Table 4-2 Pt and PTX cytotoxicity values by NCPs in murine colorectal adenocarcinoma cells.

Cell line	OxPt	NCP-2	Zn/PTX	NCP-2/PTX
CT26	7.05 ± 0.95	7.55 ± 0.81	(12.76 ± 5.53)[a]	4.66 ± 1.20 (4.66 ± 1.20)[a]
MC38	3.35 ± 0.13	3.72 ± 0.31	(10.50 ± 2.24)[a]	2.15 ± 0.28 (2.15 ± 0.28)[a]

[a] The numbers in parentheses represent PTX concentrations

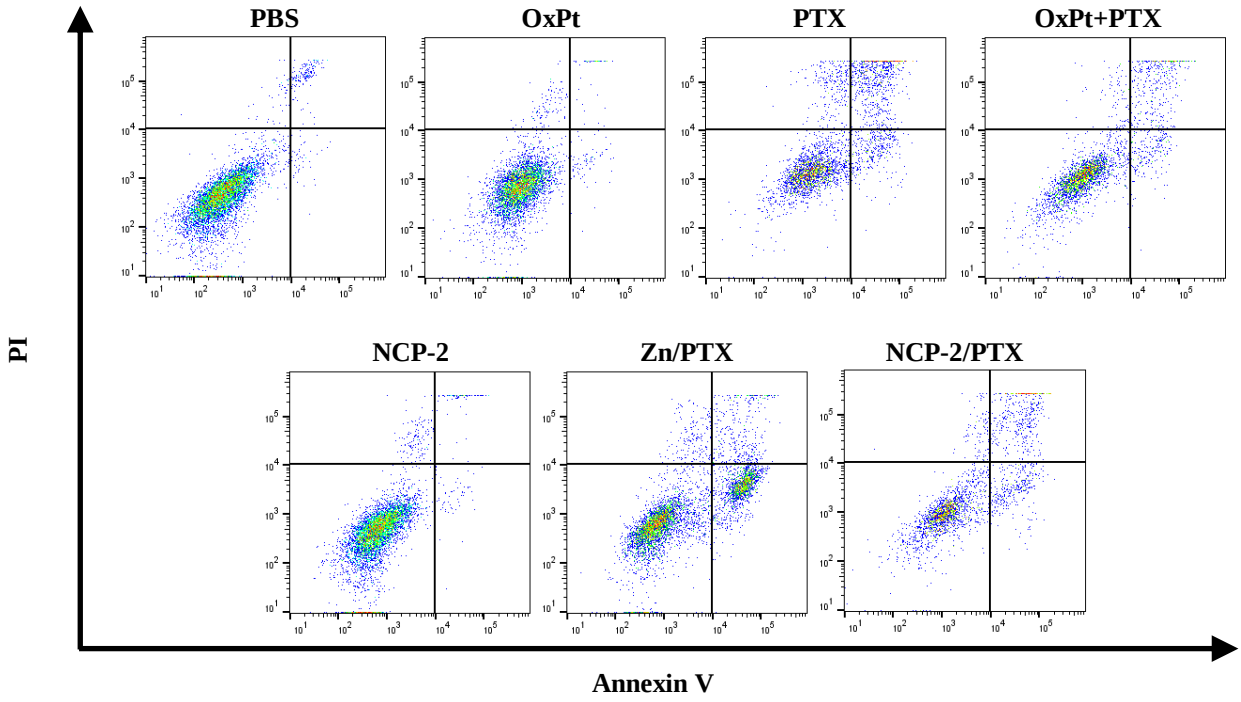

Figure 4-11 Annexin V/PI analysis of CT26 cells incubated with 5 μM OxPt and 5 μM PTX. Quadrants counterclockwise from lower left to upper left represent healthy, early apoptotic, late apoptotic, and necrotic cells, respectively.

Table 4-3 Percentages of healthy, apoptotic, and necrotic CT26 cells incubated with equivalent doses of 5 μM OxPt and/or 5 μM PTX.

	Healthy	**Early apoptotic**	**Late Apoptotic /necrotic**	**Necrotic**
PBS	92.1	2.03	4.97	0.91
Pt(dach)Cl_2	79.6	9.92	7.08	3.37
PTX	37.2	16.3	41.1	5.35
Pt(dach)Cl_2+PTX	42.2	14.4	38.2	5.16
NCP-2	87.0	5.84	6.22	0.91
Zn/PTX	64.7	26.2	6.14	3.02
NCP-2/PTX	46.3	13.7	38.0	1.88

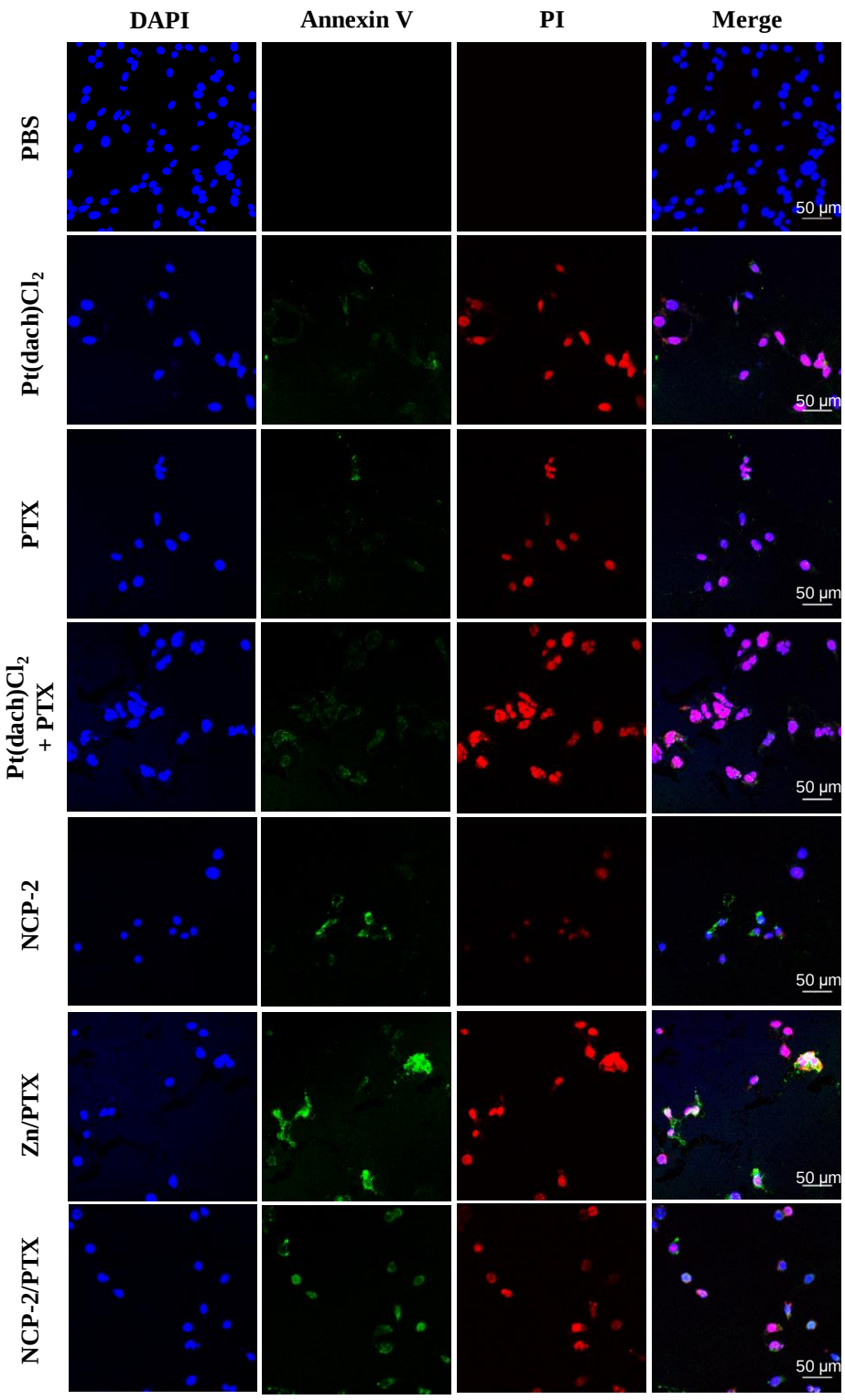

Figure 4-12 CLSM images showing the apoptosis and necrosis of CT26 cells. The first column shows DAPI staining of the nucleus; the second column shows Annexin V staining of apoptotic cells; the third column shows nuclear PI staining in necrotic cells; the fourth column shows the merged images.

Calreticulin (CRT) release from the endosplasmic reticulum and presentation on the cell surface during early apoptosis is an important hallmark of ICD.[35, 36] As OxPt and PTX are two of a handful of FDA-approved chemotherapies known to induce ICD,[35, 36] we first confirmed the cell-surface exposure of CRT in CT26 cells. Cells were treated with PBS, Pt(dach)Cl_2, PTX, OxPt+PTX, NCP-2, Zn/PTX, or NCP-2/PTX and stained with AlexaFluor488-CRT. Similar increases in CRT expression were observed in the free and NCP-treated cells (**Figure 4-13**). The CRT was confirmed to be on the cell-surface by confocal laser scanning microscopy (**Figure 4-14**).

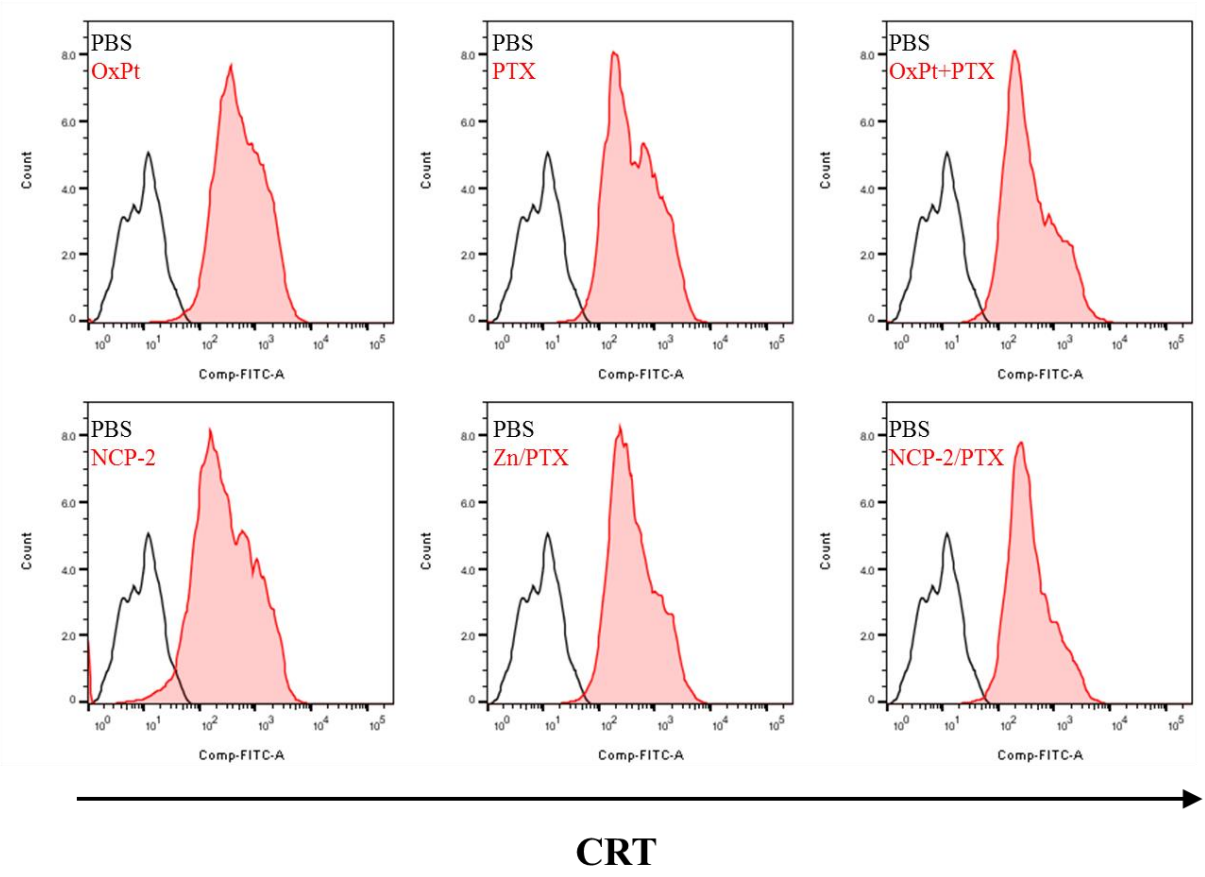

Figure 4-13 Calreticulin (CRT) analysis of CT26 cells incubated with various free drugs or NCPs at equivalent concentrations of 5 μM OxPt and 5 μM PTX.

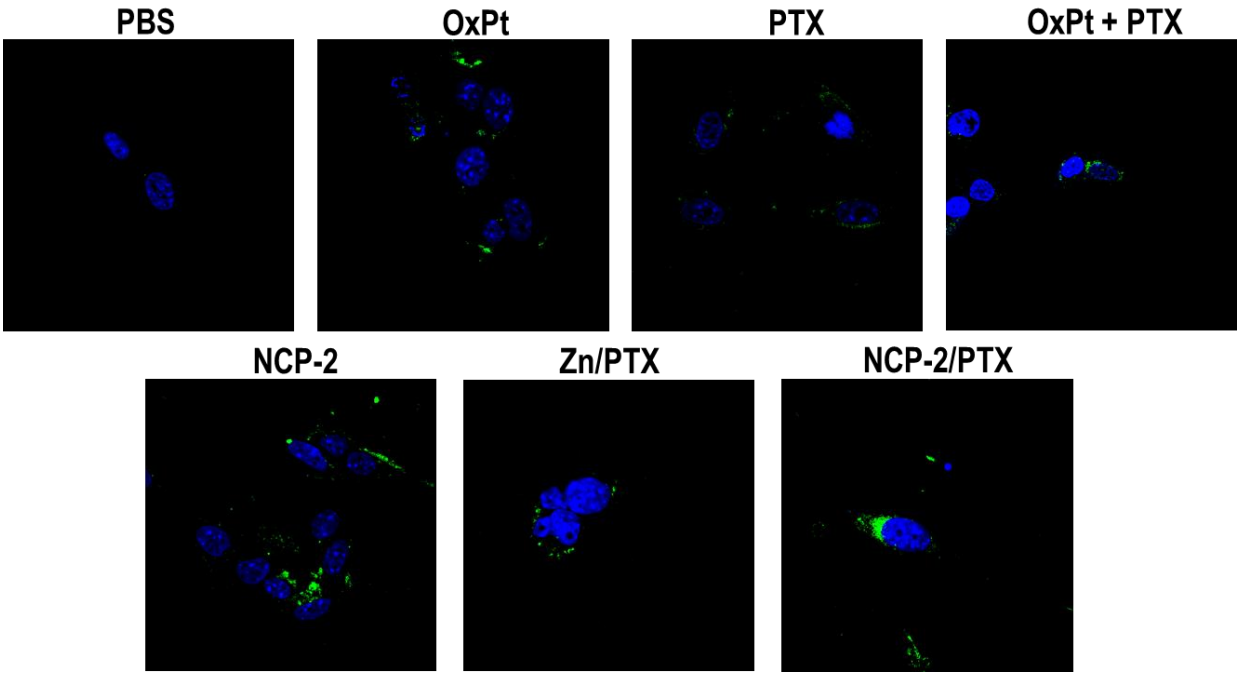

Figure 4-14 CLSM images showing the cell-surface CRT exposure of CT26 cells after treatment with free drugs or NCPs at equivalent concentrations of 5 μM OxPt and 5 μM PTX.

Post-apoptotic HMGB-1 release was quantified by enzyme-linked immunosorbent assay (ELISA) in the cell medium as another marker for ICD. As shown in **Figure 4-15**, the combination of free Pt(dach)Cl_2 and PTX led to significantly increased HMGB-1 release than either Pt(dach)Cl_2 or PTX alone (3.09 ± 0.07 vs 1.22 ± 0.03 and 0.57 ± 0.05 ng/mL for Pt(dach)Cl_2 + PTX, Pt(dach)Cl_2, and PTX respectively). Treatment with NCPs led to similar (NCP-2/PTX vs Pt(dach)Cl_2 + PTX) or increased HMGB-1 release (NCP-2 vs Pt(dach)Cl_2 and Zn/PTX vs PTX).

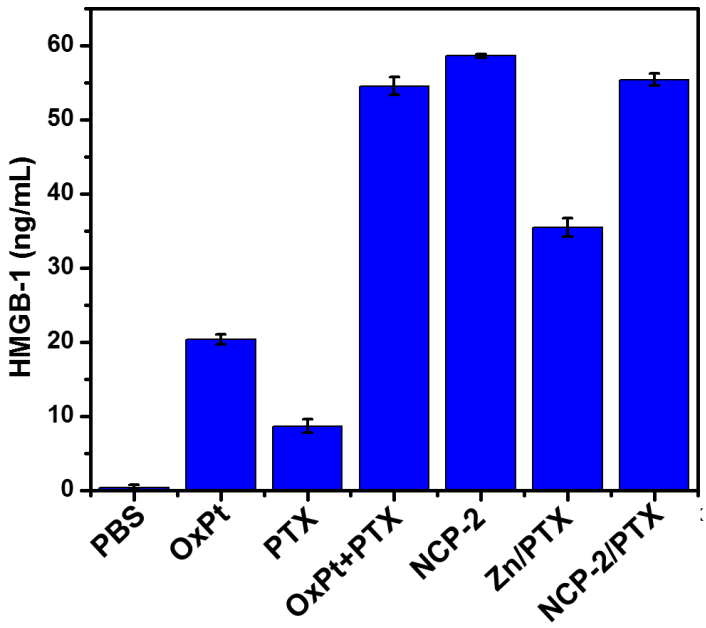

Figure 4-15 HMGB-1 release by CT26 cells after treatment with free drugs or NCPs at equivalent concentrations of 5 μM OxPt and 5 μM PTX.

We confirmed that treatment with NCP-2/PTX could release antigens to initiate an immune response in immunocompotent mice. CT26 cells treated in vitro with $Pt(dach)Cl_2$, PTX, $Pt(dach)Cl_2$ + PTX, NCP-2, Zn/PTX, or NCP-2/PTX at equivalent doses of 20 μM Pt and/or 20 μM PTX. After 24 h, the cells were washed once with PBS, collected, and 2×10^6 cells were inoculated into the right flanks of mice. Two weeks later, the mice were challenged with 5×10^6 live cells on the left flank and the mice were observed for tumor development. None of the free drugs invoked potent vaccination effects at these dose levels; 100% of mice developed tumors within two weeks of tumor challenge. In comparison, 0% of mice vaccinated with NCP-2 or NCP-2/PTX treated cells developed tumors within one month (**Figure 4-16**). NCP-2/PTX treatment of MC38 cells showed similar vaccination effects, with 0% of tumors of mice developing

tumors after vaccination within one month of tumor challenge (**Figure 4-17**). However, when the same NCP-2/PTX treated cells were inoculated into immunocompromised $Rag2^{-/-}$ mice lacking mature B and T cells, the vaccination showed no effects with 100% tumor formation within 5 days of tumor challenge (**Figure 4-18**).

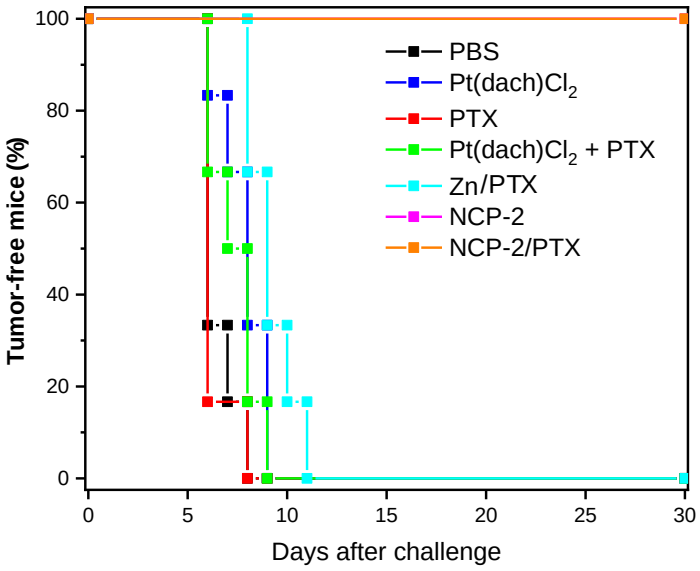

Figure 4-16 In vivo anticancer vaccination of NCP-2/PTX with treated CT26 cells in immunocompotent BALB/c mice.

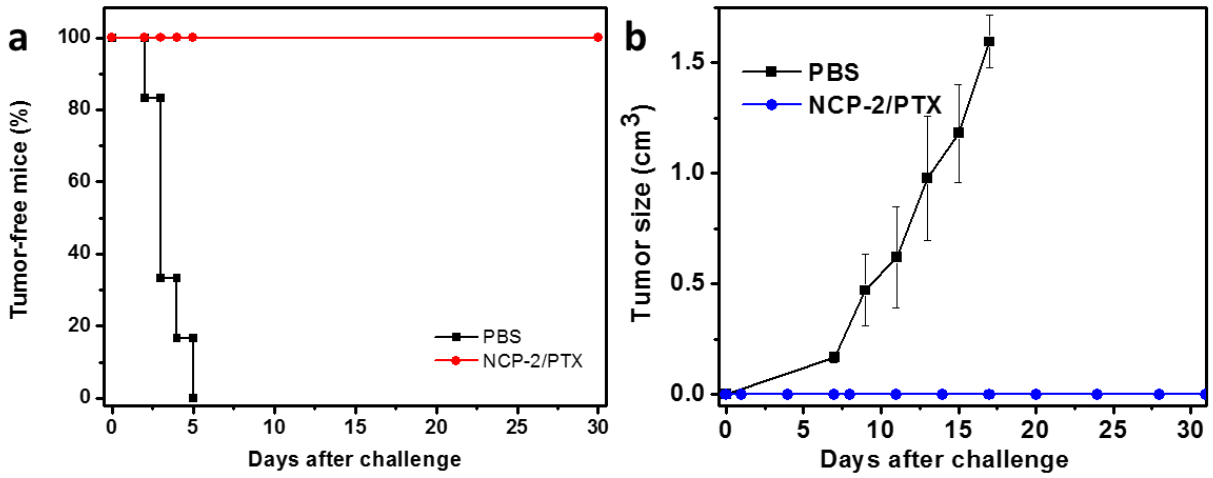

Figure 4-17 (a) In vivo anticancer vaccination of NCP-2/PTX with treated MC38 cells in immunocompetent C57BL/6 mice. (b) Tumor growth curves in mice after vaccination.

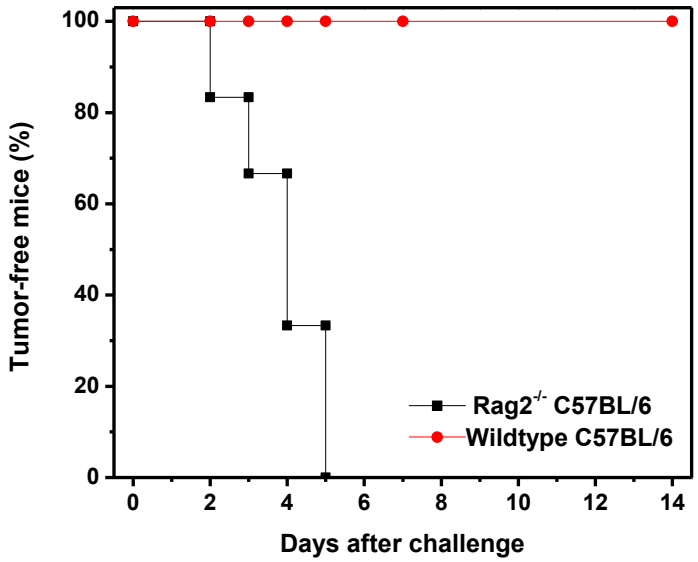

Figure 4-18 Tumor-free survival of wildtype immunocompetent or Rag2$^{-/-}$ immunocompromised C57BL/6 mice after vaccination with NCP-2/PTX-treated MC38 cells.

4.2.5 Anticancer efficacy

Due to promising signs of ICD by NCP-2/PTX in vitro, we investigated the combination of NCP-2/PTX and anti-PD-L1 on the murine colorectal tumor models, CT26 and MC38. 2×10^6

CT26 cells were inoculated onto the right flanks of BALB/c and mice were randomly divided into groups and treated with PBS, OxPt + PTX, NCP-2/PTX, or NCP-2/PTX + anti-PD-L1 beginning 7 days after treatment at equivalent doses of 0.51 mg Pt/kg and 2.14 mg PTX/kg when the tumors reached ~80-120mm^3. Mice were treated with 11 total doses of NCP-2/PTX and/or anti-PD-L1, leading to significantly delayed tumor growth, with survival for up 42 and 50 days after the first treatment, compared to 10 days for PBS (**Figure 4-19**). Interestingly, NCP-2/PTX showed no effect on CT26 tumor-bearing immunocompromised athymic nude or Rag2$^{-/-}$ Balb/c mice at the same doses (**Figure 4-20**). In the MC38 model, treatment with NCP-2/PTX or NCP-2/PTX + anti-PD-L1 extended survival for 28 and 40 days, respectively (**Figure 4-21**). The inferior results on MC38 compared to CT26 are likely related to the more suppressive tumor immune microenvironment in the latter at the time of treatment.[42]

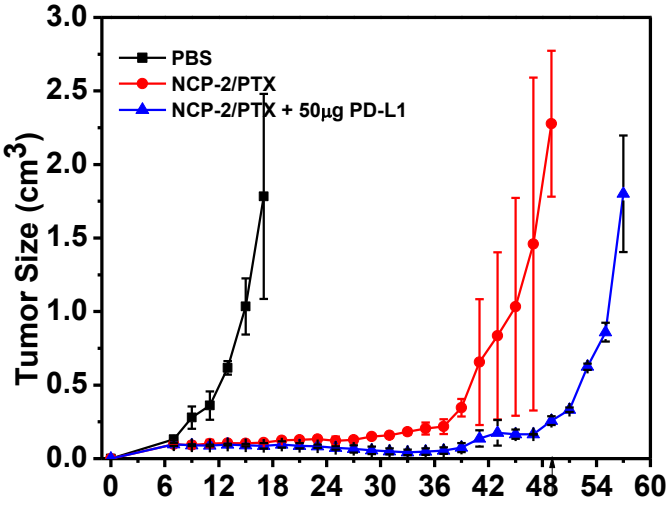

Figure 4-19 Tumor growth curves of CT26 tumor-bearing BALB/C mice after treatment with PBS or NCP-2/PTX with or without anti-PD-L1 beginning on day 7 after tumor inoculation.

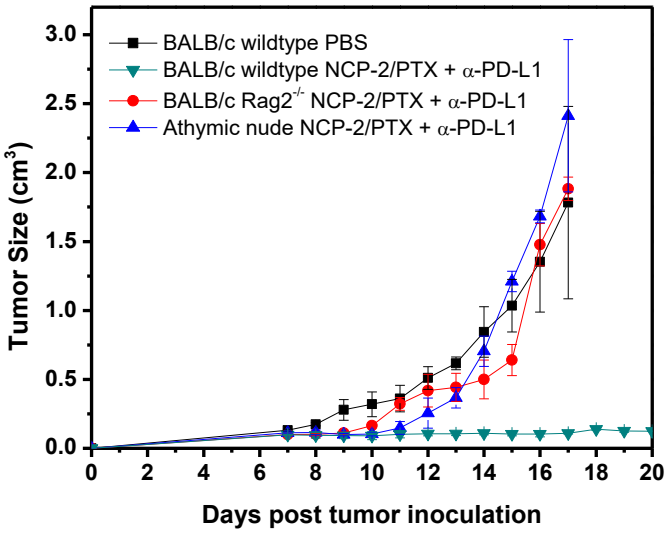

Figure 4-20 Tumor growth curves of CT26 tumor-bearing mice of different backgrounds after treatment with NCP-2/PTX+anti-PD-L1 beginning on day 7 after tumor inoculation.

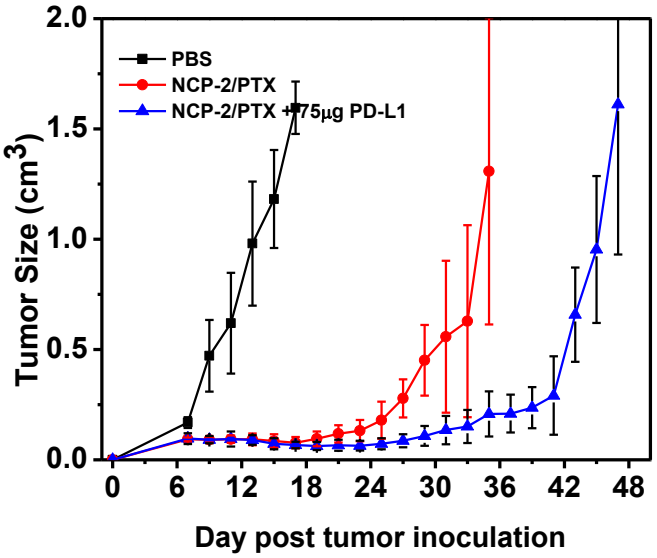

Figure 4-21 Tumor growth curves of MC38 tumor-bearing C57BL/6 mice after treatment with PBS or NCP-2/PTX with or without anti-PD-L1 beginning on day 7 after tumor inoculation.

To determine whether these effects could be recapitulated in increasingly immunosuppressive tumor microenvironments, tumors were allowed to grow longer before the start of treatment. 1×10^6 MC38 cells were inoculated onto the right flanks of C57BL/6 mice and harvested when the tumors reached ~80-120 mm^3 approximately 12 days after tumor inoculation. Though the size was approximately the same as tumors 7 days after inoculating 2×10^6 MC38 cells, the tumor infiltrating leukocyte (TIL) population was significantly different (**Figure 4-22**). The overall $CD45^+$ population was significantly lower (p=0.0022) in tumors at day 12 compared to day 7. There were significantly fewer NK cells in tumors at day 12 compared to day 7 (p=0.0201), fewer DCs (p=0.0013), and increased PD-$L1^+$ DCs (p=0.0002, **Figure 4-22**, **Figure 4-23**). There was no significant difference observed in the proportion of macrophages or myeloid derived suppressor cells (MDSCs) in the tumors between the two groups. Furthermore, though there was no significant difference in $CD4^+$ or $CD8^+$ T cells, both the proportion of PD-1^+ $CD4^+$ and PD-1^+CD8^+ cells increased significantly, indicating T cell exhaustion (**Figure 4-22**, **Figure 4-23**).

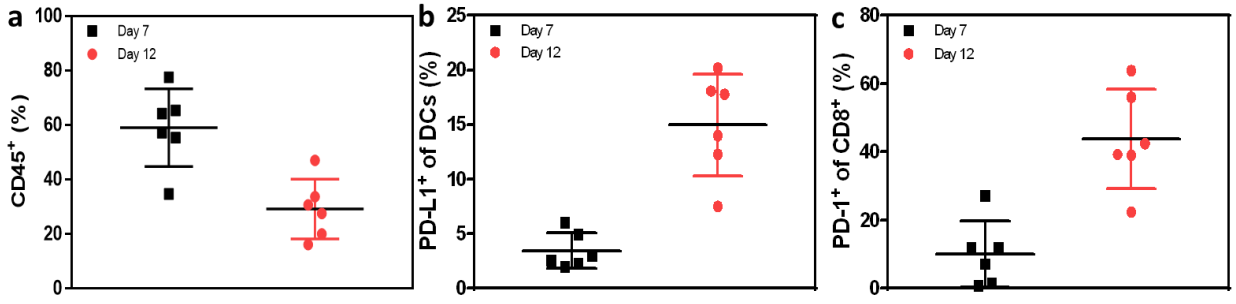

Figure 4-22 Immune profile of (a) $CD45^+$, (b) PD-L1+ DCs, and (c) PD-1^+ $CD8^+$ T cells in MC38 tumors 7 and 12 days after tumor inoculation shows a more suppressive environment develops over time.

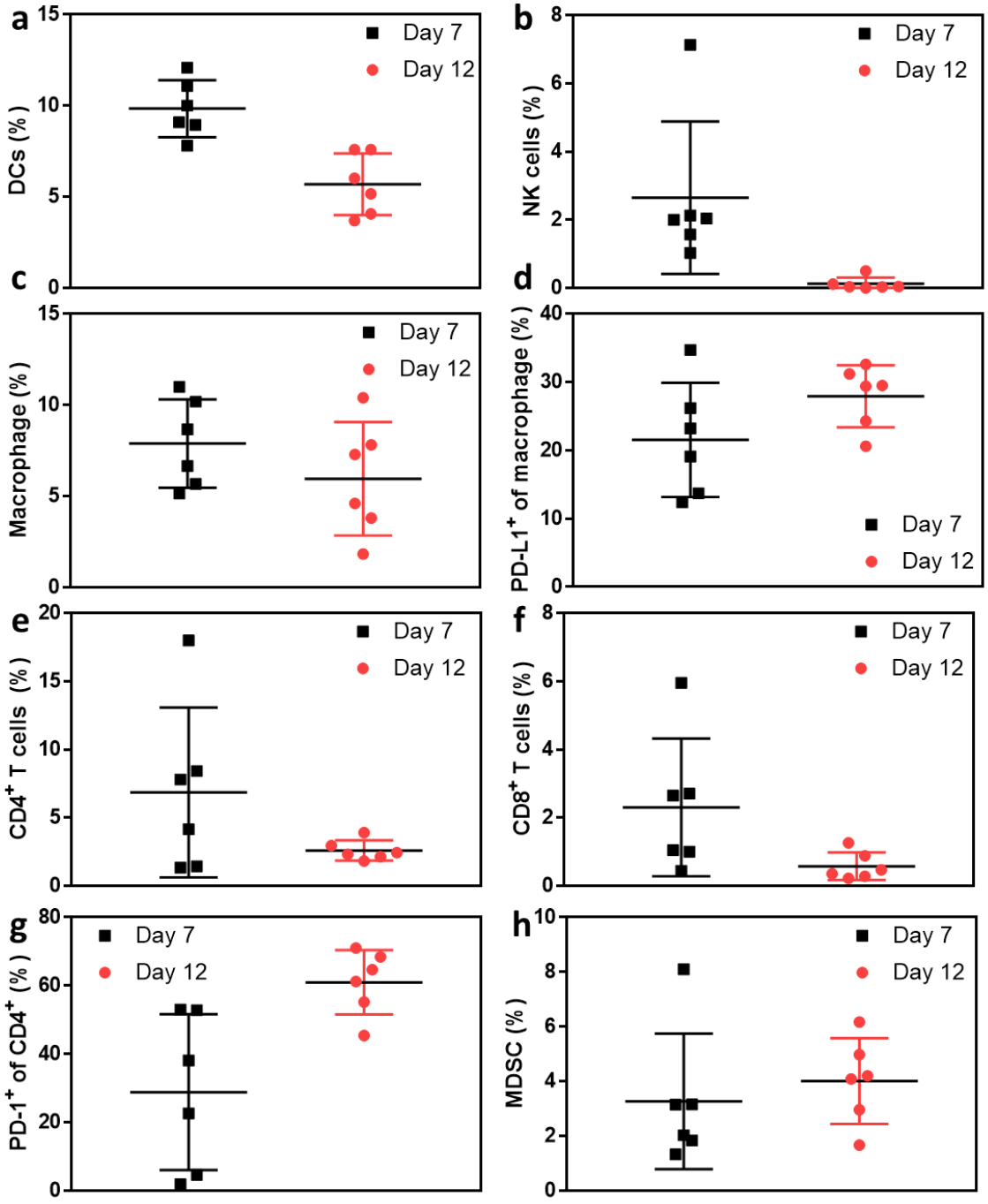

Figure 4-23 TILs in MC38 tumors 7 or 12 days after tumor inoculation. (a) Dendritic cells: $CD45^+CD11b^+F4/80^-CD11c^+$ of live cells; (b) NK cells: $CD45^+CD3\varepsilon^-NKp46^+$ of live cells; (c) Macrophages: $CD45^+CD11b^+F4/80^+$ of live cells; (d): PD-$L1^+$ of macrophages; (e) $CD4^+$ T cells: $CD45^+CD3\varepsilon^+CD4^+$ of live cells; (f) $CD8^+$ T cells: $CD45^+CD3\varepsilon^+CD8^+$ of live cells; (g) PD-1^+ of $CD4^+$ T cells; (h) MDSC: $CD45^+CD11b^+Gr\text{-}1^+Ly6C^{hi}$ of live cells.

Using the more immunosuppressive day 12 tumor model, NCP-2/PTX alone showed no significant tumor growth inhibition in either CT26 or MC38 tumor-bearing mice. However, the combination with anti-PD-L1 significantly controlled tumor growth in both models, with 92.7% and 94.1% tumor growth inhibition, defined as 1-(RTV_t/RTV_c) where RTV = endpoint tumor volume – starting tumor volume (**Figure 4-24**). Increasing the dose to 1.03 mg Pt/kg and 4.3 mg PTX/kg for each injection in MC38 tumor-bearing mice significantly enhanced the tumor growth inhibition, with or without the addition of anti-PD-L1. Interestingly, particles containing 1.03 mg Pt/kg and 2.14 mg PTX/kg at a 2:1 Pt : PTX molar ratio (**Figure 4-25, Figure 4-26**) reduced toxicity without compromising anticancer efficacy (**Figure 4-27**). The Pt drug alone in NCP-2 at 1.03 mg Pt/kg was not sufficient to reproduce the tumor growth inhibition. The combination with an equivalent 75 μg anti-PD-1 dose showed less synergy with NCP-2/PTX, resulting in less sustained tumor control. Zn/PTX by itself and the combination of free drugs (OxPt + PTX + anti-PD-L1) at equivalent doses showed nearly no anticancer efficacy (**Figure 4-28**).

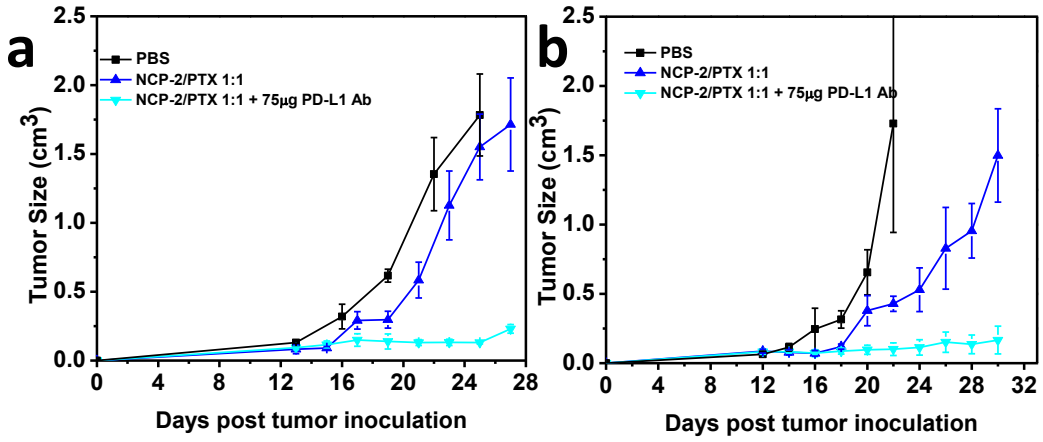

Figure 4-24 Tumor growth curves of (a) CT26 tumor-bearing BALB/c and (b) MC38 tumor-bearing C57BL/6 mice after treatment with PBS or NCP-2/PTX with or without anti-PD-L1 beginning day 12 after tumor inoculation.

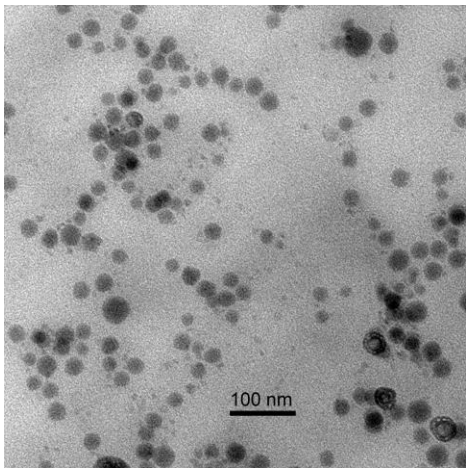

Figure 4-25 TEM image of NCP-2/PTX at a 2:1 molar drug ratio showing the approximate size and shape of the spherical nanoparticles. Bar = 100 nm.

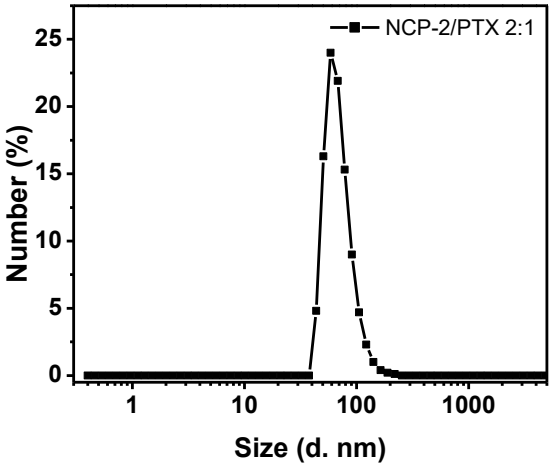

Figure 4-26 Number-average size distribution of NCP-2/PTX at 2:1 molar drug ratio in H_2O.

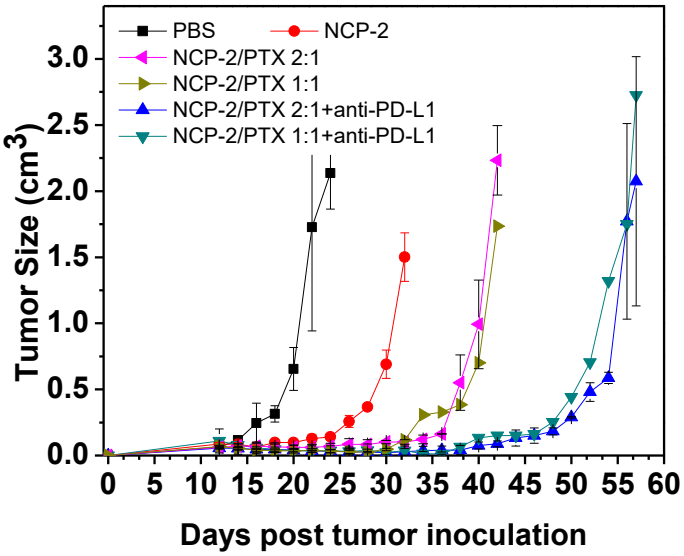

Figure 4-27 Tumor growth curves of MC38 tumor-bearing C57BL/6 mice after treatment with PBS, NCP-2, or NCP-2/PTX with or without anti-PD-L1 beginning on day 12 after tumor inoculation.

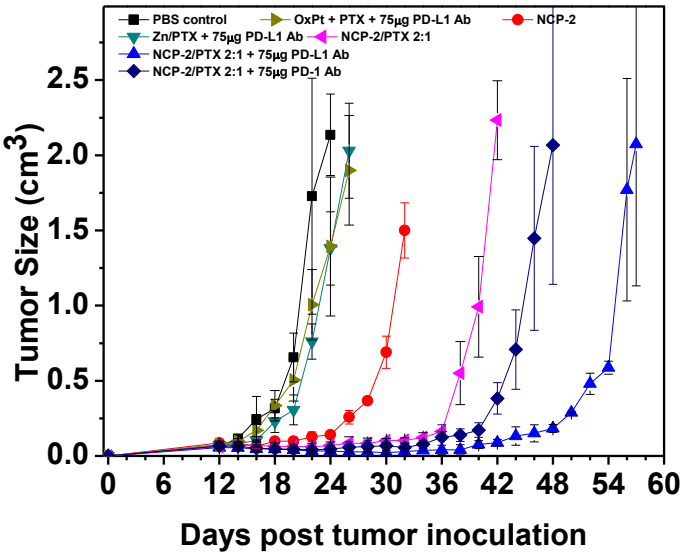

Figure 4-28 Tumor growth curves of MC38 tumor-bearing C57BL/6 mice after treatment with PBS, OxPt+PTX+anti-PD-L1, Zn/PTX+anti-PD-L1, NCP-2, or NCP-2/PTX with or without anti-PD-L1 beginning on day 12 after tumor inoculation.

4.2.6 Antitumor immunity

Due to the well-known ICD properties of OxPt and PTX, we investigated the antitumor immunity induced by NCP-2/PTX in combination with anti-PD-L1 in the syngeneic day 12 MC38 model by flow cytometry. Mice were treated with 3 doses of OxPt + PTX + anti-PD-L1, NCP-2/PTX, or NCP-2/PTX + anti-PD-L1 once every four days and euthanized 24 days after tumor inoculation. There was no significant difference in the proportion of $CD45^+$ cells in tumors with or without treatment, but the makeup of the immune cells changed. NCP-2/PTX + anti-PD-L1 significantly decreased the MDSC population compared to PBS or the combination of OxPt + PTX + anti-PD-L1 (**Figure 4-29a,b**). 50% of mice (3/6) treated with OxPt + PTX + anti-PD-L1 or NCP-2/PTX + anti-PD-L1 showed an increase in the $CD4^+$ T cell population, with no significant difference in the average (**Figure 4-29c**). NCP-2/PTX + anti-PD-L1 also led to an increase in $CD8^+$ T cells in 83% of mice (5/6) compared to PBS or OxPt + PTX + anti-PD-L1 (**Figure 4-29d**).

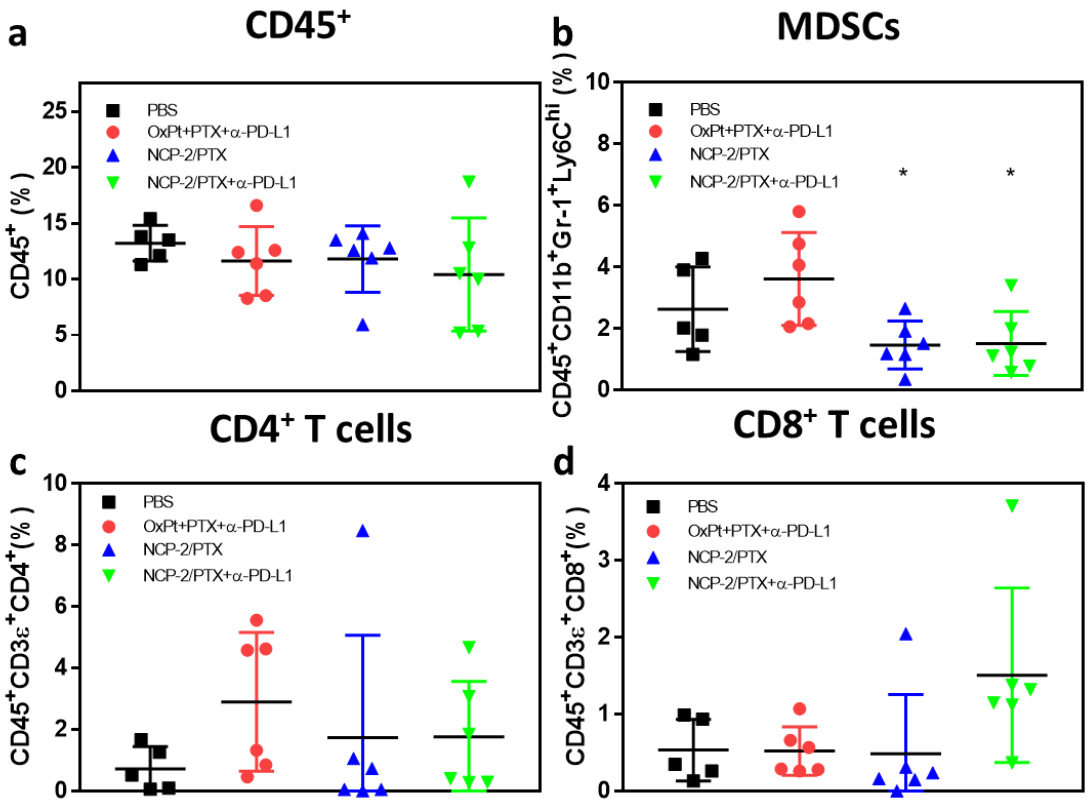

Figure 4-29 Tumor infiltrating leukocytes in MC38 tumors treated once every 4 days beginning 12 days after tumor inoculation for a total of 3 doses. 24 days after tumor inoculation, the tumors were collected to measure the tumor infiltrating lymphocytes (a) $CD45^+$, (b) MDSCs, (c) $CD4^+$ T cells, and (d) $CD8^+$ T cells.

4.3 Conclusion

We have developed an NCP combining an OxPt analogue and PTX for chemoimmunotherapy of colorectal cancers in combination with the checkpoint inhibitor, anti-PD-L1. NCP-2/PTX significantly improves the pharmacokinetics of both drugs by extending the half-lives and improving the areas under the curve. The prodrug and its encapsulation into NCPs also allowed for the use of PTX in CRCs by overcoming metabolism by P450s in the intestines and ameliorated the toxicities of peripheral neuropathy and neutropenia. The two chemotherapies are both inducers of immunogenic cell death, which can stimulate the immune system and recruit T cells. Combining

NCP-2/PTX with anti-PD-L1 can also decrease the presence of the MDSCs. In syngeneic CT26 and MC38 models treated early, NCP-2/PTX plus anti-PD-L1 can significantly delay tumor growth progression. However, more developed tumors contain fewer immunostimulatory factors and more suppressive immune mechanisms including PD-L1^{+} DCs and PD-1^{+} T cells. As a result, higher doses of NCP-2/PTX are required for efficient anticancer efficacy. We believe our NCPs carrying Pt and PTX prodrugs can thus overcome many of the current pitfalls facing chemotherapy and enhance immune checkpoint inhibitors for CRC anticancer efficacy.

4.4 Materials and methods

Materials, cell lines, and animals. All starting materials were purchased from Sigma-Aldrich and Fisher (USA) unless otherwise noted and used without further purification. DOPA), cholesterol, and DSPE-PEG2k were purchased from Avanti Polar Lipids (USA).

Murine colon adenocarcinoma cell CT26 and MC38 cells were obtained from the American Type Culture Collection (ATCC, Rockville, MD). CT26 cells were cultured in RPMI 1640 and MC38 were cultured in Dulbecco's Modified Eagle's Medium (DMEM), respectively, supplemented with 10% FBS, 100 U/mL penicillin G sodium and 100 μg/mL streptomycin sulfate in a humidified atmosphere containing 5% CO2 at 37^{o}C. Mycoplasma was tested before use by MycoAlert detection kit (Lonza Nottingham, Ltd.).

BALB/c female mice (6 weeks, 18-22 g), C57BL/6 female mice (6 weeks, 18-22 g), and Rag$^{2-/-}$ female mice (6 weeks, 18-22 g) were provided by Harlan-Envigo Laboratories, Inc (USA). Beagle dogs (7-9 kg) were kindly provided by the Illinois Institute of Technology after a washout period. We have complied with all ethical regulations for animal testing and research, with study

protocols reviewed and approved by the Institutional Animal Care and Use Committee (IACUC) at the University of Chicago.

***In vivo* pharmacokinetics and biodistribution analysis in tumor-bearing mice.** BALB/c mice were subcutaneously injected in the right flank with 2×10^6 CT26 cells. When the tumors reached ~100 mm^3, mice were intraperitoneal (i.p.) administration of NCP-2/PTX at a Pt dose of 1.54 mg/kg (6.73 mg/kg PTX). Mice were euthanized at pre-determined time points (5 min, 1 h, 3 h, 5 h, 8 h, 24 h, and 48 h post-injection). The blood, livers, lungs, spleens, kidneys, bladders and tumors were also harvested, digested with concentrated nitric acid for 48 h, and analyzed for Pt concentration by ICP-MS.

***In vivo* pharmacokinetics in Beagle dogs**. Beagles were intravenously (i.v.) injected with OxPt, PTX, or NCP-2/PTX at equivalent Pt doses of 0.51 mg/kg and 2.24 mg/kg PTX. The blood was collected at 5 min, 1 h, 3 h, 8 h, 24 h, 72 h, 96 h, 120 h, 144 h, and 168 h post-injection and centrifuged at 604 xg for 10 min to harvest the plasma. 25 μL plasma was digested with concentrated nitric acid for 24 h and analyzed for Pt concentration by ICP-MS. Another 25 μL plasma was added 5 μL 20% Triton X-100 to disrupt the lipid bilayer of the nanoparticles, chol-PTX was then extracted from plasma by adding 100 μL ethyl acetate, followed by centrifugation at 6708 xg for 10 min. The chol-PTX content was quantified by LC-MS.

Metabolism of PTX by liver microsomes. The liver of a healthy C57BL/6 mouse was homogenized and processed with a Microsome Isolation Kit (BioVision, Milvitas, CA). The microsome solution was measured for protein content with a Pierce BCA Protein Assay Kit. 0.1 mg microsome was added to a 10 nmol PTX or chol-PTX suspension in the presence of 1.0 mM EDTA, 0.1 M K_3PO_4, 50 mM $MgCl_2$, 0.1 μM NADPH, and 1 U/mL glucose-6-phosphate and incubated for 24 h at 37 °C.

Peripheral neuropathy. Healthy wildtype C57BL/6 mice were i.p. injected with PBS, OxPt + PTX, or NCP-2/PTX. Four days later, the mice were placed onto a 3/8" glass plate and allowed to acclimate for at least 10 minutes. The end of a syringe was removed and the syringe was filled with compacted ground dry ice. The dry ice tube was applied to the underside of the glass plate beneath a hind paw until the paw was removed or for 20 sec, whichever came first. The time to paw removal was recorded, with at least 4 trials per mouse and at least 5 minutes between each test.

White blood cell and neutrophil count. MC38 tumor-bearing C57BL/6 mice were treated with PBS, OxPt + PTX, or NCP-2/PTX i.p. once every four days for three total doses. Four days after the third dose, 50 μL blood was harvested from each mouse and added to a BD Trucount tube containing a bead with fluorescently-conjugated CD45 (30-F11), CD11b (M1/70), and Gr-1 (RB6-8C5) antibodies according to manufacturer's instructions with 500 μL ACK lysis buffer for flow cytometry. LSR FORTESSA (BD Biosciences) was used for cell acquisition, and data analysis

was carried out using FlowJo software (TreeStar, Ashland, OR). All antibodies were diluted 1:200 for use.

***In vitro* cytotoxicity.** CT26 cells or MC38 cells were seeded in 96-well plates at a density of 2 $\times 10^3$ cells per well and allowed to adhere for 24 h. Cells were then treated with different concentrations of free drugs or nanoparticles for another 72 h. Cell viability was detected by 3-(4,5-dimethylthiazol-2-yl)-5-(3-carboxymethoxyphenyl)-2-(4-sulfophenyl)-2H-tetrazolium (MTS) assay (Promega, Madison, WI) according to the manufacturer's instructions.

Cell apoptosis. CT26 cells seeded in 6-well plates (5×10^4 cells/well) were free drugs or nanoparticles at a dose of 5 μM Pt and/or 5 μM PTX. After 24 h, the cells were harvested, washed twice with ice-cold PBS, stained with Alexa Fluor 488-Annexin V and propidium iodide (PI) for 15 min at room temperature in the dark, and then analyzed by flow cytometry (LSR II, BD, USA).

CRT exposure analysis. CT26 cells seeded in 6-well plates (2×10^5 cells/well) were cultured with free drugs or nanoparticles at a dose of 5 μM Pt and/or 5 μM PTX for 24 h. The treated cells were collected, incubated with Alexa Fluor 488-CRT antibody (Enzo cat # ADI-SPA-601-488-F, diluted 1:100) for 2 h, stained with PI, and analyzed by flow cytometer to identify CRT exposure. The fluorescence intensity of stained cells was gated on PI^- cells.

For surface detection of CRT, CT26 cells were seeded on 10 mm^2 glass coverslips placed in 6-well plates at a density of 2×10^5 cells per well. After treatment, cells were washed with PBS

three times, incubated with Alexa Fluor 488-CRT antibody (diluted 1:100) for 2 h, stained with DAPI, and observed under CLSM using 405 nm and 488 nm lasers for visualizing nuclei and CRT expression on the cell membrane, respectively.

Detection of HMGB-1 release. CT26 cells seeded in 6-well plates (2×10^5 cells/well) were cultured with free drugs or nanoparticles at a dose of 5 μM Pt and/or 5 μM PTX for 24 h. The medium was collected for detection of HMGB-1 release by ELISA according to manufacturer instructions (Chondrex, Redmond, WA).

Antitumor vaccination. 1×10^6 CT26 or MC38 cells treated with 10 μM Pt and/or 10 μM PTX for 24 h were subcutaneously inoculated into the lower flank of 6-week-old female BALB/c wildtype mice, C57Bl/6 wildtype or $Rag^{2-/-}$ mice. Seven days later, 2×10^6 living CT26 or MC38 cells were inoculated into the contralateral flank. Mice were then monitored for the appearance of tumors for 30 days.

***In vivo* anticancer efficacy.** 2×10^6 cells CT26 or MC38 cells were subcutaneously injected into the right flank region of 6-week athymic nude mice, BALB/c wildtype or $Rag2^{-/-}$ mice, and C57Bl/6 wildtype mice, respectively. 7 days after tumor inoculation, mice were i.p. dosed with 0.51 mg/kg Pt, 2.24 mg/kg PTX, and 50 or 75 μg antibody. 1×10^6 cells CT26 or MC38 cells were subcutaneously injected into the right flank region of 6-week BALB/c wildtype mice and C57Bl/6 wildtype mice, respectively. 12 days after tumor inoculation, mice were i.p. dosed with 0.51 or 1.02 mg/kg Pt, 2.24 or 4.49 mg/kg PTX, and 50 or 75 μg antibody. Tumor growth was monitored

by measurement with a digital caliper, where tumor volumes were calculated as follows: $(\text{width}^2 \times \text{length})/2$.

Flow cytometry assay for immune response. Tumors were harvested 7 or 12 days after tumor inoculation, treated with 1 mg/mL collagenase I (Gibco™, USA) for 1 h, and ground with the rubber end of a syringe. Cells were filtered through nylon mesh filters and washed with PBS. The single-cell suspension was incubated with yellow to distinguish live/dead cells followed by anti-CD16/32 (clone 93; eBiosciences) to reduce nonspecific binding to FcRs. Cells were further stained with the following fluorochrome-conjugated antibodies: CD45 (30-F11), CD3ε (145-2C11), CD8 (53-6.7), CD4 (GK1.5), CD11b (M1/70), CD11c (N418), F4/80 (BM8), PD-1 (RMP1-30), PD-L1 (10F.9G2), and Gr-1 (RB6-8C5) for flow cytometry. LSR FORTESSA (BD Biosciences) was used for cell acquisition, and data analysis was carried out using FlowJo software (TreeStar, Ashland, OR). All antibodies were diluted 1:200 for use.

4.5 References

1. Einzig, A.I. et al. Phase II Trial of Paclitaxel in Patients with Advanced Colon Cancer Previously Untreated with Cytotoxic Chemotherapy: An Eastern Cooperative Oncology Group Trial (PA286). *Am J Ther* **3**, 750-754 (1996).
2. Chao, Y. et al. Phase II and pharmacokinetic study of paclitaxel therapy for unresectable hepatocellular carcinoma patients. *Br J Cancer* **78**, 34-39 (1998).
3. Xie, F., Ding, X. & Zhang, Q.Y. An update on the role of intestinal cytochrome P450 enzymes in drug disposition. *Acta Pharm Sin B* **6**, 374-383 (2016).
4. Habano, W. et al. Involvement of promoter methylation in the regulation of Pregnane X receptor in colon cancer cells. *BMC Cancer* **11**, 81 (2011).
5. Nakumura, T. et al. Gene expression profiles of ABC transporters and cytochrome P450 3A in Caco-2 and human colorectal cancer cell lines. *Pharm Res* **20**, 324-327 (2003).

6. Martinez, C., Garcia-Martin, E., Pizarro, R.M., Garcia-Gamito, F.J. & Agundez, J.A. Expression of paclitaxel-inactivating CYP3A activity in human colorectal cancer: implications for drug therapy. *Br J Cancer* **87**, 681-686 (2002).

7. Kumar, G. et al. Comparative in vitro cytotoxic effects of taxol and its major human metabolite 6 alpha-hydroxytaxol. *Cancer Chemother Pharmacol* **36**, 129-135 (1995).

8. Spratlin, J. & Sawyer, M.B. Pharmacogenetics of paclitaxel metabolism. *Crit Rev Oncol Hematol* **61**, 222-229 (2007).

9. Huizing, M.T. et al. Pharmacokinetics of paclitaxel and three major metabolites in patients with advanced breast carcinoma refractory to anthracycline therapy treated with a 3-hour paclitaxel infusion: a European Cancer Centre (ECC) trial. *Ann Oncol* **6**, 699-704 (1995).

10. Hertz, D.L. et al. Paclitaxel Plasma Concentration after the First Infusion Predicts Treatment-Limiting Peripheral Neuropathy. *Clin Cancer Res* **24**, 3602-3610 (2018).

11. Conte, P.F. et al. Dose-finding study and pharmacokinetics of epirubicin and paclitaxel over 3 hours: a regimen with high activity and low cardiotoxicity in advanced breast cancer. *J Clin Oncol* **15**, 2510-2517 (1997).

12. Gianni, L. et al. Nonlinear pharmacokinetics and metabolism of paclitaxel and its pharmacokinetic/pharmacodynamic relationships in humans. *J Clin Oncol* **13**, 180-190 (1995).

13. Ohtsu, T. et al. Clinical pharmacokinetics and pharmacodynamics of paclitaxel: a 3-hour infusion versus a 24-hour infusion. *Clin Cancer Res* **1**, 599-606 (1995).

14. Huizing, M.T. et al. Pharmacokinetics of paclitaxel and metabolites in a randomized comparative study in platinum-pretreated ovarian cancer patients. *J Clin Oncol* **11**, 2127-2135 (1993).

15. Joerger, M. et al. Population pharmacokinetics and pharmacodynamics of paclitaxel and carboplatin in ovarian cancer patients: a study by the European organization for research and treatment of cancer-pharmacology and molecular mechanisms group and new drug development group. *Clin Cancer Res* **13**, 6410-6418 (2007).

16. Kim, W.Y. et al. Toxicities, dose reduction and delay of docetaxel and paclitaxel chemotherapy in breast cancer without distant metastases. *J Cancer Res Ther* **7**, 412-415 (2011).

17. Cirauqui, B.C. et al. Nanoparticle albumin-bound paclitaxel in a patient with locally advanced breast cancer and taxane-induced skin toxicity: a case report. *J Med Case Rep* **8**, 6 (2014).

18. do Nascimento, T.G., de Andrade, M., de Oliveira, R.A., de Almeida, A.M. & Gozzo Tde, O. Neutropenia: occurrence and management in women with breast cancer receiving chemotherapy. *Rev Lat Am Enfermagem* **22**, 301-308 (2014).

19. Staff, N.P., Grisold, A., Grisold, W. & Windebank, A.J. Chemotherapy-induced peripheral neuropathy: A current review. *Ann Neurol* **81**, 772-781 (2017).

20. Scheithauer, W. et al. Dose modification and efficacy of nab-paclitaxel plus gemcitabine vs. gemcitabine for patients with metastatic pancreatic cancer: phase III MPACT trial. *J Gastrointest Oncol* **7**, 469-478 (2016).

21. Lustberg, M.B. Management of neutropenia in cancer patients. *Clin Adv Hematol Oncol* **10**, 825-826 (2012).

22. Crawford, J. et al. Risk and timing of neutropenic events in adult cancer patients receiving chemotherapy: the results of a prospective nationwide study of oncology practice. *J Natl Compr Canc Netw* **6**, 109-118 (2008).

23. Fontanella, C., Bolzonello, S., Lederer, B. & Aprile, G. Management of breast cancer patients with chemotherapy-induced neutropenia or febrile neutropenia. *Breast Care (Basel)* **9**, 239-245 (2014).

24. Crawford, J. et al. First Cycle Risk of Severe and Febrile Neutropenia in Cancer Patients Receiving Systemic Chemotherapy: Results from a Prospective Nationwide Study. *Blood* **104**, 2210-2210 (2004).

25. Crawford, J., Dale, D.C. & Lyman, G.H. Chemotherapy-induced neutropenia: risks, consequences, and new directions for its management. *Cancer* **100**, 228-237 (2004).

26. Kang, X. et al. Advances in drug delivery system for platinum agents based combination therapy. *Cancer Biol Med* **12**, 362-374 (2015).

27. Raymond, E., Chaney, S.G., Taamma, A. & Cvitkovic, E. Oxaliplatin: a review of preclinical and clinical studies. *Ann Oncol* **9**, 1053-1071 (1998).

28. Lovejoy, K.S. et al. Spectrum of cellular responses to pyriplatin, a monofunctional cationic antineoplastic platinum(II) compound, in human cancer cells. *Mol Cancer Ther* **10**, 1709-1719 (2011).

29. Saung, M.T. & Zheng, L. Current Standards of Chemotherapy for Pancreatic Cancer. *Clin Ther* **39**, 2125-2134 (2017).

30. Winegarden, J.D. et al. A phase II study of oxaliplatin and paclitaxel in patients with advanced non-small-cell lung cancer. *Ann Oncol* **15**, 915-920 (2004).

31. Viens, P. et al. A phase II study of a paclitaxel and oxaliplatin combination in platinum-sensitive recurrent advanced ovarian cancer patients. *Ann Oncol* **17**, 429-436 (2006).

32. Lan, Y.Q. et al. Combination chemotherapy with paclitaxel and oxaliplatin as first-line treatment in patients with advanced gastric cancer. *Cancer Chemother Pharmacol* **81**, 1007-1015 (2018).

33. Misset, J.L., Bleiberg, H., Sutherland, W., Bekradda, M. & Cvitkovic, E. Oxaliplatin clinical activity: a review. *Crit Rev Oncol Hematol* **35**, 75-93 (2000).

34. Kuo, D.Y. et al. Paclitaxel plus oxaliplatin for recurrent or metastatic cervical cancer: a New York Cancer Consortium Study. *Gynecol Oncol* **116**, 442-446 (2010).

35. Kepp, O., Senovilla, L. & Kroemer, G. Immunogenic cell death inducers as anticancer agents. *Oncotarget* **5**, 5190-5191 (2014).

36. Bezu, L. et al. Combinatorial strategies for the induction of immunogenic cell death. *Front Immunol* **6**, 187 (2015).

37. Pachman, D.R. et al. Comparison of oxaliplatin and paclitaxel-induced neuropathy (Alliance A151505). *Support Care Cancer* **24**, 5059-5068 (2016).

38. Bekaii-Saab, T.S. et al. A phase I and pharmacokinetic study of weekly oxaliplatin followed by paclitaxel in patients with solid tumors. *Clin Cancer Res* **14**, 3434-3440 (2008).

39. Liu, D., Poon, C., Lu, K., He, C. & Lin, W. Self-assembled nanoscale coordination polymers with trigger release properties for effective anticancer therapy. *Nat Commun* **5**, 4182 (2014).

40. Duan, X. et al. Immunostimulatory nanomedicines synergize with checkpoint blockade immunotherapy to eradicate colorectal tumors. *Nat Commun* **10**, 1899 (2019).

41. Brenner, D.S., Golden, J.P., Vogt, S.K. & Gereau, R.W.t. A simple and inexpensive method for determining cold sensitivity and adaptation in mice. *J Vis Exp* (2015).

42. Mosely, S.I. et al. Rational Selection of Syngeneic Preclinical Tumor Models for Immunotherapeutic Drug Discovery. *Cancer Immunol Res* **5**, 29-41 (2017).

CHAPTER 5. Immunostimulatory nanomedicines synergize with checkpoint blockade immunotherapy to eradicate colorectal tumor

5.1 Introduction

Combining the ability of NCPs to shield miRNAs from the plasma environment and the chemoimmunotherapy aspects of an OxPt analogue, this chapter discusses a synergistic drug combination delivered by NCPs for chemoimmunotherapy of colorectal cancers (CRCs) which synergizes with a checkpoint inhibitor. This body of work contains elements from each of the previous chapters – examining the intracellular distribution of NCPs after cell uptake, determining the biological triggers and release kinetics of the drug payloads, minimizing toxicity of the free drugs, and harnessing the immune system for an intricate combination of chemistry and biology.

CRC is the second leading cause of cancer-related deaths in the US, with an approximate lifetime risk of 1 in 20 people.[1] The standard therapy of surgery plus adjuvant chemotherapies is often limited by the side effects of and resistance to chemotherapies. [2, 3] Great emphasis has thus been placed on developing immunotherapies for CRC treatment,[4, 5] particularly after the Food and Drug Administration's approval of the cytotoxic T-lymphocyte-associated protein 4 (CTLA-4) antibody ipilimumab in 2011,[6] the programmed cell death protein 1 (PD-1) antibodies pembrolizumab and nivolumab in 2014,[7] and the PD-1 ligand (PD-L1) antibody atezolizumab in 2015.[8] Clinical trials of immune checkpoint inhibitors (α-CTLA-4, α-PD-1, α-PD-L1) have shown efficacy against many cancers, but limited effect in CRCs. A small subset of CRC patients having tumors with inherently high $CD8^+$ T cell infiltration and regulatory immune checkpoint overexpression have benefitted from α-PD-1 checkpoint blockade immunotherapy.[9-12] However,

this cancer phenotype represents <5% of advanced stage CRC.[13, 14] The PD-L1 antibody atezolizumab showed poor response in the predominant microsatellite stable form of CRC as a monotherapy, but improved overall response rates in combination with a MEK inhibitor or α-VEGF and standard folinic acid, 5-fluorouracil, and oxaliplatin (FOLFOX) chemotherapy.[15] There is thus an established need for therapies that can improve tumor immunogenicity and induce $CD8^+$ T cell infiltration to enhance immunotherapy for the broader population of CRC patients.

Most chemotherapy regimens are considered immunologically silent or even tolerogenic. However, a subset of chemotherapeutics have recently been shown to be pro-inflammatory and capable of inducing immunogenic cell death (ICD), suggesting their potential combination with checkpoint blockade to afford antitumor immunity. A key component of the FOLFOX regimen, OxPt, was identified as an ICD inducer.[16-19] We have recently shown that OxPt can be combined with a photosensitizer to synergize the ICD of OxPt-based chemotherapy and photodynamic therapy (PDT) to prime the tumor microenvironment for α-PD-L1 therapy.[20] However, PDT is a localized therapy and light penetration is limited to superficial tumors, severely limiting the clinical translation of PDT-based combination therapies in immunotherapy of CRC.

As reactive oxygen species (ROS) are primarily responsible for cancer cell death by PDT, we posited that ROS-based chemotherapeutics could induce strong ICD using chemicals instead of photons for effective priming of the tumor microenvironment. We report here that the ROS-producing drug, dihydroartemisinin (DHA), can efficiently induce ICD and exhibits synergy with OxPt. DHA is an active metabolite of artemisinin derivatives, an antimalarial drug well tolerated by millions of patients.[21] DHA contains an endoperoxide bridge that reacts with a ferrous iron catalyst to generate free radicals and cause oxidative stress, similar to the effects of PDT. Malignant cells alter iron metabolism to increase uptake and decrease efflux for tumor growth,

leading to an increased pool of labile iron and thus tumor-specific activity of DHA. Despite significant potential as an anticancer therapeutic, DHA's power has not been harnessed for *in vivo* antitumor treatment due to its instability in aqueous media and low bioavailability. The endoperoxide moiety that endows its antimalarial and anticancer activity reacts nonspecifically, leading to premature deactivation in circulation.

Herein, we developed self-assembled nanoscale coordination polymer (NCP) core-shell nanoparticles carrying OxPt in the core and DHA in the shell (OxPt/DHA) for their selective delivery to CRC tumors. In OxPt/DHA core-shell particles, a NCP of Zn and OxPt prodrug was coated with a lipid bilayer containing a cholesterol-DHA conjugate (chol-DHA). OxPt/DHA particles sequester the drugs from water, reductants, and proteins, enabling spatiotemporal control of drug releases in tumors and reducing systemic drug exposure. OxPt/DHA particles have desired surface properties to minimize uptake by the mononuclear phagocyte system (MPS), allowing for their selective accumulation in tumors after systemic injection. Comprised of two ICD-inducing therapeutics, OxPt/DHA elicits strong antitumor immunity in addition to anticancer efficacy, first evidenced by early cell surface exposure of calreticulin (CRT) followed by high mobility group box 1 (HMGB-1) protein release. Fragments of dead cancer cells were taken up by phagocytes, leading to T cell priming and antitumor vaccination. When supplemented with α-PD-L1, OxPt/DHA treatment completely eradicates CRC tumors, in addition to generating long-term tumor-specific immune memory response to prevent the formation and growth of new CRC tumors in mouse models.

5.2 Results

5.2.1 Synthesis and characterization of OxPt/DHA

We probed the synergy between the chemotherapeutic combination of OxPt and DHA at varying ratios on two murine colorectal cancer cell lines, CT26 and MC38. As shown in **Table 5-1**, combining OxPt with DHA led to significant reduction of the OxPt IC_{50} values (from 9.1 ± 0.7 to 1.1–3.2 μM and 10.1 ± 1.1 to 1.1–3.6 μM on CT26 and MC38 cells, respectively).

Table 5-1 OxPt and DHA IC_{50} values (μM)Reprinted from *Nature Communications* **10**, 1899 (2019).

	OxPt	**DHA**	**OxPt + DHA 1:0.5**	**OxPt + DHA 1:1**	**OxPt + DHA 1:2**
CT26 Free drug	9.1 ± 0.7	(2.6 ± 0.6)[a]	3.2 ± 0.4 (1.7 ± 0.2)[a]	1.5 ± 0.3 (1.5 ± 0.3)[a]	1.1 ± 0.3 (2.2 ± 0.5)[a]
CT26 NCP	14.1 ± 1.2	(9.9 ± 0.6)[a]	8.7 ± 0.3 (4.3 ± 0.2)[a]	6.8 ± 0.7 (6.8 ± 0.7)[a]	4.2 ± 0.7 (8.3 ± 1.3)[a]
MC38 Free drug	10.1 ± 1.1	(3.3 ± 0.5)[a]	3.6 ± 0.9 (1.8 ± 0.5)[a]	1.6 ± 0.2 (1.6 ± 0.2)[a]	1.1 ± 0.2 (2.3 ± 0.3)[a]
MC38 NCP	15.6 ± 1.5	(7.4 ± 0.6)[a]	8.9 ± 0.4 (4.4 ± 0.2)[a]	6.4 ± 0.7 (6.4 ± 0.7)[a]	4.4 ± 0.6 (8.7 ± 1.2)[a]

[a] The numbers in parentheses refer to DHA IC_{50} values.

To fix the molar ratios and prevent premature decomposition, we synthesized and encapsulated OxPt and DHA prodrugs, Pt(dach)(oxalate)(bisphosphoramidic acid) (OxPt-bp) and cholest-5-en-3-ol(3ß)-,3-(3-((dihydroartemisinincarbonyl)oxy)ethyl)disulfanyl)ethyl carbonate (chol-DHA) in NCPs (**Scheme 5-1**, **Scheme 5-2**). OxPt/DHA particles were prepared in two steps (**Scheme 5-3**). The NCP core of OxPt (OxPt-bare) was first synthesized by polymerization between Zn^{2+} ions and the phosphate groups of OxPt-bp in the presence of 1,2-dioleoyl-sn-glycero-3-phosphate (DOPA),

yielding spherical OxPt-bare particles monodispersed in organic solvents (**Figure 5-1, Table 5-2**). OxPt-bare was then coated with a mixture of 1,2-dioleyl-sn-glycero-3-phosphocholine (DOPC), cholesterol, 1,2-diastearoyl-sn-glycero-3-phosphoethanolamine-N-[amino(polyethylene glycol)2000] (DSPE-PEG2k) (molar ratio 2:1:1), and different amounts of chol-DHA to afford the core-shell nanoparticles OxPt/DHA with three different OxPt:DHA ratios (1:0.5, 1:1, and 1:2), with Z-average diameters of 73.8–103.4 nm, PDIs of 0.12–0.17, and slightly negative surface charges of -20.8–-13.0 mV in water (**Figure 5-2, Table 5-3**).

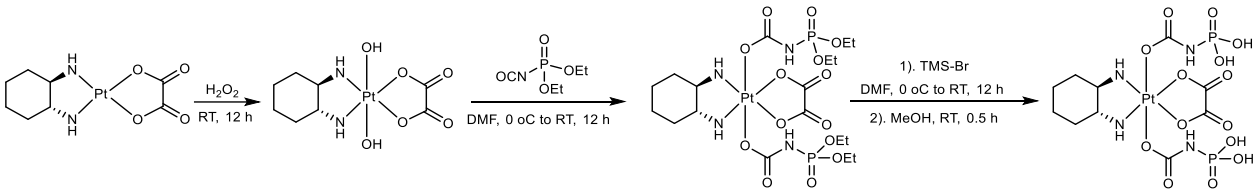

Scheme 5-1 Synthesis of OxPt-bp. Reprinted from *Nature Communications* **10**, 1899 (2019).

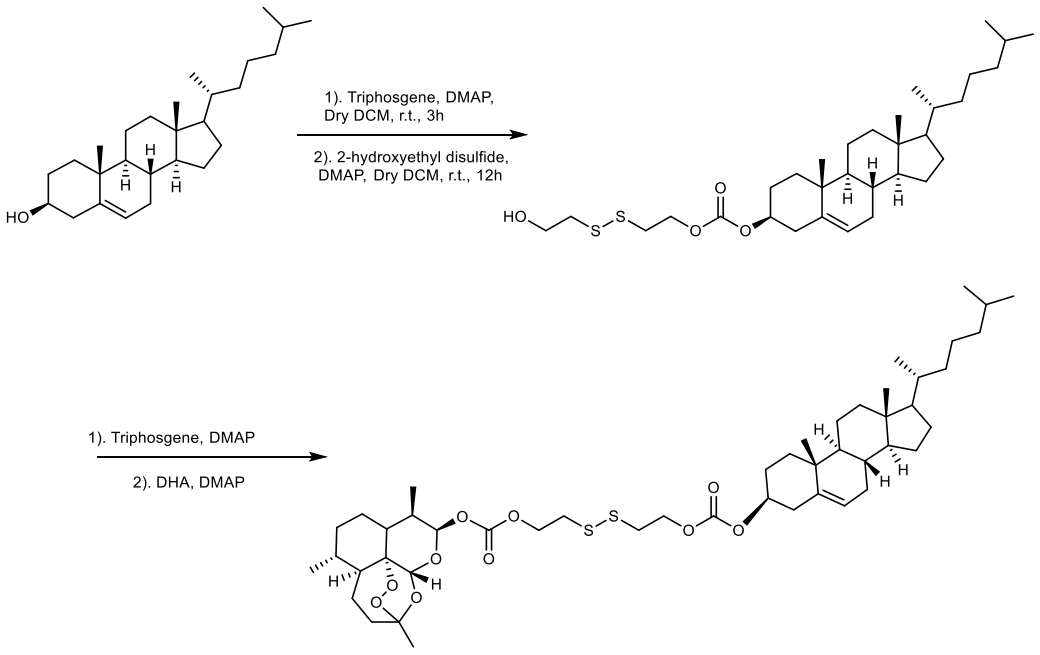

Scheme 5-2 Synthesis of chol-DHA. Reprinted from *Nature Communications* **10**, 1899 (2019).

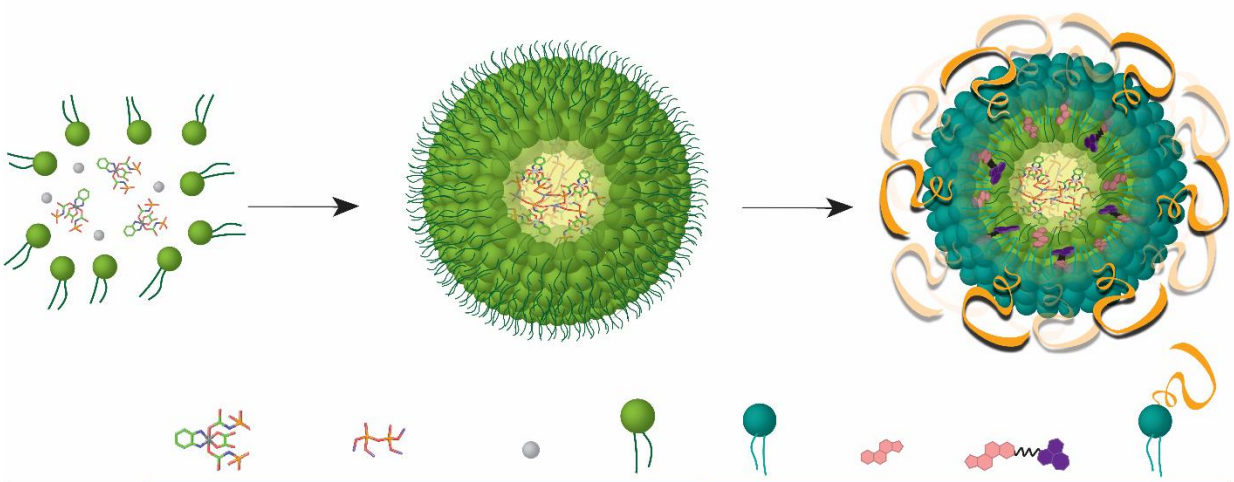

NCP	OxPt-bp	pyrophosphate	Zn^{2+}	DOPA	DOPC	Chol	Chol-DHA	DSPE-PEG
OxPt/DHA	√		√	√	√	√	√	√
OxPt NCP	√		√	√	√	√		√
Zn/DHA		√	√	√	√	√	√	√
	CORE				SHELL			

Scheme 5-3 Schematic illustration showing layer-by-layer construction of the hybrid core-shell structure of OxPt/DHA. The OxPt/DHA consists of an OxPt prodrug coordinated to Zn^{2+} ions in the core and chol-DHA in the lipid shell. Compositions of the three NCPs investigated are also shown. Reprinted from *Nature Communications* **10**, 1899 (2019).

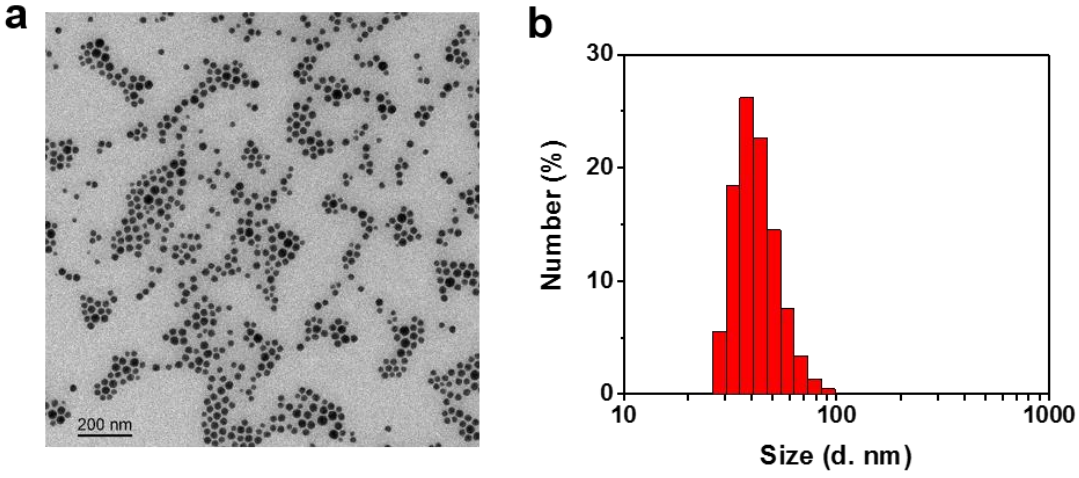

Figure 5-1 (a) TEM image of OxPt/DHA. (b) Number-average diameter of OxPt/DHA characterized by DLS. Reprinted from *Nature Communications* **10**, 1899 (2019).

Table 5-2 Characterization of nanoparticles. Reprinted from *Nature Communications* **10**, 1899 (2019).

	Z-Average (d. nm)	PDI	Number (d. nm)	Loading	ζ-potential (mV)
OxPt-bare	78.27 ± 0.18	0.159 ± 0.01	40.40 ± 3.08	28% OxPt, 16% Zn	
OxPt NCP	89.21 ± 1.17	0.136 ± 0.01	55.37 ± 2.28		-17.90 ± 0.46
OxPt/DHA	73.80 ± 0.36	0.174 ± 0.01	41.00 ± 0.62		-20.83 ± 1.25
Zn/DHA	98.60 ± 0.75	0.140 ± 0.01	63.50 ± 6.76		-23.85 ± 3.75

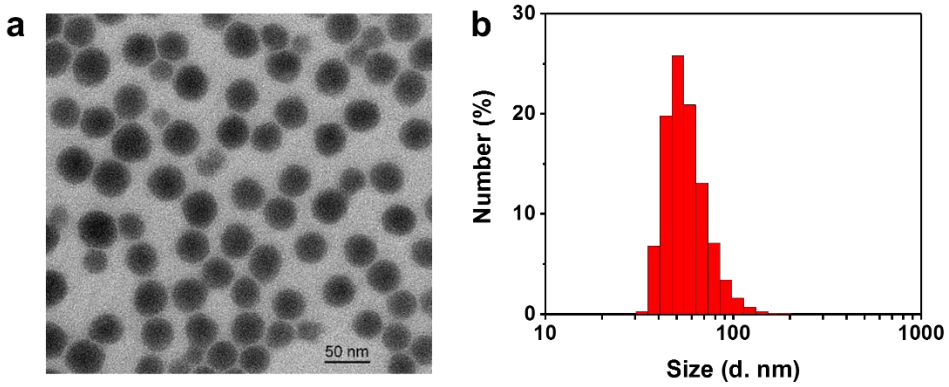

Figure 5-2 (a) TEM image of OxPt-bare. (b) Number-average diameter of OxPt-bare characterized by DLS. Reprinted from *Nature Communications* **10**, 1899 (2019).

Table 5-3 The effect of DHA loading on particle size. Reprinted from *Nature Communications* **10**, 1899 (2019).

	Z-Average (d. nm)	PDI	Intensity (d. nm)	Number (d. nm)
OxPt/DHA (1:0.5)	73.8 ± 0.36	0.174 ± 0.01	85.0 ± 4.23	41.0 ± 0.62
OxPt/DHA (1:1)	101.0 ± 2.37	0.159 ± 0.01	120.5 ± 1.36	60.8 ± 8.46
OxPt/DHA (1:2)	103.4 ± 1.01	0.116 ± 0.01	117.5 ± 1.66	69.7 ± 1.11

DHA was conjugated to cholesterol via a disulfide bond to facilitate incorporation into the shell of the nanoparticles. The lipid bilayer protects chol-DHA from exposure to water and reductants, limiting decomposition and systemic release by preventing hydrolysis and reduction. The nanoparticles were stable with no changes in size or PDIs at 4 ºC for one year or 37 ºC for 24 h in the presence of bovine serum albumin (BSA, **Figure 5-3, Figure 5-4**). The monotherapy nanoparticle controls OxPt NCP and Zn/DHA prepared in the absence of chol-DHA or with pyrophosphate replacing OxPt prodrug, respectively, showed similar sizes and morphology (**Scheme 5-3, Figure 5-5, Figure 5-6, Table 5-2, Table 5-3**).

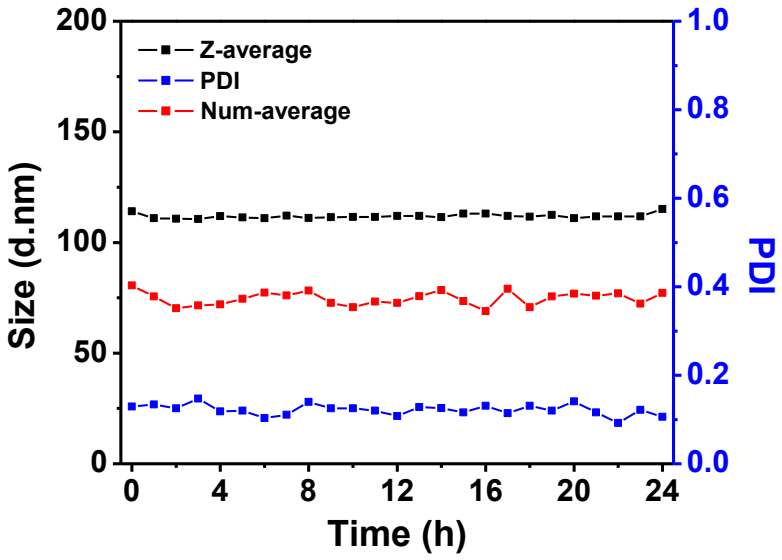

Figure 5-3 Stability test of OxPt/DHA at 37 °C in the presence of BSA (5 mg/mL). Reprinted from *Nature Communications* **10**, 1899 (2019).

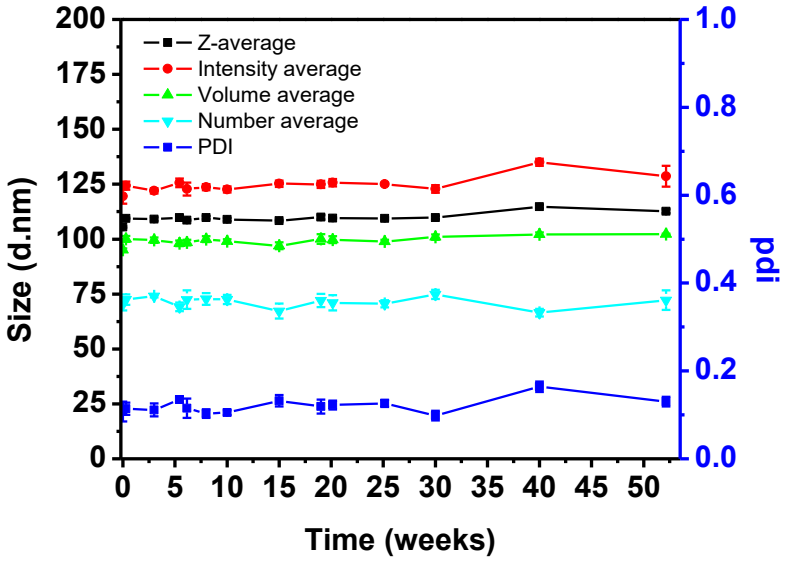

Figure 5-4 Stability test of OxPt/DHA at 4 °C. Reprinted from *Nature Communications* **10**, 1899 (2019).

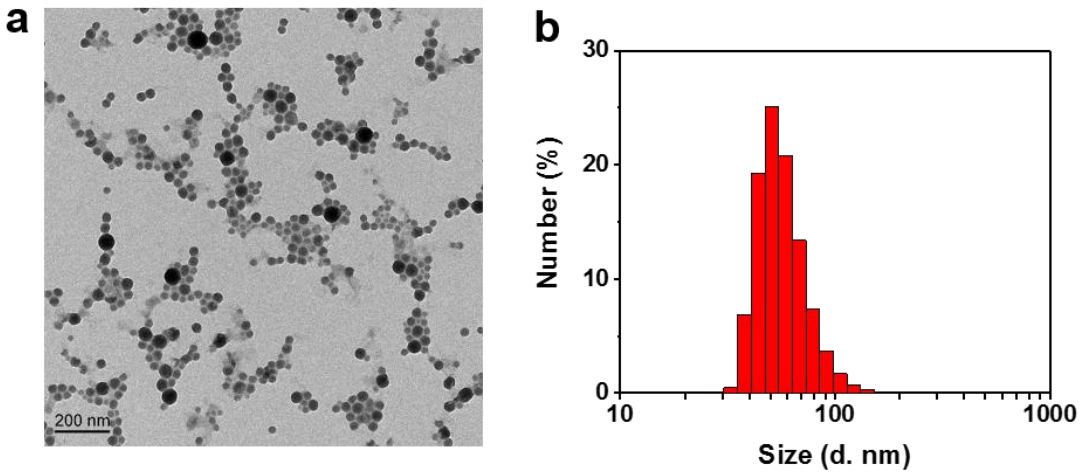

Figure 5-5 (a) TEM image of OxPt NCP. (b) Number-average diameter of OxPt NCP characterized by DLS. Reprinted from *Nature Communications* **10**, 1899 (2019).

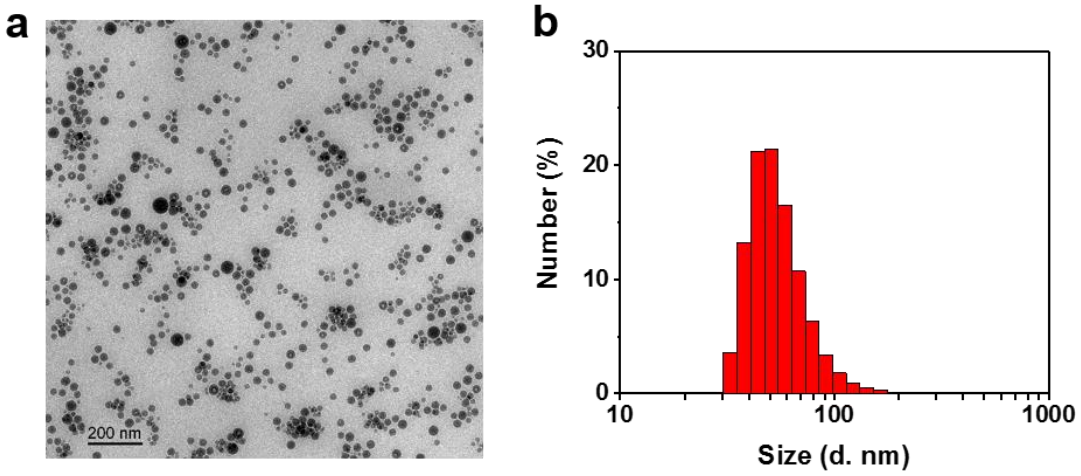

Figure 5-6 (a) TEM image of Zn/DHA. (b) Number-average diameter of Zn/DHA characterized by DLS. Reprinted from *Nature Communications* **10**, 1899 (2019).

Encapsulation into nanoparticles led to slightly higher IC_{50} than free drugs, but showed similar trends of OxPt IC_{50} reduction by adding chol-DHA (**Table 5-1**), suggesting that the drugs are readily released from NCPs. The synergy between the two drugs in OxPt/DHA was most readily observed with a OxPt : DHA molar ratio of 1 : 0.5, with a combination index of < 1 at nearly all effect levels (**Figure 5-7**).

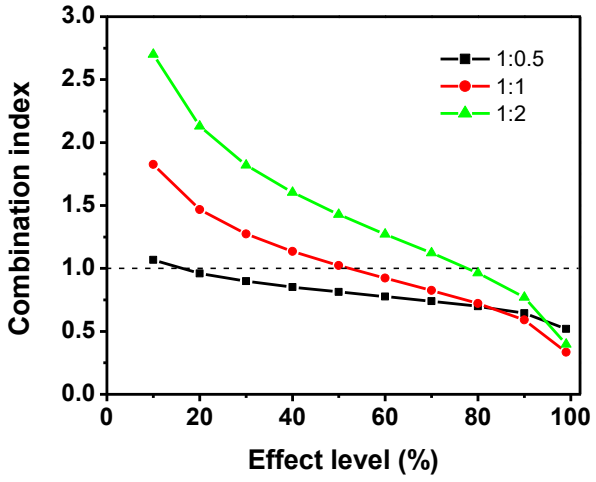

Figure 5-7 Combination Index of OxPt and DHA NCP at different effect levels. Reprinted from *Nature Communications* **10**, 1899 (2019).

This formulation was used for all further investigations. Using OxPt/DHA particles labeled with cholesterol conjugated pyropheophytin a (chol-pyro, **Scheme 5-4**), we showed that particles were taken up rapidly by cells, with ~95% of all cells showing particle fluorescence after 1 h. The fluorescence intensity significantly increased over time, indicating continual nanoparticle uptake (**Figure 5-8**). ICP-MS quantification of intracellular Pt also revealed time-dependent uptake of both nanoparticles and free OxPt. However, the uptake of nanoparticles was much less than free OxPt (**Figure 5-9**), possibly due to the surface PEG coating preventing interaction between particles and cells. The lower uptake explains why the particles have slightly higher IC_{50} than free drugs in vitro.

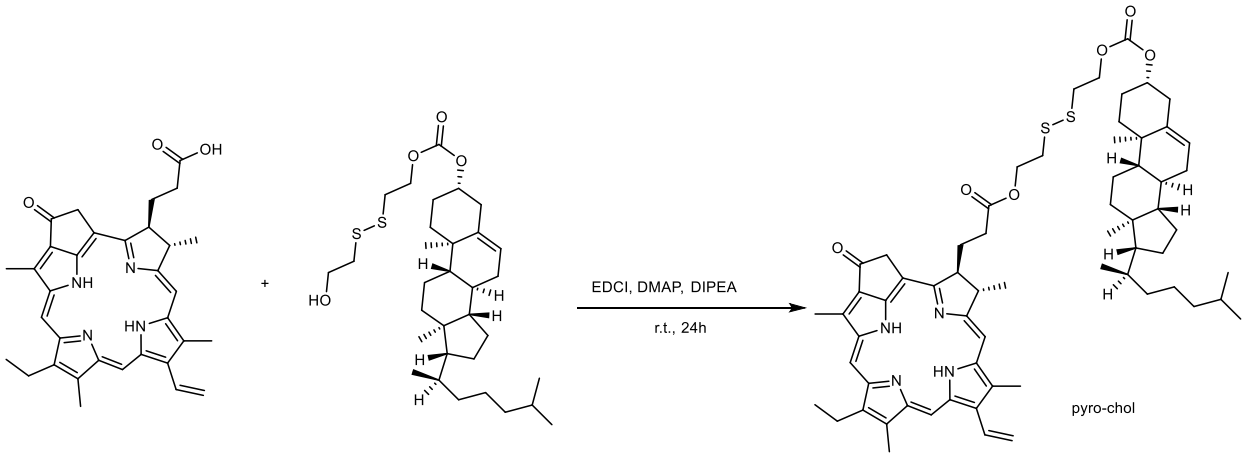

Scheme 5-4 Synthesis of chol-pyro. Reprinted from *Nature Communications* **10**, 1899 (2019).

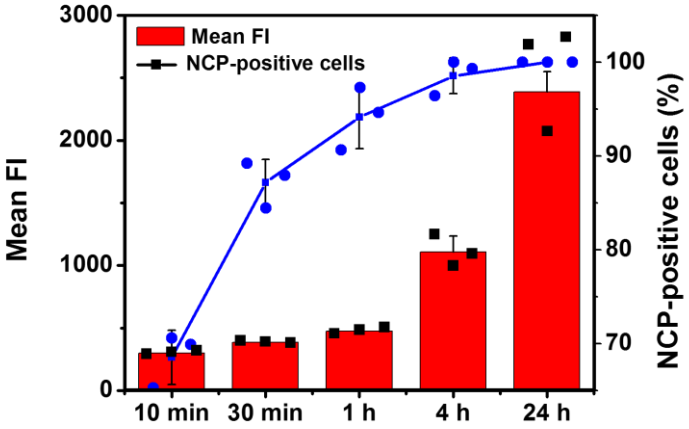

Figure 5-8 Uptake of chol-pyro-labeled NCP particles by CT26 cells with different incubation times. Reprinted from *Nature Communications* **10**, 1899 (2019).

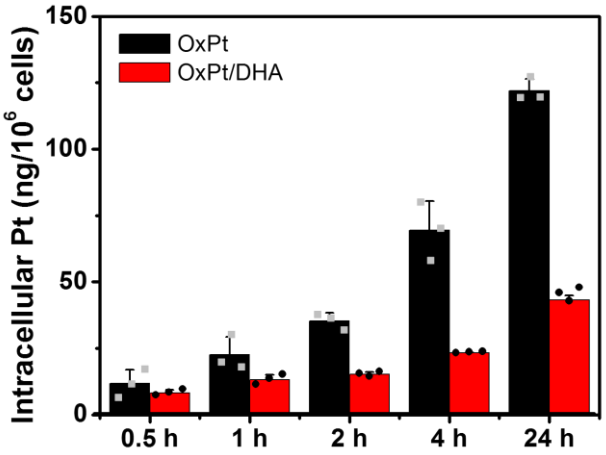

Figure 5-9 The intracellular Pt in CT26 incubated with OxPt or OxPt/DHA as determined by ICP-MS. Reprinted from *Nature Communications* **10**, 1899 (2019).

To visualize the intracellular release of drugs, fluorescent nanoparticles were synthesized by doping xylenol orange (blue) into the core and coating chol-pyro (red) and FITC-DOPE (green) on the shell, which allows simultaneous visualization of OxPt in the core, chol-DHA in the shell, and the lipid layer, respectively. In the first 10 minutes, all three dyes were primarily found on the cell surface, viewed as cyan (green and blue merged) and/or white (green, blue and red merged) in the merged image, indicating that the particles were mainly bound to the cell surface. Over time, the xylenol orange and chol-pyro nonspecifically distributed inside the cells as magenta (blue and red merged) fluorescence with varying intensity, suggesting independent release of the drugs. FITC-DOPE mainly localized to the plasma membrane (**Figure 5-10**), possibly due to the lipid bilayer fusion with endosome membranes to expose the NCP core and the trafficking of FITC-DOPE to the plasma membrane with the recycled endosomes. These data demonstrate that upon cellular uptake, the core-shell structure is disrupted to expose the OxPt NCP core and chol-DHA to high concentrations of intracellular reducing agents, such as glutathione (GSH, 5 mM) and ascorbate (100 μM), which further reduce and/or hydrolyze the prodrugs into parent drugs to exert efficacy.

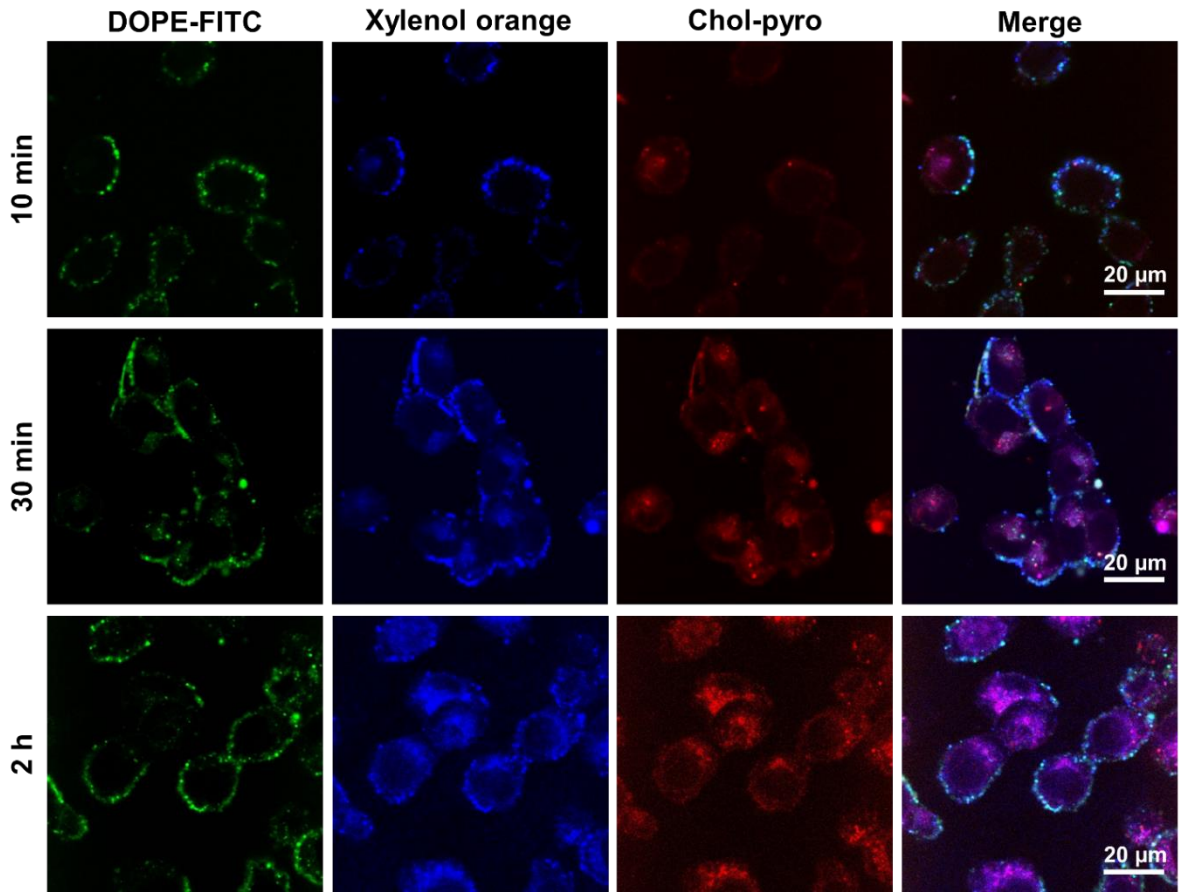

Figure 5-10 CT26 cells incubated with fluorescent nanoparticles containing xylenol orange in the core, chol-pyro in the shell, and FITC-DOPE lipid to visualize OxPt in the core, chol-DHA in the shell, and the lipid layer of OxPt/DHA, respectively, for different times were observed under confocal laser scanning microscopy (CLSM). Reprinted from *Nature Communications* **10**, 1899 (2019).

5.2.2 Triggered release of prodrugs and drugs from OxPt/DHA

The disulfide linkage of chol-DHA was cleaved by GSH at physiologically relevant concentration to release DHA (**Scheme 5-5, Figure 5-11**). However, the kinetics of DHA release in the 5 mM GSH solution of PBS was faster than that of GSH reduction alone. Although chol-DHA was stable in aprotic, organic solvents such as THF at 37 ^{o}C for >24 h, it rapid decomposed (>80%) in aqueous or protic solvents (**Figure 5-12, Figure 5-11**). The addition of acids further accelerated the decomposition of chol-DHA (**Figure 5-11**).

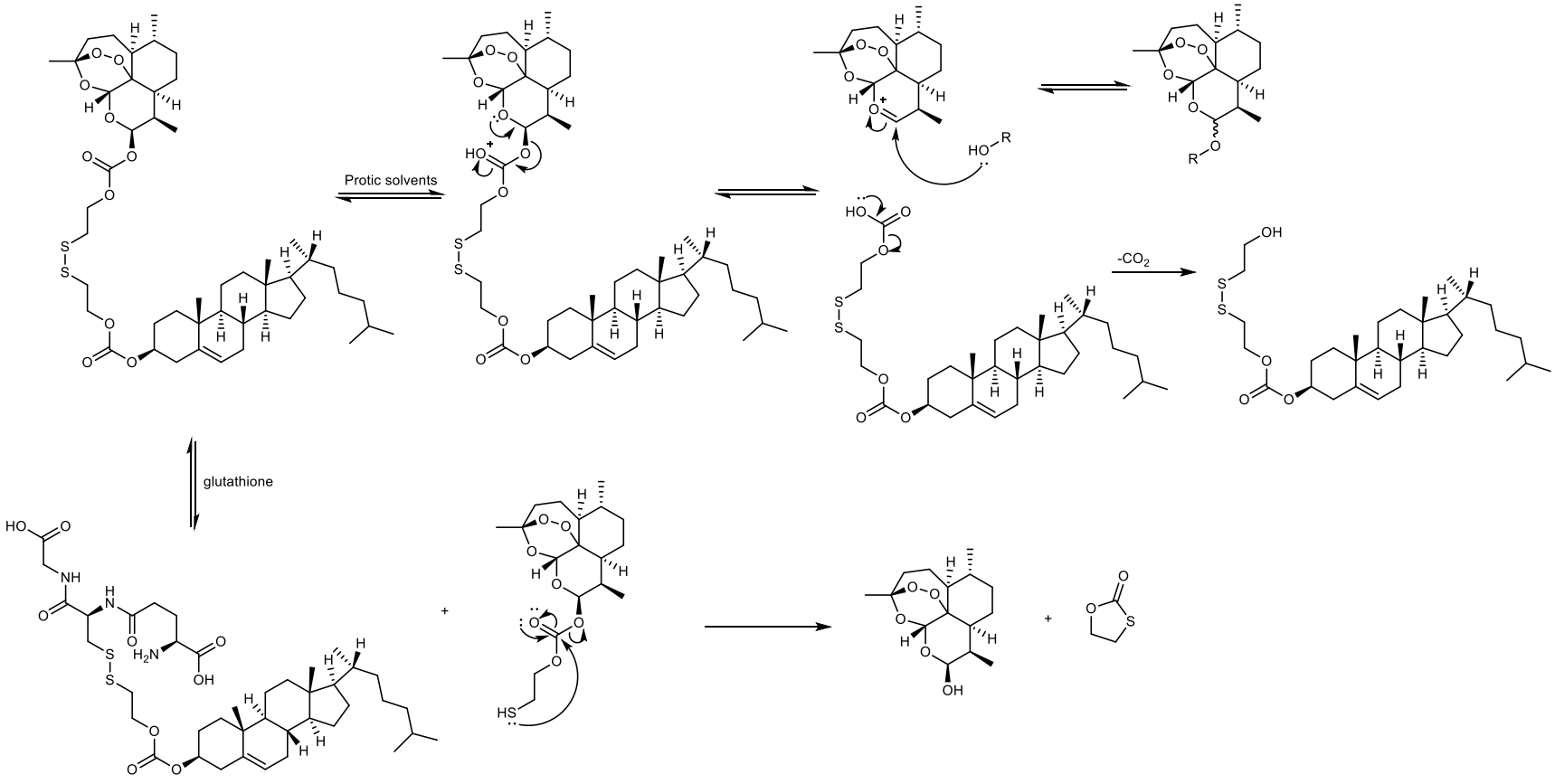

Scheme 5-5 Proposed DHA release via GSH mediated disulfide cleavage and proton-catalyzed hydrolysis. Reprinted from *Nature Communications* **10**, 1899 (2019).

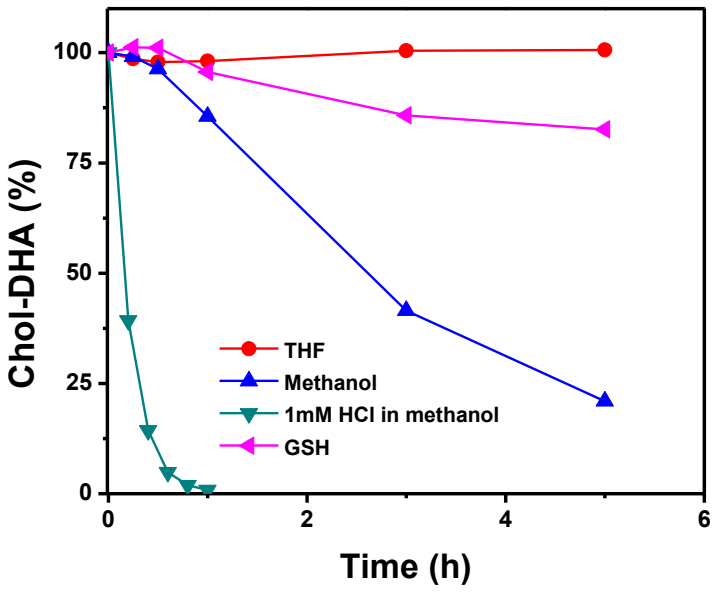

Figure 5-11 Chol-DHA remaining in different solvents when incubated at 37 °C. GSH curve was calculated by subtraction of the curve in water from the curve for 5 mM GSH water solution to show the DHA release by GSH reduction only. Reprinted from *Nature Communications* **10**, 1899 (2019).

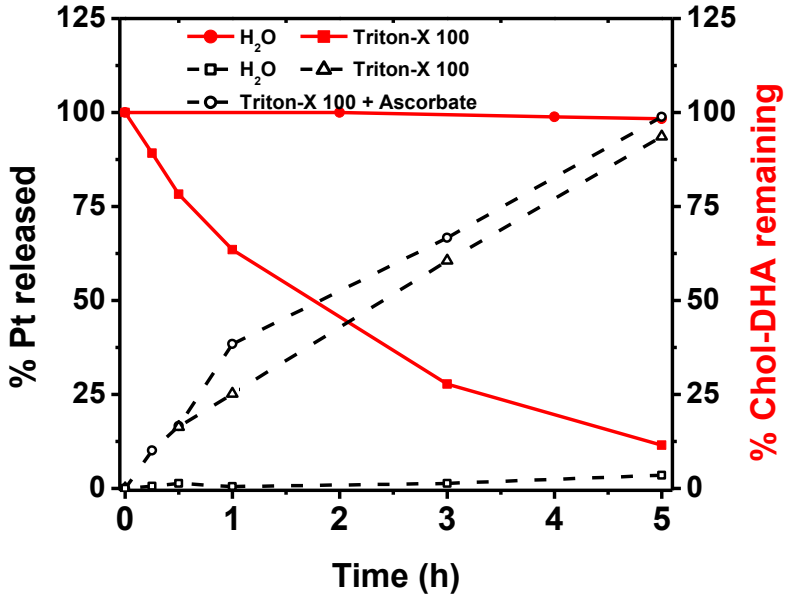

Figure 5-12 Total Pt release from and chol-DHA remaining in OxPt/DHA particle when incubated in water at 37 °C with or without 0.5% Triton X-100 and 5 mM ascorbate. Reprinted from *Nature Communications* **10**, 1899 (2019).

Based on these observations, we propose a DHA release mechanism via proton-catalyzed hydrolysis in aqueous media. The protonation of the carbonate carbonyl oxygen atom in protic solvents can reversibly cleave the C-O bond next to DHA to form a DHA cation stabilized by the nearby oxygen and a carbonate monoester. The carbonate monoester irreversibly releases CO_2, providing the driving force for the hydrolysis of DHA from chol-DHA. While GSH reduction of the disulfide linkage contributes to the release of DHA, hydrolysis of the chol-DHA carbonate linker is predominantly responsible for the DHA release (**Scheme 5-5**). Importantly, incorporation of chol-DHA into the lipid bilayer shell of OxPt/DHA prevented premature DHA release by limiting exposure to water. Incubation of OxPt/DHA in water at 37 ^{o}C for 24 h did not lead to significant loss of chol-DHA. However, disruption of the lipid bilayer of OxPt/DHA by Triton X-100 led to 90% degradation of chol-DHA in water at 37 ^{o}C within 5 h (**Figure 5-11**). The core-shell structure of OxPt/DHA thus protects DHA from exposure to water and reductants during circulation, ensuring the selective delivery of DHA to cancer cells.

The Pt(IV) prodrug OxPt-bp was also reduced via two mechanisms: direct reduction into OxPt or a two-step sequence of hydrolysis to generate Pt(dach)(oxalate)(biscarbamate) (OxPt-bc) followed by reduction to OxPt (**Scheme 5-6, Figure 5-13**). While OxPt does not release from intact OxPt/DHA particles, the disruption of the lipid bilayers upon endocytosis allows access of the robust coordination polymer to ascorbate and acidic aqueous medium, leading to release of both OxPt and OxPt-bc.

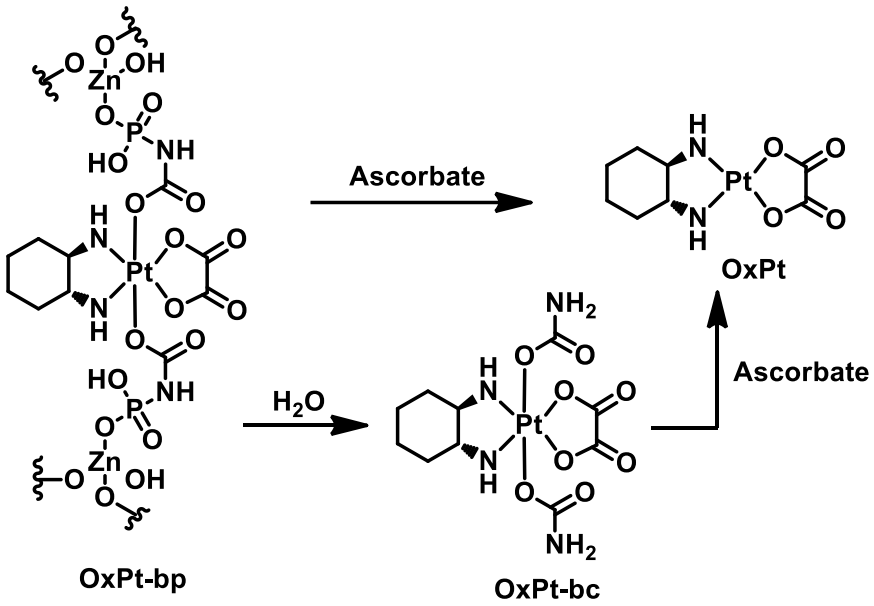

Scheme 5-6 Proposed release of OxPt via direct reduction by ascorbate or a two-step sequence of hydrolysis to generate OxPt-bc followed by reduction to OxPt. Reprinted from *Nature Communications* **10**, 1899 (2019).

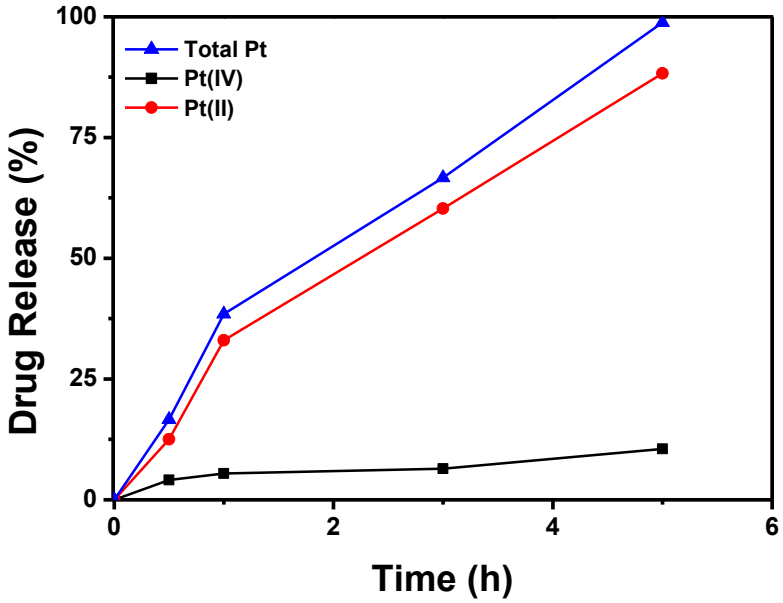

Figure 5-13 Pt compounds released from OxPt/DHA particles when incubated in water at 37 °C with 0.5% Triton X-100 and 5 mM ascorbate. Reprinted from *Nature Communications* **10**, 1899 (2019).

5.2.3 Mechanisms of cell death

The purported anti-malarial activity of DHA involves cleavage of the endoperoxide bridge by ferrous iron, generating oxygen- and carbon-based radicals. As cancer cells are highly sensitive to agents that can augment oxidative stress, we investigated whether our combination therapy can synergistically generate ROS, which can directly react with the membrane, DNA, proteins, and organelles or generate secondary products to cause damage. Both OxPt and DHA can individually induce ROS generation in tumor cells, with a significant increase when given in combination ($p < 0.001$; **Figure 5-14, Figure 5-15**). ROS is a known trigger for dysfunction of mitochondria, which regulates both autophagy and apoptosis. The generated ROS causes release of cytochrome c from mitochondria, as evidenced by the decrease in the co-localization between the mitochondria (red) and the cytochrome c (green) fluorescence (**Figure 5-16, Figure 5-17**), by disrupting membrane potential as a consequence of ROS accumulation. As a result, both OxPt and DHA induced programmed cell death by apoptosis/necrosis (**Figure 5-18, Figure 5-19**). The combination of OxPt and DHA increased both early apoptotic Annexin V^+/PI^- cells (26.8±1.4% compared to 11.9±1.0% and 14.7±1.7% for OxPt and DHA, respectively) and late apoptotic/necrotic Annexin V^+/PI^+ cells (36.2±3.0% compared to 15.6±1.5% and 31.6±2.9% for OxPt and DHA, respectively). Treatment with OxPt NCP, Zn/DHA, and OxPt/DHA led to similar trends in the ROS, cytochrome c release, and induction of apoptosis (**Figure 5-15, Figure 5-17, Figure 5-19**).

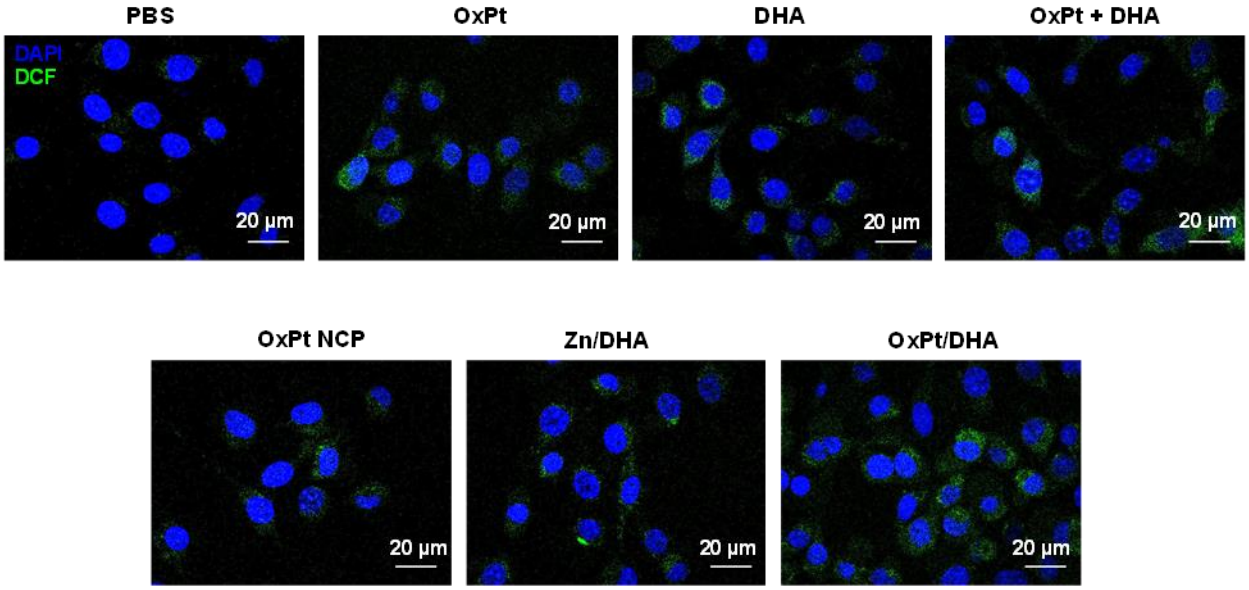

Figure 5-14 ROS generation in CT26 cells incubated with OxPt, DHA or combinations. Reprinted from *Nature Communications* **10**, 1899 (2019).

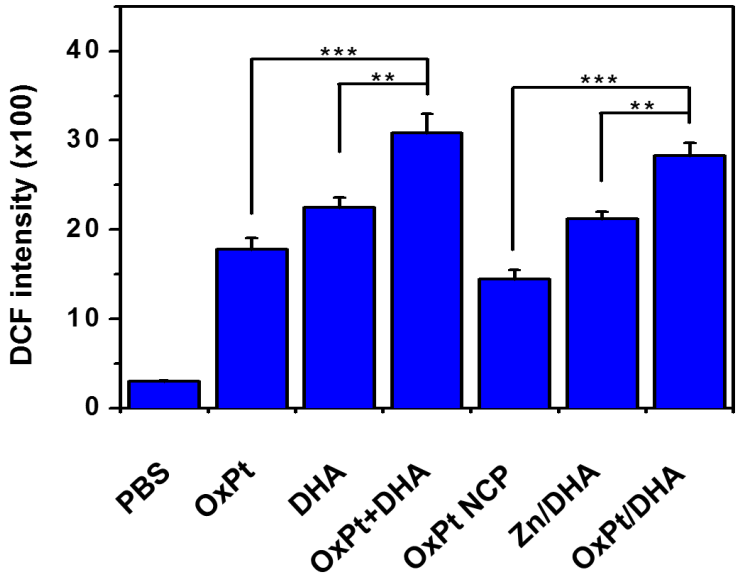

Figure 5-15 ROS generation in cells treated with OxPt/DHA, as indicated by the green fluorescence of 2',7'-dichlorofluorescein (DCF) that was oxidized from 2',7'-dichlorodihydrofluorescein diacetate (H_2DCFDA) by ROS. Reprinted from *Nature Communications* **10**, 1899 (2019).

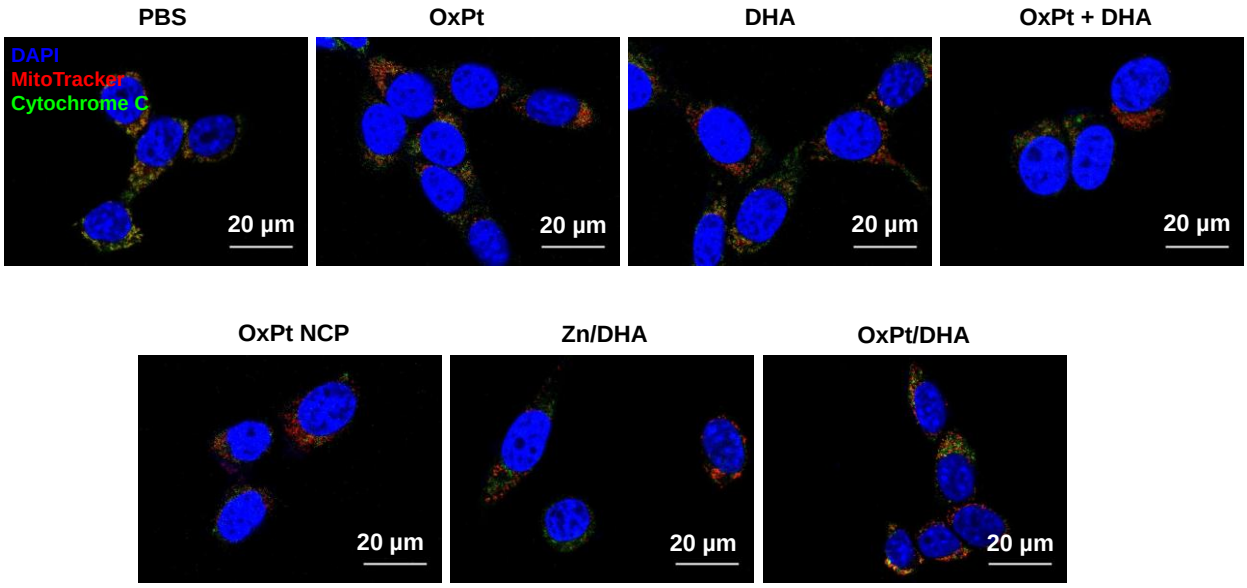

Figure 5-16 Confocal images showing the cytochrome C (Green) release from mitochondria (Red) induced by OxPt, DHA or combinations, as evidenced by the decreased colocalization of green fluorescence with red fluorescence. Reprinted from *Nature Communications* **10**, 1899 (2019).

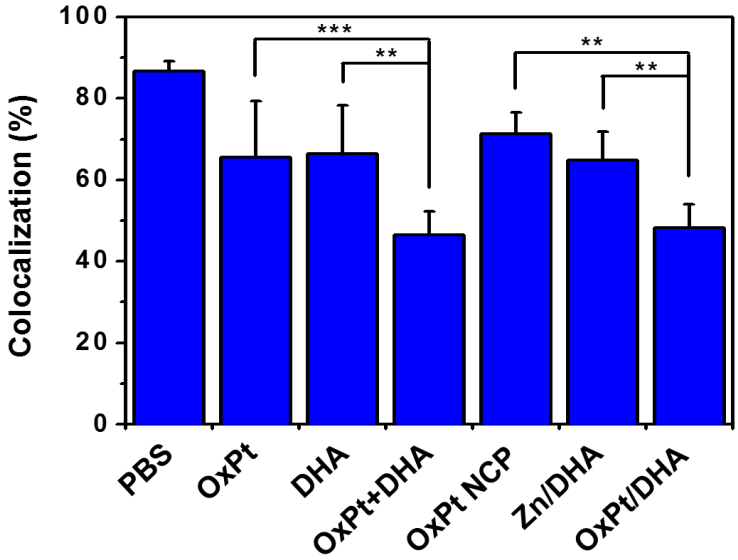

Figure 5-17 Mitochondria (red fluorescence) and cytochrome c (green fluorescence) were stained by MitoTracker Red CMXRos and anti-cytochrome c antibody, respectively. Reprinted from *Nature Communications* **10**, 1899 (2019).

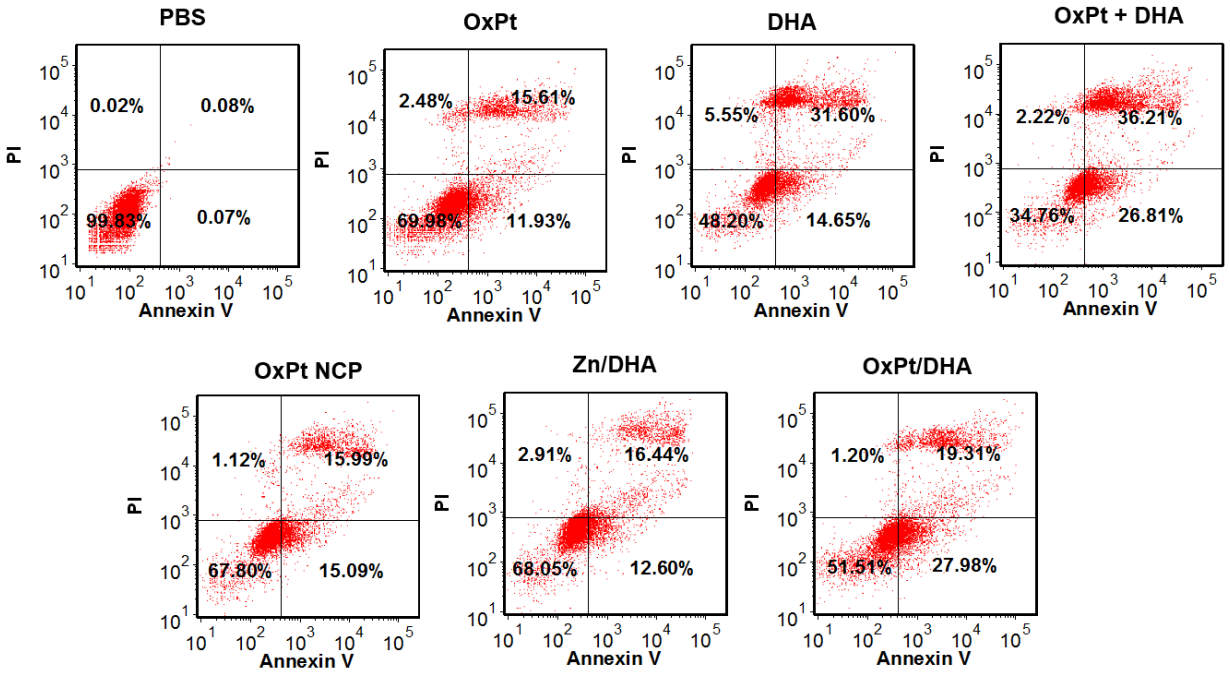

Figure 5-18 Flow cytometry analysis for apoptosis of CT26 cells induced by OxPt, DHA or combinations. Reprinted from *Nature Communications* **10**, 1899 (2019).

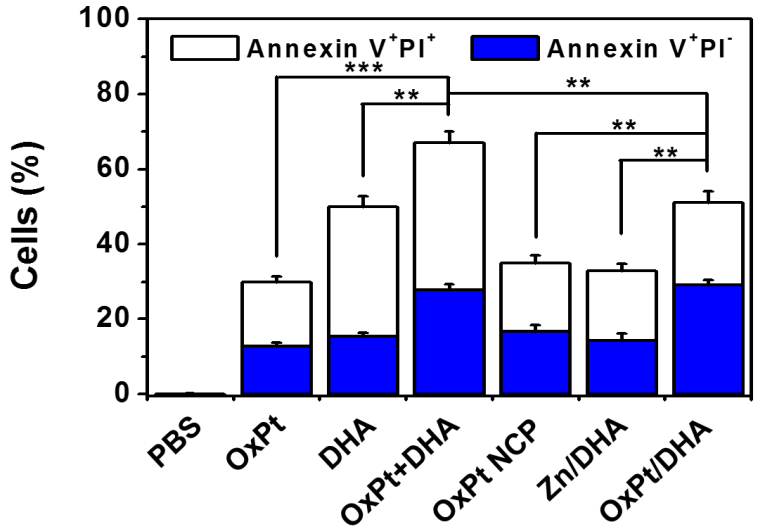

Figure 5-19 Apoptosis induced by OxPt/DHA. After treatment, cells were stained by Alexa Fluor 488-labeled Annexin V and propidium iodide (PI) and analyzed by flow cytometry. Reprinted from *Nature Communications* **10**, 1899 (2019).

In addition to mitochondrial dysfunction, ROS can also inhibit cell growth by cell cycle arrest via endoplasmic reticulum (ER) stress. G_2/M phase cell cycle arrest was observed in CT26 cells treated by either OxPt or DHA, increasing the percentages of G_2/M phases to 35.6 ± 3.7% ($p = 1.1 \times 10^{-2}$) and 34.5±3.9% ($p = 1.5 \times 10^{-2}$), respectively, from 20.8 ± 4.4% in PBS. Combining OxPt and DHA further increased the proportion of cells arrested at the G_2/M phase to 44.3 ± 3.7% ($p = 4.4 \times 10^{-2}$ and 3.4×10^{-2} compared to OxPt and DHA, respectively). Two sequential, redundant mechanisms for ER stress-regulation of the cell cycle have been suggested: first delay at the G_2 checkpoint followed by cell cycle arrest at the G_1 checkpoint.[22] Interestingly, treatment with OxPt specifically decreased the accumulation of S phase cells, whereas treatment with DHA led to approximately equal reductions of cells in the G_0/G_1 and S phases. Cells treated with OxPt NCP, Zn/DHA, and OxPt/DHA resulted in similar changes in the cell cycle as free drug treatments (**Figure 5-20, Figure 5-21**).

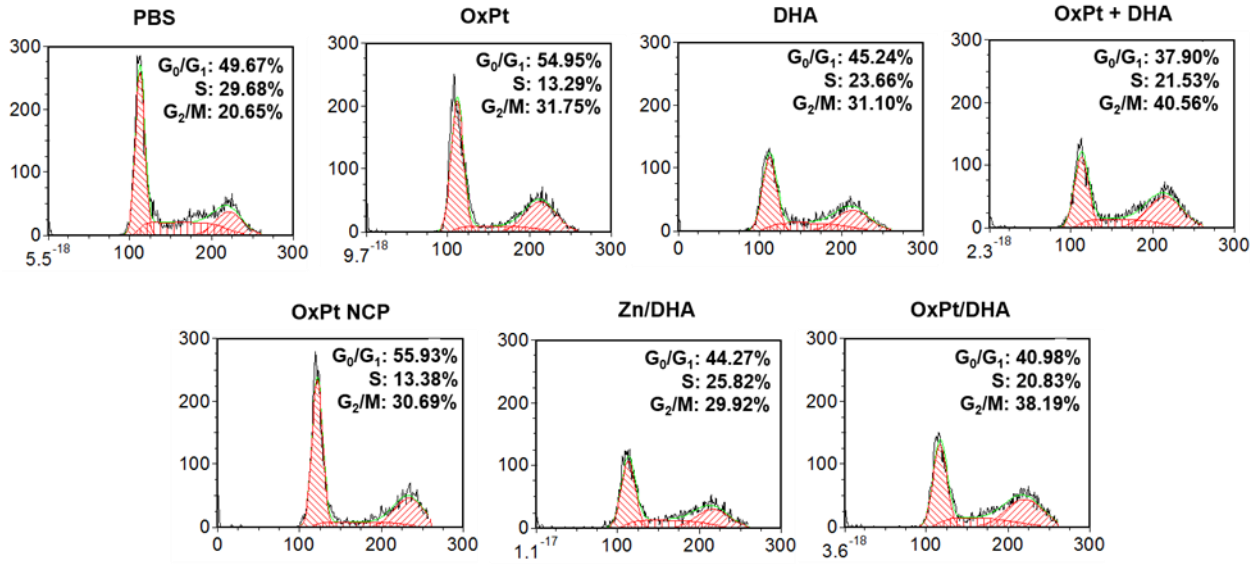

Figure 5-20 Flow cytometry analysis for cell cycle change of CT26 cells induced by OxPt, DHA or combinations. Reprinted from *Nature Communications* **10**, 1899 (2019).

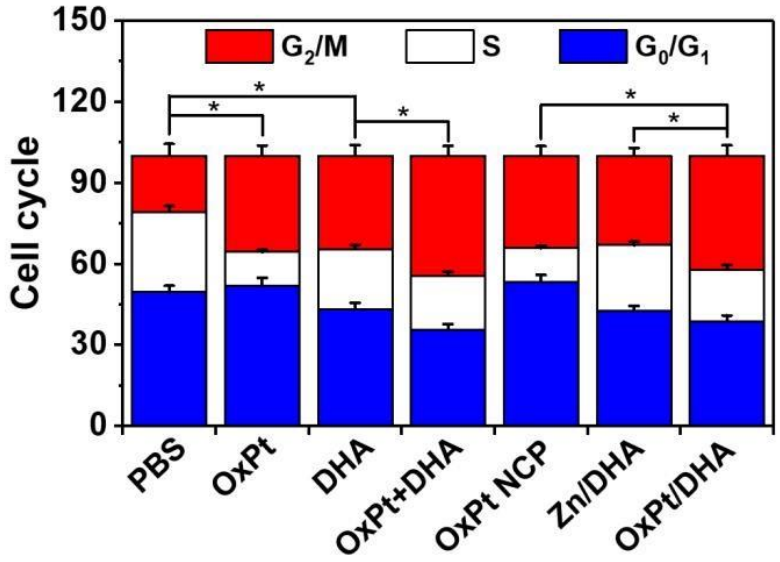

Figure 5-21 Cell cycle arrest caused by OxPt/DHA. Treated cells were fixed with 70% ethanol overnight, treated with RNase A, stained by PI, and analyzed by flow cytometry. Reprinted from *Nature Communications* **10**, 1899 (2019).

ER stress and ROS production are essential components of the intracellular pathways that govern ICD, which occur in parallel to activate danger signaling pathways that help to traffic damage associated molecular patterns (DAMPs) to the extracellular space.[16, 23-26] We confirmed that OxPt is able to induce ICD, but also demonstrated that DHA can also effectively induce ICD, as evidenced by calreticulin (CRT) cell-surface exposure (**Figure 5-22, Figure 5-23**). We further quantified the release of HMGB-1 from cells treated with both drugs by enzyme-linked immunosorbent assay (ELISA). Incubation with OxPt or DHA led to increased HMGB-1 release from cells, which was further increased by co-incubation with both drugs. (**Figure 5-24**).

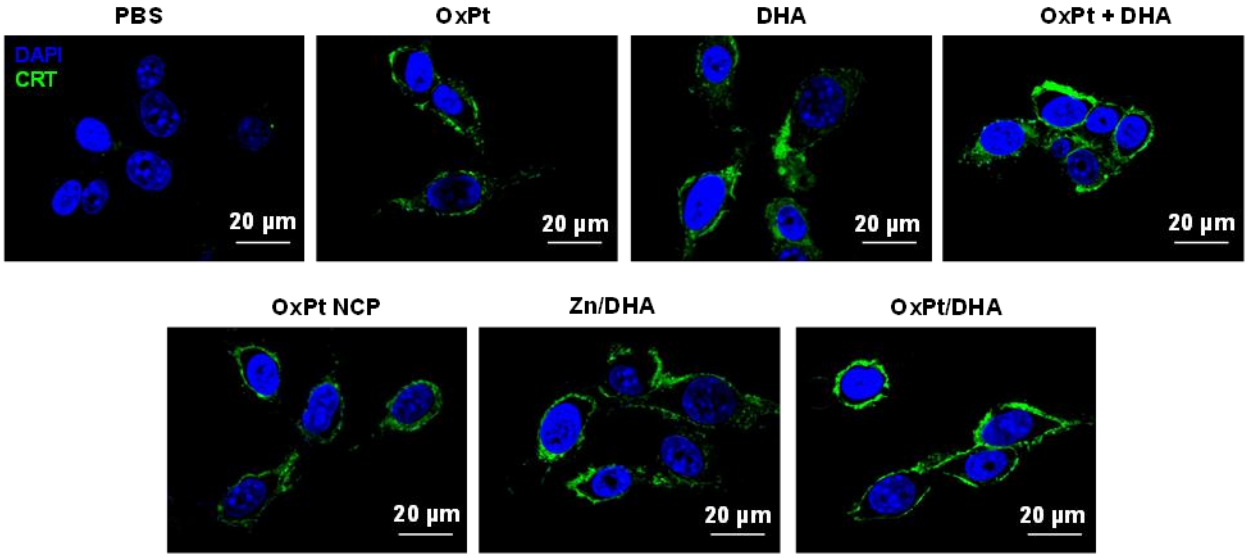

Figure 5-22 Confocal images showing the CRT exposure on CT26 cells surface after treatment with OxPt, DHA or combinations. Reprinted from *Nature Communications* **10**, 1899 (2019).

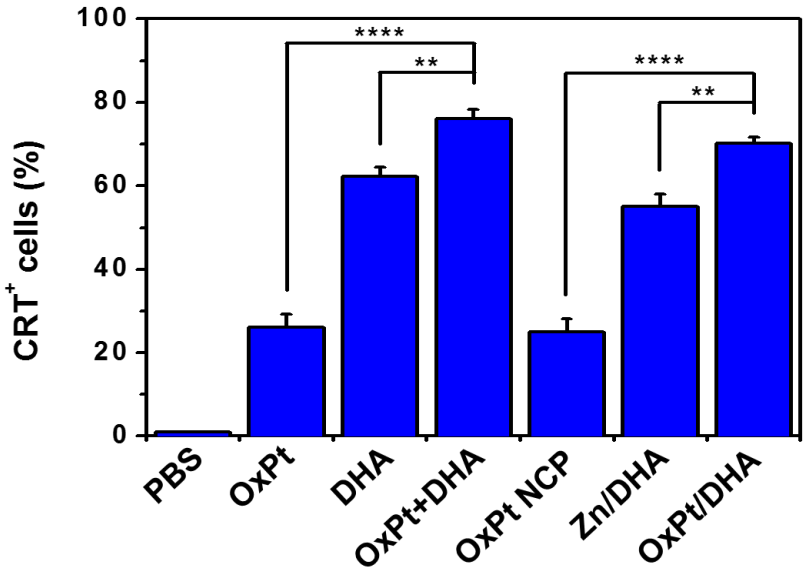

Figure 5-23 CRT exposure on cell surface upon treatment with OxPt, DHA, or combinations, as determined by flow cytometry. Reprinted from *Nature Communications* **10**, 1899 (2019).

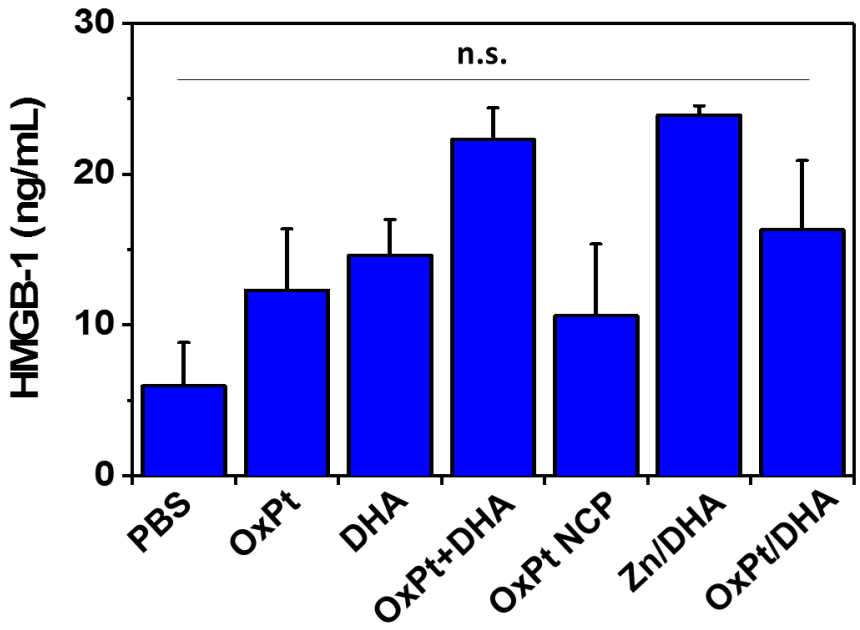

Figure 5-24 HMGB-1 release from tumor cells treated with OxPt, DHA, or combinations as detected by ELISA. Reprinted from *Nature Communications* **10**, 1899 (2019).

5.2.4 Priming tumor specific immune response

OxPt and/or DHA treated tdTomato transfected MC38 cells could be engulfed by bone marrow derived dendritic cells (DCs) and macrophages (**Figure 5-25, Figure 5-26, Figure 5-27**). Using tdTomato-MC38-OVA cells, we showed that treatment with OxPt/DHA resulted in a significantly higher cross-presentation of the ovalbumin (OVA) peptide onto MHC I, as demonstrated by staining of the SIINFEKL-H2kb complex on DCs and macrophages surface (**Figure 5-28, Figure 5-29**). This result suggests that both phagocytes are involved in presenting tumor antigens to initiate the adaptive immune response.[27]

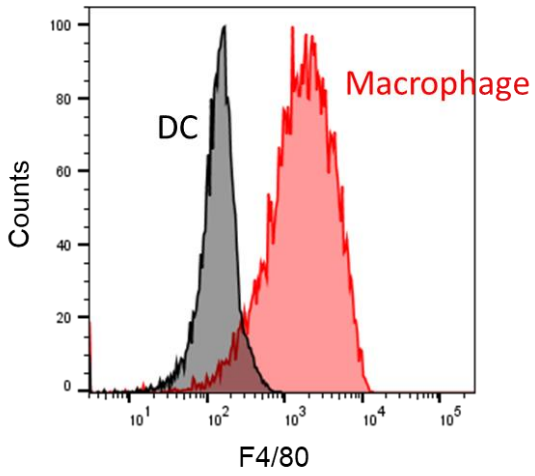

Figure 5-25 The purities of bone marrow-derived dendritic cells ($CD11b^+CD11c^+F4/80^-$) and macrophages ($CD11b^+F4/80^+$). Reprinted from *Nature Communications* **10**, 1899 (2019).

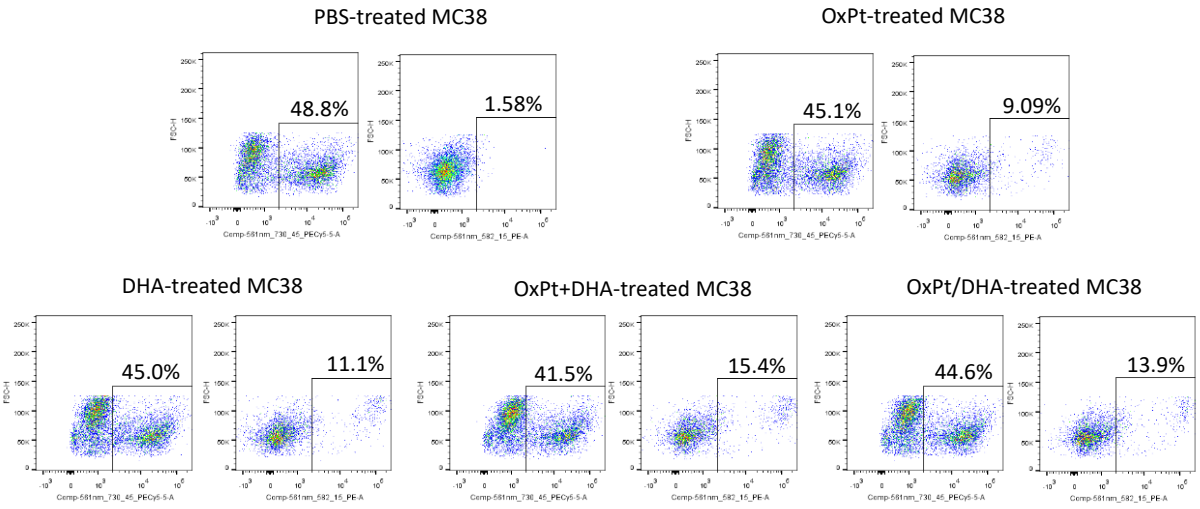

Figure 5-26 Uptake of treated MC38 cells by bone marrow-derived dendritic cells. Reprinted from *Nature Communications* **10**, 1899 (2019).

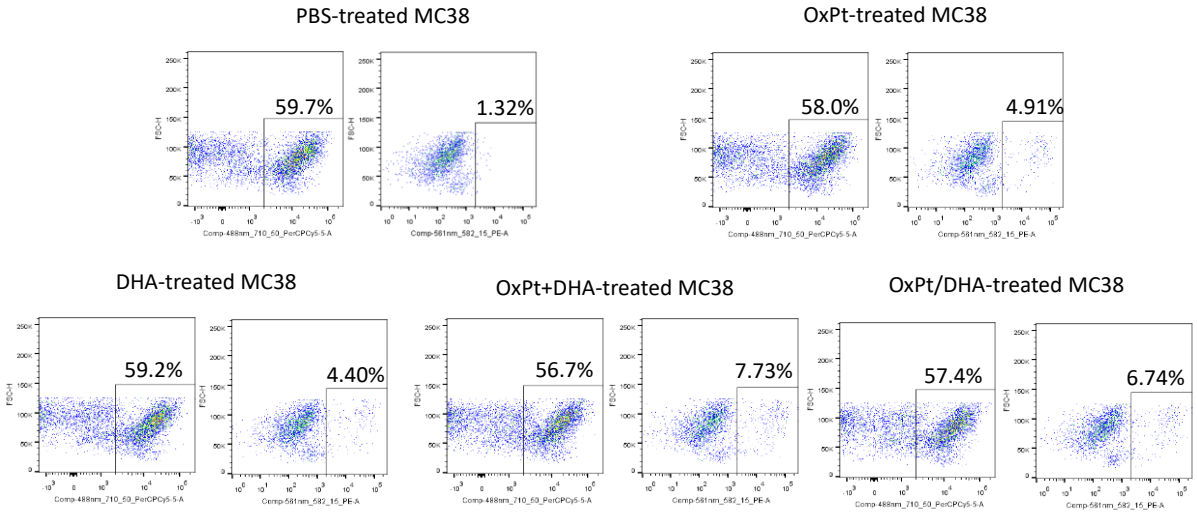

Figure 5-27 Uptake of treated MC38 cells by bone marrow-derived macrophages. Reprinted from *Nature Communications* **10**, 1899 (2019).

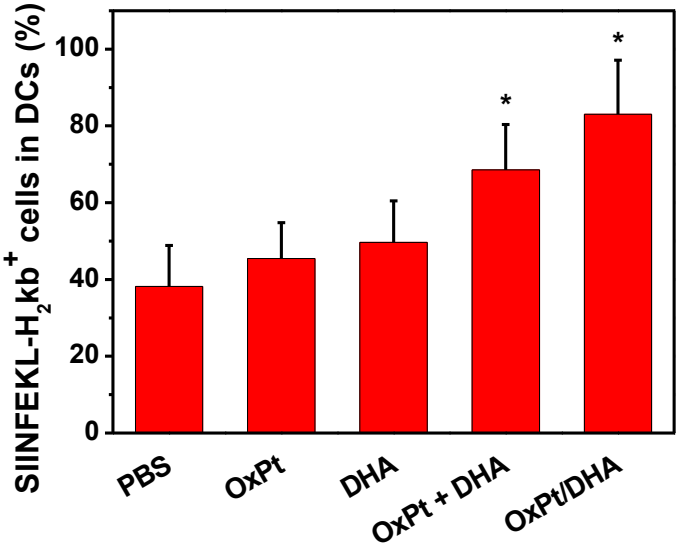

Figure 5-28 Antigen presentation profiles of DCs exposed to OxPt/DHA-treated MC38-OVA cells. Reprinted from *Nature Communications* **10**, 1899 (2019).

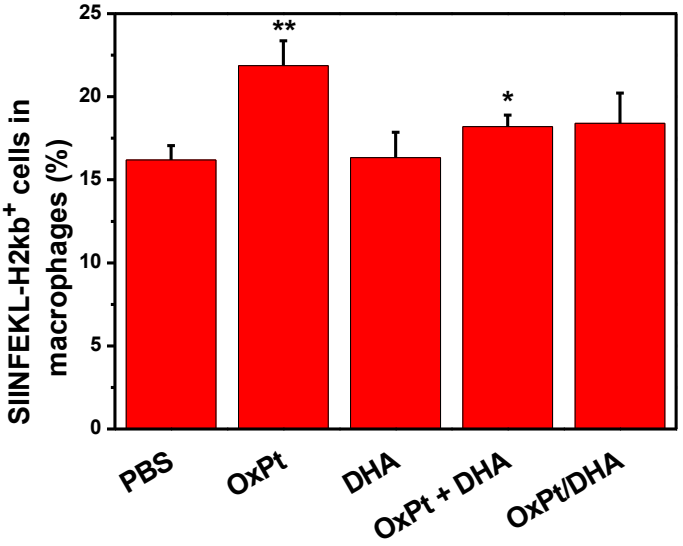

Figure 5-29 Antigen presentation profiles of macrophages exposed to OxPt/DHA-treated MC38-OVA cells. Reprinted from *Nature Communications* **10**, 1899 (2019).

To investigate whether OxPt/DHA could prime T cells, dead and/or dying MC38 cells treated with OxPt/DHA were inoculated into the footpads of C57BL/6 mice. Six days after inoculation, the regional popliteal lymph nodes were excised and stimulated with MC38 lysates *ex vivo*. Both OxPt- and DHA-treated cells were able to prime T cells for IFN-γ production (**Figure 5-30**), with the combination of OxPt and DHA showing the highest ability to prime T cells. In addition, the T cell priming ability of OxPt/DHA-treated MC38 cell lysates was much stronger than that of the known MC38 antigen KSPWFTTL (**Figure 5-31**).

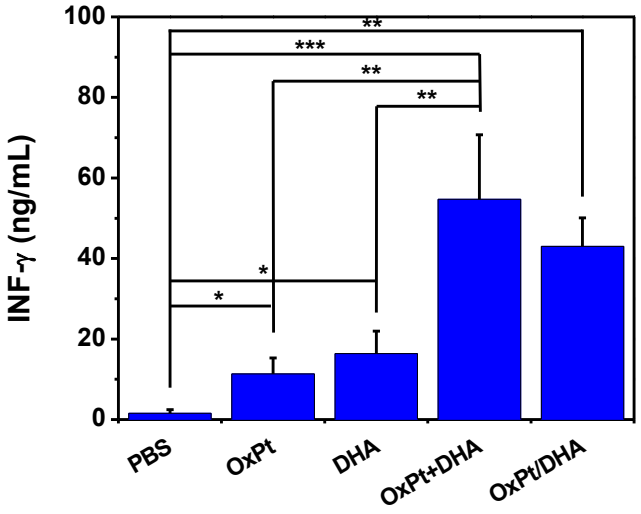

Figure 5-30 Priming of T-cell responses triggered by OxPt/DHA. MC38 tumor cells were treated with OxPt/DHA, and injected into the right footpads of C57BL/6 mice to determine the capacity of draining lymph node cells in producing IFN-γ in response to MC38 lysates. Reprinted from *Nature Communications* **10**, 1899 (2019).

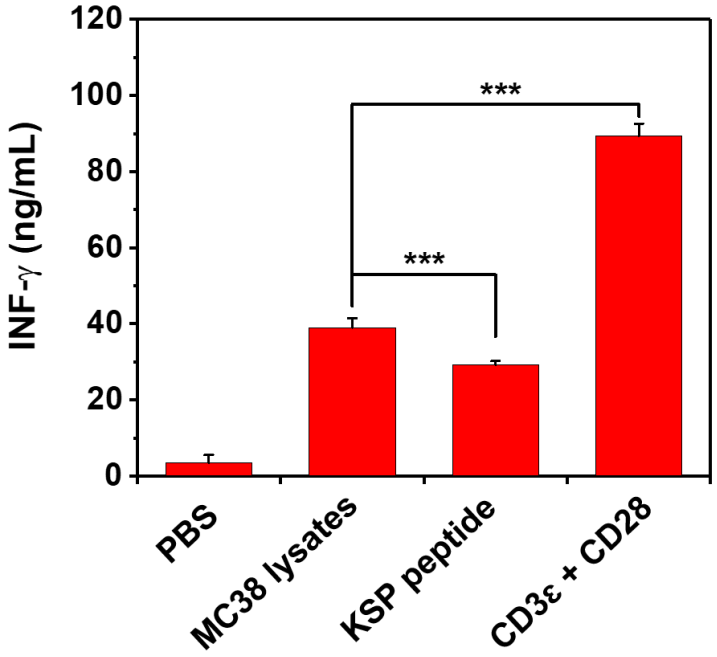

Figure 5-31 Production of IFN-γ by draining lymph node cells after stimulation by OxPt/DHA-treated MC38 cell lysates, KSP peptide, and CD3ε plus CD28. Reprinted from *Nature Communications* **10**, 1899 (2019).

Activation of T cells by OxPt and/or DHA treatment led to efficient vaccination specifically against MC38. OxPt or DHA-treated cells reduced the frequency of tumors developing from live cells to 33% and 17%, respectively, by day 30 (**Figure 5-32**). In comparison, 100% mice developed tumors with PBS-treated cells. This is consistent with *in vitro* results showing DHA is a stronger ICD inducer than OxPt, with a greater percentage of CRT^{+} cells and more HMGB-1 secretion. No tumor formation occurred when live MC38 cells were inoculated into mice vaccinated with OxPt+DHA- or OxPt/DHA-treated cells, but the immune system did not recognize the unrelated Lewis lung carcinoma LL/2 cells, leading to 100% tumor formation (**Figure 5-33**). Furthermore, these protective immune responses were lost in immunodeficient $Rag^{2-/-}$ mice, leading to 100% tumor formation in mice regardless of vaccination (**Figure 5-34**).

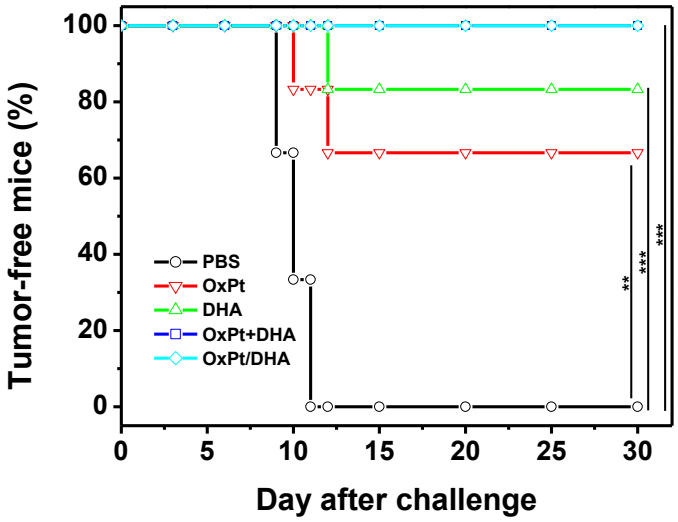

Figure 5-32 *In vivo* anticancer vaccination of OxPt/DHA on C57BL/6 mice. Reprinted from *Nature Communications* **10**, 1899 (2019).

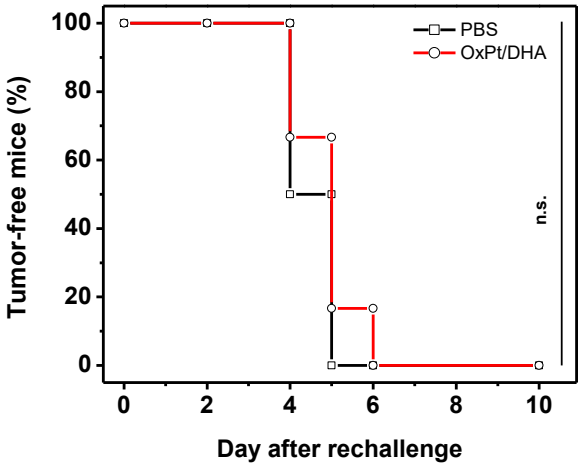

Figure 5-33 Specific antitumor immunity elicited by OxPt/DHA-treated cells. Animals immunized with OxPt/DHA-treated MC38 cells that remain tumor-free 30 d after challenge with live MC38 were rechallenged with unrelated LL/2 cells. Reprinted from *Nature Communications* **10**, 1899 (2019).

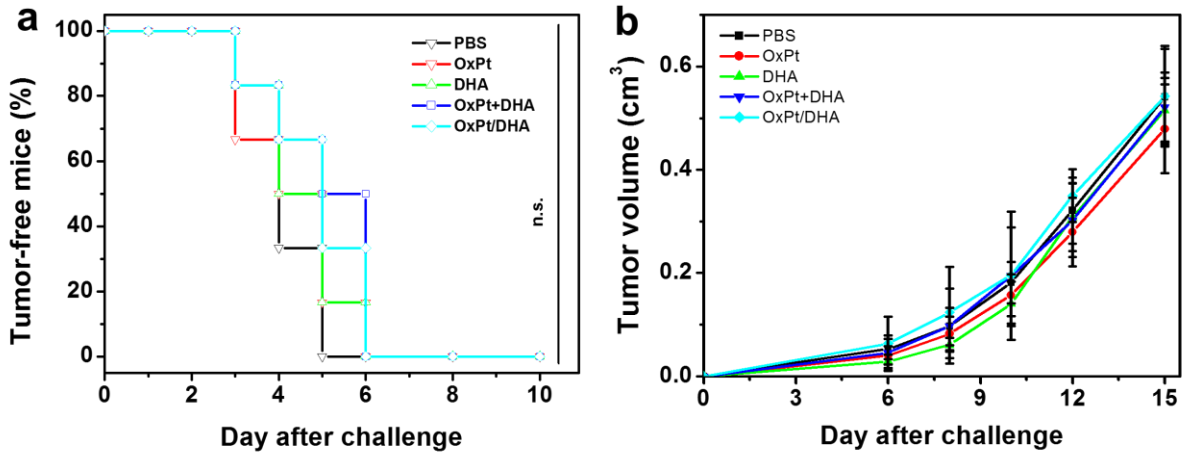

Figure 5-34 (a) *In vivo* anticancer vaccination and (b) subsequent tumor growth of OxPt/DHA on immunocompromised Rag2$^{-/-}$ C57BL/6 mice. Reprinted from *Nature Communications* **10**, 1899 (2019).

5.2.5 Anticancer efficacy

Recognizing the immunogenicity of OxPt and DHA, we investigated OxPt/DHA in combination with α-PD-L1checkpoint blockade. Syngeneic tumor models of CT26 and MC38 were established on immunocompetent BALB/c and C57BL/6 mice, respectively, and tumors were allowed to grow for approximately 12 days, reaching 80-120 mm^3 before treatment. As minimal toxicity by body weight was observed after 50 doses of Zn/DHA at 5 mg DHA/kg, 4 weekly doses of OxPt/DHA at 60 mg OxPt/kg, or one dose of OxPt/DHA at 80 mg OxPt/kg (**Figure 5-35**), we chose a dose of 8 mg OxPt/kg, 2.8 mg DHA/kg, and/or 75 μg α-PD-L1/mouse. This dose represents at least 10 times lower than the maximum tolerated dose (MTD) and allows for frequent low-dose metronomic dosing as opposed to conventional infrequent doses at or near the MTD.[28]

Mice were i.p. injected once every three days for up to 12 total doses (**Scheme 5-7**). With significant OxPt accumulation in tumors 72 h post-administration (**Figure 5-36**), this dosing

schedule allows for a dose-dense chemotherapy schedule with a near continuous presence of chemotherapy in the tumor. This is in line with the Norton-Simon hypothesis that more frequent doses will lead to greater clinical benefit by minimizing the opportunities for cancer regrowth between doses.[29] Importantly, OxPt/DHA increases the effective doses of OxPt and DHA by ~15 and 1000 times, respectively (**Table 5-4**). Nearly all of the free drugs are cleared out of or decomposed in the bloodstream within one hour of intravenous injection (**Figure 5-37, Figure 5-38**). Despite this, free OxPt leads to significant peripheral neuropathy while OxPt/DHA shows no such toxicity (**Figure 5-39**).

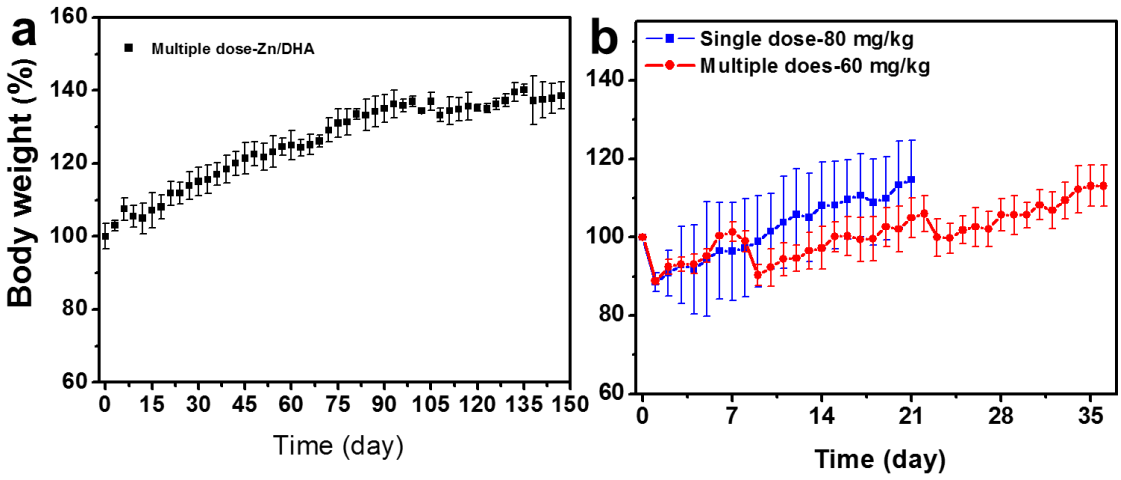

Figure 5-35 Limited toxicity by chemotherapeutic NCPs. (a) Body weight evolution of BALB/c mice after multiple injections (5 mg DHA/kg once every three days for a total of fifty doses). (b) Body weight evolution of C57BL/6 mice after single injection (80 mg OxPt/kg) and multiple injections (60 mg OxPt/kg once every week for a total of four doses) of OxPt/DHA. Reprinted from *Nature Communications* **10**, 1899 (2019).

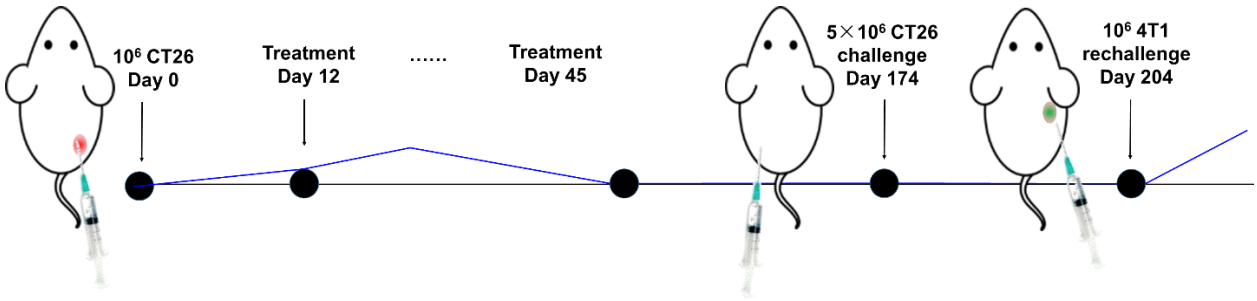

Scheme 5-7 Experimental design for the treatment and challenge of CT26 tumor-bearing mice. Tumors were allowed to grow for 12 days before treatment to form more immunosuppressive tumors. Then, tumor-bearing mice were intraperitoneally injected with OxPt/DHA combined with α-PD-L1 every three days for 12 total doses. Three months after all tumors had disappeared, mice were challenged with CT26 cells, followed by rechallenge with 4T1 one month later. Reprinted from *Nature Communications* **10**, 1899 (2019).

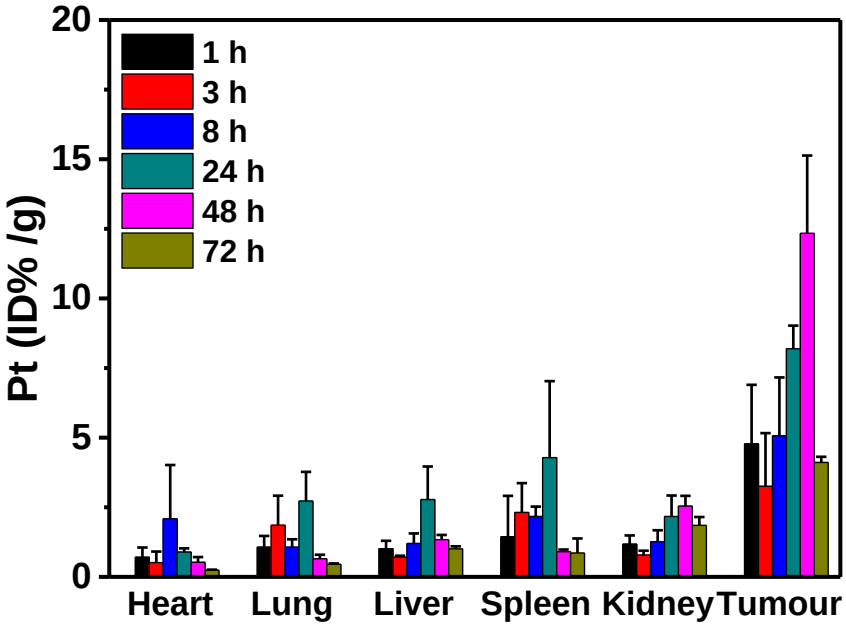

Figure 5-36 Time-dependent Pt biodistribution of OxPt/DHA after i.p. injection to CT26-bearing mice. Reprinted from *Nature Communications* **10**, 1899 (2019).

Table 5-4 OxPt and DHA pharmacokinetic information. Reprinted from *Nature Communications* **10**, 1899 (2019).

Parameter (Unit)	$t_{1/2}$ alpha (h)	$t_{1/2}$ beta (h)	AUC 0-inf (ID%mL^{-1}h)	AUMC (ID%mL^{-1}h^2)	MRT (h)
Free OxPt	0.18 ± 0.02	14.67 ± 3.04	5.77 ± 2.65	122.5 ± 77.5	20.1 ± 4.4
Free DHA[a]	(0.22 ± 0.04) [b]		(0.03 ± 0.01) [b]	(0.59 ± 0.16) [b]	(0.31 ± 0.06) [b]
OxPt/DHA	0.27 ± 0.30 (0.39 ± 0.38) [b]	20.70 ± 4.50 (7.01 ± 1.13) [b]	80.9 ± 11.2 (33.6 ± 5.8) [b]	2431.5 ± 809.7 (330.2 ± 79.8) [b]	29.51 ± 6.27 (9.79 ± 1.41) [b]

[a] This was fitted to a one-compartment model.

[b] The numbers in parentheses refer to DHA values.

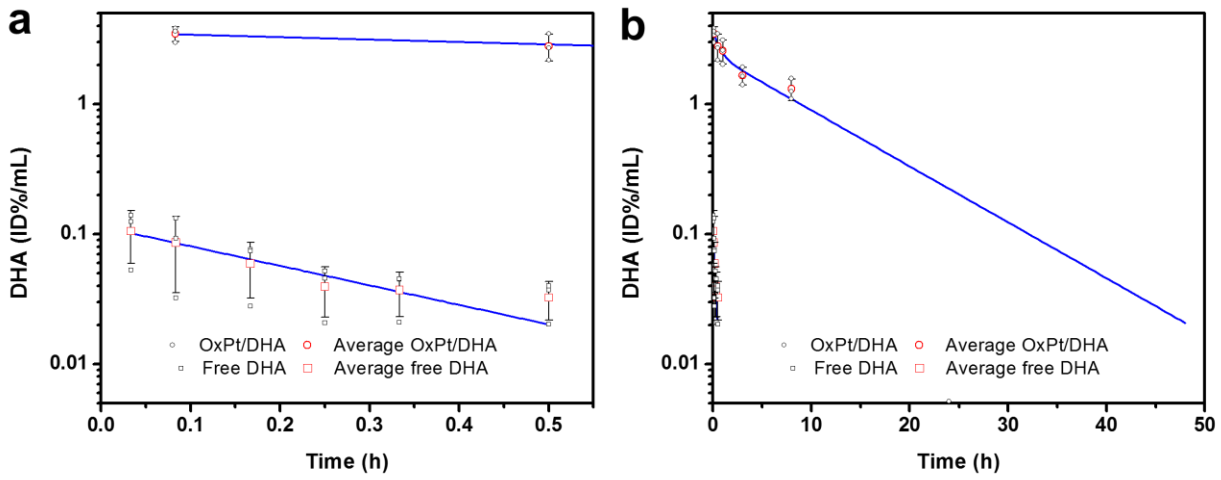

Figure 5-37 Time-dependent DHA concentrations in the bloodstream from (a) 0-0.5 and (b) 0-48 h after i.v. injection of DHA or OxPt/DHA to SD/CD rats. Reprinted from *Nature Communications* **10**, 1899 (2019).

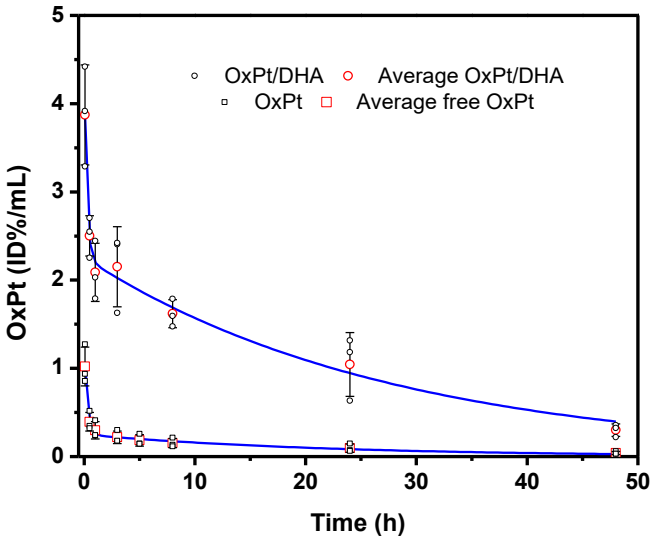

Figure 5-38 Time-dependent OxPt concentrations in the bloodstream from 0-48 h after i.v. injection of DHA or OxPt/DHA to SD/CD rats. Reprinted from *Nature Communications* **10**, 1899 (2019).

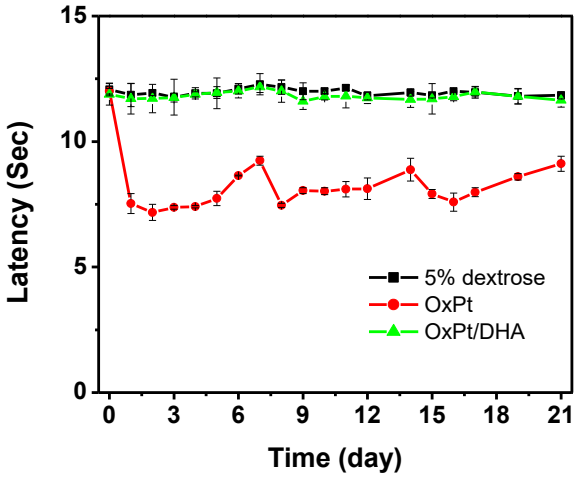

Figure 5-39 Rats dosed with OxPt (8 mg/kg) showed thermal hyperalgesia compared to those treated with OxPt/DHA (8 mg OxPt/kg and 2.8 mg DHA/kg) or 5% dextrose control, causing the rats to withdraw their paws away from a heat stimulus after ~7-8 seconds as opposed to ~12 seconds. Reprinted from *Nature Communications* **10**, 1899 (2019).

In CT26 tumor-bearing mice, the low-dose α-PD-L1 treatment alone was ineffective at controlling tumor growth. The combination of free OxPt, DHA, and α-PD-L1 proved moderately effective (203.27 ± 81.00 mm^3 on day 18 compared to 616.80 ± 46.59 mm^3 for PBS) but extremely toxic, as the body weight steadily decreased (**Figure 5-40**). All mice had to be euthanized after three doses for humanitarian reasons in accordance with our animal protocols. We hypothesized that NCPs can decrease the toxicity of OxPt and DHA by providing a favorable biodistribution profile. In CT26 tumor-bearing mice, < 5 %ID Pt/g accumulated in key organs such as the liver, spleen, and kidney indicating OxPt/DHA is not significantly uptaken by the MPS. Furthermore, there was < 3 %ID Pt/g accumulation in the heart and lung, suggesting OxPt/DHA does not aggregate in circulation. The low MPS uptake and slow clearance led to progressive accumulation in tumor to a maximum of 12.3 ± 2.8 %ID/g at 48 h post administration as a result of the enhanced permeability and retention effect compared to 0.56 ± 2.8 %ID/g by the free drug (**Figure 5-36, Figure 5-41**). OxPt NCP with or without α-PD-L1 was well tolerated and led to similar tumor growth rates, significantly controlling tumor growth and retarding tumor growth for over one month. Interestingly, though Zn/DHA did not show substantial anticancer efficacy alone or in combination with α-PD-L1 (**Figure 5-42**), it significantly enhanced the efficacy of OxPt and delayed tumor growth to ~2 cm^3 until day 66. The tumor growth curve of OxPt/DHA plus α-PD-L1 was initially similar to that of OxPt/DHA, but started to deviate around day 18, after which all of the tumors regressed and eventually disappeared on days 40-50. No tumor recurrence was observed for a period of 120 days (**Figure 5-43**).

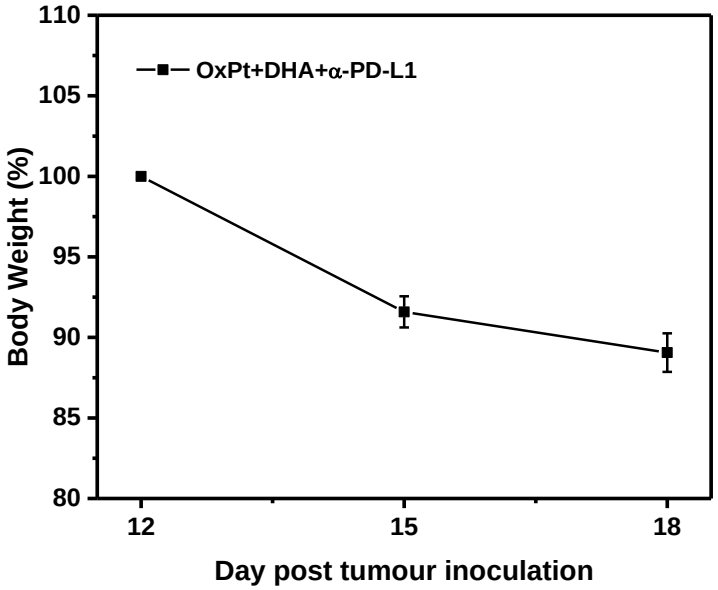

Figure 5-40 Body weight evolution of mice treated with the free OxPt, DHA and anti-PD-L1 at 8 mg OxPt/kg, 2.8 mg DHA/kg and 75 μg/mouse anti-PD-L1. Reprinted from *Nature Communications* **10**, 1899 (2019).

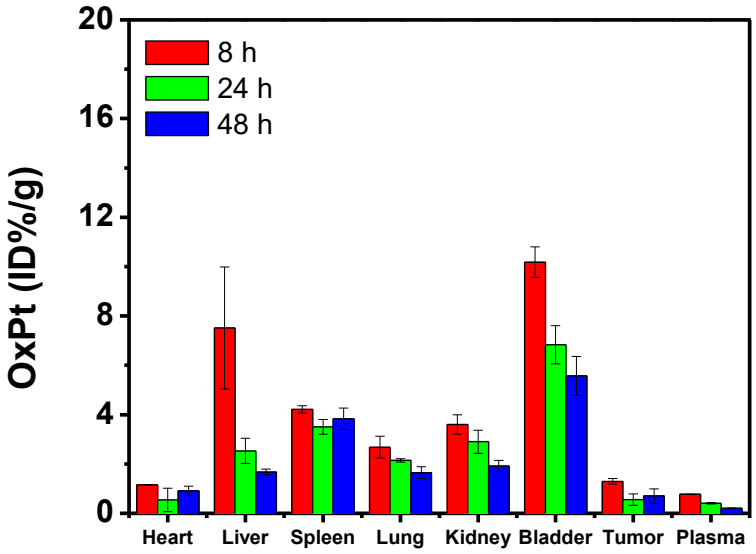

Figure 5-41 Time-dependent Pt biodistribution of free OxPt after i.p. administration. Reprinted from *Nature Communications* **10**, 1899 (2019).

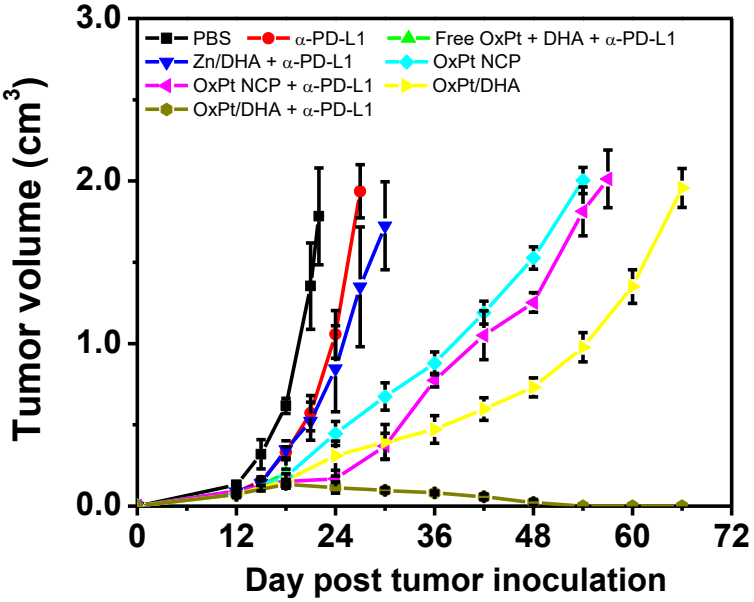

Figure 5-42 CT26 tumor growth curve after treated with various formulations. Reprinted from *Nature Communications* **10**, 1899 (2019).

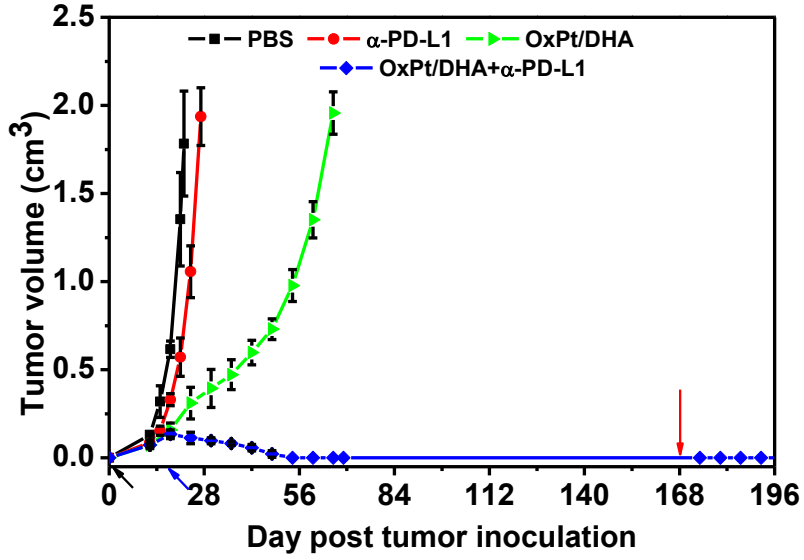

Figure 5-43 Growth curves of CT26 tumors after treatment with OxPt/DHA combined with α-PD-L1 and challenge with CT26 cells (red arrow). Reprinted from *Nature Communications* **10**, 1899 (2019).

The antitumor immune response initiated by OxPt/DHA plus α-PD-L1 resulted in a memory response; OxPt/DHA and α-PD-L1-treated mice which were tumor-free for at least 120 days were challenged with live CT26 cells on the contralateral flank. No mice grew new tumors over the next month compared to 100% tumor formation in naïve mice inoculated with the same cell passage or mice with surgically removed CT26 (**Scheme 5-8, Figure 5-43, Figure 5-44**), indicating OxPt/DHA plus α-PD-L1 generated long-lasting antitumor immunity to prevent cancer relapse. The immune memory was found to be tumor specific, as subsequent rechallenge with live murine mammary adenocarcinoma 4T1 cells in the mammary fat pad showed no difference in growth compared to cells implanted in naïve mice (**Figure 5-45**).

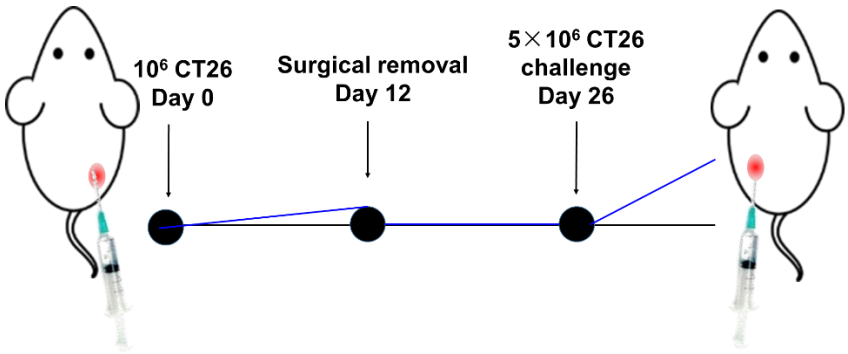

Scheme 5-8 Experimental design for surgery control of CT26 tumor-bearing mice. Reprinted from *Nature Communications* **10**, 1899 (2019).

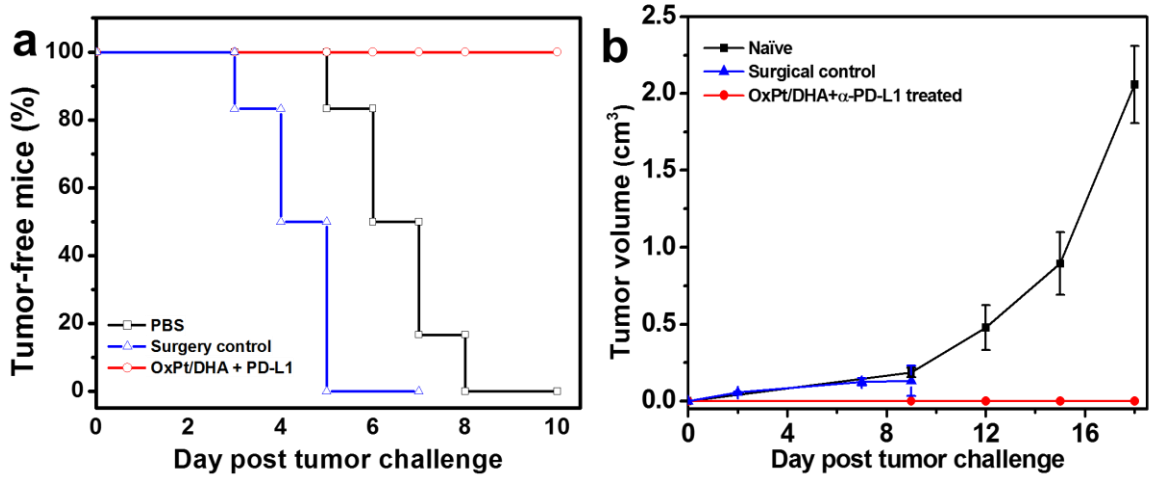

Figure 5-44 (a) Percentage tumor-free mice and (b) tumor growth curve after challenge with CT26 cells in naïve mice, mice with surgically removed CT26 tumors, or OxPt/DHA and α-PD-L1-treated mice. Reprinted from *Nature Communications* **10**, 1899 (2019).

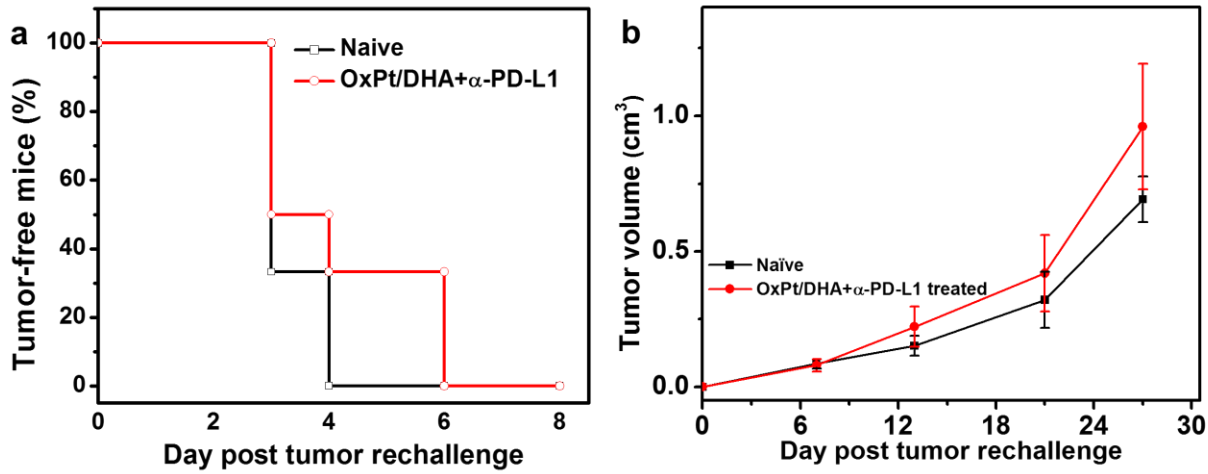

Figure 5-45 (a) Percentage tumor-free mice and (b) tumor growth curve after rechallenge with 4T1 cells in naïve mice or OxPt/DHA and α-PD-L1-treated mice. Reprinted from *Nature Communications* **10**, 1899 (2019).

We confirmed these results on the more immunosuppressive model of MC38 tumors in C57BL/6 mice, which yielded similar results under the same treatment regimen (**Figure 5-46**). The chemoimmunotherapy of free OxPt, DHA, and α-PD-L1 was initially effective at controlling tumor growth, but eventually the tumors grew aggressively and the mice had to be euthanized due to the tumor burden on day 39. OxPt/DHA showed similar anticancer efficacy, but continued to control the tumors until day 54. Tumors treated with OxPt/DHA and α-PD-L1 regressed around day 18 and were controlled for an extended period of time, but eventually grew back (**Figure 5-46**). By increasing the chemotherapy dose to 16 mg OxPt/kg and 4.6 mg DHA/kg with 75 μg α-PD-L1/mouse, 3 out of 5 treated mice were tumor free and the remaining 2 mice showed prolonged tumor growth control (**Figure 5-47**). The contribution of the immune system to OxPt/DHA and α-PD-L1 anticancer efficacy was immediately obvious as no therapeutic effect was observed when MC38 tumors implanted in immunodeficient $Rag^{2-/-}$ mice were treated with OxPt/DHA plus α-PD-L1 (**Figure 5-48**).

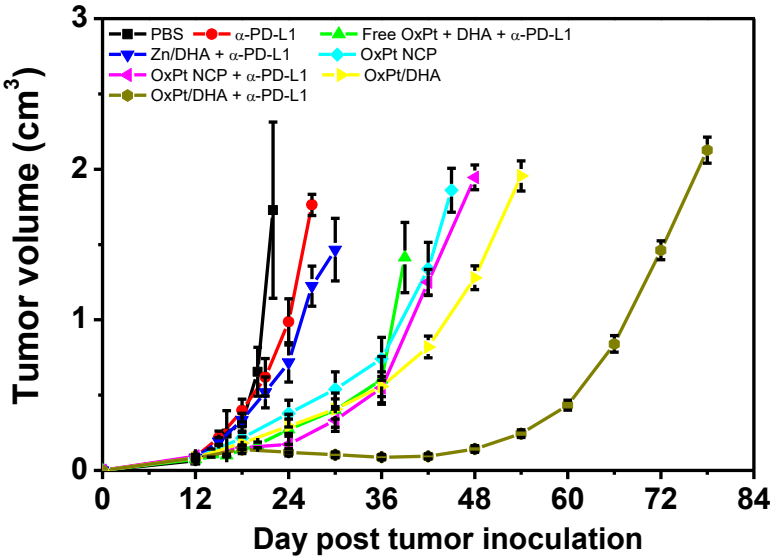

Figure 5-46 Therapeutic effect of various formulations on C57BL/6 at equivalent doses of 8 mg/kg OxPt. Reprinted from *Nature Communications* **10**, 1899 (2019).

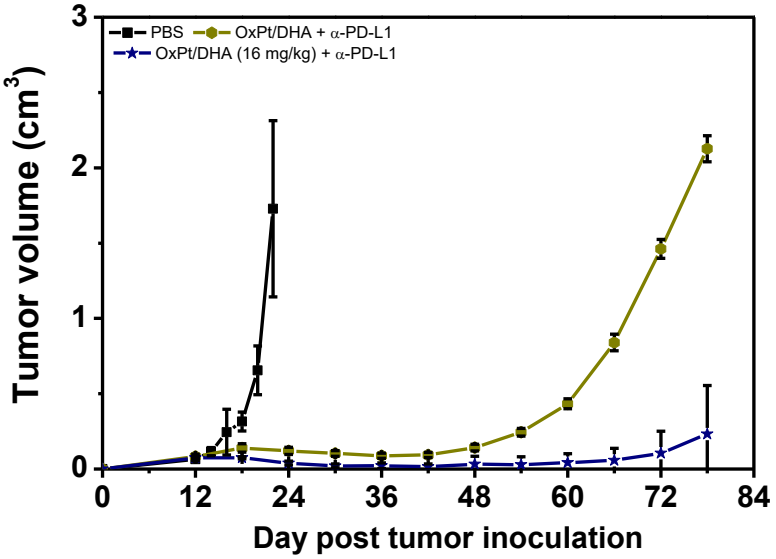

Figure 5-47 Comparing the therapeutic effect of OxPt/DHA plus α-PD-L1 on wildtype C57BL/6 at doses of 8 mg/kg OxPt and 16 mg/kg OxPt with 75μg α-PD-L1. Reprinted from *Nature Communications* **10**, 1899 (2019).

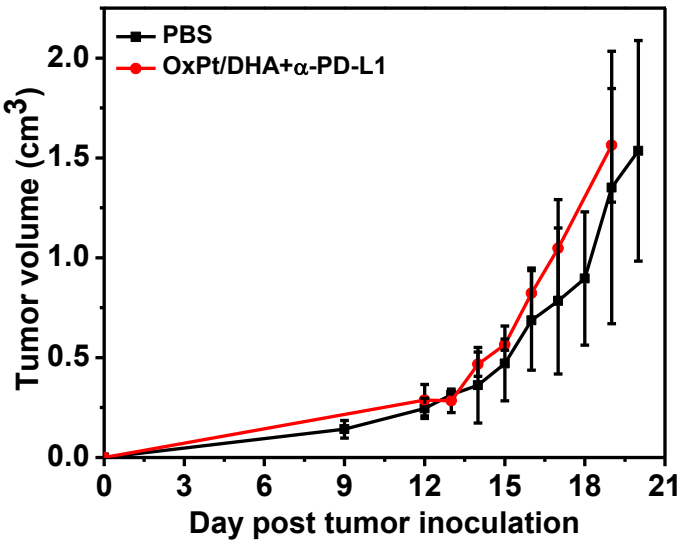

Figure 5-48 Therapeutic effect of OxPt/DHA plus α-PD-L1 on C57BL/6 $Rag2^{-/-}$ mice at a dose of 8 mg/kg OxPt. Reprinted from *Nature Communications* **10**, 1899 (2019).

5.2.6 Antitumor immunity

Immunogenic therapies are known to induce an innate immune response, including rapid infiltration of phagocytic DCs and macrophages. As the activation of DCs may constitute the first of several steps in the immune development process,[30] we first investigated the intratumoral levels of antigen-presenting innate cells. We observed increased tumor infiltration of $CD11c^+$ and $F4/80^+$ cells two days after the first treatment with OxPt/DHA plus α-PD-L1 (**Figure 5-49**). The main function of DCs is to process antigen materials and present them to the T cells to promote immunity,[31, 32] while macrophages can engulf and digest cellular debris and secrete pro-inflammatory cytokines to recruit other immune cells in addition to presenting antigens to DCs.[33] The enhanced infiltration of DCs and macrophages in tumors might result from the improved immunogenicity caused by OxPt/DHA, allowing for efficient antigen capture and presentation. We also investigated the infiltration of DCs and macrophages 12 days after the first treatment. The

percentage of DCs slightly, though not significantly, increased in tumors treated with OxPt/DHA plus α-PD-L1 (**Scheme 5-9, Figure 5-50a**). As this is also equivalent to the third day after the fourth treatment, the lower infiltration may also coincide with DC migration to the regional lymph nodes for antigen presentation.[34] The percentages of macrophages was still significantly increased in mice treated with either OxPt/DHA alone or in combination with α-PD-L1 (**Figure 5-50b**). Only OxPt/DHA with α-PD-L1 significantly increased the percentage of M1 macrophages in total macrophages in tumors (**Figure 5-50c**), suggesting the combination treatment enhances polarization to M1 macrophages or recruits more M1 macrophages into tumors to facilitate antigen presentation. By recruiting DCs and macrophages to phagocytize dying and/or dead cancer cells and enhancing the processing/presentation of tumor associated antigens to T cells, OxPt/DHA may have increased the density of $CD8^+$ T cells in tumors to potentiate checkpoint blockade immunotherapy.

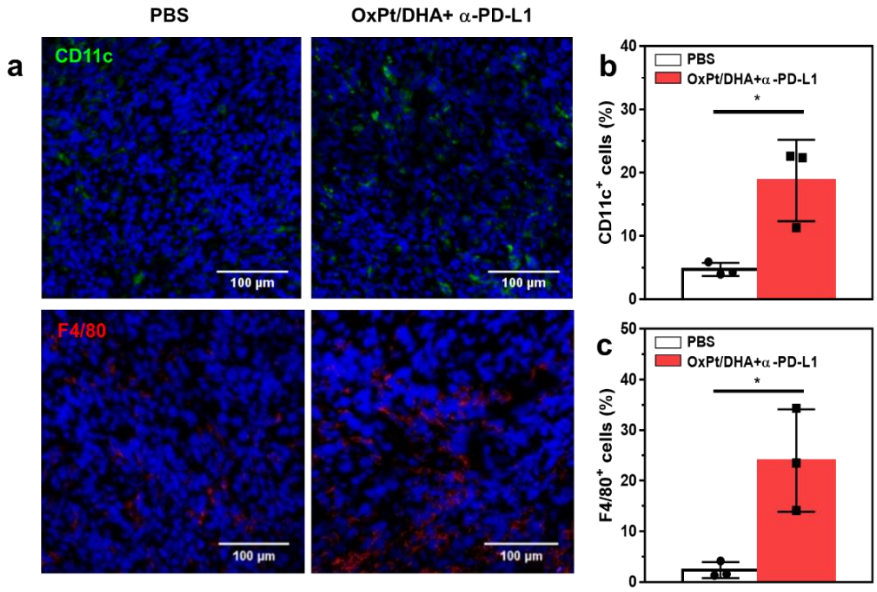

Figure 5-49 (a) Immunofluorescence analysis showing the infiltration of dendritic cells and macrophages two days after treatment. The densities of (b) $CD11c^+$ and (c) $F4/80^+$ cells in the whole tumors two days after treatment, from the confocal images of immunofluorescence staining. Reprinted from *Nature Communications* **10**, 1899 (2019).

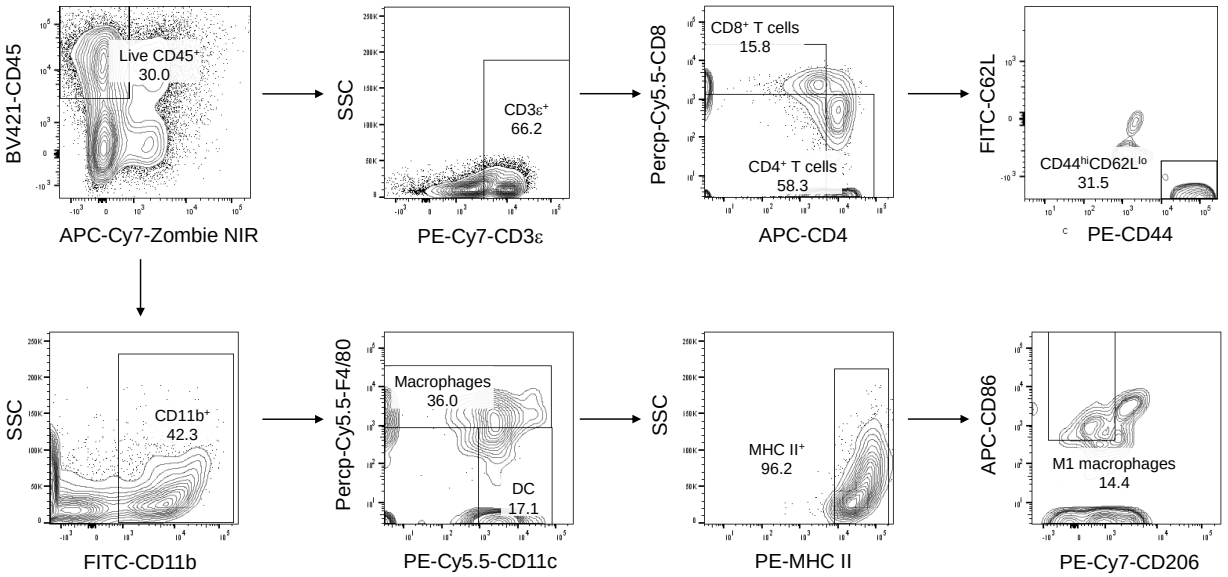

Scheme 5-9 Gating strategies for flow cytometry studies. All cells were gated from Zombie NIR negative cells. Total leukocytes were gated on $CD45^+$ cells; $CD4^+$ T cells were gated on $CD4^+CD3\varepsilon^+CD45^+$ cells; $CD8^+$ T cells were gated on $CD8\alpha^+CD3\varepsilon^+CD45^+$ cells; effector memory cells were gated on $CD44^{hi}CD62L^{lo}$ $CD8\alpha^+CD3\varepsilon^+CD45^+$ cells; macrophages were gated on $F4/80^+CD11b^+CD45^+$ cells; M1 macrophages were gated on $CD86^+CD206^-$ $MHCII^+F4/80^+CD11b^+CD45^+$ cells; dendritic cells were gated on $CD11c^+F4/80^-CD11b^+CD45^+$ cells. Reprinted from *Nature Communications* **10**, 1899 (2019).

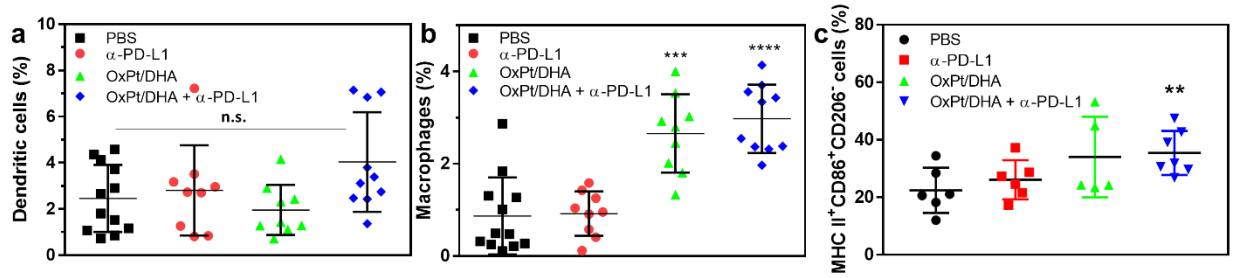

Figure 5-50 OxPt/DHA promotes innate immune cell infiltration. Proportion of (a) dendritic cells and (b) macrophages out of all cells in tumors and (c) M1 macrophages cells out of all macrophages in tumors by flow cytometry of cell-surface staining 12 days after the first treatment. Reprinted from *Nature Communications* **10**, 1899 (2019).

Tumors with low densities of $CD8^+$ T cells, such as MC38, do not generally respond to PD-1/PD-L1 blockade.[35-37] Effective combination therapy can increase the intratumoral infiltration of

$CD8^+$ T cells to significantly increase the response rate. Immunofluorescence analysis performed 12 days after the first treatment with OxPt/DHA plus α-PD-L1 showed significant increase in the density of infiltrating $CD3\varepsilon^+$ cells, which were primarily $CD8^+$ (**Figure 5-51, Figure 5-52**), providing the evidence for treatment-related change in the tumor microenvironment increasing the number of cytotoxic T cells. The flow cytometry data also showed that mice treated with OxPt/DHA had an increase in the number of $CD8^+$ T cells in tumors, which increased further when α-PD-L1 was added (**Figure 5-53a**), but no significant difference was observed in total $CD45^+$ leukocyte or $CD4^+$ T cell infiltration (**Figure 5-53b,c**). $CD8^+$ T cells increased 0.97-fold ($p = 2.5 \times 10^{-2}$) and 4.09-fold ($p = 2.7\times10^{-5}$) in tumors treated with OxPt/DHA alone or with α-PD-L1, compared with PBS group, respectively. The immune response was further determined to be MC38-specific by Enzyme-Linked ImmunoSpot (ELISPOT) assay to detect the presence of tumor antigen-specific T cells in the leukocyte-abundant spleens of MC38 tumor-bearing mice (**Figure 5-53d**). The harvested splenocytes were stimulated with KSPWFTTL, the tumor associated antigen peptide presented by MHC I $H\text{-}2K^b$, for 48 h to detect the antigen specific $CD8^+$ T cells. The number of antigen-specific IFN-γ producing T cells was significantly increased in tumor-bearing mice treated with OxPt/DHA, indicating that OxPt/DHA effectively generates tumor-specific T cell response, which could be further enhanced by the addition of α-PD-L1. Further investigation demonstrated a significant increase in $CD44^{high}CD62L^{low}$ effector memory T cells in the spleen after treatment with OxPt/DHA plus α-PD-L1 (**Figure 5-53e**), which suggests that T cells might be involved in the long-term memory response. However, the exact subset of responsible immune cells remains to be elucidated.

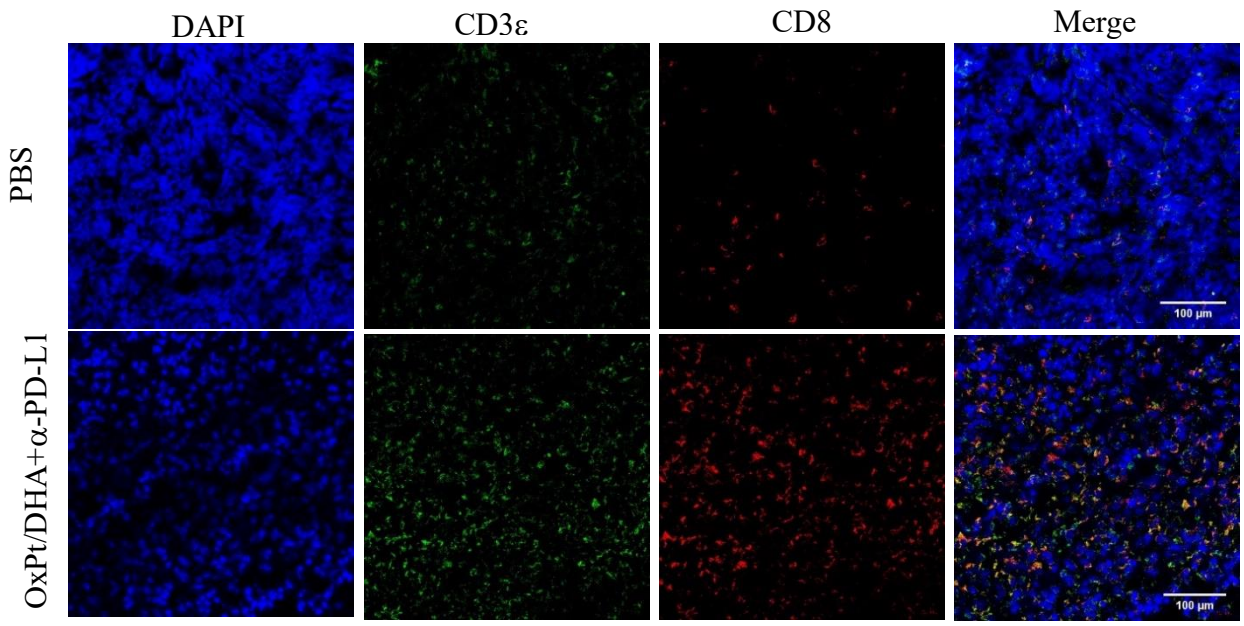

Figure 5-51 $CD8^+$ T cell infiltration into the tumors of MC38 tumor-bearing mice 12 days after the first treatment. Reprinted from *Nature Communications* **10**, 1899 (2019).

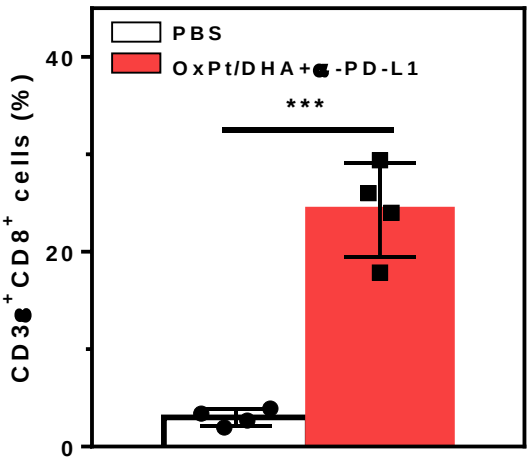

Figure 5-52 The density of $CD8^+$ T cells in the whole tumors, analyzed from the confocal images of immunofluorescence staining. Reprinted from *Nature Communications* **10**, 1899 (2019).

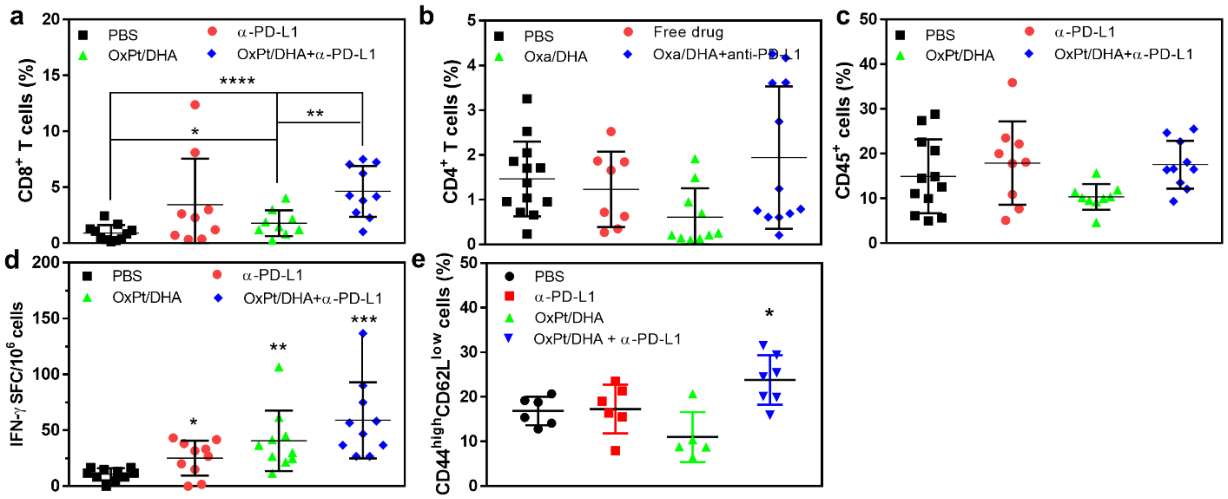

Figure 5-53 OxPt/DHA promotes tumor-specific T cell response. (a) $CD8^+$ T cells, (b) $CD4^+$ T cells, and (c) $CD45^+$ cells in tumors by flow cytometry of cell-surface staining 12 days after the first treatment. (d) KSP antigen-specific IFN-γ producing T cells detected by ELISPOT assay 12 days after the first treatment. (e) The percentage of effector memory T cells in total CD8+ T cells in spleens after treatment with OxPt/DHA with α-PD-L1. Reprinted from *Nature Communications* **10**, 1899 (2019).

5.3 Discussion

As a well-tolerated antimalarial drug, DHA is a strong candidate for anticancer therapy. Higher levels of iron in tumors catalytically decomposes the reactive endoperoxide to generate ROS. However, the low bioavailability and rapid decomposition of DHA in sera present two major obstacles to using DHA in cancer therapy. By synthesizing a cleavable prodrug and encapsulating it into the lipid bilayer shell of an NCP, DHA can be shielded from the water in circulation and released only after particle dissociation upon cellular uptake. Intracellular release of DHA from chol-DHA can occur via disulfide cleavage and hydrolysis. The OxPt-bp coordination polymer can also release free OxPt directly by ascorbate reduction or via hydrolysis to OxPt-bc followed by reduction (**Scheme 5-5, Scheme 5-6**). The dual release pathways for both DHA and OxPt may be beneficial in avoiding resistance mechanisms. Specifically, OxPt-bc prodrug is resistant to

deactivation by GSH and thiol-containing proteins, allowing for prolonged drug exposure when reduced to parent OxPt by ascorbate in cytosols and even nuclei of cancer cells.

Chemotherapies are often beleaguered by toxicities arising from accumulation in healthy tissues, which can be alleviated with nanoparticle delivery.[38-40] OxPt/DHA are optimally sized pegylated nanoparticles that are large enough to avoid renal filtration (~10 nm) but small enough to penetrate through the leaky tumor vasculatures in tumors.[41-43] The use of ~20 mol% PEG in this formulation helps to reduce plasma protein binding, thus minimizing MPS uptake after systemic injection.[44-48] OxPt/DHA showed low uptake in the liver and other major organs associated with clearance, and significantly increased both the single and repeated dose MTDs of OxPt. Mice were dosed near the free drug MTD, but only one tenth the single dose MTD of the NCP formulation, allowing for dose-dense metronomic chemotherapy. This significantly reduced the most common dose-limiting toxicity of peripheral neuropathy while maintaining strong anticancer efficacy and immunity, suggesting that OxPt/DHA may be a strong clinical candidate.

Nanoparticle-supported chemoimmunotherapy has become increasingly studied to alter the tumor microenvironment in recent years.[49-52] Though many chemotherapeutic agents mediate their cytotoxic effects by inducing immunologically silent or tolerogenic apoptosis, certain chemotherapies kill cancer cells via immunogenic apoptosis. This changes the cell surface composition and releases DAMPs, of which there are three hallmarks: (i) the pre-apoptotic exposure of CRT on the cell surface, (ii) release of ATP during the blebbing phase of apoptosis, and (iii) post-apoptotic exodus of the chromatin-binding protein HMGB-1.[53] While OxPt is a known ICD inducer, we have directly shown that treatment of CRC cells with DHA causes translocation of CRT to the cell surface and HMGB-1 release. This facilitates the recruitment of antigen presenting cells (APCs) into the tumor bed (stimulated by ATP), the engulfment of dying

tumor cells and their debris by APCs (stimulated by CRT),[23, 54] and optimal antigen presentation to T cells (stimulated by HMGB-1).[55, 56] DHA-treated CRC cells were uptaken more by phagocytes and led to strong T cell priming and antitumor vaccination. Altogether, these processes result in a potent IFN-γ-mediated immune response, which eventually can lead to tumor rejection.[57]

OxPt/DHA combined with α-PD-L1 is highly effective in treating well-developed tumors of CT26, likely due to innately high T cell and low suppressor cell infiltration.[58, 59] This treatment led to eradication of 6/6 tumors and tumor-specific immune responses resulting in vaccination against subsequent live cell challenge. In contrast, the MC38 tumor model is highly immunosuppressive, with myeloid derived suppressor cells constituting >50% of the $CD45^+$ immune cells in tumors.[58] A higher dose of OxPt/DHA could approximately recapitulate the effects observed in CT26, with tumor eradication in 3/5 mice and long-term tumor control in the other two. Treatment with OxPt/DHA led to ICD in tumors followed by infiltration of and engulfment by phagocytes. These APCs can present tumor-specific antigens to naïve T cells in the lymph nodes and eventual T cell infiltration into the tumors as part of the adaptive immune response. Anti-PD-L1 ameliorates immune suppressive mechanisms of tumor cells causing immune evasion and T cell anergy and/or exhaustion (**Scheme 5-10**).[60]

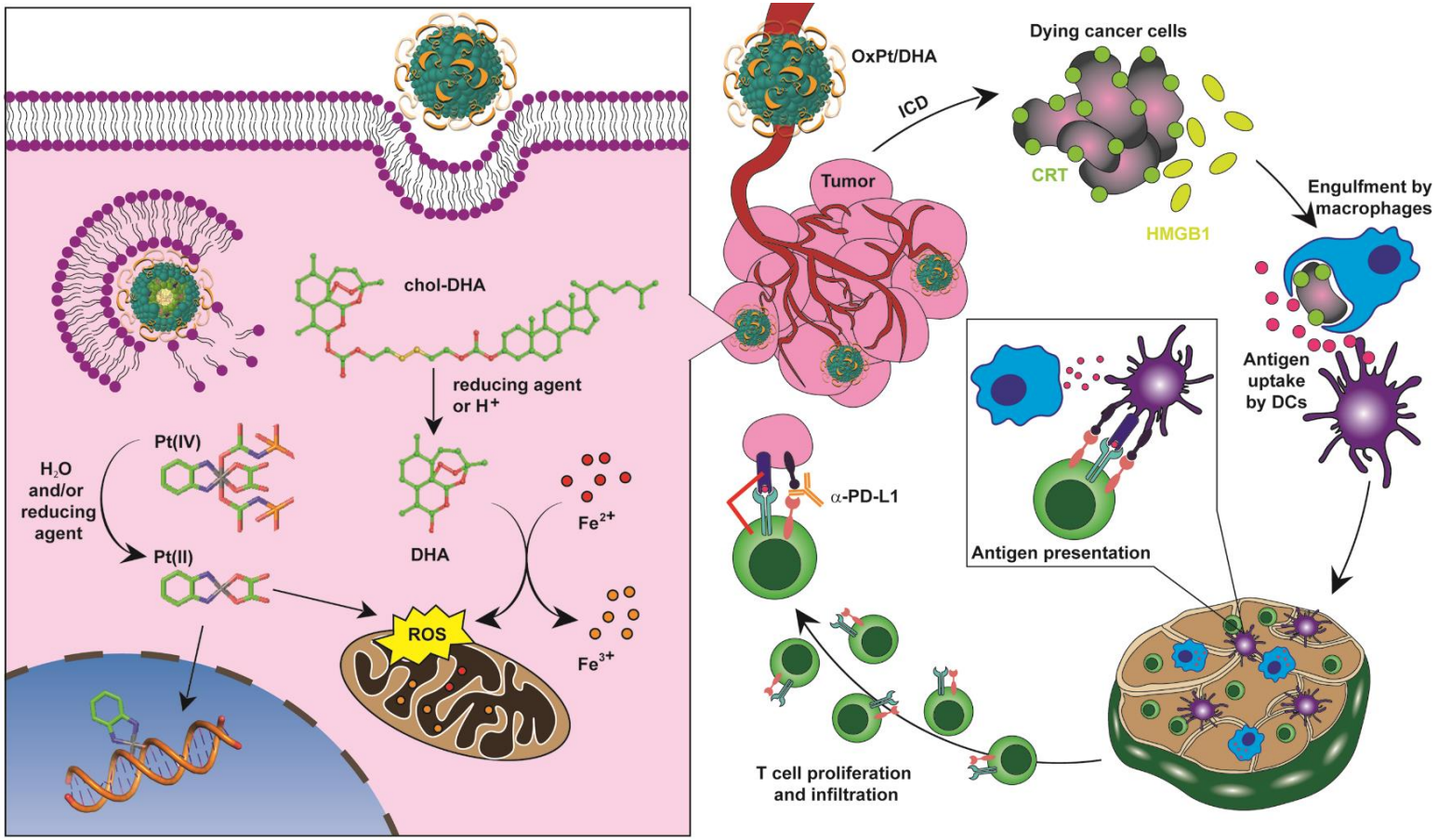

Scheme 5-10 Anticancer and immune mechanisms of OxPt/DHA. left, The disruption of the lipid bilayer of OxPt/DHA upon endocytosis exposes the chol-DHA and OxPt prodrugs to triggered release by hydrolysis and/or reduction. The resultant parent drugs exhibit the expected mechanisms of action of DNA adduct formation and/or ROS generation. right, Systemically delivered OxPt/DHA can accumulate in the tumors and release the drug payload, as shown on the left, for immunogenic cell death of the cancer cells. Cell-surface CRT expression and release of DAMPs, such as HMGB-1, lead to phagocytosis by macrophages and/or dendritic cells, which travel to the regional lymph node to prime T cells. Macrophages can release the antigens for DC uptake and subsequent T cell activation. The tumor-specific T cells proliferate and infiltrate into the tumor, where they can exert their cytotoxic effects. The anti-PD-L1 prevents the binding of tumor PD-L1 and T-cell PD-1, thereby inhibiting deactivation of the T cells. Reprinted from *Nature Communications* **10**, 1899 (2019).

5.4 Conclusion

In summary, we present an approach to initiate and stimulate immune-mediated eradication of cancer cells using synergistic nanomedicines. OxPt/DHA nanoparticles efficiently prevent the decomposition and degradation by encapsulation of and increase tumor uptake of DHA and OxPt prodrugs to harness the anticancer and immunostimulatory properties of ROS-producing DHA and OxPt. By inducing CRT exposure and HMGB-1 release, OxPt/DHA directly converted treated tumors into an *in situ* vaccine, recruiting antigen-presenting DCs and macrophages, facilitating cancer cell phagocytosis, enhancing antigen processing and presentation, and finally increasing intratumoral infiltration of $CD8^+$ T cells to significantly potentiate checkpoint blockade immunotherapy. The animals treated by metronomic dosing of OxPt/DHA and α-PD-L1 were tumor-free for at least three months and immunized against live tumor cell challenge by generating a long-term antitumor immunity. The scalable and tunable nature of NCP synthesis should allow their rapid optimization to lead to potential clinical candidates for combination therapy with immune checkpoint inhibitors.

5.5 Materials and methods

Materials, Cell Lines, and Animals. All starting materials were purchased from Sigma-Aldrich and Fisher (USA), unless otherwise noted, and used without further purification. 1,2-dioleoyl-snglycero-3-phosphate (DOPA), 1,2-dioleyl-sn-glycero-3-phosphocholine (DOPC), cholesterol, and 1,2-distearoyl-sn-glycero-3-phosphoethanolamine-N-[amino(polyethylene glycol)2000] (DSPE-PEG2k) were purchased from Avanti Polar Lipids (USA).

Murine colon adenocarcinoma cell CT26 and MC38 cells, mouse mammary carcinoma cell 4T1, mouse Lewis lung carcinoma cell LL/2 were all obtained from the American Type Culture Collection (ATCC, Rockville, MD). CT26 cells were cultured in RPMI 1640, MC38, 4T1 and LL/2 were grown in Dulbecco's Modified Eagle's Medium (DMEM), respectively, supplemented with 10% FBS, 100 U/mL penicillin G sodium and 100 μg/mL streptomycin sulfate in a humidified atmosphere containing 5% CO_2 at 37ºC. Mycoplasma was tested before use by MycoAlert detection kit (Lonza Nottingham, Ltd.).

BALB/c female mice (6 weeks, 18-22 g), C57BL/6 female mice (6 weeks, 18-22 g), $Rag^{2-/-}$ female mice (6 weeks, 18-22 g), and SD/CD female rats (6 weeks, 160-200 g) were provided by Harlan-Envigo Laboratories, Inc (USA). We have complied with all ethical regulations for animal testing and research, with a study protocol reviewed and approved by the Institutional Animal Care and Use Committee (IACUC) at the University of Chicago.

Preparation and characterization of OxPt/DHA. OxPt-bare was synthesized according to our previous reported method with minor modifications.[61] Briefly, an aqueous solution of OxPt-bp (5 mg, 25 mg mL^{-1}) was added to a 5mL of 0.3M Triton X-100/1.5M 1-hexanol in cyclohexane and stirred vigorously for 15 min in the presence of DOPA (4 mg, 200 mg mL^{-1} in $CHCl_3$). An aqueous solution of $Zn(NO_3)_2$ (20 mg, 100 mg mL^{-1}) was added to a 5mL of 0.3M Triton X-100/1.5M 1-hexanol in cyclohexane and stirred vigorously for 5 minutes. The $Zn(NO_3)_2$-containing microemulsion was added dropwise to the Pt-containing microemulsion and stirred vigorously for 30 min at room temperature. After the addition of 10 mL ethanol, OxPt-bare was obtained by centrifugation at 11,628g. The resulting pellet was washed once with 50% cyclohexane/ethanol and once with THF/ethanol and finally redispersed in THF and filtered through a 200nm syringe

filter.The loadings of OxPt in the particles were determined by inductively coupled plasma-mass spectrometry (ICP-MS, Agilent 7700X, Agilent Technologies, USA) after digestion with nitric acid. OxPt/DHA was prepared by adding a THF solution (80 μL) of DOPC, cholesterol, DSPE-PEG2k, chol-DHA (3:1.5:1.5:1), and OxPt-bare to 500 μL of 30% (v/v) ethanol/water at 50 °C. OxPt/DHA particles with higher DHA:OxPt ratios were similarly prepared by increasing the amounts of chol-DHA. The mixture was stirred at 1,700 rpm for 1 min. THF and ethanol were completely evaporated and the solution was allowed to cool down to room temperature. The particle size and ζ-potential were determined by dynamic light scattering (DLS) using a Zetasizer (Nano ZS, Malvern, UK). Transmission electron microscopy (TEM, Tecnai Spirit, FEI, USA) was used to observe the morphology. To determine chol-DHA loading, OxPt/DHA was centrifuged at 11,337g for 30 min, the supernatant was removed and the particles were re-suspended in THF which dissolves the lipid layer to release chol-DHA. The amount of chol-DHA in the nanoparticle suspension was then determined by liquid chromatography-mass spectrometry (LC-MS, Agilent 6540, Agilent Technologies, USA). The stability of OxPt/DHA was evaluated at 4 ^{o}C in 5% dextrose or 37 ^{o}C in phosphate buffered solution (PBS) containing BSA. The chol-DHA content in the nanoparticles was also determined by LC-MS before or after the addition of Triton X-100 to disrupt the lipid bilayer.

***In vitro* cytotoxicity.** CT26 cells or MC38 cells were seeded in 96-well plates at a density of 2 $\times 10^3$ cells per well and allowed to adhere for 24 h. Cells were then treated with different concentrations of free OxPt, free DHA, free OxPt plus DHA (OxPt+DHA), OxPt NCP, Zn/DHA, or OxPt/DHA at 1:0.5, 1:1 or 1:2 molar ratios of OxPt to DHA for another 72 h. Cell viability was

detected by 3-(4,5-dimethylthiazol-2-yl)-5-(3-carboxymethoxyphenyl)-2-(4-sulfophenyl)-2H-tetrazolium (MTS) assay (Promega, Madison, WI) according to the manufacturer's instructions.

Preparation of fluorescently labeled NCP particle. 0.5 g OxPt-bp was mixed with 1.52 mL water and 0.98 mL 3 M NaOH to prepare a neutralized OxPt-bp stock solution. The solution was added to excess amount of xylenol orange solid to prepare a saturated solution. The saturated solution was centrifuged at 12000 rpm for 5 min to remove any solid before used to prepare bare NCP particle.

Bare particle was prepared according to our previously reported method by changing the prodrug solution to xylenol orange-saturated prodrug solution. Coated fluorescent particle was prepared by the same method as OxPt/DHA particle. 30% of DOPC was changed to DOPE-FITC and all Chol-DHA was changed to chol-pyro.

Apoptosis analysis. CT26 cells seeded in 6-well plates (5×10^4 cells/well) were treated with free OxPt, free DHA, OxPt+DHA, OxPt NCP, Zn/DHA, or OxPt/DHA at a concentration of 10 μM OxPt and/or 5 μM DHA for 24 h, then harvested, washed twice with ice-cold PBS, stained with Alexa Fluor 488-Annexin V and propidium iodide (PI) for 15 min at room temperature in the dark, and then analyzed by flow cytometry (LSR II, BD, USA).

Cell cycle assay. Treated CT26 cells as described above were collected, washed twice with ice cold PBS, fixed with 70% ethanol at 4ºC overnight and treated with RNase A for 45 min, and followed by PI staining for 30 min. The alteration of cell cycle was analyzed by flow cytometry.

ROS generation. CT26 cells were treated with free OxPt, free DHA, OxPt+DHA, OxPt NCP, Zn/DHA, or OxPt/DHA at a concentration of 10 μM OxPt and/or 5 μM DHA for 24 h, then incubated with 10 μM H_2DCFDA (Thermo Fisher, USA) for another 1 h. The cells were collected, washed twice with ice-cold PBS, and analyzed by flow cytometry.

Cytochrome c release. After treatment with free OxPt, free DHA, OxPt+DHA, OxPt NCP, Zn/DHA, or OxPt/DHA at a concentration of 10 μM OxPt and/or 5 μM DHA for 24 h, CT26 cells were stained with MitoTracker Red CMXRos (100 μM) for 1 h, then fixed with 4% paraformaldehyde for 10 min, permeabilized with 0.2% Triton X-100 for 10 min, incubated with anti-cytochrome c (eBioscience, diluted 1 : 100) for 2 h, stained with DAPI for 10 min, and observed under CLSM (Olympus, FV1000).

CRT exposure analysis. CT26 cells seeded in 6-well plates (2×10^5 cells/well) were cultured with free drugs or nanoparticles at a dose of 10 μM OxPt and/or 5 μM DHA for 24 h. The treated cells were collected, incubated with Alexa Fluor 488-CRT antibody (Enzo cat # ADI-SPA-601-488-F, diluted 1:100) for 2 h, stained with PI, and analyzed by flow cytometer to identify CRT exposure. The fluorescence intensity of stained cells was gated on PI^- cells.

For surface detection of CRT, CT26 cells were seeded on 10 mm^2 glass coverslips placed in 6-well plates at a density of 2×10^5 cells per well. After treatment, cells were washed with PBS three times, incubated with Alexa Fluor 488-CRT antibody (diluted 1:100) for 2 h, stained with

DAPI, and observed under CLSM using 405 nm and 488 nm lasers for visualizing nuclei and CRT expression on the cell membrane, respectively.

Detection of HMGB-1 release. CT26 cells seeded in 6-well plates (2×10^5 cells/well) were cultured with free drugs or nanoparticles at a dose of 10 μM OxPt and/or 5 μM DHA for 24 h. The medium was collected for detection of HMGB-1 release by ELISA according to manufacturer instructions (Chondrex, Redmond, WA).

Phagocytosis assay. Bone-marrow-derived dendritic cells and macrophages were isolated according to previously published protocols.[65, 66] Briefly, the hind legs of mice were cut away just above the hip and below the ankle. The muscle was cut away and the bones were soaked in 70% ethanol for 30 seconds. In a sterile environment, the ends of each bone were cut away and an insulin syringe filled with RPMI complete media was inserted into the exposed end of the bone and used to flush out the bone marrow into a cell culture dish filled with RPMI complete media. This process was repeated until the bone appeared white and translucent. For DC activation, bone-marrow-derived monocytic cells were cultured with GM-CSF (20 ng/mL) and IL-4 (10 ng/mL) for 6 days, then non-adherent cells in the culture supernatant were harvested and the expression of CD11c, CD11b, F4/80 and Gr-1 was analyzed by flow cytometry to determine the purity of DC before further use. For macrophage differentiation, bone-marrow-derived monocytic cells were cultured with M-CSF (20 ng/mL) for 6 days, then adherent cells were harvested and the expression of CD11c, CD11b and F4/80 was analyzed by flow cytometry to determine the purity of macrophage before further use. TdTamato transfected MC38 tumor cells were first incubated with

OxPt/DHA at 10 μM OxPt and 5 μM DHA for 24 h, then treated tumor cells were co-cultured with F4/80-labelled (eBioscience) macrophages or CD11c-labelled (eBioscience) DCs at ratio of 1:1 for 4 h at 37 °C. Cells were then collected, washed twice with cold PBS, resuspended in PBS, analyzed by flow cytometry, and calculated as the percentage of $TdTamato^+$ cells within $F4/80^+$ macrophages or $CD11c^+$ DCs.

Antigen presentation. Bone-marrow-derived dendritic cells or macrophages were co-cultured with PBS-, OxPt-, DHA-, OxPt+DHA-, or OxPt/DHA-treated MC38 cells. After 48h, the cells were washed twice with PBS and stained with anti-CD16/32 (clone 93; eBiosciences) to reduce nonspecific binding to FcRs followed by CD11b (M1/70), CD11c (N418), F4/80 (BM8), and SIINFEKL/H-2Kb (25-D1.16), and yellow fluorescence dye (all from eBioscience).

Priming assay. 1×10^6 MC38 cells were treated with 100 μM OxPt and/or 50 μM DHA for 24 h, and then injected into the footpads of C57Bl/6 mice. Six days later, popliteal lymph node cells were collected by homogenizing and filtering the organ through a sterile cell strainer (40 μm; Fisher Scientific). 1×10^5 lymph node cells were cultured in complete culture medium in the presence of MC38 cell lysates killed by freeze-thaw cycle in 200 μL medium in round-bottom 96-well plates. Three days later, the supernatants were harvested and IFN-γ secretion was determined by ELISA (eBioscience). The ability of OxPt/DHA treated MC38 cell lysates to enhance the secretion of INF-γ by T cells was also compared with a known antigen KSPWFTTL and the positive control CD3ε plus CD28.

Antitumor vaccination. 1×10^6 MC38 cells treated with 10 μM OxPt and/or 5 μM DHA for 24 h were subcutaneously inoculated into the lower flank of 6-week-old female C57Bl/6 mice or $Rag^{2-/-}$ mice. Seven days later, 2×10^5 living MC38 cells were inoculated into the contralateral flank. Mice were then monitored for the appearance of tumors for 30 days.

***In vivo* pharmacokinetics and biodistribution analysis.** SD/CD rats were intravenously (i.v.) injected with OxPt/DHA at an OxPt dose of 6 mg/kg (2.14 mg/kg DHA). The blood was collected at 5 min, 30 min, 1 h, 3 h, 5 h, 8 h, 24 h, and 48 h post-injection and immediately centrifuged at 604 x g for 10 min to harvest plasma samples. 25 μL plasma was digested with concentrated nitric acid for 24 h and analyzed for Pt concentration by ICP-MS. Another 25 μL plasma was added 5 μL 20% Triton X-100 to disrupt the lipid bilayer of the nanoparticles, chol-DHA was then extracted from plasma by adding 100 μL ethyl acetate, followed by centrifugation at 6708g for 10 min. The chol-DHA content was quantified by LC-MS.

BALB/c mice were subcutaneously injected in the right flank with 1×10^6 CT26 cells. When the tumors reached ~100 mm^3, mice were intraperitoneal (i.p.) administration of OxPt/DHA at an OxPt dose of 8 mg/kg (2.86 mg/kg DHA). The blood was collected at 1 h, 3 h, 5 h, 8 h, 24 h, 48 h, and 72 h post-injection and immediately centrifuged at 604g for 10 min to harvest plasma samples. The content of Pt and chol-DHA were quantified by ICP-MS and LC-MS, respectively. The livers, lungs, spleens, kidneys, bladders and tumors were also harvested, digested with concentrated nitric acid for 24 h, and analyzed for Pt concentration by ICP-MS.

***In vivo* toxicity on mice.** Balb/c mice received i.p. doses of Zn/DHA at 5 mg/kg DHA every three days for a total of fifty doses. C57Bl/6 mice were received a weekly i.p. dose of OxPt/DHA at 60 mg/kg OxPt (21.5 mg/kg DHA) for a total of four doses or a single i.p. dose at 80 mg/kg OxPt (28.6 mg/kg DHA). The activity level and body weights of the mice were monitored for toxicity.

SD/CD rats received weekly i.v. doses of OxPt/DHA or free OxPt at 8 mg/kg OxPt (2.86 mg/kg DHA) for a total of three doses to measure peripheral neuropathy. A hind paw was subjected to a constant heat source through a 3/8" glass pane and tested for the time to withdrawal to measure peripheral neuropathy.

***In vivo* anticancer efficacy.** 1×10^6 cells CT26 or MC38 cells were subcutaneously injected into the right flank region of 6-week BALB/c, C57Bl/6 wild type or $Rag^{2-/-}$ mice, respectively. 12 days after tumor inoculation, mice were i.p. dosed with 8 mg/kg OxPt, 2.86 mg/kg DHA, and/or 75 μg PD-L1 antibody once every 3 days for up to 12 doses. Tumor growth was monitored by measurement with a digital caliper, where tumor volumes were calculated as follows: $(\text{width}^2 \times \text{length})/2$.

Tumor-free BALB/c mice were challenged with 5×10^6 CT26 cells on the contralateral flank three months after the tumors disappeared. The mice were monitored for 1 month and then rechallenged with 5×10^4 unrelated 4T1 cells.

Surgery control. 1×10^6 cells CT26 were subcutaneously injected into the right flank region of 6-week BALB/c. 12 days after tumor inoculation, mice were anesthetized for surgical removal of the tumors with skin glue to close the wound. Two weeks after surgery, 5×10^6 live CT26 cells

were subcutaneously injected into the left flank and monitored for tumor development and growth, as previously described.

Immunofluorescence assay. Tumors were collected 2 days or 12 days after the first treatment, and frozen tissue sections of 5 μm thickness were prepared using a cryostat. The sections were fixed in acetone for 10 min at -20°C, blocked with 2% BSA for 1 h, and incubated with individual primary antibodies against CD11c (eBioscience), F4/80 (eBioscience), CD3ε (Santa Cruz) or CD8 (Thermo Scientific) overnight at 4 ºC, followed by incubation with dye-conjugated secondary antibodies for 1 h at room temperature. After staining with DAPI for another 10 min, the sections were then washed twice with PBS and observed under CLSM.

Flow cytometry assay for immune response. Tumors were harvested on 12 days after the first treatment, treated with 1 mg/mL collagenase I (Gibco™, USA) for 1 h, and ground with the rubber end of a syringe. Cells were filtered through nylon mesh filters and washed with PBS. The single-cell suspension was incubated with anti-CD16/32 (clone 93; eBiosciences) to reduce nonspecific binding to FcRs. Cells were further stained with the following fluorochrome-conjugated antibodies: CD45 (30-F11), CD3ε (145-2C11), CD8 (53-6.7), CD11b (M1/70), CD11c (N418), F4/80 (BM8), MHC II (AF6-120.1), CD86 (PO3), CD206 (C068C2), CD44 (IM7), CD62L (MEL-14), and Zombie NIR (eBioscience). LSR FORTESSA (BD Biosciences) was used for cell acquisition, and data analysis was carried out using FlowJo software (TreeStar, Ashland, OR). All antibodies were diluted 1:200 for use.

ELISPOT assay. Tumor-specific immune responses to IFN-γ was measured *in vitro* by ELISPOT assay (Mouse IFN-γ ELISPOT Ready-SET-Go!®; Cat. No. 88-7384-88; eBioscience). A Millipore Multiscreen HTS-IP plate was coated overnight at 4 °C with anti-Mouse IFN-γ capture antibody (diluted 1:250). Single-cell suspensions of splenocytes were obtained from MC38 tumor-carrying mice on 12 days after the first treatment and seeded onto the antibody-coated plate at a concentration of 2×10^5 cells/well. Cells were incubated with or without KSPWFTTL stimulation (10 μg/ml; in purity 495%; PEPTIDE 2.0) for 48 h at 37°C and then discarded. The plate was then incubated with biotin-conjugated anti-IFN-γ detection antibody (diluted 1:250) at room temperature for 2 h, followed by incubation with Avidin-HRP for 2 h at room temperature. 3-amino-9-ethylcarbazole (AEC) substrate solution (Sigma, Cat. AEC101) was added for cytokine spot detection.

5.6 References

1. Siegel, R.L., Miller, K.D. & Jemal, A. Cancer statistics, 2015. *CA: a cancer journal for clinicians* **65**, 5-29 (2015).
2. Sharif, S., O'Connell, M.J., Yothers, G., Lopa, S. & Wolmark, N. FOLFOX and FLOX regimens for the adjuvant treatment of resected stage II and III colon cancer. *Cancer Invest* **26**, 956-963 (2008).
3. Loon, K.V. & Venook, A.P. Curable Patient With Metastatic Colorectal Cancer: Balancing Effective Therapies and Toxicities. *Journal of Clinical Oncology* **32**, 991-996 (2014).
4. Xiang, B., Snook, A.E., Magee, M.S. & Waldman, S.A. Colorectal cancer immunotherapy. *Discov Med* **15**, 301-308 (2013).
5. Midgley, R. & Kerr, D. Immunotherapy for colorectal cancer: a challenge to clinical trial design. *Lancet Oncol* **1**, 159-168 (2000).
6. Ledford, H. Melanoma drug wins US approval. *Nature* **471**, 561 (2011).
7. Fleisher, B. & Ait-Oudhia, S. A retrospective examination of the US Food and Drug Administration's clinical pharmacology reviews of oncology biologics for potential use of therapeutic drug monitoring. *Onco Targets Ther* **11**, 113-121 (2018).

8. Alsaab, H.O. et al. PD-1 and PD-L1 Checkpoint Signaling Inhibition for Cancer Immunotherapy: Mechanism, Combinations, and Clinical Outcome. *Front Pharmacol* **8**, 561 (2017).

9. Llosa, N.J. et al. The vigorous immune microenvironment of microsatellite instable colon cancer is balanced by multiple counter-inhibitory checkpoints. *Cancer Discov* **5**, 43-51 (2015).

10. Le, D.T. et al. PD-1 Blockade in Tumors with Mismatch-Repair Deficiency. *N Engl J Med* **372**, 2509-2520 (2015).

11. Overman, M.J. et al. Nivolumab ± ipilimumab in treatment (tx) of patients (pts) with metastatic colorectal cancer (mCRC) with and without high microsatellite instability (MSI-H): CheckMate-142 interim results. *Journal of Clinical Oncology* **34**, 3501-3501 (2016).

12. Overman, M.J. et al. Nivolumab in patients with metastatic DNA mismatch repair-deficient or microsatellite instability-high colorectal cancer (CheckMate 142): an open-label, multicentre, phase 2 study. *Lancet Oncol* **18**, 1182-1191 (2017).

13. Boland, C.R. & Goel, A. Microsatellite instability in colorectal cancer. *Gastroenterology* **138**, 2073-2087 e2073 (2010).

14. Vilar, E. & Gruber, S.B. Microsatellite instability in colorectal cancer-the stable evidence. *Nat Rev Clin Oncol* **7**, 153-162 (2010).

15. Ebert, P.J.R. et al. MAP Kinase Inhibition Promotes T Cell and Anti-tumor Activity in Combination with PD-L1 Checkpoint Blockade. *Immunity* **44**, 609-621 (2016).

16. Tesniere, A. et al. Immunogenic death of colon cancer cells treated with oxaliplatin. *Oncogene* **29**, 482-491 (2010).

17. Sato, E. et al. Intraepithelial CD8+ tumor-infiltrating lymphocytes and a high CD8+/regulatory T cell ratio are associated with favorable prognosis in ovarian cancer. *Proc Natl Acad Sci U S A* **102**, 18538-18543 (2005).

18. Gonzalez-Aparicio, M. et al. Oxaliplatin in combination with liver-specific expression of interleukin 12 reduces the immunosuppressive microenvironment of tumours and eradicates metastatic colorectal cancer in mice. *Gut* **60**, 341-349 (2011).

19. Hernandez-Alcoceba, R. & Berraondo, P. Immunochemotherapy against colon cancer by gene transfer of interleukin-12 in combination with oxaliplatin. *Oncoimmunology* **1**, 97-99 (2012).

20. He, C. et al. Core-shell nanoscale coordination polymers combine chemotherapy and photodynamic therapy to potentiate checkpoint blockade cancer immunotherapy. *Nature communications* **7** (2016).

21. Tu, Y. The discovery of artemisinin (qinghaosu) and gifts from Chinese medicine. *Nat Med* **17**, 1217-1220 (2011).

22. Thomas, S.E. et al. p53 and translation attenuation regulate distinct cell cycle checkpoints during endoplasmic reticulum (ER) stress. *J Biol Chem* **288**, 7606-7617 (2013).

23. Obeid, M. et al. Calreticulin exposure dictates the immunogenicity of cancer cell death. *Nat Med* **13**, 54-61 (2007).

24. Green, D.R., Ferguson, T., Zitvogel, L. & Kroemer, G. Immunogenic and tolerogenic cell death. *Nat Rev Immunol* **9**, 353-363 (2009).

25. Zitvogel, L. et al. Immunogenic tumor cell death for optimal anticancer therapy: the calreticulin exposure pathway. *Clin Cancer Res* **16**, 3100-3104 (2010).

26. Ghiringhelli, F. et al. Activation of the NLRP3 inflammasome in dendritic cells induces IL-1beta-dependent adaptive immunity against tumors. *Nat Med* **15**, 1170-1178 (2009).

27. Liu, X. et al. CD47 blockade triggers T cell-mediated destruction of immunogenic tumors. *Nat Med* **21**, 1209-1215 (2015).

28. Munzone, E. & Colleoni, M. Clinical overview of metronomic chemotherapy in breast cancer. *Nat Rev Clin Oncol* **12**, 631-644 (2015).

29. Simon, R. & Norton, L. The Norton-Simon hypothesis: designing more effective and less toxic chemotherapeutic regimens. *Nat Clin Pract Oncol* **3**, 406-407 (2006).

30. Hespel, C. & Moser, M. Role of inflammatory dendritic cells in innate and adaptive immunity. *Eur J Immunol* **42**, 2535-2543 (2012).

31. Cella, M., Sallusto, F. & Lanzavecchia, A. Origin, maturation and antigen presenting function of dendritic cells. *Curr Opin Immunol* **9**, 10-16 (1997).

32. Mellman, I. & Steinman, R.M. Dendritic cells: specialized and regulated antigen processing machines. *Cell* **106**, 255-258 (2001).

33. Unanue, E.R. Antigen-presenting function of the macrophage. *Annu Rev Immunol* **2**, 395-428 (1984).

34. McWilliam, A.S., Nelson, D., Thomas, J.A. & Holt, P.G. Rapid dendritic cell recruitment is a hallmark of the acute inflammatory response at mucosal surfaces. *J Exp Med* **179**, 1331-1336 (1994).

35. Postow, M.A., Callahan, M.K. & Wolchok, J.D. Immune Checkpoint Blockade in Cancer Therapy. *J Clin Oncol* **33**, 1974-1982 (2015).

36. Ribas, A. et al. Association of response to programmed death receptor 1 (PD-1) blockade with pembrolizumab (MK-3475) with an interferon-inflammatory immune gene signature. *Journal of Clinical Oncology* **33**, 3001-3001 (2015).

37. Chen, P.L. et al. Analysis of Immune Signatures in Longitudinal Tumor Samples Yields Insight into Biomarkers of Response and Mechanisms of Resistance to Immune Checkpoint Blockade. *Cancer Discov* **6**, 827-837 (2016).

38. Ljubimova, J.Y. et al. Toxicity and efficacy evaluation of multiple targeted polymalic acid conjugates for triple-negative breast cancer treatment. *J Drug Target* **21**, 956-967 (2013).

39. Xiong, Y., Zhao, Y., Miao, L., Lin, C.M. & Huang, L. Co-delivery of polymeric metformin and cisplatin by self-assembled core-membrane nanoparticles to treat non-small cell lung cancer. *J Control Release* **244**, 63-73 (2016).

40. Quader, S. & Kataoka, K. Nanomaterial-Enabled Cancer Therapy. *Mol Ther* **25**, 1501-1513 (2017).

41. Huynh, E. & Zheng, G. Cancer nanomedicine: addressing the dark side of the enhanced permeability and retention effect. *Nanomedicine (Lond)* **10**, 1993-1995 (2015).

42. Sykes, E.A., Chen, J., Zheng, G. & Chan, W.C. Investigating the impact of nanoparticle size on active and passive tumor targeting efficiency. *ACS Nano* **8**, 5696-5706 (2014).

43. Taniguchi, R. et al. Adequately-Sized Nanocarriers Allow Sustained Targeted Drug Delivery to Neointimal Lesions in Rat Arteries. *Mol Pharm* **13**, 2108-2116 (2016).

44. Choi, H.S. et al. Design considerations for tumour-targeted nanoparticles. *Nat Nanotechnol* **5**, 42-47 (2010).

45. Davis, M.E., Chen, Z.G. & Shin, D.M. Nanoparticle therapeutics: an emerging treatment modality for cancer. *Nat Rev Drug Discov* **7**, 771-782 (2008).

46. Allen, T.M. & Cullis, P.R. Drug delivery systems: entering the mainstream. *Science* **303**, 1818-1822 (2004).

47. Irvine, D.J., Hanson, M.C., Rakhra, K. & Tokatlian, T. Synthetic Nanoparticles for Vaccines and Immunotherapy. *Chem Rev* **115**, 11109-11146 (2015).

48. Chinen, A.B., Ferrer, J.R., Merkel, T.J. & Mirkin, C.A. Relationships between Poly(ethylene glycol) Modifications on RNA-Spherical Nucleic Acid Conjugates and Cellular Uptake and Circulation Time. *Bioconjug Chem* **27**, 2715-2721 (2016).

49. Jin, H. et al. Tumor Ablation and Therapeutic Immunity Induction by an Injectable Peptide Hydrogel. *ACS Nano* **12**, 3295-3310 (2018).

50. Lu, Y. et al. Exploiting in situ antigen generation and immune modulation to enhance chemotherapy response in advanced melanoma: A combination nanomedicine approach. *Cancer Lett* **379**, 32-38 (2016).

51. Meckes, B., Banga, R.J., Nguyen, S.T. & Mirkin, C.A. Enhancing the Stability and Immunomodulatory Activity of Liposomal Spherical Nucleic Acids through Lipid-Tail DNA Modifications. *Small* **14** (2018).

52. Luan, X. et al. Tumor priming using metronomic chemotherapy with neovasculature-targeted, nanoparticulate paclitaxel. *Biomaterials* **95**, 60-73 (2016).

53. Krysko, D.V. et al. Immunogenic cell death and DAMPs in cancer therapy. *Nat Rev Cancer* **12**, 860-875 (2012).

54. Obeid, M. et al. Calreticulin exposure is required for the immunogenicity of gamma-irradiation and UVC light-induced apoptosis. *Cell Death Differ* **14**, 1848-1850 (2007).

55. Apetoh, L. et al. The interaction between HMGB1 and TLR4 dictates the outcome of anticancer chemotherapy and radiotherapy. *Immunol Rev* **220**, 47-59 (2007).

56. Apetoh, L. et al. Toll-like receptor 4-dependent contribution of the immune system to anticancer chemotherapy and radiotherapy. *Nat Med* **13**, 1050-1059 (2007).

57. Kroemer, G., Galluzzi, L., Kepp, O. & Zitvogel, L. Immunogenic cell death in cancer therapy. *Annu Rev Immunol* **31**, 51-72 (2013).

58. Mosely, S.I. et al. Rational Selection of Syngeneic Preclinical Tumor Models for Immunotherapeutic Drug Discovery. *Cancer Immunol Res* **5**, 29-41 (2017).

59. Goodwin, T.J. & Huang, L. Investigation of phosphorylated adjuvants co-encapsulated with a model cancer peptide antigen for the treatment of colorectal cancer and liver metastasis. *Vaccine* **35**, 2550-2557 (2017).

60. Juneja, V.R. et al. PD-L1 on tumor cells is sufficient for immune evasion in immunogenic tumors and inhibits CD8 T cell cytotoxicity. *The Journal of Experimental Medicine* (2017).

61. Liu, D., Poon, C., Lu, K., He, C. & Lin, W. Self-assembled nanoscale coordination polymers with trigger release properties for effective anticancer therapy. *Nat Commun* **5**, 4182 (2014).

62. Sheldrick, G.M. Crystal structure refinement with SHELXL. *Acta Crystallogr C Struct Chem* **71**, 3-8 (2015).

63. Dolomanov, O.V., Bourhis, L.J., Gildea, R.J., Howard, J.A.K. & Puschmann, H. OLEX2: a complete structure solution, refinement and analysis program. *Journal of Applied Crystallography* **42**, 339-341 (2009).

64. Sheldrick, G.M. A short history of SHELX. *Acta Crystallogr A* **64**, 112-122 (2008).

65. Madaan, A., Verma, R., Singh, A.T., Jain, S.K. & Jaggi, M. A stepwise procedure for isolation of murine bone marrow and generation of dendritic cells. *Journal of Biological Methods* **1**, e1 (2014).

66. Gonçalves, R. & Mosser, D.M. The isolation and characterization of murine macrophages. *Current protocols in immunology*, 14.11. 11-14.11. 16 (2015).

CHAPTER 6. Summary Discussion and Future Directions

6.1 Summary

There exists a wide variety of treatment options for cancer patients, which can be given individually, concurrently, or sequentially depending on the individual's needs and the makeup of the tumor(s). Despite decades of research and development of new treatment strategies, cancer remains a deadly disease with a large footprint. Nanotechnology offered a promise of improving known and existing cancer therapies by improving tumor deposition to enhance anticancer efficacy and reduce off-target side effects. However, nanotechnology has mostly fallen short of these ambitions and has shown limited application in clinical settings, particularly with respect to chemotherapies and biological therapies.

This body of work uses rational chemical design to address known challenges addressing cancer therapy and drug delivery by nanoparticles as they exist in the current state of the field. Long-circulating nanoparticles lead to greater potential for tumor accumulation of the drugs, while the NCP design largely limits the detrimental effects associated with prolonged free drug circulation. NCPs can solubilize and isolate precious cargoes to reduce the total drug dosed and limit degradation by enzymes (e.g. nucleases and P450s) or the environment (e.g. blood). The NCP nanotechnology described here carries a Pt(IV) phosphoramic acid-containing prodrug, which can be reduced to a Pt(II) species, and a lipid- or cholesterol-conjugated disulfide-containing prodrug, which can be cleaved to the parent species. Investigations showed that the NCP layers dissociate after cell internalization, exposing the components to intracellular conditions and releasing the parent species. The drug cargoes can then exert the expected mechanisms of action, leading to cancer prevention and/or treatment in a variety of human and murine cancer models grown on mice. The work evolves from addressing a specific change (miRNA levels) in human xenograft tumors on immunocompromised mice to broad immune activation to combine chemotherapy with immunotherapy.

6.1.1 Implications on the field

A high-profile meta-analysis of nanoparticle delivery literature highlighted low accumulation of nanoparticles in solid tumors, raising critical questions about the state of the field. In fact, the NCPs described here do not vastly outperform the described field, but have consistently shown greater therapeutic windows – the ratio of toxic drug dose to effective drug dose – and/or improved anticancer effect than the parent drug counterparts. The prodrugs in NCPs lead to sustained active drug levels for longer periods of time than observed with administration of the related free drugs. Taken together, these suggest that the proportion or concentration of nanoparticles in the tumor may not be as relevant as the levels of active drug compound, assuming the cargo's mechanism(s) of action is retained. The chemical design of nanoparticles is crucial, as significantly different release kinetics were observed between chol-PTX and chol-DHA under the same conditions due to the possibility of hydrolysis as a release mechanism. Thus, the various covalent and non-covalent methods of drug loading warrant investigation to determine how release kinetics and mechanisms of the payloads from the nanoparticle affect efficacy.

These works have highlighted miRNA and chemotherapy, but when taken together with the other concurrent work in the Lin group, NCPs have proven to be a versatile nanocarrier technology. As a platform, this allows for a nearly limitless sea of opportunities for cancer medicines, including application of previously under- and unutilized classes of drugs. Ultimately, the goal is to improve the therapeutic outcome for human cancer patients, rather than murine ones. NCPs have demonstrated the potential for clinical translation, and will have the opportunity to make an impact on cancer treatment via the work of Dr. Lin's startup company, Coordination Pharmaceutical, Inc., which is currently running two phase 1 clinical trials on treating advanced tumors with NCPs.

6.1.2 Limitations of work

NCPs are a promising clinical platform, but the results reported in this thesis are not necessarily directly translatable to cancer patients. Human cancer biology is extremely complex, and the models used to examine both mechanism and effect might not recapitulate human disease. First, the release kinetics and mechanisms are investigated in solution with somewhat arbitrary concentrations and ratios between the conjugates and reagents (i.e. ascorbate and glutathione). Modeling the intracellular or intratumoral environment by adding only a few reagents (Triton X-100, ascorbate, glutathione) eliminates the majority of biological components which may be confounding factors in vitro or in vivo. This simplification also necessitates a fairly homogenous mixture, which discounts the effects and limitations of spatial distribution for both the drug payloads and the reducing agents. Second, most toxicity and anticancer efficacy studies performed were relatively short-term and superficial investigations. Body weight is an easy readout for toxicity, but does not necessarily reflect some toxicities like depletion of WBCs or uncontrolled stimulation of the immune system. Similarly, ELISAs of proteins and cytokines in the blood are helpful indications that the liver or spleen are not significantly damaged, but these were evaluated on the order of days and weeks after treatment, rather than months and years for which patients can live with the side effects of treatment. Third, the anticancer efficacy studies were performed by implanting human or murine cancer cells that had been grown ex vivo for a significant amount of time. While this form of research has many advantages, tumors are forming from cells with mostly similar genetic makeups which discounts inter- and intrapatient heterogeneity of human tumors. The most important caveat to this work is that mice, rats, and dogs used for preclinical research are not that closely related to humans. Therefore, the implications of these works should be limited to illustrating potential as a new drug delivery agent.

6.2 Future directions

NCPs' modular synthesis lends itself to exchanging components to accommodate different drug payloads. I have demonstrated that this can be useful to deliver nucleic acids and small molecules with reactive moieties, but there are many more molecules that have shown strong results in vitro with limited in vivo activity. Specifically, some possible NCP components can be active drug metabolites, therapeutic peptides, therapeutic siRNAs or miRNAs. Alternately, the biocompatible Zn component of the NCP core can be exchanged for other metals with radiosensitizing or imaging properties, such as Hf or Gd, respectively.

Additional investigations into the reported NCPs can address the limitations described earlier. The release mechanism(s) and kinetics of prodrugs from NCPs and active compounds from prodrugs can be studied in more representative biological environments, such as intratumorally. Probing the nanoparticles' effects on kidney function and bone marrow cells can lead to further characterization of the long-term toxicity profile of the nanoparticles. Experimentally and technically, these next steps are simplest to investigate in subcutaneously implanted tumors on the flanks of mice. However, use of more representative or advanced autochthonous models and ultimately larger animals like dogs and non-human primates can yield more meaningful data.

For a broader impact, the described NCPs and the other previously reported NCPs should be systematically compared to establish rational design principles. Currently, there are NCPs with or without a Pt(IV) phosphoramic acid component, a DSPE- or cholesterol-disulfide-conjugated component, and a DSPE or cholesterol-alkyl-conjugated component. Systematic analysis can determine if and how each of these components affect nanoparticle packing, stability, pharmacokinetics, biodistribution, drug release, etc. In total, this can start to understand why NCPs appear to succeed where other nanocarriers have failed.